Anisotropic Interaction Potentials between Helium and Linear Molecules from Crossed Beam Experiments

Thesis by

Jarosław W. Winniczek

In Partial Fulfillment of the Requirements
for the Degree of
Doctor of Philosophy

California Institute of Technology
Pasadena, California
1985

Submitted May 28, 1985

in memory of
Mark Olson

ACKNOWLEDGEMENTS

Behind every thesis and its author stands the advisor. He not only provides the material support and environment, but more importantly, the inspiration, guidance and scientific atmosphere to bring a graduate student's work to fruition. My advisor, Professor Aron Kuppermann is no exception. His constant attention to detail has provided much insight into understanding experimental results and solving technical difficulties. He gave me great independence in the course of this work, allowing me to learn from my sometimes costly mistakes. Yet, he was available to give his full guidance when I needed it. By providing ample opportunity for experience, rather than handing down orders and preconceived ideas, he was and is a true teacher. I thank him for all that he has done.

I owe very special thanks to Dave Moll and Charlie Koerting. Not only have both been sources of scientific advice and discussion, but most importantly they were great friends. Some of my most pleasant times were spent with them and their wives (or fiancées), Sharon and Sierra. We climbed mountains; we explored deserts; we wandered through narrow canyons; we sailed around islands; we skied down slopes; we slept under the stars and in the rain; we forded roaring mountain streams and rivers; in short, we had a wonderful time.

The other members of the Kuppermann group, past and present, deserve special thanks for all the comradeship they provided. They include: Mark Keil, Ron Rianda, Jack Kaye, Dorothy Flanagan, Jim Garvey, Diane Hood, Joe Wong, Vasil Babamov, Kerry Walzl, Garth Parker, Antonio Laganà, Paul Hipes, Steve Cuccaro and Jin Qiu. I could not possibly forget to mention Adria McMillan and Heidi Tanciar, the fantastic group secretaries. Roza Kuppermann, group member for the longest time by far, was always a gracious hostess at the beach or in Altadena.

I would also like to acknowledge the friendship of individuals whom I had the pleasure of knowing during my studies at Caltech: Matt Johnson, Albert Lin, Francis Celii, Maureen Hanratty, Calvin Thomsen, and the residents, past and present, of M-J House.

This thesis would not have been possible without the valuable assistance from the Chemistry Department shops personnel. Bill Schuelke, Tony Stark, Guy Duremberg, Delmar Dill and Ray Garcia of the instrument shop, Jim Olson and Jim Gangwer of the maintenance shop, with Tom Dunn and Jack Guledjian of the electronics shop, all have been involved in the construction, design and maintenance of the crossed-molecular beam apparatus. They provided much innovation and skill in designing and implementing additions to the experiment when all I could give them was a disorganized verbal description of what I needed. Not only did they perform superb work, but they were also good friends. It was a distinct pleasure to work with these guys.

Dr. Randy Sparks and Brian Reid deserve special thanks for providing the design for the multi-channel scaler used in the inelastic scattering experiments.

This thesis is dedicated to the memory of Mark Olson. Mark was a truly wonderful and warm friend. He was a great companion on hikes in the local mountains and national parks. He loved to attend concerts, films and plays. He had a rare combination of unpredictable spontaneity and extreme constraint. His honesty and unpretentiousness were remarkable, at times quite humorous. I miss him very much.

I would like to thank my aunts Olga and Gabriela for all the care and concern they have shown me. Finally, I thank my parents, Hildegarda and Sergiusz, for all the love and support they have provided and continue to provide.

ABSTRACT

Anisotropic interaction potentials between helium and linear molecules have been studied experimentally and theoretically to examine the relationship between the potential and the scattering differential cross-section, and to extract these potentials from crossed-molecular beam data.

Chapter 2 presents the measurement of total (elastic and inelastic) differential scattering cross sections for He + CO_2, CS_2, OCS at a relative collision energy of about 65 meV with a crossed molecular beam apparatus. Anisotropic interaction potentials were extracted from these data, by way of an infinite order sudden approximation analysis. Several different anisotropic potential models were used in this analysis. The necessity for considering the anisotropy in the position of the well minimum as well as of its depth is demonstrated. A potential is proposed for He + OCS that reflects the symmetry of OCS, with a minimum number of modeling parameters.

In Chapter 3 a detailed sensitivity analysis of the total and rotational state-to-state differential cross-section (DCS) is performed on an empirical potential energy surface for He + CO_2. The infinite order sudden approximation is used to calculate the cross-sections. The sensitivity analysis consists of: 1) a large scale modification of

the parameters that determine the anisotropic potential, and 2) an infinitesimal variation of these parameters to obtain a relative sensitivity function for the DCS. From these we demonstrate the effect each potential parameter has on the cross-sections. Despite the fact that this highly quantum system displays no classical effects such as rainbow scattering, we have shown that the quantal DCS oscillations contain significant information regarding the depth and width of the potential well and its anisotropy. Much of this information can be extracted from total-DCS scattering data. However the rotationally inelastic DCS contain a substantial amount of additional information regarding the shape of the potential energy surface.

Some of the conclusions reached in Chapter 3 indicate that the measuring of rotationally inelastic differential cross-sections can provide significantly greater insight into the nature of the potential than does the total DCS. In Chapter 4 we develop the means for simulating experimentally observable data from the potential for a given set of apparatus conditions. In Chapter 5 we describe modifications made to the crossed-beam apparatus in order to observe this inelasticity and present preliminary results for He + CO_2.

TABLE OF CONTENTS

CHAPTER 1

INTRODUCTION

The detailed nature of van der Waals type interaction potentials between molecules is of great interest in understanding a wide range of phenomena, which include equations of state for gases and liquids, gas transport properties, and spectral line broadening. Van der Waals interaction potentials are rather weak compared to the forces that hold molecules together (by two to three orders of magnitue), yet characteristcally they have a similar shape, a strongly repulsive region at small distances separation, which falls down to an atractive well with increasing distance, the well rises to weak monotonically decreasing attractive region at large distances. In the past several years a concerted effort has been undertaken by experimentalists and theorists at quantifing the shape of a many of these potetenial energy surfaces. Although excellent methods have been developed for predicting the above mentioned phenomena, they depend upon the knowledge of the potential energy surface. Currently, the most direct and conclusive approach for the determination of the potential is offered by crossed molecular beam experiments. The region of the potential to which these experiments are most sensitive is the vicinity of the attractive well. Since this well results from the balance between the competing long-range atractive and the short range repuslive forces, its *ab-initio* evaluation is more difficult than for the adjacent regions. As a result, the experimental approach is the best one for the determination of the potential well characteristics.

The major significance of a crossed-beam experiment is that it permits the observation of effects which are the result of a single collision. The direction and velocity with which the collision partners leave the region of interaction will be a function of that interaction. Depending upon the nature of the potential the collision may be elastic or inelastic. Rotational inelasticity arises when then potential is anisotropic, i.e. it lacks spherical symmetry. Vibrational and electronic exciations are possible only at higher collision energies.

In this thesis, interaction potentials between helium and various linear molecules are extrated from crossed-beam data. A beam of helium atoms intersects a beam of molecules under conditions that preclude more than one collision. A detector measures the number and in some cases, the velocity of the He atoms scattered by the molecular beam as a function of the angle away from the axis of the He beam. The potential is extracted from the data by a fitting procedure, where parameters characterizing the potential are varied and adjusted untill the potential can be used to accurately simulate the observed data. This requires that the potential model be flexible and unbiased with respect to a specific shape, and that the simulation procedure accurately reflects the conditions of the experiment.

In Chapter 2 we present empirically measured total (sum of elastic and inelastic) differential cross-sections (DCS) for the scattering of helium by carbon dioxide, carbon disulfide and carbonyl sulfide. From these data we extract the interaction potentials between the three scattering systems. Careful attention is paid to the simulation of experimental conditions in the potential fitting procedure to ensure that the potentials obtained are not affected by experimental artifacts. To ensure that the final results are not biased by the potential model, we employ a large number of models, both isotropic (spherical) and anisotropic. These models are appropriately manipulated to show that only anisotropic potentials provide a good accounting of the observed data, and that this anisotropy is with respect to the position of the van der Waal well minimum as well as the depth of that minimum.

In Chapter 3 we provide a detailed analysis of the sensitivity of the total, elastic, and rotationally inelastic differential cross-sections to the parameters of the He + CO_2 potential. We wish to know: a) How do features of the potential effect the observed cross-sections? b) How sensitive are the data to a given potential parameter and therefore how significant is this parameter? These questions are important in understanding the results of Chapter 2 as well as predicting the results and sensitivites of data which measure rotationally inelastic cross-sections.

The conclusions of Chapter 3 indicate that the measuring of rotationally inelastic differential cross-sections can provide significantly greater insight into the nature of the potential than does the total DCS. In Chapter 4 we develop the means for simulating experimentally observable data from the potential for a given set of apparatus conditions. In Chapter 5 we describe modifications made to the crossed-beam apparatus in order to observe this inelasticity and present preliminary results for He + CO_2.

CHAPTER 2

POTENTIALS FOR
He + CO_2,He + CS_2, and He + OCS

Anisotropic Intermolecular Potentials for He + CO_2,He + CS_2, and He + OCS from Crossed Beam Scattering Experiments [a]

Jarosław W. Winniczek [b] and Aron Kuppermann

Arthur Amos Noyes Laboratory of Chemical Physics [c]
California Institute of Technology, Pasadena, California 91125

(received)

Crossed molecular beams total (elastic and inelastic) differential scattering cross sections have been measured for He + CO_2, CS_2, OCS at a relative collision energy of about 65 meV. Anisotropic interaction potentials were extracted from these data, by way of an infinite order sudden approximation analysis. Several different anisotropic potential models were used in this analysis. The necessity for considering the anisotropy in the position of the well minimum as well as of its depth is demonstrated. A potential is proposed for He + OCS that reflects the symmetry of OCS, with a minimum number of modeling parameters.

---

[a] This work was supported in part by the Air Force Office of Scientific Research (Contract No. F49620-79-C-0187).

[b] Work performed in partial fulfillment of the requirements for the Ph. D. degree in Chemistry at the California Institute of Technology.

[c] Contribution No. —

1. INTRODUCTION

Interaction potentials between an atom and a molecule have been and continue to be subjects of a large body of theoretical and experimental work.[1,2] The successful application of the infinite order sudden approximation (IOSA) to many systems has made possible the prediction of a wide range of phenomena.[1-3,11-13] However, the prediction from first principles of these potentials is still difficult in the range where there is a transition between the long range attractive van der Waals forces and the short range repulsive forces. The accurate determination of the potential requires the analysis of a variety of experimental data; the differential cross section (DCS) is one of the most sensitive observables to the potential.

A potential that has attracted a particularly large interest is one for He + CO_2.[3-6,11-15] Which of its characteristics account for various features of the DCS? How uniquely can they be obtained from the data? Is there evidence for potential anisotropy in the data and how can it be studied?

These questions have been addressed previously. Pack[14] showed that anisotropy of r_m dampens the DCS quantal oscillations, while ϵ anisotropy has a much smaller effect on on the DCS. Eno and Rabitz[7] computed sensitivity coefficients for Pack's[14] Lennard-Jones potential to show that the DCS is most sensitive to r_m, with decreasing sensitivity for ϵ, r_m anisotropy, and ϵ anisotropy. Raff and coworkers[11,12] compared the effects of variations of potential energy surface topography on the observed integral inelastic cross sections and total differential cross sections for He + CO_2; they found that the total (elastic plus inelastic) DCS is by far more sensitive to potential anisotropy than the state resolved integral cross sections. Faubel *et al.*[9,10] measured the He + O_2 and He + N_2 DCS's, where the total DCS oscillations are very slightly dampened and potential anisotropy can only be extracted by measuring the rotationally inelastic DCS. The DCS for He + CO_2 was first observed by Keil *et al.*[5] and further analyzed by Parker *et al.*[4] to extract a potential which provied a good fit to their data. Recently, Keil and Parker[3] fitted the He + CO_2 DCS along with a large set of data which included integral cross sections, transport properties, and linewidths. However, as we will point out, they did not correctly account for certain instrumental parameters in analyzing the DCS data. Because of this problem they could not obtain the correct He + CO_2 potential.

In this paper we present and analyze total (elastic and inelastic) differential scattering cross section data for He + CO_2, CS_2 and OCS. In section 2 we summarize the infinite order sudden approximation (IOSA) and show that it is valid for the analysis of the data collected. In section 3 we list various anisotropic potential forms used to fit our data. In section 4 we describe our crossed-molecular beam apparatus and its operating conditions. In section 5 we describe the data analysis procedure used to extract an interaction potential from the data. In section 6 we present our data and various potential models that fit the data. We demonstrate the need for anisotropy in well minimum position as well as in the well depth in order to account for all the features of the scattering data. An anisotropic potential for He + OCS is proposed that includes the lack of an inversion center with a minimum number of variable parameters. In section 7 we calculate various bulk properties for He + CO_2 from our best fit potential and compare them to reported experimental measurements. The paper concludes with a summary of our results and conclusions in section 8.

2. THEORY

The theoretical basis for extraction of non-spherically symmetric potentials from differential scattering cross-section data for atom-linear molecule collisions is the infinite order sudden approximation (IOSA) for rotationally inelastic transitions. Parker and Pack have presented an excellent derivation of the IOSA;[13] hence we will only demonstrate its highlights and how it applies specifically to obtaining non-spherical intermolecular potentials. At the collision energies under consideration here, vibrational excitations are not accessible, while vibrational deexcitations are not possible since the molecules of interest herein are in their vibrational ground states.[23] Therefore, it is reasonable to treat the target molecule as a rigid rotor of length R (the distance between the end atoms) and with a moment of inertia I. Let $\underset{\sim}{r}$ be the position vector of the incident atom with respect to the center-of-mass of the molecule and γ be the angle between $\underset{\sim}{r}$ and the oriented molecular axis $\underset{\sim}{R}$. The nuclear motion Hamiltonian for this system is therefore

$$\hat{H} = -\frac{\hbar^2}{2\mu r}\frac{\partial^2}{\partial r^2}r + \frac{\hat{L}^2}{2\mu r^2} + \frac{\hat{j}^2}{2I} + V(r,\gamma) \qquad (1)$$

where μ is the atom-molecule reduced mass, and $\hat{L}$ and $\hat{J}$ are the orbital angular momentum and molecular angular momentum operators, respectively.

Solution of the corresponding nuclear motion Schrödinger equation can be achieved by expanding the scattering wave function in eigenfunctions of the total angular momentum $\hat{\mathbf{J}} \equiv \hat{J} + \hat{L}$. This yields a set of radial differential equations in the coefficients of this expansion coupled by the matrix elements of $V(r,\gamma)$ in the expansion basis set. These equations can be decoupled by imposing the centrifugal sudden approximation[18,19] and the energy sudden approximation.[16.17] This involves replacement of the orbital and molecular angular momentum operators in (1) by the constants

$$\hat{L}^2 \simeq \hbar^2 \bar{l}(\bar{l}+1) \tag{2}$$

and

$$\hat{j}^2 \simeq \hbar^2 \bar{j}(\bar{j}+1) \tag{3}$$

where $\bar{l}$ and $\bar{j}$ are effective angular momentum quantum numbers which are chosen differently to accommodate various versions of the theory. Collectively, these two approximations are known as the IOSA,[13] which yields the decoupled ordinary differential equations

$$\left[\frac{d^2}{dr^2} + k_{\bar{j}}{}^2 - \frac{\bar{l}(\bar{l}+1)}{r^2} - \frac{2\mu}{\hbar^2}V(r,\gamma)\right]\phi_{\bar{l}}(r;\gamma) = 0 \tag{4}$$

in terms of which the differntial cross sections of interest can be calculated as indicated below. Equation (4), in which γ plays the role of a parameter (since it does not appear in differential operators), can be solved in a manner analogous to a spherical potential problem,[21] by requiring that the wave function vanish at the origin and that at large r it behave as

$$\phi_{\bar{l}} \underset{r\to\infty}{\longrightarrow} k_{\bar{j}}^{-1/2}\left\{\mathrm{e}^{-i(k_{\bar{j}}r-\bar{l}\pi/2)} - \mathrm{e}^{i[k_{\bar{j}}r-\bar{l}\pi/2+2i\eta_{\bar{l}}(\gamma))]}\right\} \tag{5}$$

where $\eta_{\bar{l}}(\gamma)$ is the phase shift for a given fixed atom-molecule orientation and the wave vector $k_{\bar{j}}$ is given by[13]

$$k_{\bar{j}}^{2} = \frac{2\mu}{\hbar^2}\left[E - \frac{\hbar^2\bar{j}(\bar{j}+1)}{2I}\right] \tag{6}$$

for a given total energy E.

The scattering amplitude for a given angle of incidence γ is obtained in a manner identical to that for a spherical scattering problem[21]

$$f^{k_{\bar{j}}}(\gamma \mid \theta) = \frac{i}{2k_{\bar{j}}}\sum_{l}(2l+1)\{1-\mathrm{e}^{2i\eta_l(\gamma)}\}P_l(\cos\theta) \tag{7}$$

It can be shown that the rotational state-to-state differential cross-section is given in this approximation by[13]

$$\sigma(j' \leftarrow j \mid \theta) = \frac{k_{\bar{j}}^2}{(2j+1)k_j{}^2}\sum_{m_j}\left| < j'm_j|f^{k_{\bar{j}}}(\gamma \mid \theta)|jm_j >_{\mathrm{BF}}\right|^2 \tag{8}$$

Note that this result is independent of the choice of $\bar{l}$. (The matrix elements of $f(\gamma \mid \theta)$ are evaluated in the spherical harmonics of the body–fixed coordinates - BF).

The implication of the IOSA is that the approach angle γ does not change appreciably during the collision.[13,15,17] This can be related to two operationally more tangible conditions which ensure the validity of the IOSA: a) the relative collision translational energy is large compared to the spacing between rotational energy levels - i.e., the collision is not strongly influenced by the rotation b) rotational transitions occur at small impact parameters, i.e., at low values of orbital angular momentum. The first condition is easily met by the systems considered in this paper where the relative collisional energy of 65 meV is much greater than the largest spacing of 6 meV between consecutive open rotational states. The second condition is met by systems which have a small well depth relative to the collisional energy, implying that the incident atom is mainly influenced by the repulsive wall of the interaction potential which occurs at short distances r. The well depths for the collisions studied herein and other helium-molecule systems are less than 8 meV.[3-5,8-10,28-36]

The total differential cross-section, from a state j to all accessible states j', can be obtained by summing equation (8) over all j'. If $\bar{j}$ is chosen to be equal to j then this sum yields

$$\sigma(\theta) = 1/2 \int_0^{\pi} |f(\gamma \mid \theta)|^2 \sin\gamma \, d\gamma \tag{9}$$

This expression is independent of the initial rotational state j, and hence represents the total differential cross-section for all initial states.

3. POTENTIAL MODELS

In order to insure a reasonable uniqueness and reliability of the potential derived from experimental data, we have employed several parametrized models for the He-molecule potential. These include highly flexible central field potentials as well as anisotropic potentials. The spherical models were chosen to demonstrate their inappropriateness as models of the interaction of He with the molecules considered in this work. The anisotropic potential models were chosen for their simplicity, flexibility and physical reasonability. Simplicity is an important criterion, since an excess of parameters in a least-squares fitting procedure can lead to an over-determined system with high correlations between parameters, yielding a final potential that is not unique.

3.1. Anisotropy Parameterization

We consider three forms for expressing the anisotropy of a potential.

1) Legendre expansion representation

A reasonably obvious form for expressing the angular dependence of an atom-rigid linear molecule potential is a Legendre polynomial expansion

$$V(r,\gamma) = \sum_{n=0}^{\infty} V_n(r) P_n(\cos\gamma) \tag{10}$$

The $V_n(r)$'s are spherical-type potentials with several parameters each. If the expansion proceeds beyond $n = 2$ the number of parameters becomes too large to insure the uniqueness and independence of each parameter.

2) Multi-center representation

An alternate means for constructing an atom-molecule anisotropic potential is to express it as a sum of pairwise isotropic atom-atom potentials:[4]

$$V(r,\gamma) = \sum_{i=1}^{n} V_i(r_i) \tag{11}$$

where

$$r_i = [r^2 + z_i^2 - 2rz_i \cos\gamma]^{1/2} \tag{12}$$

and z_i is the distance from the center-of-mass of the molecule to the center of atom i; it may be positive or negative.

3) Angular-dependent parameter representation

A third way of specifying anisotropy, is by giving a γ dependence to the parameters of an otherwise spherical potential,[14]

$$V(r,\gamma) = V\left[r, \epsilon(\gamma), r_m(\gamma), \beta(\gamma)\right] \tag{13}$$

where ϵ is the well depth, r_m is the well minimum position, and β is a shape parameter which depends on the parameterization of V. Some parameterizations may have more than one shape parameter, all of which may have angular dependence. The angular dependence of any parameter A (such as ϵ, r_m, β) may be expressed in terms of Legendre polynomials[14]

$$A(\gamma) = \sum_{n=0}^{\infty} A^{(n)} P_n(\cos\gamma) \tag{14}$$

In general, for symmetric molecules, the expansion is carried only to two non-vanishing terms $n = 0$ and $n = 2$, because an excess of parameters may not yield a unique potential via the least squares procedure as the data are not sensitive enough for their determination. Another parameterization for $A(\gamma)$ (also for symmetric molecules), especially useful for r_m, is an elliptical form[5]

$$r_m(\gamma) = r_{m\perp}\left[\frac{1 + q\sin^2\gamma}{1+q}\right]^{1/2} \tag{15}$$

where

$$q \equiv \left[\frac{r^2_{m\perp}}{r^2_{m\parallel}} - 1\right] \tag{16}$$

while $r_{m\perp}$ is r_m for the $\gamma = \frac{\pi}{2}$ configuration and $r_{m\parallel}$ is r_m for $\gamma = 0$ or π.

Since each parameter has been given an angular dependence, the angular dependence of the potential can be complicated such that its expansion contains Legendre polynomials to large orders. We then expect that the angular-dependent parameter representation would be the most flexible potential form.[4,5]

3.2. Shape Parameterization

The shape of the anisotropic potential in any of the three representations given above can be expressed in terms of well known spherical-like potentials. The potentials we consider are:

1) Lennard-Jones (LJ)[24a]

$$V(r) = \epsilon\left[\left(\frac{r_m}{r}\right)^{12} - 2\left(\frac{r_m}{r}\right)^{6}\right] \tag{17}$$

This potential is quite simple, but not very flexible. The width of the well is fixed and is approximately fitted by a $\beta = 6.3$ Morse potential of equal depth and well position.

2) Morse [41]

$$V(r) = \epsilon\left[\mathrm{e}^{2\beta(1-r/r_m)} - 2\mathrm{e}^{\beta(1-r/r_m)}\right] \tag{18}$$

The shape parameter β gives the Morse much greater flexibility in specifying the well width than the LJ. It determines not only the well width but also the long range van der Waals' part of the potential to which scattering experiments do not have much sensitivity. The van der Waals dispersion terms are quite amenable to theoretical calculation, and inculsion of them in a potential is appropriate for improving the Morse potential.

3) Lennard-Jones-Dispersion (LJ8)

The Lennard-Jones potential may be modified to include the C_6 dispersion term. This gives some flexibility to the well width but it is subject to the control of the dispersion term [4]

$$V(r) = \frac{2\epsilon r_m^{12} - C_6 {r_m}^6/2}{r^8} - \frac{C_6}{r^6} - \frac{3\epsilon {r_m}^8 - 3C_6 {r_m}^2/2}{r^8} \tag{19}$$

4) Morse-Spline-van der Waals (MSV)

A better parameterization is one in which the dispersion and well width are more independent. At short distances we use the Morse potential, while at long distances we use the van der Waals dispersion potential. The two are joined with a cubic spline.[28,36,37]

$$V(r) = \epsilon\left[\mathbf{e}^{2\beta(1-r/r_m)} - 2\mathbf{e}^{\beta(1-r/r_m)}\right] \tag{20a}$$

$$\text{for} \quad r \le r_{MS}$$

$$V(r) = \left[S_1(r_{SV} - r)^2 + S_3\right](r_{SV} - r)$$

$$+ \quad \left[S_2(r - r_{MS})^2 + S_4\right](r - r_{MS}) \tag{20b}$$

for $r_{MS} < r < r_{SV}$

$$V(r) = -\frac{C_6}{r^6} - \frac{C_8}{r^8} \tag{20c}$$

for $r \geq r_{SV}$

where $r_{MS} = r_m(1 + \ln 2/\beta)$ is the inflection point of the Morse function.The spline coefficients S_1, S_2, S_3 and S_4 are determined by continuity conditions imposed on the potential and its derivative at r_{MS} and r_{SV}. The Spline-van der Waals junction is maintained at $r_{SV}/r_m = 1.6$.[27–30]

5) Morse-Morse-Spline-van der Waals (MMSV)

The MSV potential still has some inflexibility since the well width parameter β also affects the repulsive wall. This interdependence can be removed by using a different Morse function for the repulsive region to yield [27,36,37]

$$V(r) = \frac{\epsilon}{\omega}\left\{\mathrm{e}^{2(\beta' - r\beta\omega/r_m)} - 2\mathrm{e}^{(\beta' - r\beta\omega/r_m)}\right\} \tag{21a}$$

for $r/r_m < 1 - \ln 2/\beta$

$$V(r) = V_{\mathrm{MSV}}(r) \tag{21b}$$

for $r/r_m \geq 1 - \ln 2/\beta$

where $\omega = \dfrac{\beta' - \ln 2}{\beta - \ln 2}$

The constant ω is used to impose a smooth transition between the two Morse functions.

6) Simons-Parr-Finlan-Dunham (SPFD)

Another very flexible potential is the SPFD (Simons-Parr-Finlan-Dunham) potential which includes a van der Waals term. It is esentially a polynomial in r^{-1} and is given by $^{38-40}$

$$V(r) = \epsilon\left\{b_0\lambda^2\left(1+\sum_{i=1}^{N} b_i\lambda^i\right) - 1\right\} \qquad (22a)$$

$$\text{for} \quad r \le r_f$$

$$V(r) = -\frac{C_6}{r^6} - \frac{C_8}{r^8} \qquad (22b)$$

$$\text{for} \quad r > r_f$$

$$\text{where} \quad \lambda = 1 - \frac{r_m}{r}$$

The two highest order shape parameters b_{N-1} and b_N are fixed by smoothness conditions in joining to the van der Waals point at r_f, which is made equal to $1.6r_m$. In general N is 2 or 3, giving one or two shape parameters, b_0 and b_1. The SPFD potential is not well behaved for $r < 0.6r_m$, and oscillates in that region. This problem can be eliminated by replacing it by an exponential of the form^{24} $V(r) = Ae^{-br}$ for $r < r_W$, where A and b are fixed by smoothness at r_W. The choice for r_W is usually $0.7r_m$, and has little effect on the final results since experimental data are not sensitive to this highly repulsive region.

7) Hartree-Fock Dispersion (HFD) [32,33]

$$V(r) = \epsilon e^{\beta(1-r/r_m)} - \frac{C_6}{r^6} - \frac{C_8}{r^8} e^{-(\alpha r_m/r-1)^2} \qquad (23a)$$

$$\text{for} \quad r < \alpha r_m$$

$$V(r) = \epsilon e^{\beta(1-r/r_m)} - \frac{C_6}{r^6} - \frac{C_8}{r^8} \qquad (23b)$$

$$\text{for} \quad r \geq \alpha r_m \; .$$

Only one of ϵ, β, or α can be specified for a given potential: the other two are fixed by the requirement that at r_m the potential be equal to $-\epsilon$ and its derivative vanish. For the purposes of this study we will either vary α or ϵ, in addition to r_m.

The potentials with the correct long range behavior are the MSV, MMSV, SPFD, and HFD. We would then expect that they should give the most accurate representation of the potential. The long range dispersion terms constrain the potential in regions where the sensitivity of the experiment is low, while giving it the necessary flexibility in regions of greater sensitivity. The van der Waals dispersion term coefficients C_6 and C_8 for He + CO_2 have been accurately calculated by Pack.[26] Both coefficients have significant anisotropy which can represented by a second order Legendre expansion

$$C_n(\gamma) = C_n^{(0)} + C_n^{(2)} P_2(\cos\gamma)$$

where $n = 6$ or 8

The differential cross-section is most sensitive to the spherical average of the C_6 coefficient $C_6^{(0)}$.[6] The sensitivitites for the anisotropy of C_6 ($C_6^{(2)}$) and for the C_8 coefficient with its anisotropy ($C_8^{(0)}$ and $C_8^{(2)}$) are at least a factor of 50 smaller than for than for $C_6^{(0)}$.[6] In the fitting procedure described in section 5 the dispersion coefficients are assumed to be known, i.e., are not treated as fitting parameters. Therefore for the purposes of this paper, $C_6^{(0)}$ must be known with the greatest accuracy, while the other coefficients are less significant and need not be known as accurately. This is fortunate since at present calculations for the dispersion terms for He + CS_2 and He + OCS have not been published, and hence they must be approximately derived from those for He + CO_2 and the polarizibilities $\alpha(X)$ [24ab,25,26], where $X = CO_2$, CS_2, and OCS. For $C_6^{(0)}$ a quite reliable relation is

$$C_6^{(0)}(X) = C_6^{(0)}(CO_2)\frac{\alpha(X)}{\alpha(CO_2)}$$

The expressions for the other coefficients are more complicated and are less accurate.

The disperison term for the multi-center potentials is splined into each of the three centers i using

$$V_i(r_i)_{VDW} = \frac{-1}{3}\left(\frac{C_6(\gamma)}{r^6} + \frac{C_8(\gamma)}{r^8}\right)$$

where r_i is the distance from the center i to a point in space with the coordinates (r, γ), and is given by equation (12). As a result, in the dispersion region the $V_i(r_i)$ contain γ-dependent parameters. This means that physically the potential is no longer a sum of three spherically symmetric potentials having different centers, over the full range of r. This procedure is adopted because of numerical convenience, since the resulting fits are not strongly affected by it.

For the multi-center potential we use the spectroscopic bond distances[22] to locate the origins of each of the central potentials from the center-of-mass of the molecule; the z_i in equation (12) is not treated as an adjustable parameter in the least-squares parameter fitting procedure. This provides a reasonable constraint on the potential, such that the least-squares algorithm produces a physically acceptable potential.

4. EXPERIMENTAL

The crossed molecular beam apparatus used in these experiments is depicted in Figure 1. The basic constituents are a doubly differentially pumped supersonic primary (probe) beam source, an effusive secondary (target) beam source, and a doubly differentially pumped mass spectrometer. The beams cross at right angles, while the mass spectrometer detects the scattered signal at angles in the plane or out of the plane of the beams. This section will attempt to present a reasonably thorough description of the apparatus, with emphasis on improvements made since previous descriptions.[28,42–45] The primary and secondary beam sources along with the movable detector are mounted on a 130 cm diameter base (Fig. 1). The base is covered by a stainless steel bell jar, which may be raised to permit access to internal components. The 1250 liter vacuum chamber is pumped by four liquid nitrogen (l –N_2) trapped 6 inch oil diffusion pumps and 2 l –N_2 and refrigeration-trapped mercury pumps with a total pumping speed of 1850 l/sec. Pressures as low as 2×10^{-8} torr can be achieved with no load on the system.

The primary beam (PB) is produced via a supersonic expansion through a 70 micron diameter nozzle (Nz) consisting of platinum or molybdenum electron microscope aperture. The central portion of the resultant beam is collected by a 0.64 mm diameter conical brass skimmer

(Sk) at a distance of 11 mm from the nozzle. The edge of the skimmer aperture is sharp and has an inner surface half-angle of 28 degrees and outer surface angle of 34 degrees. The skimmer-nozzle distance is remotely variable, and was optimized at 11 mm for strongest scattered signal and smallest background. The gas that does not pass through the skimmer is pumped by a 6 inch oil diffusion pump (DP1) with a 250 l/sec pumping speed for helium (400 l/sec for air). The pressure in this chamber is 2×10^{-3} torr[48] with a 1300 torr stagnation pressure of He behind the nozzle. This pressure is limited by the pumping speed of DP1, and not by dimer formation. After passing the skimmer the beam enters a second differentially pumped chamber. This is pumped by a 100 l/sec (for helium) mercury diffusion pump. Under the above conditions the pressure in this chamber is 4×10^{-5} torr.[48] The chamber contains a chopper (Ch) to modulate the beam at 160 Hz for lock-in signal detection. Also enclosed in the chamber is a slotted-disk velocity selector (VS)[47] used for measuring the beam velocity distribution; it is moved out of the beam path during scattering experiments. The beam emerges into the scattering chamber through a collimating aperture (1.52 mm diamter) 79 mm from the scattering center.

The velocity distribution data obtained with the VS consist of signal from the mass-spectrometer as a function of the selector rotational frequency to which the velocity is directly proportional. These (after correction for the fact that a mass spectrometer is a number density detector rather than a flux detector) are fitted via least-squares to the function [46]

$$f(v) = cv^3 \mathbf{e}^{-\frac{m}{2kT_s}(v-v_s)^2} \tag{24}$$

where m is the mass of the beam molecule. In this expression there are two variable parameters T_s and v_s. The constant c is determined be requiring $f(v)$ to be normalized over v. The gas stream temperature T_s and stream velocity v_s are related to the effective nozzle stagnation temperature T_0, a Mach number M, and the heat capacity ratio $\gamma = C_p/C_v$ [46]

$$T_s = \frac{T_0}{1 + \frac{\gamma - 1}{2} M^2} \tag{25}$$

and

$$v_s{}^2 = \frac{kT_s \gamma M^2}{m} \tag{26}$$

The secondary beam (SB) enters the scattering center directly from a capillary array (CA), located 6 mm before it. The array consists of 2 micron diameter glass tubules 610 microns long fused into a single disk, with a 50% open area to gas flow.[49] The array is held in place by an o-ring which vacuum seals and exposes a 1.6 mm diameter region of the disk. This assembly is mounted on a block which may be tilted up via a remotely activated pneumatic bellows so as to uncross the beams. In the crossed position the bellow presses the source assembly firmly against a fixed flat surface to ensure precise alignment.

The secondary beam conditions are chosen to maximize the intensity, mimimize the angular spread and eliminate secondary collisions of the primary beam with secondary beam molecules. The first criterion requires the greatest stagnation pressure behind the capillary array, while the other two require a lower stagnation pressure. Also, a lower stagnation pressure reduces the formation of van der Waals dimers. An optimum pressure occurs in the range of 3 to 5 torr. This results in a scattering chamber pressure of approximately 3×10^{-7} torr, for condensible (on l-N_2 cooled surfaces) gases such as CO_2 , CS2, and OCS. These pass through the capillary array with little expansion cooling as their low Mach number ($M \approx 1$) indicates . This was determined by measuring the velocity distribution of the secondary beam, with the capillary array placed in the position of the primary beam nozzle.

The optimal operating condition of the beam sources are summarized in Table I. The angular distributions were measured using the mass spectrometer, and characterized approximately by the shape of a cosine squared distribution.

Primary beam atoms that are scattered by the secondary beam, pass through a detector entrance aperture of 1.52 mm diameter, 8.0 cm from the scattering region. This aperture is equipped with a gate valve (GV) which separates the scattering (main) chamber from a buffer chamber. A second aperture, also 1.52 mm in diameter, 4.5 cm away from the first one, isolates this buffer chamber from the main part of the mass spectrometer (MS) vacuum chamber. The center of the mass spectrometer ionization region is located 2.4 cm from that second aperture. The penumbral cone determined by these apertures is 4 degrees and spans a 5.8 mm diameter at the scattering region. The umbral cone angle is 0.67 degrees with a 1.6 mm diameter span at the scattering center. This ensures that the entire scattering region is in full view of the mass spectrometer. The angular resolution, as determined from the angles subtended by the umbral and penumbral projections at the ionization region, is in the range 0.67 to 1.41 degrees. However, the overall apparatus angular resolution ($\Delta\theta_{lab}$) is a composite of this and the size of the scattering volume. The value of this parameter is crucial; a correct potential cannot be obtained from the data without it. For the beam conditions under consideration, the overall angular apparatus resolution was determined to be 1.5 degrees by a careful analysis of He + Ar scattering data. The potential parameters for an MMSV and a SPFD potential were fitted along with $\Delta\theta_{lab}$ to the He + Ar scattering data obtained on our apparatus. The potential parameter values agreed with those obtained at other laboratories.[33–36] The same value of $\Delta\theta_{lab}$ was obtained by making it the only variable parameter and fitting it to our data with the SPFD potential parameters fixed at values obtained at those laboratories. This is a new value of the resolution parameter and supersedes the value of about 1.9 deg. which we previously reported.[28–30] The main reason for this change is that the previous value of $\Delta\theta_{lab}$ was obtained by fitting the data to a very rigid Lennard-Jones potential.[24] We will discuss the implications of this change in $\Delta\theta_{lab}$ on the He + CO_2 potential in section 6.

The detector buffer chamber is pumped by a 5 l/sec ion pump and the mass spectrometer chamber is pumped by a 25 l/sec ion pump. During experiments a liquid helium cryopump (CP) carries most of the pumping load of the main MS chamber. The pump is surrounded by a l–N_2–cooled jacket. The ionizer (I) directly below the cryo-pump is cooled with l–N_2 to reduce radiation heating of the pump. This shielding allows the pump to operate for over four hours with an initial fill of one liter of liquid He. The cryo-pump has an estimated pumping speed of 300 to 400 l/sec at pressures 7.0 to 15×10^{-10} torr. A bake-out is necessary in order to maintain these pressures.

The mass-spectrometer ionizer is a high-efficiency electron-impact device, [50] operated at 15 mA to 25 mA emission current. The ions produced in it are focused into a quadupole mass filter and after mass selection are detected by a Channeltron[51] electron multiplier. The Channeltron may be operated in a pulse counting (digital) mode or current measuring (analog) mode. In the pulse counting mode the Channeltron pulses are passed through a pulse amplifier-discriminator[52] and proceed to a gated phase sensitive pulse counter.[53] The counter is controlled and read by a PDP11/03 computer.[54] The gating signal originates at a photodiode light sensor on the primary beam chopper (Ch); it is amplified, shaped, phase shifted and then serves as the gate for the counter. The computer reads the counter at twice the 160 Hz chopper frequency, i.e., when the chopper passes the primary beam and when it blocks the beam. The computer then subtracts the "blocked" signal from the "unblocked" to obtain a phase sensitive digital lock-in reading. Due to the finite length of the read cycle, followed by a counter clear pulse, the counter has a reduced duty time of 95%. This, however, is not a problem since we further gate our signal to an 85% duty time so as not to count pulses while the primary beam intensity rises and falls as the chopper teeth edges cross the beam path. The duration of the gate is maintained by a quartz oscillator to ensure precision and reproducibility of each gate pulse.

In the analog detection mode the Channeltron current is measured by a home-built electrometer with a sensitivity of about 50 picoamperes.[56] The electrometer output goes into a PAR HR-8 phase sensitive lock-in amplifier,[55] which also makes use of the chopper photodiode. The lock-in output is read by an analog-to-digital converter of the PDP-11/03.

As stated above, the mass-spectrometer has two angular degrees of freedom. It may by positioned from 12 degrees below the plane of the beams to 40 degrees above that plane. Motion in the plane of the beams ranges from -20 to 110 degrees, where the positive angular direction is from the primary beam to along the secondary beam, with the primary beam axis serving as the orgin. The positioning reproducibility in both directions is better than ±0.05 degrees.

Accurate and precise alignment is a necessary prerequisite for good scattering intensity measurements. The principal axis of alignment consists of: the primary beam nozzle, the skimmer, the exit aperture, a 0.05 mm alignment pin placed at the scattering center, the two detection apertures and cross-hairs at the back of the mass spectrometer housing. All of these are made to lie along a line to the specified tolerances of 0.05 mm with the aid of a precision surveyor's telescope. After this alignment is completed the secondary beam source is aligned with the scattering center pin, where the latter is rotated to 90 degrees from the primary beam axis.

The in- and out-of-plane angles are measured wth the help of two sychro position sensors.[57] The accuracy of these sensors is determined by measuring the distance along a rotation arc at a large radius. The agreement of the sensor readings with these measurements is within 0.05 degrees. The accuracy with which the detector tracks the scattering center is measured as the distance from the scattering center pin to the front aperture. The maximum variation is 0.1 mm over the full range of both angular degrees of freedom; this corresponds to a maximum deviation of 0.1 degrees in the tracking of the scattering center, which occurs at large (c.a. 40 deg.) out-of-plane angles.

Data are collected in the range of 2 to 20 degrees (out of the plane of the beams) at intervals of 0.25 degree for up to 10 degrees, every 0.5 degree up to 15 degrees and every degree thereafter. We use the digital pulse counting mode for these experiments in preference over the analog mode since it is inherently simpler and requires shorter measurement times at larger angles for equivalent data quality. The modulated signal is accumulated at a given angle with the beams crossed, thereafter the secondary beam source is tilted up to uncross the beams and the modulated component of the background signal is measured and then subtracted from the crossed signal. A reference signal at 4.5 degrees is repetitively measured after every three to five successive angles to provide a normalization and to compensate for any drift in sensitivity. The entire angular scattering intensity distribution is measured six times, giving a total accumulation time of 5 minutes per angle at low angles to 2 hours at the largest angles. These six measurements are averaged; the standard deviation at each angle defines the error bars for use in the weighted least squares procedure.

5. DATA ANALYSIS

The process of extracting a potential from differential cross-section data begins by proposing a good model of the potential with a reasonable initial guess of the appropriate parameters. This model is the basis of a computer simulation of the data. A least-squares fitting procedure is employed to iteratively adjust the potential parameters until the best possible match is made between experimental and modeled data.

The simulation of data can be divided into two parts a) calculation of the cross-section in the center-of-mass frame by means outlined in the theory section for a range of relative collision energies and scattering angles; b) transformation of these results to a laboratory reference frame and averaging over the velocity and angular distributions of the beams as well as the effective resolution of the detector.

Rotationally inelastic collisions occur for systems with anisotropic potentials. In general, this inelasticity should be considered in transforming the total differential cross sections to the laboratory frame. However, since the changes in rotational quantum number are small[6] and the collision energy is much greater than the rotational spacings[6] for the systems under consideration, it is possible to transform the total differential cross sections as if they were purely elastic without any loss of accuracy.[15]

The DCS calculation is done as follows:

(1) The phase shifts are calculated at a set of relative collision velocities w_n and approach angles γ (see equation 5). The w_n are picked to represent the full range of collision velocities as determined from the operating conditions of the beams. The approach angles are chosen to correspond to Gauss-Legendre integration points. The phase shifts are calculated to a specified precision by the JWKB method[58,20b] or for the low partial waves in some cases, by Numerov integration[59] of the Schrödinger equation (eq. 4).

    It was found that a 12-point Gauss-Legendre quadrature over γ is virtually identical to a 48-point quadrature for the conditions of our calculation. The inversion symmetry of CO_2 and CS_2 further reduces the number of points by a half, requiring the phase shift calculation at only six values of γ.

(2) The scattering amplitudes are calculated using equation (7) for a set of center-of-mass scattering angles θ_m. The partial wave summation is truncated when several successive phase shifts become less than a specified value (usually 0.001 radian). This requires phase shifts to be calculated up to a maximum l which lies in the range 150 to 350 depending on the target molecule considered.

(3) The square of the scattering amplitude is integrated over the approach angle γ, using equation (9). This yields center-of-mass differential cross-sections $\sigma(w_n, \theta_m)$ at relative collision velocities

w_n and scattering angles θ_m.

The transformation and averaging procedure is done as follows:

(1) A set of Gaussian integration points is obtained for the distribution of beam velocities based on the characteristics summarized in Table I. The range of integration is specified by cut-off probabilities of the velocity distributions; the integration points are designated $v_{\mathrm{p}i}$ and v_{sj} for the primary and secondary beams, respectively.

(2) A set of Gaussian integration points are obtained for the spread of beam interaction angles, designated at ς_k. The ς_k are determined from a convolution of the individual beam spreads as given in Table I.

(3) Cross sections $\sigma(w_{ijk}, \theta_m)$ are interpolated from $\sigma(w_n, \theta_m)$ where the w_{ijk} are the relative collision velocities corresponding to $\{v_{\mathrm{p}i}, v_{sj}, \varsigma_k\}$.

(4) The center-of-mass cross-sections $\sigma(w_{ijk}, \theta_m)$ are transformed to the laboratory reference frame by multiplying by the Jacobian factor[62] $J_{lab}^{ijk}(\theta_m)$ (appropriate for a number density detector)[28] to yield $\mathrm{I}(\theta_{lab}^{ijk})_{ijk}$, a laboratory scattering intensity, where θ_{lab}^{ijk} depends on θ_m. By interpolation the $\mathrm{I}(\theta_{lab}^{ijk})ijk$ are converted to $\mathrm{I}(\theta_{lab}^{c})_{ijk}$, where the θ_{lab}^{c} are a set of θ_{lab} angles used subsequently in a quadrature.

(5) A Gaussian quadrature (summation of $\mathrm{I}(\theta_{lab}^{c})_{ijk}$) over $v_{\mathrm{p}}, v_{\mathrm{t}}$, and ς (i, j, k) yields $\mathrm{I}(\theta_{lab}^{c})$.

(6) At each angle θ^c_{lab}, the $I(\theta^c_{lab})$ are averaged over the effective angular width of the detector. We say "effective" since this resolution represents not only the angular width of the detector but also contributions from the finite scattering volume. For these experiments the effective angular resolution angle is 1.5 degrees FWHM with an assumed cosine squared distribution in θ_{lab}. The scattering intensities averaged over the effective angular range of the detector are interpolated to give $I(\theta^e_{lab})$ at the experimental angles θ^e_{lab}.

The least-squares procedure for the potential parameter determination is done by minimizing the quantity[60]

$$\chi^2 = \sum_{i=1}^{n} w_i[F_i - \alpha I_i(p_1, ..., p_k)]^2 \tag{27}$$

with respect to the parameters $p_1, ..., p_k$ for laboratory angles $\theta_{lab\ i}$ $(i = 1, ..., n)$. The F_i are the measured scattering intensities; the I_i are the calculated intensities based on the potential parameters which are being optimized; and the w_i are weighting factors which are given in terms of the experimental error bars (or standard deviations) ΔF_i

$$w_i = (\Delta F_i)^{-2} \tag{28}$$

Since the experimentally measured intensities F_i are arbitrarily normalized, the calculated intensities I_i must be scaled to them. The scaling factor α is obtained in closed form by minimizing χ^2 with respect to α.

Following Keil and Kuppermann[27] we use a "goodness-of-fit" statistical index

$$G \equiv (\Delta\alpha/\alpha)_{0.95} = \frac{1}{\alpha} t(n-k)_{1-0.05} \left[\frac{\chi^2}{(n-k)\sum_{i=1}^{n} \mathrm{w}_i \mathrm{I}_i^2} \right] \qquad (29)$$

where $t(n-k)_{1-y}$ is Student's t-distribution for a confidence level y of the scaling factor α, with n data and k adjusted parameters.

The parameters are optimized according to a nonlinear weighted least-squares regression algorithm introduced by Marquardt.[61] The process is iterative, requiring five to fifteen cycles before convergence is attained, depending upon an initial guess for the parameters.

6. RESULTS AND DISCUSSION

The scattering intensities of He colliding with CO_2, CS_2, and OCS are plotted in Figures 2, 3, and 4 respectively, as a function of the laboratory scattering angle. The data have been multiplied by the sine of the laboratory scattering angle θ so as to emphasize quantal oscillations and display their relative contribution to the integral cross section.[1] While prominent oscillations have been observed for scattering of He with various diatomics [9,10,29] and highly symmetric polyatoms such as CH_4 and SF_6,[8,30] our current data by comparison show a substantial dampening of these oscillations, as has been previously observed for He + CO_2 and other highly anisotropic systems.[3,4] The rainbow scattering angle structure is completely obscured as is the case for systems with spherical potentials. [6,33]

The questions that form immediately are: what features of the potential account for the oscillation dampening? How unique are these features? And, how well can these be extracted from the data?

As we mentioned in the introduction, these questions have been addressed previously. However, we claim that the He + CO_2 potential presented by Keil *et al.*[5], Parker *et al.*[4], and Keil and Parker[3] is inaccurate for the fact that all three of these papers used the value of angular resolution of the detector of Keil *et al.*[28] which we showed to be incorrectly determined (see Section 4.). Although many of the qualitative conclusions reached by Keil and Parker[3,4,5] will remain the same, the actual potential that we present will naturally be different. The angular resolution of the detector determines how the detection system dampens the observed oscillations. Therefore to correctly account for the actual quantal oscillation dampening it is necessary to distinguish it from the intrumental dampening. Since Keil and Parker used an angular resolution that was too large, they underestimated the extent of the quantal dampening. Keil *et al.*[28] made a similar mistake for He + Ar where they obtained a well that was too shallow and also too wide; Aziz *et al.*[35] have pointed out the possible source of this error and reported the correct He + Ar potential. There are many factors that contribute to the dampening of the oscillation; the r_m anisotropy is the most pronounced. The shape of the well, i.e. the well depth and particularly well width contribute significantly to the shape of the oscillations.[6] In fact the width parameter is very important one; it can dampen the oscillation more significantly than the well depth.[6] Low angle He + CO_2 DCS oscillations ($\theta < 12°$) are dampened by a decrease in well width, while higher angle oscillations ($\theta > 12°$) are dampened by an increase.[6] An increase in well depth dampens oscillations only in the range $5° < \theta \leq 12°$; outside this range the oscillations increase with increasing well depth.[6] The angular range for the He + CO_2 and He + Ar experiments is 2 to 20 degrees. For most of this range the an increase of well width can be compensated for by an decrease in the depth; very roughly we can say that the well capacity (depth times width) remains fixed. Only the first and last oscillations (or dampened remenants) in this range do not follow this "fixed well capacity rule." From this one may deduce as to why the Keil*el al.* He + Ar well is too shallow and too wide. In fact the widths of the Keil and Parker[3,4,5] He + CO_2 potentials are consitently greater than those reported for other He scattering system[8-10,33-35] (except those reported by Keil *et al.*[28-30]). On this basis we feel that the questions mentioned in the previous paragraph must be consided again, with careful accounting of all DCS oscillation dampening factors.

We first may address the uniqueness question by suggesting that a spherical potential may be constructed with appropriate values for its parameters, that can model our data without resorting to anisotropic potentials. Referring again to Figures 3 through 4, we note that the calculated scattering intensity curves for the best spherical fit have significantly more oscillatory structure than our data, for all three systems. The parameters for these spherical fits are given in Table II. We have used the very flexible SPFD and MMSV[27] forms (equations 21 and 22). The goodness-of-fit statistic G (eq. 29) and the relative χ^2 (eq. 27) reflect a rather poor fit for CS_2 and OCS and at best a marginal fit for CO_2. Even though previous experience dictates that for these experiments G in the range of 1.8 to 2.0% gives acceptable fits (G less than 1.3% gives very good fits),[4,27-30] we should not *a priori* give full credence to the results. The well depth ϵ, is very large, much deeper than reported for helium collisions with various diatomics, such as CO,[29] which were satisfactorily modeled with spherical potentials. It is also much deeper than the spherical average of the well depth for our anisotropic fits to He + CO_2, which as shown below, is in the range of 3.8 to 4.3 meV, depending on the potential model used. It is also much deeper than the well depth of the spherical average of these anisotropic potentials, which is about 2.8 meV. Presumably if these experiments and data reduction methods are not capable of detecting potential anisotropy, they should then sample the spherical average of the actual potential and not the spherical limit potential (the potential constructed from the spherical averages of the angle-dependent parameters of the actual potential). The same can be said for the well width and repulsive steepness parameters, which yield a very narrow well with a steep repulsive part, which is inconsistent with previous empirical isotropic[33,34] and anisotropic potentials[3,8–10] as well as our anisotropic fits. Clearly therefore the spherically symmetric potential model does not satisfactorily represent the interaction of He with CO_2, CS_2 and OCS; and hence we must include anisotropy into the potential models. This is consistent with the conclusions reached previously for similar systems.[4,5]

In section 3 we have proposed several means of including anisotropy and several means of characterizing the radial shape of the anisotropic potential. Since the various combinations would produce well over a hundred different potential models, it would not be practical, or very informative to present an exhaustive survey. We will concentrate only on several reasonable choices for He + CO_2. The best of these will be used to analyze He + CS_2 and He + OCS.

6.1. Potentials for He + CO_2

In Tables III and IV we present the best fit results for a variety of multi-center and parameter expansion potentials for He + CO_2. Conspicuously absent are the results for Legendre expansion potential fits of equation (10). We repeatedly tried different types of fits to the $V_n(r)$ with terms up to second order, but with minimal success.[4,8] The major problem associated with these potentials is multiple minima along a radius of constant γ, in the repulsive region, and in some cases an attractive region at small r for γ close to the molecular axis. Both of these characteristics tended to develop in the process of least squares adjustment of potential parameters, and are physically unacceptable. Also, the parameters tend to be highly correlated, yielding a potential of questionable uniqueness. In addition, if we examine equation (10) we see no reason for the $V_n(r)$ to have a general shape of the spherical potentials in section 3.2 . The shape of $V(r,\gamma)$ at a fixed γ should have a form given by those potentials, but there is no *a priori* basis for selecting $V_n(r)$ to have one of those forms. However, is is reasonable that the $n = 0$ term should be shaped that way since it is the spherical average of the potential.[1,9,10] We have expanded all our resultant potentials (of Tables III and IV) to $n = 6$ order, and found that only the $n = 0$ terms had a repulsive region at small r, a well at 3 to 4 Ångstroms and weak monotonically decreasing attractive region at large r, as required physically. In many cases the $n = 2$ terms could also be described by this behavior, and in certain cases the $V_2(r)$ were the negatives of a typical van der Waals potential. But no $n = 4$ (or greater) term could be described as a van der Waals type, and most of the potentials in Tables III and IV have significant $V_6(r)$ terms. We therefore conclude that the Legendre expansion potentials are unsuitable as good models for He + CO_2 and similar systems using equations (17) thru (23) for the form of the r-dependent coefficients, and we forgo them in further consideration and discussion.

The multicenter potentials in Table III all give very good fits to the data, as is evident by the low values of G or χ^2. Varying six parameters in place of five produces somewhat better fits if we compare MSV-m1 to MSV-m2 and SPFD-m2 to SPFD-m3. However, an even better improvement in fit is acheived if the six parameters are chosen differently as in MMSV-m and SPFD-m1. The MMSV-m emphasizes and improves the shape of the repulsive region by separating it from the parameters that define the shape of the well. The function of the b_1 shape parameter in the SPFD is not as region specific, and we have a better fit in the SPFD-m1 where the b_0's for each of the centers are different and the

b_1's are fixed. The Morse-m yielded the best fit with six parameters; but since it does not include the long range van der Waals forces and differs significantly from the other multi-center potentials it has to be taken cautiously. The validity of the multi-center and parameter expansion potentials will be discussed later.

The angular-dependent parameter potentials of Table IV give a range of fits to the data; most are very good. Especially noteworthy are the four parameter LJ8-e and the three parameter HFD-e. In the case of the HFD we were unable to vary additional parameters, such as the anisotropy of α or the values of $\epsilon^{(0)}$ and $\epsilon^{(2)}$, since this variation yielded a potential with unacceptable behavior at certain angles. The LJ-e gives a good fit despite its lack of long range dispersion terms, but the results are deceptive; the anisotropy of the well depth is unrealistically extreme, producing well depth ranging from 0.04 ($\gamma = 0$) to 5.24 meV ($\gamma = \pi/2$). The other potentials have values of $r_m(\gamma)$ close to one another, and while the agreement in well depths is not as good, it is still quite reasonable.

The angular-dependent parameter potentials give a particularly straightforward visualization of the anisotropy, especially the elliptical parameterization of $r_m(\gamma)$ - much better than the multi-center potentials, which nonetheless fully account for the anisotropy (as we shall see later). Yet one may wonder how real these anisotropies are? Even though, they do give much better fits to the data than the spherical potentials. This improvement in fit might, for example, be due to a greater number of parameters in the region of sensitivity of these experiments. The results of Table V will clear up some of these questions, as shown below.

The best fit potential of Table IV is SPFD-e. Let us determine the degradation in this fit as the potential anisotropy is decreased. First we lessen the anisotropy of ϵ by decreasing $\epsilon^{(2)}/\epsilon^{(0)}$ to -0.47 and keeping it fixed at this value while optimizing the remaining parameters. The well minimum ($r_m(\gamma)$) does not change appreciably, but the average well depth increases, and the well narrows (b_0 is larger), with a slight reduction in quality of fit. We now remove all depth anisotropy (setting $\epsilon^{(2)} = 0$) and optimize b_1 instead. As can be seen by the results of test B, the well deepens and narrows even further with a significant decrease in the quality of fit. Perhaps the choice of b_1 as the new variational parameter was not a good one, since the optimized value is close to original fixed value of -6.1. Let us instead introduce anisotropy in the shape parameter b_0 (test C). The fit is better than for test B but not as good as for test A in which there was some ϵ anisotropy. The interesting fact is that the anisotropy of b_0 is such that the well is wider at the angles for which the previous fits (with ϵ anisotropy) gave a deeper well, ($\gamma = \pi/2$), and narrower at the angles for which previously the well was shallower ($\gamma = 0$). In very general terms, the fitting procedure is trying to keep the well capacity (depth times width) somewhat constant. However, if the well depth has the anisotropy given in Table IV, the inclusion of b_0 anisotropy in SPFD-e produces no marked improvement in the potential nor does it change the other parameters, and the resulting final ${b_0}^{(2)}/{b_0}^{(0)}$ is small (less than 0.02).

Table IV shows a greater agreement between the position of the well minima and of their anisotropies for the several potential models than the well depths and their anisotropies. This suggests and other ample evidence confirms[6,7] that our data are more sensitive to the well position than to its depth. We can then assume that the omission of r_m anisotropy and inclusion of ϵ anisotropy will produce a poorer fit to the data. This is indeed the case to a small extent (in Table V, thest D gives G = 1.69% wheras thest B gives G = 1.61%). This test D is however still much better than the spherical case. The striking feature of the results obtained by eliminating the r_m anisotropy (compare test D and A in Table V) is the increase in the well depth, and in its anisotropy as well as a narrowing of its width. The inclusion of shape anisotropy (test E) has a minor effect on the results or on the quality of fit (as compared to test D). The ϵ anisotropy provides the proper regulation of the well capacity, and it is of the correct sign though somewhat greater than the ones in Table IV, in the range of -0.47 to -0.70, which provide a better fit than test E.

In Fig. 5 we have plotted the laboratory scattering intensity for these anisotropy tests. All of the curves are very similar at angles below 5 degrees. The potentials with no r_m anisotropy (tests D and E) show the most deviation in the region at 4.5 degrees. The region from 5 to 9 degrees demonstrates the need for both r_m and ϵ anisotropy; the oscillations are not as dampened if only r_m or ϵ anisotropies are present, nor does the inclusion of β anisotropy with that for r_m properly dampen this oscillation. The range from 7 to 20 degrees demonstrates the importance of r_m anisotropy, which alone is responsible for significant dampening of quantum oscillations. Yet this region is influenced by ϵ or β anisotropies. The curves with no ϵ anisotropy do fall within the upper ranges of the data error bars, so the effectiveness of this region in establishing ϵ or β anisotropy is rather marginal. The role of r_m anisotropy is absolutely essential in establishing the He + CO_2 potential. Although $r_m(\gamma)$ is the most important parameter, and should be determined first before adjusting the other parameters, it is nonetheless evident that well depth anisotropy does play a crucial role in defining the potential and the resulting laboratory scattering intensity, and it is not just an arbitrary parameter chosen to improve the quality of fit.

We fitted our data to several potential models and obtained well positions and their anisotropies. Even if well depth anisotropy is ignored the final best fit $r_{m\perp}$ and q are very close to the results in Table IV. The two parameters which specify $r_m(\gamma)$ are crucial in determining the well depth and shape parameters, as is evident from Table V. Our experience in constructing the results of Table IV indicates that these $r_m(\gamma)$ parameters should be determined first before any other anisotropy is introduced. Otherwise, starting the fitting procedure at arbitrary initial values of all potential parameters and varying r_m and ϵ anisotropies produces very unsatisfactory results. We therefore conclude that the parameters which specify $r_m(\gamma)$ are the ones which are most precisely determined, and from the discussion in the previous paragraph, are crucial in establishing the values of the other parameters. However, $r_m(\gamma)$ cannot be the only angle-dependent parameter. The well depth must also have such a dependence.

In Table VI we present several features of each of the best potentials from Tables III and IV which have been reduced to and MMSV form. Features of interest are the minimum location r_m, well depth ϵ, the well width as characterized by β, and the repulsive steepness as characterized by β'. β is derived by finding the zero crossing of the potential and its inflection point; we present both. β' is found by fitting it to eq. 21a with all other parameters given. These five features are evaluated at $\gamma = \pi/2, \pi/4$, and 0; expanded to zeroth and second Legendre orders; and determined for the spherical average of the potential.

With some reservation we included the analysis of the potential at $\gamma = 0$. Our experimental data are not very sensitive to regions near the molecular axis, and misleading conclusions can be drawn if too much weight is placed upon the shape of the potential in these regions. A configuration space analysis shows that the solid angle element (which contributes to eq. (9)) will be greatest at $\gamma = \pi/2$, while at $\gamma = 0$ it will be zero. On these grounds the helium atom is more likely to hit the molecule perpendicular to its axis than along that axis. This means that about 70% of the sensitivity lies in the range $\gamma = \pi/4$ to $\gamma = \pi/2$ ($\cos(\pi/4) \approx 0.7$). The differential scattering cross-section will mainly be influenced by this portion of the potential (unless it favors the collinear orientation so strongly as to force most collisions to occur in an aligned configuration; a situation which does not occur in the systems being considered). The extracted potential will be most similar to the real potential in this range, while in the range near the axis it will reflect the intrinsic biases of the given model as that model tries to best match the regions of highest sensitivity. Care should be taken so as not to infer too much from the structure of the model potential near $\gamma = 0$.

All of the potential models in Table VI agree very well on the position and anisotropy of the well minimum. Despite the warnings of the previous paragraph the agreement is very good even at $\gamma = 0$. The standard deviation for $r_m(\gamma)$ is approximately 1% for each of the the three values of γ given. It can be said with reasonable confidence that $r_m(\gamma)$ is model-independent and that we have established its angular dependence. The minima location follows the overall shape of the CO_2 molecule; the difference between $r_m(0)$ and $r_m(\pi/2)$ is about 1.1 Å which correlates with the CO bond distance of 1.16 Å. This correspondence is not an internal bias of any of the potentials used; all of these are capable of a wide range of behavior including elongation perpendicular to the

CO_2 axis.

As expected, there is less agreement among the potentials in Table VI regarding the well depth and its anisotropy. The expectation is motivated by the above discussions regarding the need for well depth anisotropy. Although it is clear that $\epsilon(\gamma)$ has γ dependence, it is not completely clear how this relates to the width of the well; every potential in Table VI manipulates ϵ and β differently. The first drive in the fitting process is to establish $r_m(\gamma)$, to which the cross-section is most sensitive; it is not as sensitive to the other parameters which are therefore much more subject to the biases of a given model.

We have observed that the parameters of the fitted multi-center potentials exhibit a greater correlations between various parameters than for the angular dependent parameter potentials.. This is due to the fact that for the former potentials a changes in one of the parameters affects the potential globally in more pronounced way than for the latter potential. As an example, let us compare the MSV-m1, MSV-m2, and MMSV-m potentials to each other. For these potentials the well width and wall shape parameters are specified in different ways. The MSV-m1 is a six-fitted-parameter potential; the r_m, ϵ and β for each center are adjusted in the fitting procedure. The MSV-m2 is a five-fitted-parameter potential; the β's for the three centers are set equal to one another in the fitting procedure. The MMSV-m is a six-fitted-parameter potential, where the β's for the three centers are made equal to each other as well as the the β''s and are therefore treated as two fitting parameters. The MSV-m1 and MSV-m2 potentials are very similar to each other in quality of fit and value (Table VI). They differ the most at and near $\gamma = \pi/2$, where the MSV-m1 is deeper, narrower, and steeper (on the wall). In general, the well is narrower when β is higher, and the wall becomes steeper when β' increases. The MMSV-m potential provides a somewhat better fit than the two MSV-m ones. It is not as similar to either of them as they are to each other: the well is shallower and wider; the minimum position is greater; and the wall is steeper for all γ. The repulsive wall shape parameter β' has a strong influence on the fitting of the other parameters for these potentials. This influence is also observed if we compare the angular-dependent parameter potentials MSV-e and MMSV-e although it is not as pronounced.

A potential that gave a very good fit, but one which we can reject is the Morse-m. It has an extreme anisotropy in well depth (the latter ranging from 1.9 to 8.13 meV), and a very narrow and steep well. By contrast the Morse-e potential gave a very poor fit with a shallow and wide well. This extreme behavior of both potential is caused primarily by inadequate flexibility in the form of the Morse potential for which the well parameters determine the behavior in the van der Waals dispersion region.

The other potentials are much more difficult to reject; all are quite physically reasonable. We may suspect to some extent those that have a rather steep repulsive wall, such as the MMSV-e or even the MMSV-m. However, a selection of potentials for He interacting with various molecules[1-5,8-10,27-30] shows that many MMSV type potentials do have larger β' than β (eq. 21), also sensitivity analysis shows[6] that the DCS is much less sensitive to β' than to β making β' a less relaible parameter. Otherwise there is no reason to favor any of the potentials in Table VI other than by the quality of fit. The two best "fits" are the SPFD-m1 and SPFD-e. We have chosen to depict these graphically in Figures 6 through 9. In both cases the contours (Figures 6 and 8) are smooth. The fixed angle plots (Figures 7 and 9) further confirm a regular and smooth potential. The contours for the two potentials do have similar overall features, but the details are different. This is expected, since there simply is not enough information in the data (Figure 2) to unequivocally establish the shape of the potential. These contours should be viewed as representing the basic features of the real potential but not the specific details.

6.2. Potentials for He + CS_2

The best potential fits for He + CS_2 data are presented in Tables VII and VIII. We have chosen the potential forms that gave the best fits for He + CO_2. The quality of fit to experimental data is not as good as for He + CO_2, but nonetheless reasonably good. Substantial improvement in quality of fit occurs if the repulsive wall is made steeper as in the MMSV-e (Table VII) or MMSV-m (Table VIII). The poorer fit of the other potentials is manifest at scattering angles above 14 degrees (see Fig. 3 - note: $I(\theta)\ \sin\theta$ is not plotted for MSV-m). At angles below 14 degrees agreement between the various models is very good.

The characteristics of the He + CS_2 potentials are presented in Table IX. All of the potentials have similar well positions, depths and widths. The Morse-m deviates the most from the average of the others - but since it does not have the correct long-range behavior we reject it more readily than the others (as in the case of He + CO_2). The MMSV-m has the shallowest well and greatest r_m anisotropy. Since it provides the best fit to the data we claim it as most representative of the real potential. The contours and sectional views are shown in Figures 10 and 11.

The reliability level of the He + CS_2 potentials is lower than for He + CO_2. This is based on the larger fluctuation between the various forms and the poorer fits to the data. We can attribute some of these differences to the van der Waals dispersion coefficients. The CS_2 ones were obtained from the accurately calculated CO_2 coefficients by the use of a polarizibility correction (see end of Sec. 3) and are therefore less accurate than those for CO_2.

6.3. Potentials for He + OCS

The best potential fits for He + OCS data are presented in Tables X and XI, with Table XII displaying the features transformed to a common MMSV form. Once again we have used those potential forms that gave the best and most physically reasonable results for the He + CO_2 system. As is evident from the tables, all the potentials afforded very good fits. However, since the dispersion constants are not as well known for He + OCS we should hold less trust in these results than in the He + CO_2 ones.

In Table X we present the best fits for two different three-center MSV potentials. In these cases we decided to use three different centers and fit only five parameters; r_m(O), ϵ(O), r_m(S), ϵ(S) and one β assumed to be the same for all three centers. We chose the r_m(C) and ϵ(C) parameters for the carbon center as the average of the corresponding He + CO_2 and He + CS_2 multi-center potential values. For those systems we found that the central atom potential had less effect on the cross-section than the outer atom potential. In addition varying the C-centered potential produced smaller changes in the potential or the quality of fit, as most of these changes were compensated for by the two outer potentials. The difference between the MSV-m1 and MSV-m2 potentials is in the way the van der Waals dispersion terms are included. For the MSV-m2 they are included in the same way as outlined at the end of section 3. For the MSV-m1 the potential centered at the carbon was splined to a zero valued dispersion term, while the O centered potential was splined one half of the He + CO_2 term, and the S centered potential was splined to one half of the He + CS_2 term. These dispersion terms were evaluated using the r_i (eq. 11 amd 12) and not r as was done for the other multi-center potentials (end of section 3).

The MSV-m1 fitted the data better than the MSV-m2, and hence we display it in Figures 12 and 13 which show the potential as contours and angular sectional views, respectively. From Table XII we see that the two potetials are not so different considering the fact that we cannot expect too much detail regarding the potential from our data.The position of the repulsive wall is in agreement with those for He + CO_2 and He + CS_2, being greater at the S end, as can be seen by comparing the values of r (for $\gamma = 0, \pi$) at which the potentials crosses zero (see Figs. 12, 8 and 10). The well is deeper at the S end as would be expected from bond polarizabilities of -C=S and -C=0,[24ab,25] (the former being greater) and from the He + CO_2 and CS_2 potential parameter results. However, the well near the O in OCS is much shallower than in CO_2, and hence physically unrealistic. This emphasizes our previous warning on trusting the characteristics of a potential in a region of low sensitivity near the molecular axis. We must be even more cautious with a lower symmetry potential extracted from our limited data. Yet,we can consider the MSV-m1 or MSV-m2 potentials to be very reasonable models which display many of the overall features of the real potential.

The angle-dependent potentials were defined for systems with a center of symmetry. As a result, when applied to the asymmetric OCS system, they are expected to represent the average of the two halves of the correct potential about the plane perpendicular to the OCS-axis and passing through the center-of-mass of the molecule. We did not attempt to employ angle-dependent potentials without an inversion center since these would have too many degrees of freedom; expansion of $r_m(\gamma)$ and $\epsilon(\gamma)$ to second or third order with β would give seven to nine parameters, an excessive number for the information content of the DCS data. The centro-symmetric potential fits to the OCS data are given in Table XI. The Morse-e potential gives a good fit, but is physically very unreasonable; both the r_m and ϵ anisotropies are extreme and reversed. The MMSV-e is such a good fit that no useful or additional informaion can be obtained by including more parameters in fitting the data. Also, the amplitudes in the DCS oscillations (see Figure 4) are significantly dampened, and it would be unrealistic to expect them to reflect the subtle details of the actual potential.

In Table XII we show an average of the MSV-m1 and MSV-m2 potentials about the center-of-mass of the OCS, to facilitate comparison between the centrosymmetric MMSV-e potential. The MSV-m1-average shows a good similarity to the MMSV-e, while the MSV-m2-average is rather different from the MMSV-e. On the basis of the MSV-m1-average we can consider the MMSV-e to be a reasonable approximation to a center-of-mass average of the actual potential.

7. INTEGRAL CROSS SECTIONS AND BULK PROPERTIES

The validity of our He + CO_2 potential can be tested by its ability to predict a variety of observed phenomena, which include integral cross section $Q(v_{He})$ (as a function of He velocity), binary diffusion coefficient $D_{He,CO_2}(T)$, viscosity curvature $\eta_{He,CO_2}(T)$, and second virial coefficient $B_{He,CO_2}(T)$. The expressions for these quantities have been derived and presented in several publications[13,2], and hence we will forgo listing them here. The figures in which we compare experimental data to our calculations are sufficent in substantiating the validity of our potential. All of the bulk property calculations are for the SPFD-e potential.

Butz *et al.*[63] have measured the total integral cross sections $Q(v_{He})$ as a function of the velocity of a He beam interacting with a cell of CO_2 gas. To model these data the total integral cross sections are calculated at a range of collision energies they are then averaged over the distribution of velocities of the bulk CO_2 gas and the He beam. In Figure 14 we show calculations of $Q(v_{He})$ on our SPFD-e potential (Table IV) and compare then to the data of Butz *el al.*.[63] Our potential predicts averaged integral cross sections that for all velocities are about 3% lower than the experimental; however there is very good agreement in the relative intensities. Butz *el al.* have given a 15 % upper error limit on their measurements which includes estimates of the extent of systematic errors to which experiments of this type are highly susceptible.[64,65] Our calculations are well within these error bars.

In Figure 15 we compare experimental[66] binary diffusion coefficients $D_{He,CO_2}(T)$ for He in CO_2 to those calculated from our potential . The agreement is excellent for the entire measured temperature range of 180 to 600 K.

In Figure 16 we compare calculated mixture viscosity coefficients to experimental viscosities $\eta_{x_{CO_2}}(T)$ at two mole fractions x_{CO_2} of CO_2 to ones obtained experimentally by Kestin and Ro[67]. We also compare the interaction viscosity (transport of momentum along a velocity gradient) coefficients $\eta_{He,CO_2}(T)$ to those extracted from Kestin and Ro's data by Keil and Parker[3]. The interaction viscosity coefficients η_{He,CO_2} can be extracted from the experimental mixture viscosities; they cannot be measured directly. (The mixture viscosities are a function of the mole fraction of the two constituents, the interaction viscosity coefficients, and the binary diffusion coefficient.) For all three cases the agreement is once again excellent.

Finally, in Figure 17 we compare the calculated second virial coefficients $B(T)$ to experimentally measured ones.[68] The agreement is very good at temperatures above 200 K and fair below. The experimental data are from three different laboratories; the points with the largest error bars are from the one source[68a], while the ones with the smallest error bars are from a different source[68b]. Its is difficult to determine how conservatively or liberally these error bars were assigned by the respective authors. Our assessment is that the low error bars may be reported somewhat conservatively, and hence our potential has allowed a very accurate calculation of the second virial coefficient as function of temperature.

Our He + CO_2 potential is capable of predicting a variety of observables. However, we should point out that the bulk properties disscussed above, can be equally well predicted by the Parker-Keil-Kuppermann[4,5] and Keil-Parker[3] potentials. Yet these potential are rather different from ours. In fact, Parker and Pack[13,31] have proposed a He + CO_2 potential that was able to predict the viscosity and diffusion coefficients very well but failed to predict the integral and differential cross-section data. It is therefore, quite evident that the bulk properties are much less sensitive to the potential energy surface topography then is the differential cross-section. This is not surprising since the expressions for the diffusion, viscosity and virial coefficients are integrals over several variables, and thereby contain significant averaging. The total integral cross section curve is rather structureless, and at low velocities of He includes large energy averaging over the CO_2 velocity. The variety of potentials that could easily yield the same bulk properties is much larger than those that could reproduce a similar differential cross section. These properties are only useful in substantiating the validity of the potentials which are extracted from crossed beam DCS data.

8. CONCLUSIONS

We have measured the total differential scattering cross-sections (DCS) for He + CO_2, CS_2, and OCS. From these we obtained realistic interaction potentials that exhibit significant anisotropies in well minimum position as well as in the well depth. Isotropic potentials do not satisfactorily represent the potential that produces the scattering data. Clearly the scattering data is not the result of a spherical average of the real potential. This is particularly evident if they are compared to He + atom and He + diatomic-molecule scattering data.[9,10,29]

With He + CO_2 we have clearly demonstrated that not only is the well minimum position (r_m) anisotropy important in accounting for the observed data, but the depth (ϵ) anisotropy is also detected and accounts for many features in the DCS. Although the r_m anisotropy accounts for most of the dampening of the quantal oscilations; ϵ anisotropy is also responsible for some of the dampening as well as for the shape of the oscillation. Also very important is the width of the well, to which we were unable to ascribe any anistropy. Crucial to the extraction of a potential from the DCS was a knowledge of the long term dispersion coefficients. Potential forms that do not have provisions for them, could not be sucessfully fitted to the DCS; either the potential was physically unreasonable or the fit was poor.

Two models for characterizing the potential anisotropy which have demonstrated a high degree of flexibility as well as simplicity are the parameters expansion potential to second order in Legendre polynomials; and the multi-center potential. These were coupled with two very flexible spherical-like potential forms, to correctly describe the shape of the potential along a given angle of approach. Both the MMSV (or MSV) and the SPFD forms have good control of well depth as well as including the needed dispersion terms.

Both the parameter expansion and multicenter models have allowed us to extract very similar potentials from the DCS. In all three cases we found that r_m corresponds to the geometry of the molecule (CO_2, CS_2 and OCS). While the potential minimum is located perpendicular to the molecular axis. In the case of He + OCS, we have proposed a non-centro-symmetric potential constructed of three MSV potentials centered on the three OCS nuclei. Only five parameters were adjusted; the C-centered MSV was chosen on the basis of the He + CO_2 and He + CS_2 potentials.

Although our results yield the most accurate and detailed potentials for these systems to date, nonetheless we cannot state that these models are identical with the actual potential in every aspect. First of all, any technique that relies on a collision to probe the potential will be most sensitive to that potential in the regions where the collision is most probable; perpendicular to the axis of the CO_2, CS_2, and OCS molecule. Second, our experiment detects a wide range of rotationally inelastic collisions which are unresolved and thereby dampen many features in the total DCS. However, these result provide significant limits on the range of many potential parameters and unambiguously establish the presence of certain features.

ACKNOWLEDGEMENTS

We would like to thank Toni Stark, Guy Duremberg, Bill Schulke, Jim Olson, and Tom Dunn of the Instrument and Electronics Shops of the Division of Chemistry and Chemical Engineering for their talented technical support in the maintenance, repair, and modification of the apparatus.

2.9 REFERENCES

1. G. Scoles, *Ann. Rev. Phys. Chem.* **31**, 81 (1980).
2. *Atom-Molecule Collision Theory: A Guide for the Experimentalist* R. B. Bernstein ed. (Plenum, New York, 1979).
3. M. Keil and G. A. Parker, *J. Chem. Phys.* **82**, 1947 (1985).
4. G. A. Parker, M. Keil, and A. Kuppermann, *J. Chem. Phys.* **78**, 1145 (1983).
5. M. Keil, G. A. Parker, and A. Kuppermann, *Chem. Phys. Lett.* **59**, 443 (1978).
6. J. W. Winniczek and A. Kuppermann, (to be submitted).
7. L. Eno and H. Rabitz, *J. Chem. Phys.* **74**, 3859 (1981).
8. R.T Pack, G. A. Pfeffer, and J. P. Toennies, *J. Chem. Phys.* **80**, 4940 (1984).
9. M. Faubel, K. H. Kohl, J. P. Toennies, and F. A. Gianturco, *J. Chem. Phys.* **78**, 5629 (1984).
10. M. Faubel, K.-H. Kohl, and J. P. Toennies, *Faraday Discuss. Chem. Soc.* **73**, 205 (1982).
11. P. M. Agrawal and L. M. Raff, *J. Chem. Phys.* **75**, 2163 (1981).
12. C. L. Stroud and L. M. Raff, *J. Chem. Phys.* **72**, 5479 (1980).
13. G. A. Parker and R. T Pack, *J. Chem. Phys.* **68**, 1585 (1978).
14. R. T Pack, *Chem. Phys. Lett.* **55**, 197 (1978).
15. G. Rotzoll and A. Lubbert, *J. Chem. Phys.* **71**, 2275 (1979).
16. V. Khare, *J. Chem. Phys.* **68**, 4631 (1978).
17. D. Secrest, *J. Chem. Phys.* **62**, 710 (1975).
18. P. McGuire and D. J. Kouri, *J. Chem. Phys.* **60**, 2488 (1974).
19. R. T Pack, *J. Chem. Phys.* **60**, 633 (1974).
20. D. S. Saxon, *Elementary Quantum Mechanics* (Holden-Day, San Francisco, 1968).
21. A. S. Davydov, *Quantum Mechanics* (Pergamon, Oxford 1976), 2nd edition, tr. D. ter Haar.
22. G.Herzeberg, *Molecular Spectra and Molecular Structure III. Electronic Spectra and Electronic Structure of Polyatomic Molecules*, (Van Nostrand Reinhold, New York, 1966).
23. The vibrational energies for $CO2_2$, CS_2 and OCS are given in ref. 22, the lowest of which is the CS_2 bending mode: 396.7 cm^{-1} for which 86%

of the CS_2 molecules are in the ground state at a temerature of 298 K. The other two CS_2 vibrational modes have a 96% and a 100% ground state relative populations. For CO_2 the ground state relative populations for the three vibrational modes are 97%, 100% and 100%. For OCS these populations are 92%, 98% and 100%.

24. J. O. Hirshfelder, C. F. Curtiss, and R. B. Bird, *Molecular Theory of Gases and Liquids* (Wiley, New York 1964); (a) page 22 and 32, (b) page 950, (c) page 949.
25. N. J. Bridge and A. S. Buckingham, *Proc. R. Soc. Edinburgh Sect.* **A295**, 334 (1966).
26. R. T Pack, *J. Chem. Phys.* **64**, 1659 (1976).
27. M. Keil and A. Kuppermann, *J. Chem. Phys.* **69**, 3917 (1978).
28. M. Keil, J. T. Slankas, and A. Kuppermann, *J. Chem. Phys.* **70**, 482 (1979).
29. M. Keil, J. T. Slankas, and A. Kuppermann, *J. Chem. Phys.* **70**, 482 (1979).
30. J. T. Slankas, M. Keil, and A. Kuppermann, *J. Chem. Phys.* **70**, 1482 (1979).
31. R. T Pack, *J. Chem. Phys.* **61**, 2091 (1974).
32. J. Hepburn, G. Scoles, and R. Penco, *Chem. Phys. Lett.* **36**, 451 (1975).

33. K. M. Smith, A. M. Rulis, G. Scoles, R. A. Aziz, and V. Nain, *J. Chem. Phys.* **67**, 152 (1977).
34. K. M. Smith, A. M. Rulis, G. Scoles, R. A. Aziz, and G. Duquette *J. Chem. Phys.* **63**, 2250 (1975).
35. R. A. Aziz, P. W. Riley, U. Buck, G. Maneke, J. Schleusener, G. Scoles, and U. Valbusa, *J. Chem. Phys.* **71**, 3637 (1979).
36. C. H. Chen, P. E. Siska, and Y. T. Lee, *J. Chem. Phys.* **59**, 601 (1973).
37. A. L. J. Burgmans, J. M. Farrar, and Y. T. Lee, *J. Chem. Phys.* **64**, 1345 (1976).
38. R. W. Bickes and R. B. Bernstein, *Chem. Phys. Lett.* **26**, 457 (1974).
39. J. L. Dunham, *Phys. Rev.* **41**, 721 (1932).
40. G. Simons, R. G. Parr, and J. M. Finlan, *J. Chem. Phys.* **59**, 3229 (1973).
41. P. M. Morse, *Phys. Rev.* **34**, 57 (1929).

42. A. Kuppermann, R. J. Gordon, and M. J. Coggiola, *Faraday Discuss. Chem. Soc.* **55**, 145 (1973).

43. M. J. Coggiola, Ph. D. thesis, California Institute of Technology 1975.

44. J. T. Slankas, Ph. D. thesis, California Institute of Technology 1979.

45. M. Keil, Ph. D. thesis, California Institute of Technology 1978.

46. J. B. Anderson and J. B. Fenn, *Phys. Fluids* **8**, 780 (1965).

47. H. U. Hostettler and R. B. Bernstein, *Rev. Sci. Instrum.* **31**. 872 (1960).

48. This is the corrected pressure which takes into account the fact that a Bayard-Alpert ion gauge has a sensitivity for helium 10 times smaller than that for air.

49. Galileo Electro-Optics Corp., Sturbridge, Massachusetts.

50. Extranuclear Laboratories Inc., Pittsburgh, Pennsylvania.

51. Channeltron Model No. 4816, Galileo Electro-Optics Corp., Sturbridge, Massachusetts.

52. Model A-101. AMPTEK Inc., Bedford, Massachusetts.

53. The phase sensitive counter is an in-house built counter with a Phase Control Unit (phase shifter) model 4114 Evans Electronics, Berkeley, California.

54. Digital Equipment Corporation, Maynard, Massachusetts.

55. Princeton Applied Research Corporation, Princeton, New Jersey.

56. The electrometer is in-house built by the Department of Chemistry Electronics Suport Group. The chief part of the unit is a high performance FET operational amplifier with a 100 Mega Ohm electrometer feedback; Model LH0022CH, National Semiconductor Corp., Santa Clara, California.

57. Angular position encoder manufactured by: Clifton Precision, div. of Litton Systems Inc., Chatsworth, California; and Bendix Corporation, South Montrose, Pennsylvania; Decoder and display manufactured by Data Device Corporation, Bohemia, New York.

58. R. T Pack, *J. Chem. Phys.* **60**, 633 (1974).

59. K. Smith, *The Calculation of Atomic Collision Processes* (Wiley, New York 1971).

60. N. R. Draper and H. Smith, *Applied Regression Analysis* (Wiley, New York 1966).

61. D. W. Marquardt, *J. Soc. Indust. Appl. Math.* **11**, 431 (1963)

62. T. T. Warncock and R. B. Bernstein, *J. Chem. Phys.* **49**, 1878 (1966).

63. H. P. Butz, R. Feltgen, H. Pauly, and H. Vehmeyer, *Z. Physik* **247**, 70 (1971).

64. E. W. Rothe, Ph. D. Thesis, University of Michigan (1959).

65. C. A. Linse, J. J. H. Van Den Biesen, E. H. Van Veen, C. J. N. Van Den Meijdenberg, and J. J. M. Beenakker, *Physica* **99A**, 145 (1979).

66. (a) S. C. Saxena and E. A. Mason, *Mol. Phys.* **2**, 379 (1959); (b) B.K.Annis, A. E. Humphereys, and E. A. Mason, *Phys. Fluids* **12**, 78 (1969); (c) R. E. Walker, N deHass, and A. A. Westenberg *J. Chem. Phys.* **32**, 1314 (1960) (d) J. C. Giddings and S. L. Seager, *Ind. Eng. Chem. Fundam.* **1**,277 (1962); (e) S. L. Seager, L. R. Geertson, and J. C. Giddings, *J. Chem. Eng. Data* **8**, 168 (1963); (f) J. N. Holsen and M. R. Strunk, *Ind. Eng. Chem. Fundam.* **3**, 143 (1964); (g) B. A. Ivankin and P. E. Suetin, *Soviet Phys. Tech. Phys.* **9**, 866 (1964); (h) A. E. Loiko, G. A. Ivankin, and P. E. Suetin, *ibid.* **19**, 434 (1974); (i) N. D. Kosov and A. F. Bogatyrev, *Teplofiz. Massoperenos* **7**, 497 (1968); (j) A. G. Karpushin adn N. D. Kosov, *Fizika (Alma-Alta)* **1**, 127 (1970); (k) I. Nagata and T.Hasegawa, *J. Chem. Eng. Jpn.* **3**, 143 (1970); (l) K. R. Harris, T. N. Bell, and P. J. Dunlop, *Can. J. Chem.* **50**, 1874 (1972); (m) P. S. Arora, H. L. Robjohns, I. R. Shankland, and P. J. Dunlop, *Chem. Phys. Lett.* **59**, 478 (1978).

67. (a) J. Kestin and S. T. Ro, *Ber. Bunsenges. Phys. Chem.* **78**, 20 (1974); (b) R. DiPippo, J. Kestin, and K. Oguchi, *J. Chem. Phys.* **46**, 4758 (1967)

68. (a) T. L. Cottrell and R. A. Hamilton, *Trans. Faraday Soc.* **52**, 156 (1956); (b) R. C. Harper, Jr. and J. G. Miller, *J. Chem. Phys.* **27**, 36 (1957); (c) J. Brewer, Tech. Ref. AD663448 (1967) Available from the Clearinghouse for Federal Scientific and Technical Information; (d) T. N. Bell and P. J. Dunlop, *Chem. Phys. Lett.* **84**, 99 (1981).

Table I. Molecular Beam Characteristics

Characteristic	Probe Beam	Target Beam		
Gas	He	CO_2	CS_2	OCS
Stagnation Temperature/K	298	298	298	298
Stagnation Pressure/torr	1330	4.4	4.4	4.4
Angular Spread FWHM[a]/degrees	1.0[b]	3.0[b]	3.0[b]	3.0[b]
Most probable velocity/(km/sec)	1.76	0.49[c]	0.37[c]	0.42[c]
Velocity FWHM ($\Delta v/v$)	0.12	0.8	0.8	0.8
Mach number	12.7	1.06	1.06	1.06
Effective Heat capacity ratio γ	1.06	2.20	2.20	2.20

[a] Full width at half maximum.

[b] The effective detector acceptance angle of 1.5 deg is greater than the actual detector acceptance angle (see text) since it includes the effects of the finite size of the scattering volume.

[c] These most probable velocities give a relative collision energy of 65 meV with helium.

Table II. Spherical Potential Best Fits

System/Potential	r_m	ε	β or b_0[a]	β' or b_1[a]	r_s/r_m[a]	C_w[b]	G/%[c]	χ^2[c]
He + CO_2								
MMSV	3.34	6.09	11.39	19.12	1.37	0.82	2.00	72.4
SPFD	3.34	5.96	104.5	-7.33	1.40	0.84	2.09	74.9
SPFD	3.39	6.21	107.6	-7.25	1.41	1.0	2.17	87.7
He + CS_2								
SPFD	3.82	5.52	65.67	-5.70	1.67	0.98	3.59	156.6
He + OCS								
SPFD[d]	3.94	5.79	85.92	-7.19	1.34	1.781	3.08	204.2
SPFD[e]	3.97	6.33	147.8	-9.49	1.32	0.623	2.28	112.5

[a] β and β' apply to the MMSV potential (eq. 21) while b_0 and b_1 apply to the SPFD potential (eq. 22); r_s is the van der Waals spline point.

[b] C_w is a multiplier for the C_6 and C_8 van der Waal's coefficients, i.e., $C'_{6 \text{ or } 8} = C_w C_{6 \text{ or } 8}$.

Table II. Continued

---

[c] See equations 27 to 29.

[d] Use C_6 and C_8 for He + CO_2.

[e] Use C_6 and C_8 for He + CS_2.

Table III. Multicenter Potentials for He + CO_2

Potential Type[a]	Center[b]	r_m/Å	ε/meV	Shape(1)[c]	Shape(2)[c]	G/%[d]	χ^2[d]
MSV-m1	C	3.14	3.19	11.00			
	0	3.14	1.54	6.47		1.15	23.9
MSV-m2	C	3.18	2.88	7.90			
	0	3.15	1.24	7.90[e]		1.18	26.1
MMSV-m	C	3.26	3.27	5.37	13.26		
	0	3.45	0.51	5.37[e]	13.26[e]	1.08	21.3
SPFD-m1	C	3.21	4.51	77.15	-6.0[f]		
	0	3.37	0.66	22.84	-6.0[f]	1.05	19.9
SPFD-m2	C	3.12	3.51	66.52	-7.04		
	0	3.22	0.82	66.52[e]	-7.04[e]	1.11	22.5
SPFD-m3	C	3.15	3.33	60.66	-6.0[f]		
	0	3.21	0.98	60.66[e]	-6.0[f]	1.15	24.6
Morse-m	C	3.22	4.83	17.11	-		
	0	3.23	1.74	4.21	-	0.99	18.5

[a] Refer to equation (11). Potentials at each center are of the same spherical type, as discussed in section IIIB. The designation "-m" is for classification and refers to multicenter.

[b] The C-0 bond distance is fixed at 1.162 Å. For systems with long range van der Waals dispersion terms each center contributes one third of the dispersion. The dispersion terms are given as:

$$C_6 = 9.98 + 2.31\ P_2\ (\cos\gamma)\ \text{eV}\cdot\text{Å}^6 \qquad \text{and}$$

$$C_8 = 46.4 + 48.4\ P_2\ (\cos\gamma)\ \text{eV}\cdot\text{Å}^8$$

They are splined to the potential at $r/r_m = 1.6$ for all cases.

Table III. continued

---

[c] The shape parameters are defined by equations (18), (20), (21), and (22) for the Morse, MSV, MMSV, and SPFD parameterizations respectively. The second shape parameter for MMSV or SPFD is β' or b_1 respectively.

[d] G is the goodness-of-fit statistic of eq. (29); while χ^2 is unitless as defined by eqs. (27) and (28).

[e] This parameter is the same as the analogous one for the potential centered at the C. Both were varied as one parameter.

[f] This parameter is fixed and was not varied via least squares.

Table IV. Angular-dependent-parameter potentials for He + CO_2

Potential type[a]	$r_{m\perp}$ /Å[b]	q[b]	$\varepsilon^{(0)}$/meV[c]	$\varepsilon^{(2)}/\varepsilon^{(0)}$[c]	shape(1)[d]	shape (2)[d']	G/%[e]	χ^2[e]
SPFD-e	3.10	-0.477	3.99	-0.697	54.45	-6.14[f]	0.99	18.3
MSV-e	3.11	-0.437	4.29	-0.477	7.05		1.27	31.5
MMSV-e	3.11	-0.437	4.19	-0.568	6.91	16.16	1.16	26.5
HFD-e	3.19	-0.424	(3.61)[g]	(-0.727)[g]	(6.08)[g]	(α=1.07)[g]	1.63	50.1
LJ8-e	3.14	-0.465	3.70	-0.690			1.23	29.8
LJ-e	3.13	-0.490	3.51	-0.988			1.30	33.0
Morse-e	3.22	-0.548	3.23	-0.687	5.00		2.50	117.8
	$r_m^{(0)}$/Å[h]	$r_m^{(2)}/r_m^{(0)}$[h]						
SPFD-p	3.54	0.226	3.88	-0.773	52.57	-6.1[f]	0.99	18.4
MSV-p	3.41	0.206	4.35	-0.439	7.11		1.40	36.6
LJ8-p	3.56	0.224	3.69	-0.679			1.24	30.1

---

[a] Refer to equation (13). The designations "-e" and "-p" are for classification and refer to elliptical expansion of $r_m(\gamma)$ and second order Legendre expansion of $r_m(\gamma)$. The dispersion terms used in the

Table IV. continued

MSV, MMSV, SPFD, HFD and LJ8 are

$$C_6 = 9.98 + 2.31\ P_2\ (\cos\gamma)\ \mathrm{eV}\cdot\text{Å}^6 \quad \text{and} \quad C_8 = 46.4 + 48.4\ P_2\ (\cos\gamma)\ \mathrm{eV}\cdot\text{Å}^8\ ;$$

and are splined at $r/r_m = 1.6$

[b] Eliptical expansion of $r_m(\gamma)$ is given by eqs (15-16).

[c] Legendre expansion of $\varepsilon(\gamma)$ is given by eq. (14).

[d] This shape parameter is β of eqs. (18, 20 and 21) or b_0 of eq. (22).

[d'] This shape parameter is β' of eq. (21), or b_0 of eq. (22).

[e] G is defined by eq. (29), the "goodness-of-fit" statistic. χ^2 is given by eqs. (27-28) and is unitless.

[f] This parameter is fixed in the least squares fitting procedure.

[g] The well depth and its anisotropy are derived. The shape parameter corresponds to β of eq. (20) and was derived from the zero crossing of the potential. Only three parameters were varied; $r_{m\perp}$, q, and α [see eq. (23)].

[h] Legendre expansion of $\gamma_m(\gamma)$ is given by eq. (14).

Table V. SPFD[a] angular-dependent-parameter potentials to test anisotropy for He + CO_2

Test	r_m/Å[b]	q[b]	$e^{(0)}$/meV[c]	$e^{(2)}/e^{(0)}$[c]	$b_0^{(0)}$[d]	$b_0^{(2)}/b_0^{(0)}$[d]	b_1	G/%[e]	χ^2[e]
A	3.09	-0.480[f]	4.34	-0.470[f]	60.06	0[f]	-6.1[f]	1.12	25.3
B	3.09	-0.440	4.83	0[f]	67.10	0[f]	-5.90	1.61	48.2
C	3.09	-0.490	3.98	0[f]	58.99	0.616	-6.1[f]	1.41	36.8
D	3.39	0[f]	5.77	-0.802	103.93	0[f]	-7.15	1.69	52.4
E	3.39	0[f]	5.76	-0.802	103.80	0.052	-7.14	1.67	52.0

[a] See equation (22). Note: see a) of table III.

[b] See equations (15) and (16).

[c] See equation (14).

[d] The first shape parameter b_0 was expanded to a second Legendre order eq. (14).

[e] See eq. (29) for G and eqs. (27) and (28) for χ^2 which is unitless (reduced).

[f] This parameter was fixed in the least squares fitting.

Table VI. Summary of Characteristics of Best Fit Potentials for He + CO_2

Potential type[a]	Characteristic[b]	r_m/Å	ε/meV[c]	β_z[d]	β_i[d]	β_r[d]
MSV-m1	$\gamma = \pi/2$	3.11	5.93	9.72	11.0	10.5
	$\gamma = \pi/4$	3.67	4.08	7.04	13.0	7.20
	$\gamma = 0$	4.2	2.8	8.0	8.5	8.9
	L = 0	3.45	4.62	8.27	9.13	9.43
	L = 2	0.74	-2.21[f]	-1.37[g]	-1.26[g]	-2.21[g]
	S	3.75	2.72	7.50	8.53	7.49
MSV-m2	$\gamma = \pi/2$	3.12	4.96	7.64	8.29	7.62
	$\gamma = \pi/4$	3.72	4.14	8.08	8.69	8.01
	$\gamma = 0$	4.2	2.8	9.7	9.8	10.4
	L = 0	3.51	4.24	7.90	8.38	8.32
	L = 2	0.74	-1.36[f]	1.54[f]	1.54[f]	1.64[f]
	S	3.85	2.69	8.35	9.13	8.97
MMSV-m	$\gamma = \pi/2$	3.26	4.30	5.23	5.34	13.15
	$\gamma = \pi/4$	3.78	2.81	8.38	3.06	13.77
	$\gamma = 0$	4.2	2.4	10.7	8.5	17.8
	L = 0	3.59	3.41	7.30	5.55	14.23
	L = 2	0.71	-1.45	3.05[f]	1.18[g]	4.82[f]
	S	3.93	2.44	9.63	6.09	15.06

Table VI. continued

Potential type^{a}	Characteristic^{b}	r_m/Å	ε/meV^{c}	$\beta_z{}^{d}$	$\beta_i{}^{d}$	$\beta_r{}^{d}$
SPFD-m1	$\gamma = \pi/2$	3.20	5.83	7.92	8.10	7.51
	$\gamma = \pi/4$	3.69	3.11	7.30	8.60	9.30
	$\gamma = 0$	4.3	2.1	7.9	7.3	11.3
	$L = 0$	3.50	4.28	7.88	8.59	8.40
	$L = 2$	0.72	-2.86^{f}	0^{f}	-0.71^{f}	2.00^{f}
	S	3.79	2.45	7.71	8.98	10.84
SPFD=m2	$\gamma = \pi/2$	3.10	5.07	8.07	8.71	8.10
	$\gamma = \pi/4$	3.79	3.68	7.67	11.3	7.99
	$\gamma = 0$	4.2	2.6	9.8	13.0	10.0
	$L = 0$	3.53	3.98	7.92	8.78	8.52
	$L = 2$	0.80^{f}	-1.51^{f}	1.08^{f}	0.30^{f}	0.93^{f}
	S	3.92	2.60	7.82	9.00	12.90
SPFD-m3	$\gamma = \pi/2$	3.12	5.14	7.54	8.28	7.39
	$\gamma = \pi/4$	3.76	3.78	7.54	10.1	7.58
	$\gamma = 0$	4.2	2.7	9.1	6.6	9.7
	$L = 0$	3.52	4.10	7.62	8.06	7.93
	$L = 2$	0.78	-1.59^{f}	1.10^{f}	0.85	1.34^{f}
	S	3.87	2.59	7.45	8.91	12.94
Morse-m	$\gamma = \pi/2$	3.21	8.13	14.6	15.8	16.9
	$\gamma = \pi/4$	3.29	4.12	13.5	21.5	18.3

Table VI. continued

Potential type[a]	Characteristic[b]	r_m/Å	ε/meV[c]	β_z[d]	β_i[d]	β_r[d]
	$\gamma = 0$	4.3	1.9	5.4	5.4	4.9
	L = 0	3.42	5.78	12.15	13.55	16.59
	L = 2	0.71[f]	5.22[f]	-7.71[g]	-8.91[g]	-3.58[g]
	S	3.28	4.38	14.02	17.91	17.95
SPFD-e	$\gamma = \pi/2$	3.10	5.38	7.54	9.33	7.67
	$\gamma = \pi/4$	3.74	3.29	7.54	8.04	7.71
	$\gamma = 0$	4.3	1.2	7.5	8.6	7.7
	L = 0	3.52	3.99	7.54	8.53	7.69
	L = 2	0.81	-2.78	0	0	0
	S	3.76	2.50	6.85	7.15	7.83
MSV-e	$\gamma = \pi/2$	3.11	5.31	7.08	7.10	7.08
	$\gamma = \pi/4$	3.67	3.77	7.03	7.03	7.03
	$\gamma = 0$	4.2	2.2	7.0	7.0	7.0
	L = 0	3.48	4.29	7.05	7.05	7.05
	L = 2	0.70	-2.05	0	0	0
	S	3.66	2.91	6.80	7.11	7.22
MMSV-e	$\gamma = \pi/2$	3.11	5.38	6.91	6.91	16.16
	$\gamma = \pi/4$	3.67	3.60	6.91	6.91	16.16
	$\gamma = 0$	4.2	1.8	6.91	6.91	16.16
	L = 0	3.48	4.19	6.91	6.91	16.16
	L = 2	0.70	-2.38	0	0	0
	S	3.65	2.89	9.40	7.38	15.25

Table VI. continued

Potential type[a]	Characteristic[b]	r_m/Å	ε/meV[c]	β_z[d]	β_i[d]	β_r[d]
HFD-e	$\gamma = \pi/2$	3.19	5.22	5.98	4.33	6.29
	$\gamma = \pi/4$	3.73	2.70	6.14	5.36	6.46
	$\gamma = 0$	4.2	1.6	6.2	7.2	6.5
	$L = 0$	3.55	3.61	6.08	6.37	6.40
	$L = 2$	0.69	-2.62	0.15	0.34	0.16
	S	3.65	2.78	6.02	6.07	6.44
LJ8-e	$\gamma = \pi/2$	3.14	4.98	6.42	6.03	7.79
	$\gamma = \pi/4$	3.76	3.06	6.71	6.43	7.97
	$\gamma = 0$	4.3	1.1	6.5	6.3	7.8
	$L = 0$	3.55	3.67	6.59	6.61	7.90
	$L = 2$	0.78	-2.55	0.17[f]	0.17[f]	0.11[f]
	S	3.72	2.63	6.61	6.58	7.92
SPFD-p	$\gamma = \pi/2$	3.14	5.38	7.44	8.60	7.66
	$\gamma = \pi/4$	3.74	3.13	7.44	8.58	7.69
	$\gamma = 0$	4.3	0.9	7.4	8.9	7.6
	$L = 0$	3.54	3.88	7.44	8.41	7.67
	$L = 2$	0.80	-3.00	0[f]	0[f]	0
	S	3.75	2.48	6.79	7.05	7.83

Table VI. continued

Potential type[a]	Characteristic[b]	r_m/Å	ε/meV[c]	β_z[d]	β_i[d]	β_r[d]
LJ8-p	γ = π/2	3.16	4.94	6.44	6.06	7.80
	γ = π/4	3.06	3.76	6.71	6.59	7.97
	γ = 0	4.4	1.2	6.6	6.3	7.9
	L = 0	3.56	3.69	6.60	6.61	7.90
	L = 2	0.80	-2.50	0.19[f]	0.19[f]	0.12[f]
	S	3.75	2.56	6.62	6.63	7.92
Average[h]	γ = π/2	3.14	5.2	7.2	7.4	8.8
		(0.05)	(0.4)	(1.1)	(1.4)	(2.8)
	γ = π/4	3.73	3.4	7.3	7.9	8.8
		(0.04)	(0.5)	(0.6)	(2.5)	(2.8)
	γ = 0	4.2	2.0	8.0	8.1	9.9
		(0.07)	(0.7)	(1.4)	(1.8)	(3.5)
	L = 0	3.52	4.0	7.3	7.6	9.1
		(0.04)	(0.7)	(1.0)	(0.7)	(1.6)
	L = 2	0.75	-2.3	0.5	0.2	0.7
		(0.04)	(0.7)	(1.0)	(0.7)	(1.5)
	S	3.77	2.6	7.5	7.6	9.9
		(0.09)	(0.2)	(1.1)	(1.2)	(3.1)

---

[a] Please refer to tables III and IV for details concerning potential types.

[b] The characteristics include: profiles of the potential at approach angles γ = π/2, π/4, and 0; Legendre expansion of the potential parameters for orders L = 0 and L = 2, and the shape of the spherical average of the potential (S).

Table VI. continued

---

[c] The well minimum is found numerically using Newton's method for the zero of the potential derivative. The "L = 0" and "L = 2" are the Legendre projections of the parameter (as a function of angle $\chi(\gamma)$ ($\chi = r_m, \varepsilon, \beta$).

$$\chi_L = (L + \tfrac{1}{2}) \int_{-1}^{1} \chi(\gamma)\, P_L(\cos\gamma)\, d\cos\gamma$$

[d] The β's are the MMSV type (eqs. 20 and 21). β_z is found from the zero point of the potential r_z,

$$\beta_z = \frac{\ln 2}{1 - r_z/r_m}$$

β_i is found from the potential's inflection point r_z $\left(\frac{d^2V(r_z)}{dr^2} = 0\right)$

$$\beta_i = \frac{\ln 2}{r_i/r_m - 1}$$

The value β in the repulsive region is found by iteratively fitting β' in equation (21a) with given $\beta = \beta_z, \varepsilon$, and r_m to the potential at $r = 0.8\ r_z$.

[f] Expansion terms of higher Legendre order exist for this parameter, and are at least 5% of the zeroth term.

[g] Expansion terms of higher Legendre order exist for this parameter, and are at least 25% of the zeroth order.

[h] The value of the above parameters (except for Morse -m) are averaged. The standard deviations are in parentheses below each parameter.

Table VII. Angular-dependent-parameter potentials for He + CS_2

Potential Type[a]	r_m /Å[b]	q[b]	$\varepsilon^{(0)}$/meV[c]	$\varepsilon^{(2)}/\varepsilon^{(0)}$[c]	shape(1)[d]	shape(2)[d']	G/%[e]	χ^2[e]
MMSV-e	3.58	-0.506	4.28	-0.549	7.53	20.3	1.59	32.8
MSV-e	3.51	-0.543	4.31	-0.579	7.38		1.87	41.0
SPFD-e	3.61	-0.510	4.25	-0.658	62.0	-6.1[f]	1.84	39.4

[a] See note a of Table IV except of the dispersion terms which are $C_6 = 33.28 + 10.64\ P_2\ (\cos\gamma)$, $C_8 = 137.21 + 160.20\ P_2\ (\cos\gamma)$.

[b-e] see corresponding notes of Table IV.

[f] This parameter is fixed, but if it is varied with the others there is no change in the quality of fit or in b_1, which changes to -6.11.

Table VIII. Multicenter Potentials for He + CS_2

Potential Type[a]	Center[b]	r_m/Å	ε/meV	shape(1)[c]	shape(2)[c]	G/%[d]	χ^2 [d]
MSV-m	C	3.68	4.04	8.44		1.80	38.2
	S	3.64	0.98	9.17			
MMSV-m	C	3.76	3.94	6.80	19.56	1.26	18.5
	S	3.90	0.52	6.80[e]	19.56[e]		
SPFD-m1	C	3.67	5.34	67.22	-6.0[f]	1.82	38.8
	S	4.11	0.33	25.08	-6.0[f]		
SPFD-m2	C	3.52	5.04	70.38	-8.91	1.88	41.4
	S	4.07	0.18	70.38[e]	-8.91[e]		
Morse-m	C	3.69	4.80	17.12		1.43	25.9
	S	4.80	1.71	4.02			

---

[a] See note a of Table III.

Table VIII. Continued.

---

[b] The C-S bond distance is fixed at 1.554 Å. The van der Waal's dispersion terms are: $C_6 = 33.28 + 10.64\ P_2\ (\cos\gamma)$; $C_8 = 137.21 + 160.20\ P_2\ (\cos\gamma)$. Each center contributes one-third of the dispersion. These are splined to the potential at $r/r_m = 1.6$.

[c−f] See corresponding notes of Table III.

Table IX. Summary of Characteristics of Best Fit Potentials for He + CS_2

Potential type[a]	Characteristic[b]	$r_m/\text{Å}$	ε/meV[c]	β_z[d]	β_i[d]	β_r[d]
MMSV-e	$\gamma = \pi/2$	3.58	5.46	7.53	7.63	20.34
	$\gamma = \pi/4$	4.41	3.70	7.53	7.56	20.34
	$\gamma = 0$	5.1	1.9	7.5	7.5	20.3
	L = 0	4.13	4.28	7.53	7.53	20.34
	L = 2	1.03	-2.35	0.0	0.0	0.0
	S	4.53	2.31	11.19	8.95	19.49
MSV-e	$\gamma = \pi/2$	3.51	5.55	7.38	7.38	7.38
	$\gamma = \pi/4$	4.43	3.68	7.38	7.38	7.38
	$\gamma = 0$	5.2	1.8	7.4	7.4	7.4
	L = 0	4.11	4.31	7.38	7.38	7.38
	L = 2	1.14	-2.49	0.0	0.0	0.0
	S	4.56	2.18	6.79	7.39	7.51
SPFD-e	$\gamma = \pi/2$	3.61	5.64	7.88	8.21	7.61
	$\gamma = \pi/4$	4.45	3.55	7.88	8.54	7.66
	$\gamma = 0$	5.2	1.5	7.9	8.2	7.6
	L = 0	4.16	4.25	7.88	8.69	7.64
	L = 2	1.05	-2.79	0.0	-0.11	0.03
	S	4.55	2.27	7.02	7.51	7.90

Table IX. Continued.

Potential type[a]	Characteristic[b]	r_m/Å	ε/meV[c]	β_z[d]	β_i[d]	β_r[d]
MSV-m	$\gamma = \pi/2$	3.63	5.38	8.29	8.94	8.38
	$\gamma = \pi/4$	4.41	4.07	8.85	11.95	9.45
	$\gamma = 0$	5.1	2.6	11.0	12.1	12.7
	L=0	4.11	4.47	8.79	9.39	9.44
	L=2	1.02^f	-2.06^f	1.96^f	2.07^g	2.70^g
	S	4.69	2.20	9.57	11.00	11.0
MMSV-m	$\gamma=\pi/2$	3.73	4.92	6.71	7.17	21.12
	$\gamma=\pi/4$	4.52	3.11	10.55	5.91	25.86
	$\gamma=0$	5.1	2.1	13.7	8.6	32.9
	L=0	4.20	3.79	10.17	7.31	22.02
	L=2	0.99^f	-1.94^g	5.91^g	0.90^f	7.58^g
	S	4.85	2.07	14.41	15.31	24.18
SPFD-m1	$\gamma=\pi/2$	3.67	5.99	7.81	7.77	7.56
	$\gamma=\pi/4$	4.54	2.69	5.84	3.92	9.51
	$\gamma=0$	5.2	1.8	8.1	8.3	10.2
	L=0	4.15	4.06	7.39	8.40	8.49
	L=2	1.11^f	-3.17^g	-0.35^g	-0.08^f	1.70^f
	S	4.67	2.00	7.01	6.60	10.10

Table IX. Continued.

Potential type^a	Characteristic^b	r_m/Å	ε/meV^c	$\beta_z{}^d$	$\beta_i{}^d$	$\beta_r{}^d$
SPFD-m2	$\gamma=\pi/2$	3.54	5.28	8.66	11.83	9.32
	$\gamma=\pi/4$	4.60	3.37	7.22	8.02	6.42
	$\gamma=0$	5.2	1.6	9.6	9.5	11.3
	L=0	4.22	3.66	7.58	9.35	8.84
	L=2	1.13^f	-1.99	1.68^g	1.66^g	-1.25^g
	S	4.70	2.37	8.62	10.76	7.93
Morse-m	$\gamma=\pi/2$	3.76	5.43	13.20	20.26	18.21
	$\gamma=\pi/4$	5.62	2.26	4.50	4.49	3.86
	$\gamma=0$	6.3	2.0	5.2	5.3	5.2
	L=0	4.96	3.06	6.98	10.13	12.08
	L=2	1.82	-1.97^g	-5.35^g	-12.03^g	-14.59^g
	S	5.52	2.18	4.43	4.48	3.61
Average-h	$\gamma=\pi/2$	3.61 (0.07)	5.5 (0.3)	7.8 (0.6)	10.0 (5.)	12.0 (6.)
	$\gamma=\pi/4$	4.48 (0.07)	3.5 (0.4)	8.4 (1.6)	7.6 (2.5)	12.0 (8.)
	$\gamma=0$	5.2 (0.05)	1.9 (0.3)	11. (6.)	8.8 (1.6)	15. (9.)
	L=0	4.15 (0.04)	4.1 (0.3)	8.3 (0.9)	8.3 (0.9)	12. (6.)
	L=2	1.07 (0.06)	-2.4 (0.4)	1. (2.)	0.6 (0.9)	1.5 (3.)
	S	4.65 (0.11)	2.2 (0.1)	9.2 (2.8)	9.7 (3.0)	12.6 (6.6)

Table IX. Continued

---

[a] Please refer to Tables VII and VIII for details concerning the potential types

[b - g] See corresponding notes for Table VI

[h] The averages are for all the above potentials (except for Morse-m) with the standard deviations given in parenthesis.

Table X. Three-center MSV Potentials For He + OCS

Potential[a] Type	Center[b]	Z/Å[b]	r_m/Å	ε/meV	β	G[c]	χ^2[c]
MSV-m1[d]	C	0.523	3.80	0.69	6.23	1.07%	26.3
	S	-1.037	3.90	3.75	6.23[f]		
	O	1.683	3.90	0.17	6.23[f]		
MSV-m2[e]	C	0.523	3.79	0.63	5.84	1.16	28.6
	S	-1.037	3.68	2.95	5.84[f]		
	O	1.683	4.14	0.72	5.84[f]		

[a] Refer to equation (11). These are three center potentials with an MSV spherical potential at each center.

[b] The distance z is from the center-of-mass of the OCS molecule, c is fixed in the least-squares parameter fitting procedure.

[c] See eq. (29) for G and eqs. (27-28) for χ^2.

[d] The long range dispersion part of this potential was constructed by giving the MSV potential centered at the O one-half of the He + CO_2 dispersion terms as given in Table III (see eq. (20c)), and by giving the MSV potential centered at the S one-half of the He + CS_2 dispersion terms. While the C-centered MSV is given dispersion terms of value zero.

[e] The long range dispersion part of this potential was constructed in the same manner as for the He + CO_2 and CS_2 multi-centered potentials. The dispersion coeficients are the same as given in Table X (footnote g).

Table XI. Angular-dependent-parameter Potentials for He + OCS

Potential Type[a]	r_{m_1}/Å[b]	q[b]	$\varepsilon^{(0)}$/meV[c]	$\varepsilon^{(2)}/\varepsilon^{(0)}$[c]	β	β'	G[d]	χ^2[d]
Morse-e	4.50	0.978	3.04	1.14	5.16		1.19%	31.6
MMSV-e[e]	3.59	-0.474	4.34	-0.228	7.38	5.90	1.17	29.6

[a] Refer to equation (13). The designation "-e" classifies the potential as having an elliptical form for $r_m(\gamma)$.

[b] Elliptical form for $r_m(\gamma)$ is given by eqs. (15-16).

[c] Legendre expansion of $\varepsilon(\gamma)$ is given by eq. (14).

[d] G is defined by eq. (29). χ^2 is given by eqs. (27-28).

[e] Approximated dispersion terms for He + OCS are given as (see text for deprivation)
$C_6 = 21.63 + 6.37\ P_2\ (\cos\gamma)\ \text{eV} \cdot \text{Å}^6$ and $C_8 = 91.81 + 104.30\ P_2\ (\cos\gamma)\ \text{eV} \cdot \text{Å}^8$

Table XII. Summary of Characteristics of Best Fit Potentials for He + OCS

Potential Type[a]	Characteristic[b]	r_m/Å	ε/meV[c]	β_z[d]	β_i[d]	β_r[d]
MMSV-e	$\gamma=\pi/2$	3.59	4.83	7.36	7.36	5.90
	$\gamma=\pi/4$	4.32	4.09	7.36	7.36	5.90
	$\gamma=0$	4.9	3.3	7.36	7.36	5.90
	L=0	4.07	4.33	7.36	7.36	5.90
	L=2	0.92	-0.99	0.0	0.0	0.0
	S	4.43	2.61	6.63	7.38	6.30
MSV-m1	$\gamma=0$	5.2	0.8	7.9	13.5	7.8
	$\gamma=\pi/4$	4.34	1.60	6.34	6.39	6.32
	$\gamma=\pi/2$	3.76	4.60	5.80	5.92	5.71
	$\gamma=3\pi/4$	4.55	4.07	7.06	6.90	7.01
	$\gamma=\pi$	4.9	3.9	7.9	7.6	7.9
	L=0	4.21	3.51	6.40	6.52	6.42
	L=1	-0.10	-1.56	-0.46	-0.36	-0.29
	L=2	0.92	-1.70	1.27	1.04	1.44
	L=3	0.35	-0.30	0.32[f]	0.17[f]	0.39
	S	4.53	2.34	6.90	7.02	7.03
MSV-m2	$\gamma=0$	5.7	1.2	7.5	8.0	8.0
	$\gamma=\pi/4$	4.95	1.59	6.34	6.50	6.15
	$\gamma=\pi/2$	3.62	4.17	5.31	5.69	5.23
	$\gamma=3\pi/2$	4.34	3.75	6.10	6.71	6.00

Table XII. Continued.

Potential Type[a]	Characteristic[b]	r_m/Å	ε/meV[c]	β_z[d]	β_i[d]	β_r[d]
MSV-m2	$\gamma=\pi$	4.7	4.7	6.7	8.3	7.1
(Continued)	L=0	4.28	3.14	5.93	6.14	6.08
	L=1	0.43	-1.64	0.18	0.23	-0.05
	L=2	1.10	-0.91	1.19	1.04	1.65
	L=3	0.10[g]	0.21[g]	-0.03[f]	0.22[f]	0.53[f]
	S	4.79	1.72	6.23	6.24	6.61
MSV-m1[h]	$\gamma=0$	5.4	1.8	7.3	7.5	8.0
	$\gamma=\pi/4$	4.70	2.29	5.94	5.13	6.45
	$\gamma=\pi/2$	3.62	4.17	5.31	6.22	5.23
MSV-m2[h]	$\gamma=0$	5.0	2.2	7.8	9.6	8.0
	$\gamma=\pi/4$	4.51	2.79	6.91	6.83	6.90
	$\gamma=\pi/2$	3.76	4.60	5.80	6.07	5.71

---

[a] Please refer to tables X and XI for details concerning the potential types.

[b] The characteristics include: Profiles of the potential at approach angles $\gamma=0$, $\pi/4$, $\pi/2$, and for the non-centrosymmetric potential, also at $\gamma=3\pi/4$ and π; Legendre expansion of the potential parameters for orders up to L=3 (the L=1 and L=3 terms are zero for the centro-symmetric potentials); and the shape of the spherical average of the potential (S).

Table XII. Continued.

c) - g) See corresponding notes for Table VI.

h) Average of the corresponding non-centrosymmetric potential about a plane perpendicular to the molecular axis and passing through the center-of-mass of the OCS; i.e., $V(r,\gamma) = 1/2\ [V(r,\gamma) + V(r,\pi - \gamma)]$.

Figure 1. Vertical cut view of the crossed molecular beam apparatus, drawn approximately to scale. DP = diffusion pumps, PB = primary beam source - beam axis is parallel to drawing, Nz = nozzle (64 mm), Sk = skimmer, VS = velocity selector, Ch = beam modulation chopper, SB = secondary beam source - beam axis is perpendicular to plane of drawing, θ_h = in plane angle of detector as measured from the PB axis, θ_v = out-of-plane angle of detector, MS = mass spectrometer detector, GV = gate valve in front of the mass spectrometer entrance apperture, IP_b = 5 l/sec ion pump for buffer chamber, I = ionizer and ion focus lenses (ℓ-N_2 cooling coils around filament not shown), CEM = Channeltron electron multiplier (Model 4816), CP = liquid He cryopump (350 l/sec), IP = 25 l/sec ion pump, IG = ionization gauge, BV = bake out and vent valve.

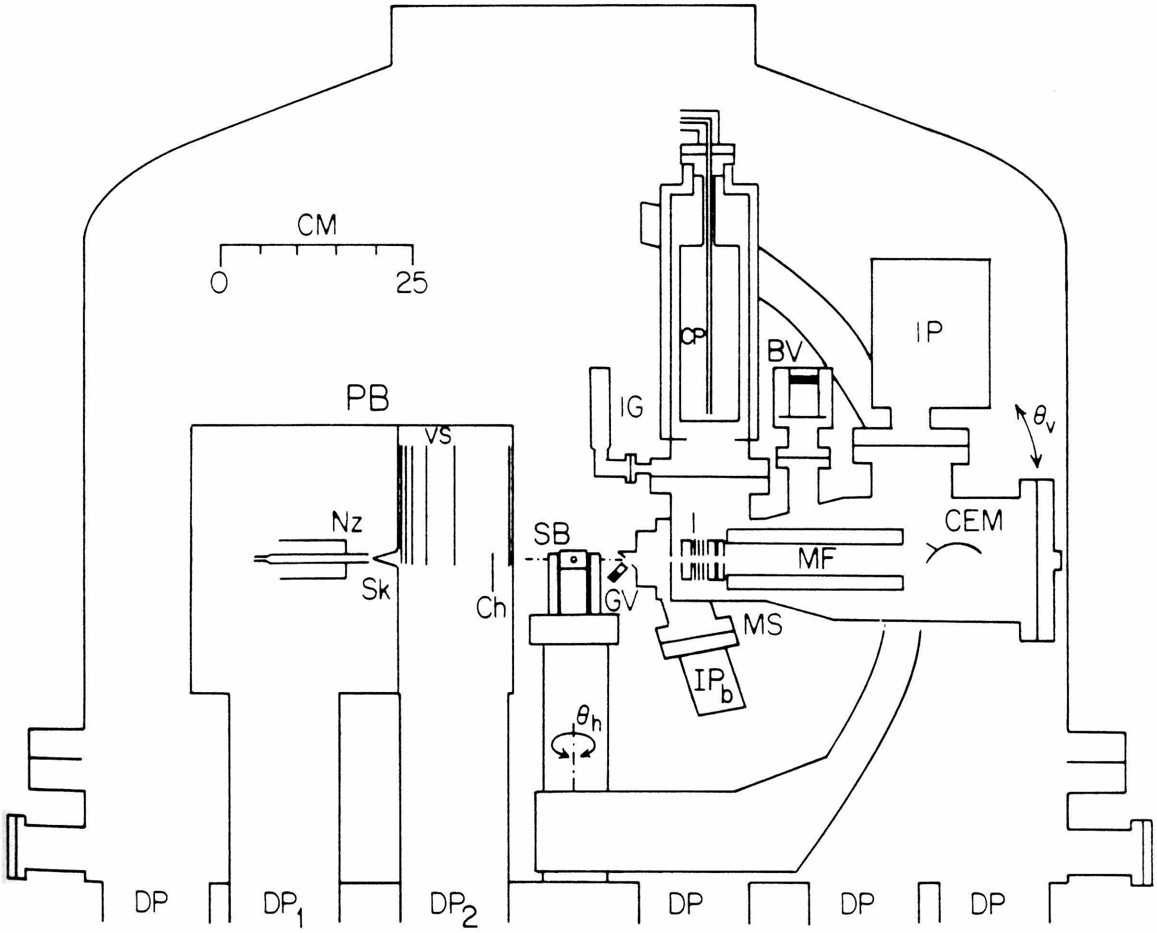
CM
0
25
PB
VS
Nz
Sk
Ch
SB
GV
IG
CP
BV
IP
θ_v
I
MF
CEM
MS
IP_b
θ_h
DP
DP_1
DP_2
DP
DP
DP

Figure 1.

Figure 2. Laboratory differential cross section for out-of-plane scattering of He by CO_2. Experimental points are plotted with their error bars. The solid curve is the calculated cross-section from the best fit anisotropic potential SPFD-e (see Table IV). The broken curve is for the best fit spherical potential (see Table II).

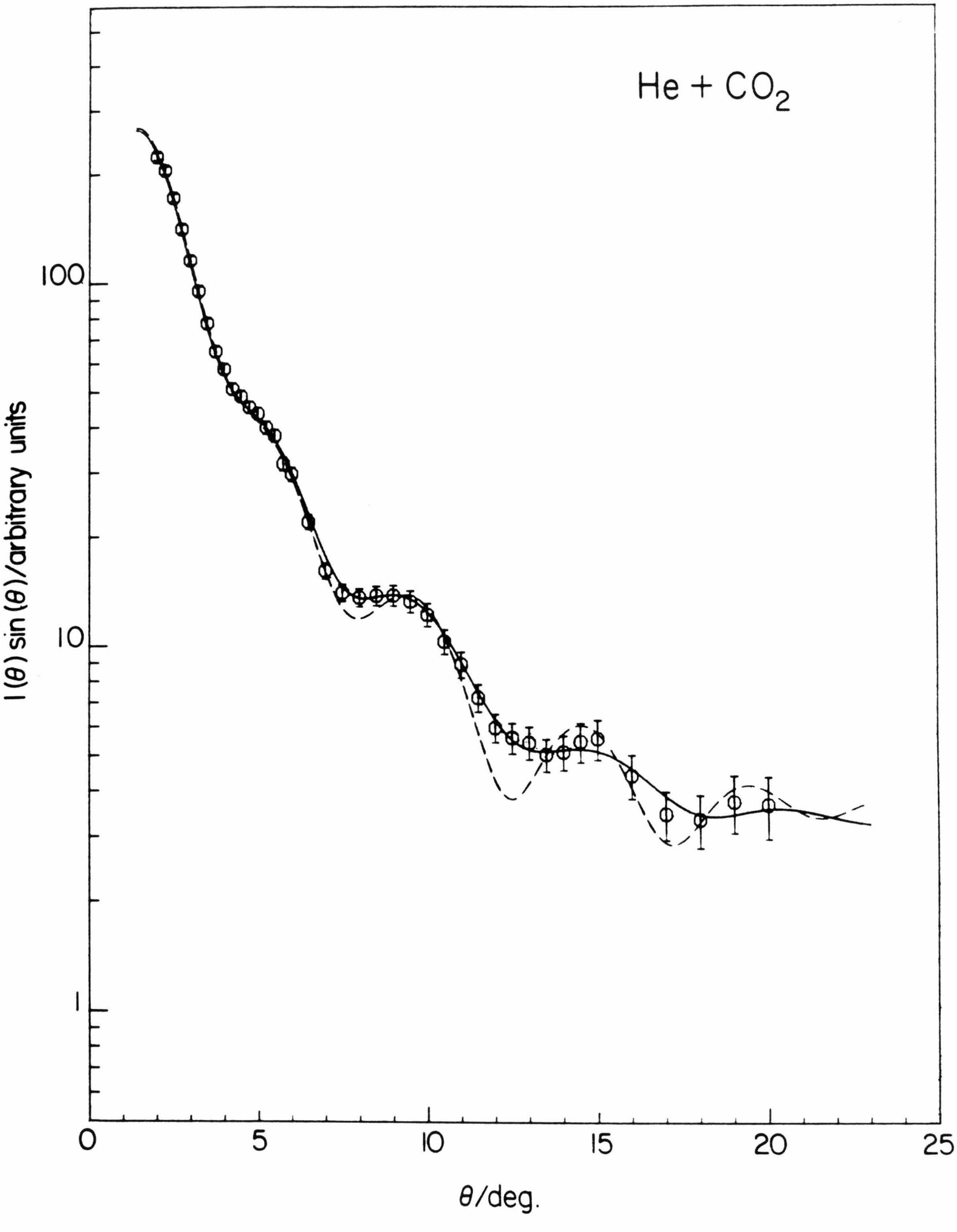
He + CO_2
100
10
1
0
5
10
15
20
25
$I(\theta)\sin(\theta)$/arbitrary units
θ/deg.

Figure 2.

Figure 3. Laboratory differential cross section for out-of-plane scattering of He by CS_2. Experimental points are plotted with their error bars. The solid curve is the calculated cross section for the best fit anisotropic potential MMSV-m (see Table VIII). The broken curve is for the best fit spherical potential (see Table II).

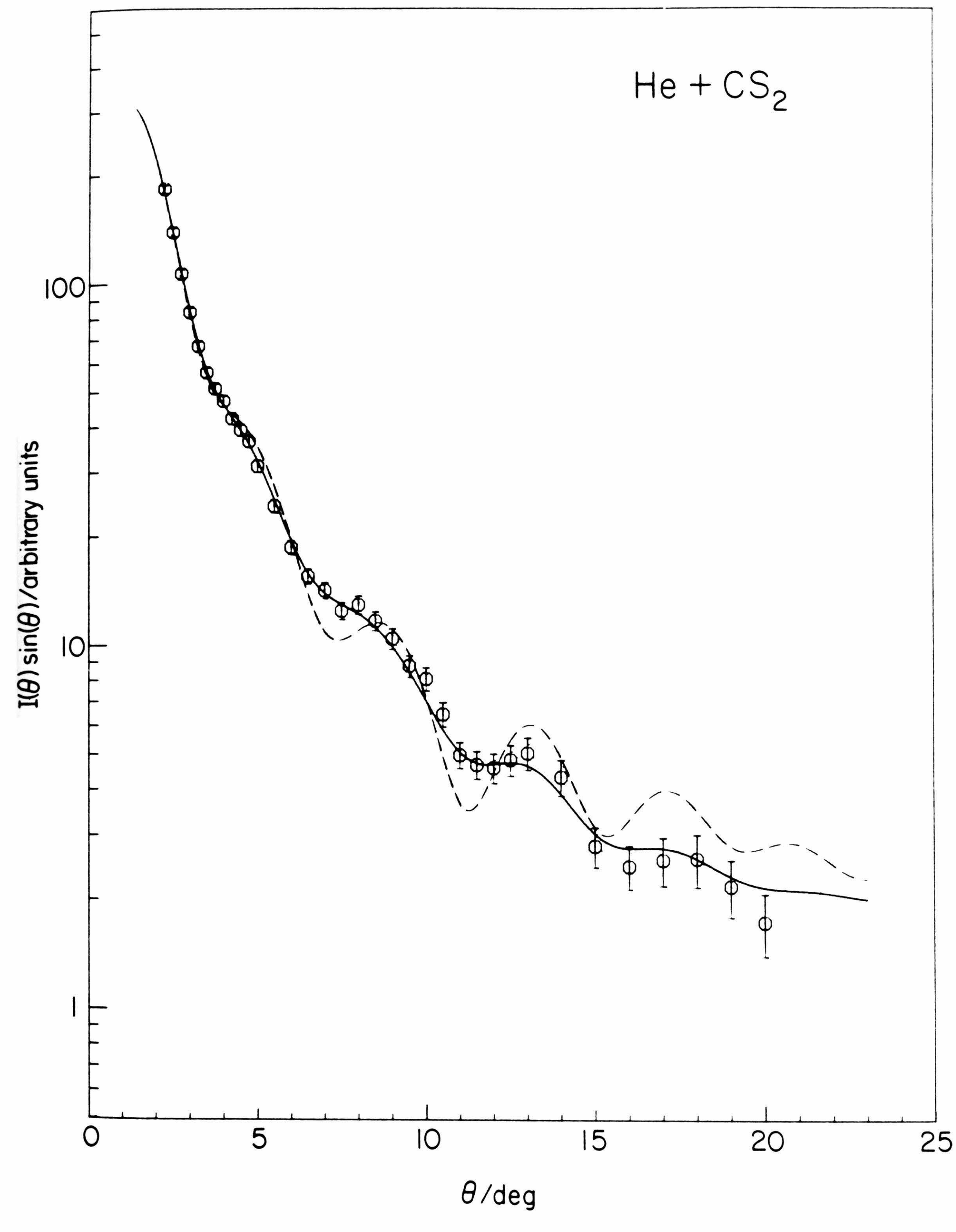

Figure 3.

Figure 4. Laboratory differential cross section for out-of-plane scattering of He by OCS. Experimental points are plotted with their error bars. The solid curve is the best fit anisotropic potential, the three-center MSV (see Table X). The broken curve is for the best fit spherical potential (see Table II).

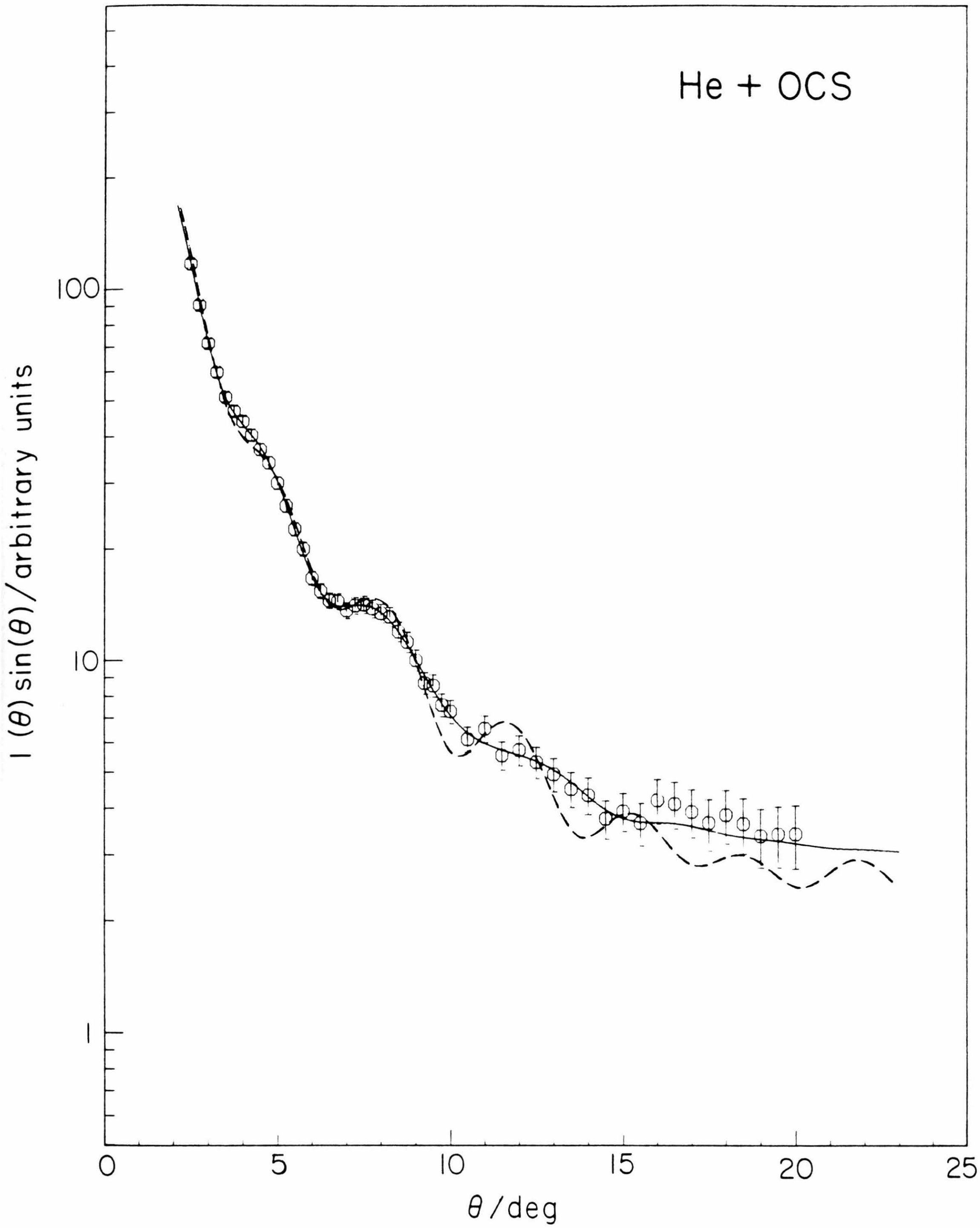

Figure 4.

Figure 5. Calculated laboratory cross sections for test of He + CO_2 anisotropy. The potentials are those listed in Table V. The solid curve is for a potential with r_m and ϵ anisotropy (test A). The long dashed curve is for the potential with no ϵ anisotropy (test B). The short dashed curve is for the potential with r_m and β anisotropy (test C). The short-long dashed curve is for the potential with no r_m anisotropy (tests D and E, for which the plot are indistinguishable).

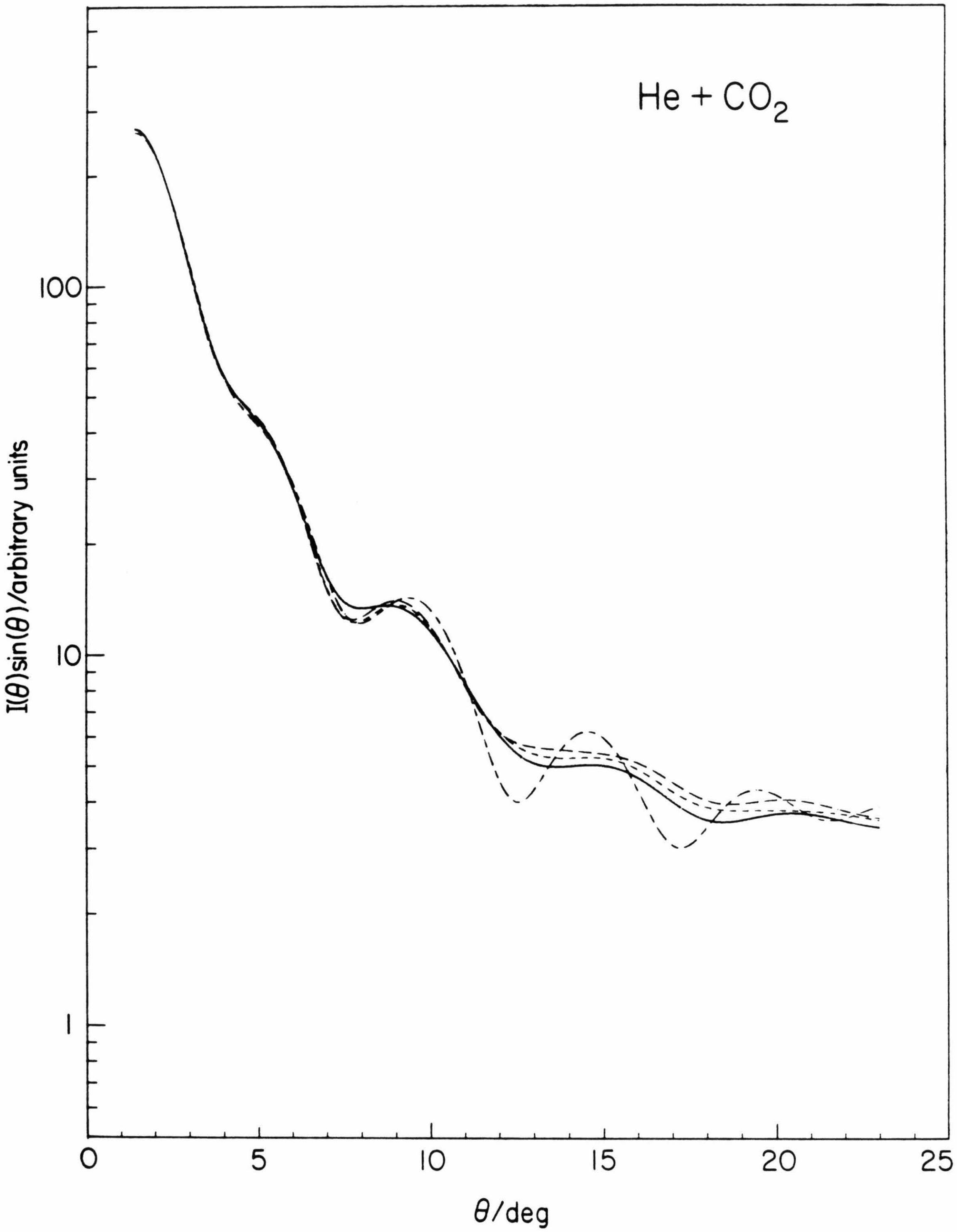

Figure 5.

Figure 6. Equipotential contours for the He + CO_2 SPFD-m1 potential (see Tables III and VI). The indicated contour values are in meV, while the tick marks are in Ångstroms. The attractive region is indicated by solid curves, the repulsive by the small dashes, and the zero of the potential by the large dashes. The minimum of the potential is -5.83 meV at r = 3.20 Åand $\gamma = \pi/2$. The saddle point is at r = 4.3 Å$\gamma = 0$ (and also $\gamma = \pi$) with a value of 2.1 meV. The centers of the C and O atoms are separated by 1.1621 Å.

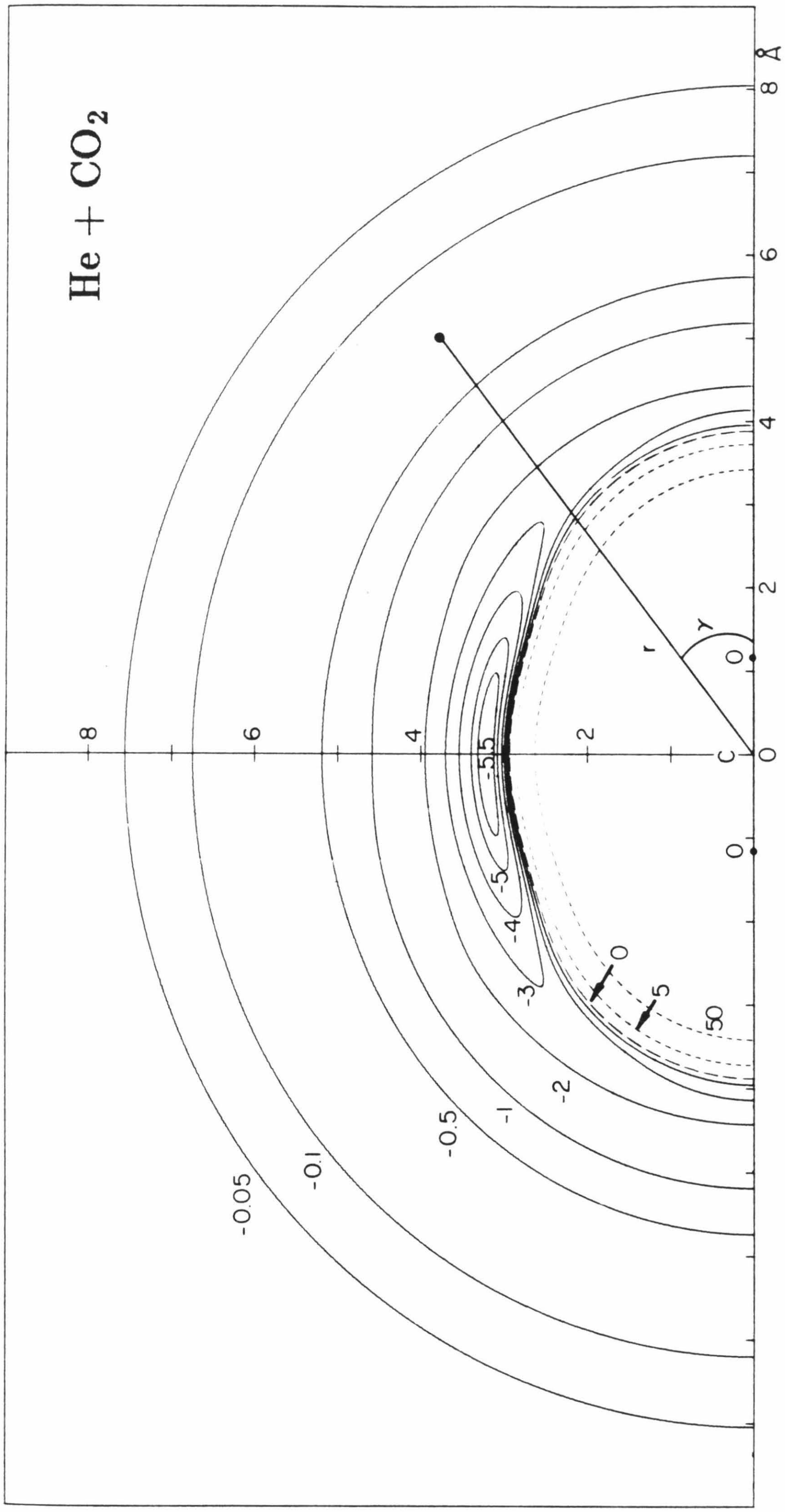

Figure 6.

Figure 7. He + CO_2 SPFD-m1 potential for three fixed approach angles γ, 0, 45, and 90 degrees and the spherical average of the potential (dashed curve). Please refer to Table VI for numerical details.

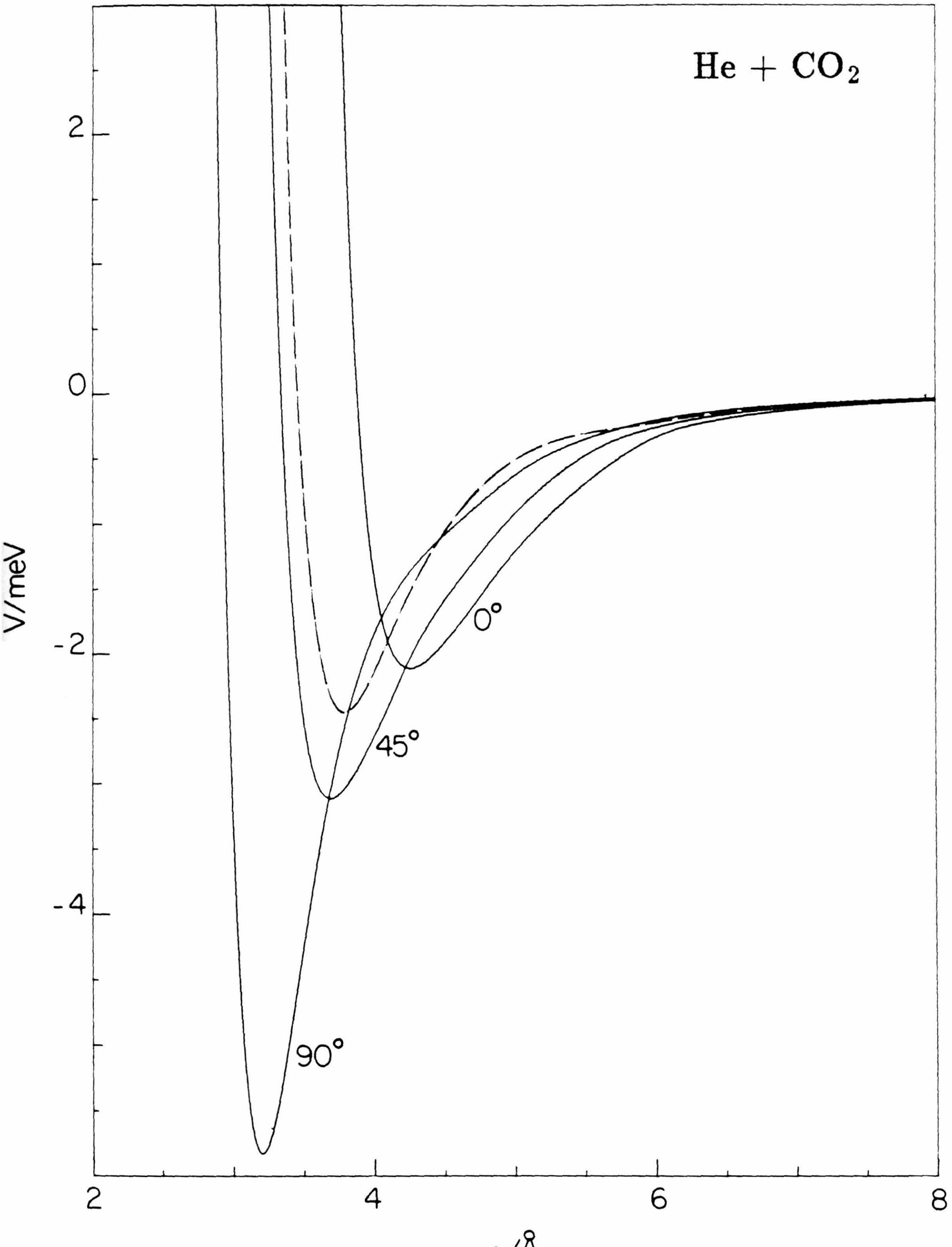

Figure 7.

Figure 8. Equipotential contours for the He + CO_2 SPFD-e potential (see Tables III and VI). The indicated contour values are in meV, while the tick marks are in Ångstroms. The attractive region is indicated by solid curves, the repulsive by the small dashes, and the zero of the potential by the large dashes. The minimum of the potential is -5.38 meV at $r = 3.10$ Åand $\gamma = \pi/2$. The saddle point is at $r = 4.3$ Å$\gamma = 0$ (and also $\gamma = \pi$) with a value of 1.2 meV. The centers of the C and O atoms are separated by 1.1621 Å.

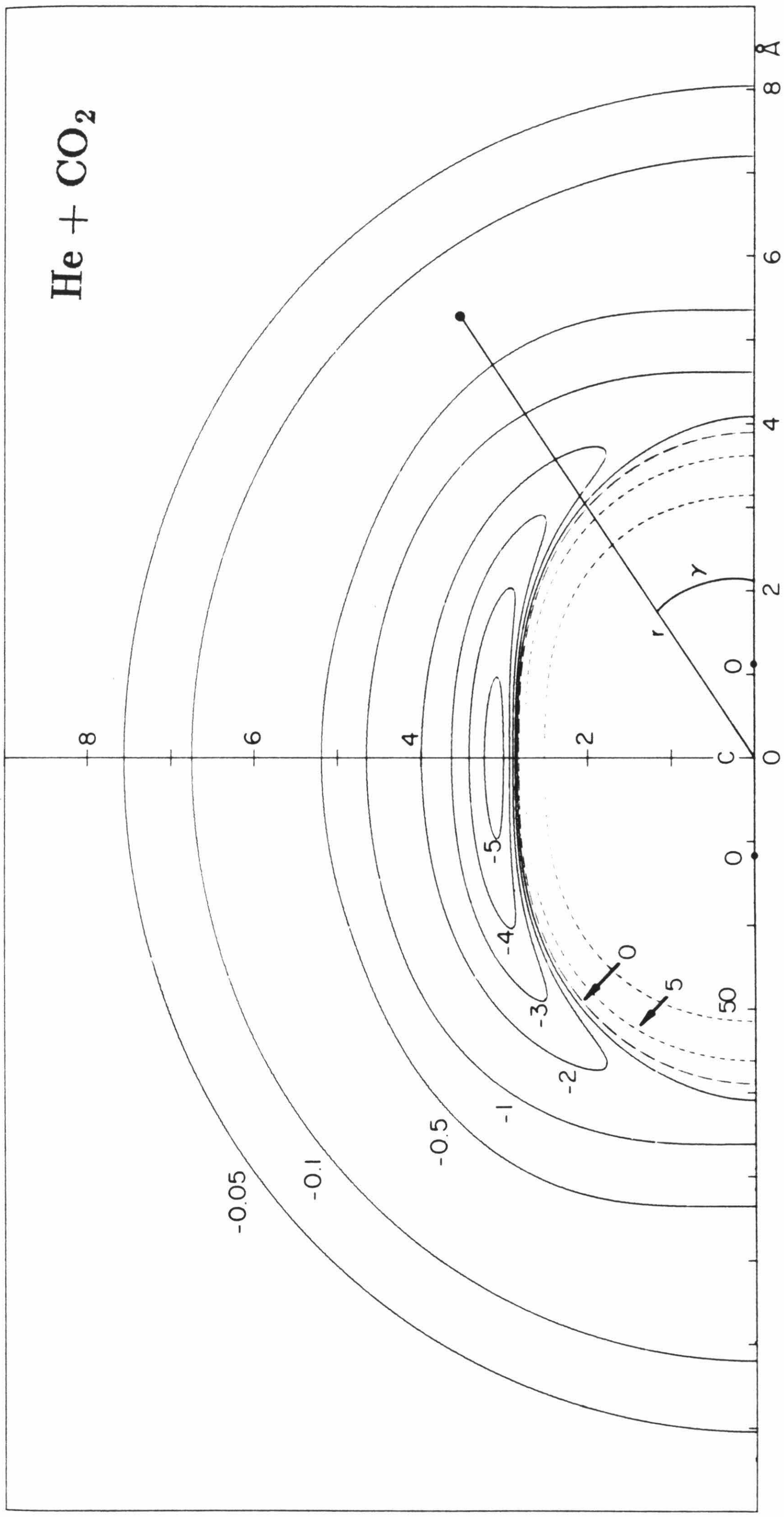

Figure 8.

Figure 9. He + CO_2 SPFD-e potential for three fixed approach angles γ, 0, 45, and 90 degrees and the spherical average of the potential (dashed curve). Please refer to Table VI for numerical details.

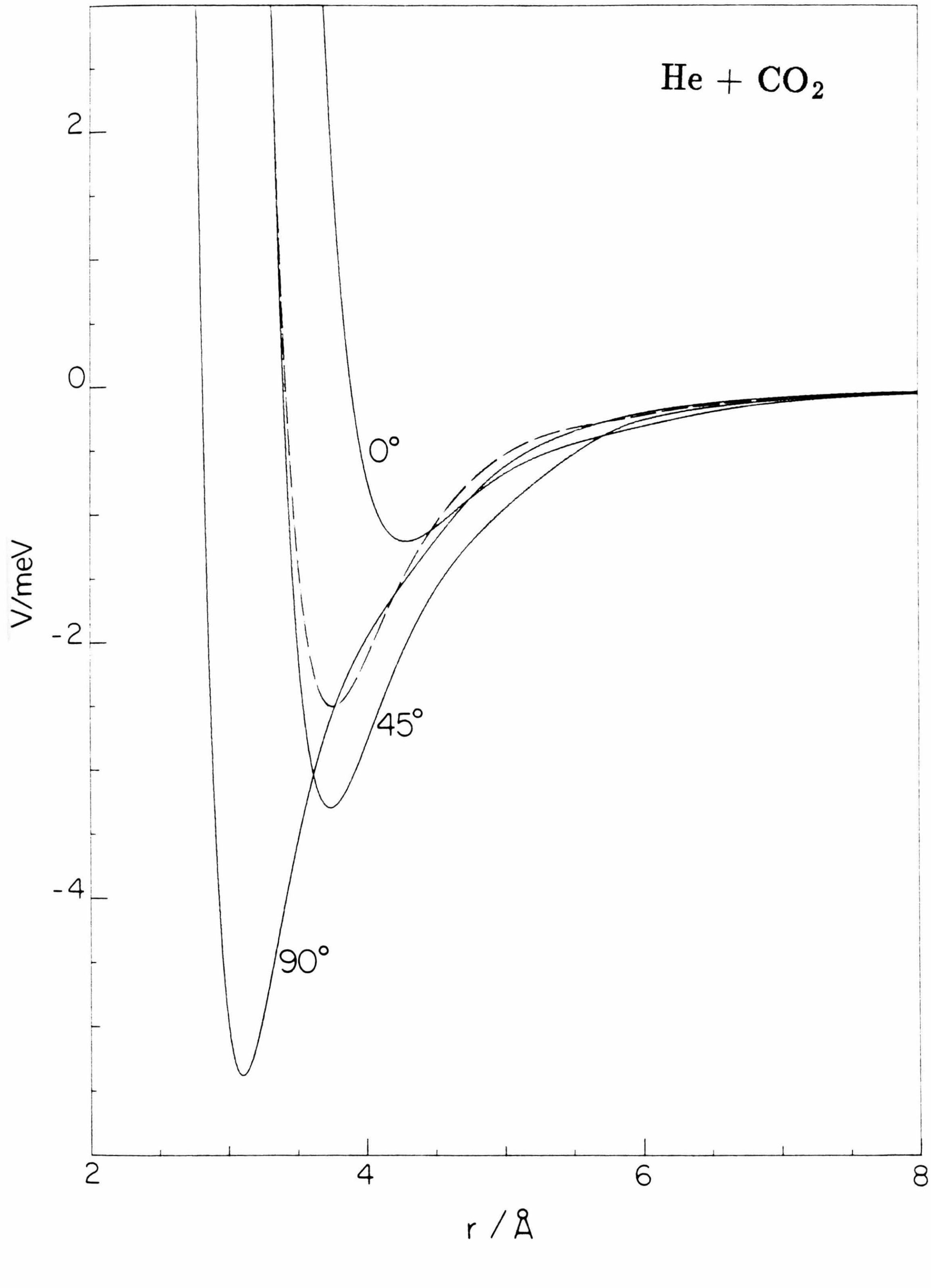

Figure 9.

Figure 10. Equipotential contours for the He + CS_2 MMSV-m potential (see Tables VII and IX). The indicated contour values are in meV, while the tick marks are in Ångstroms. The attractive region is indicated by solid curves, the repulsive by the small dashes, and the zero of the potential by the large dashes. The minimum of the potential is -4.92 meV at r = 3.73 Åand $\gamma = \pi/2$. The saddle point is at r = 5.1 Å$\gamma = 0$ (and also $\gamma = \pi$) with a value of 2.1 meV. The centers of the C and S atoms are separated by 1.554 Å.

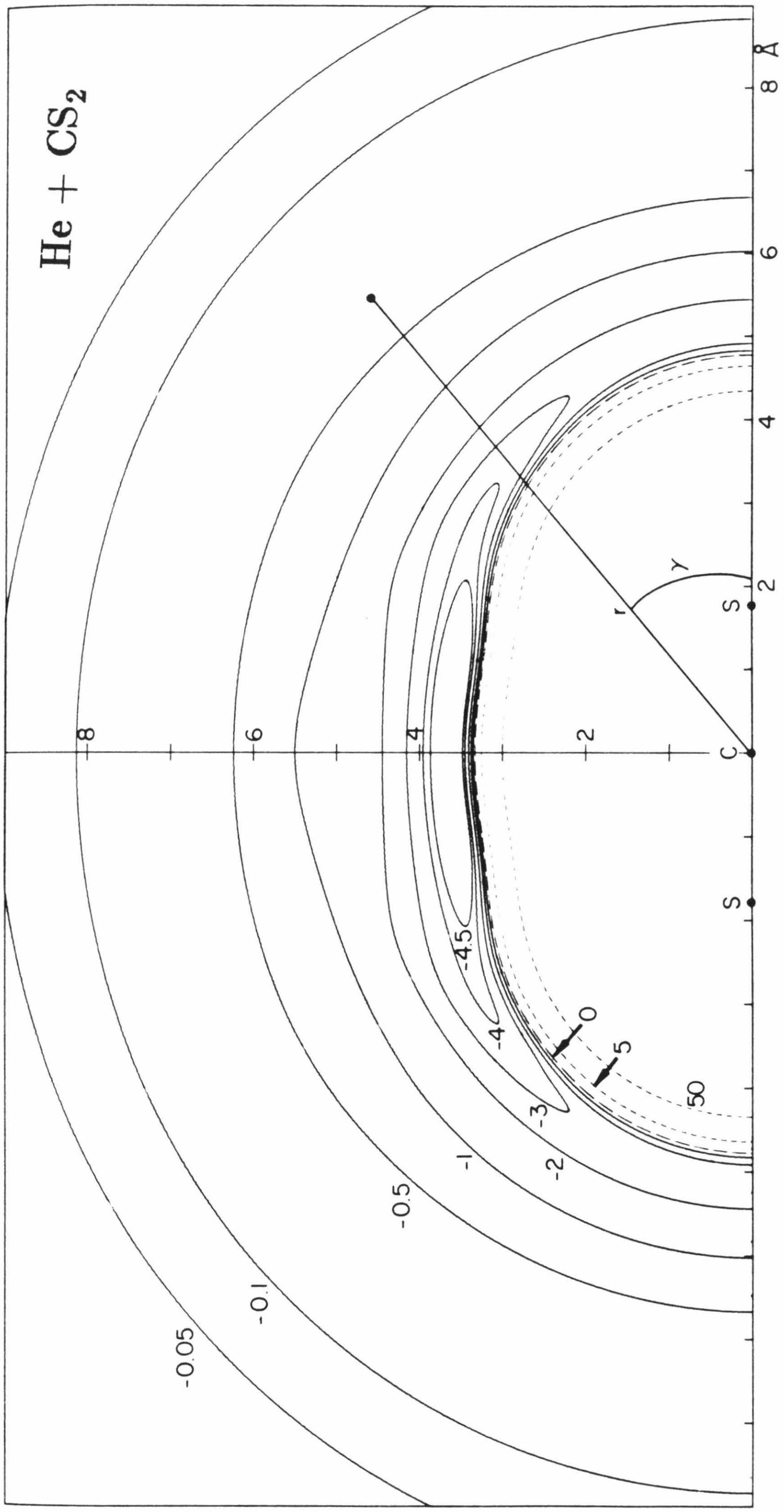

Figure 10.

Figure 11. He + CS_2 MMSV-m potential for three fixed approach angles γ, 0, 45, and 90 degrees and the spherical average of the potential (dashed curve). Please refer to Table IX for numerical details.

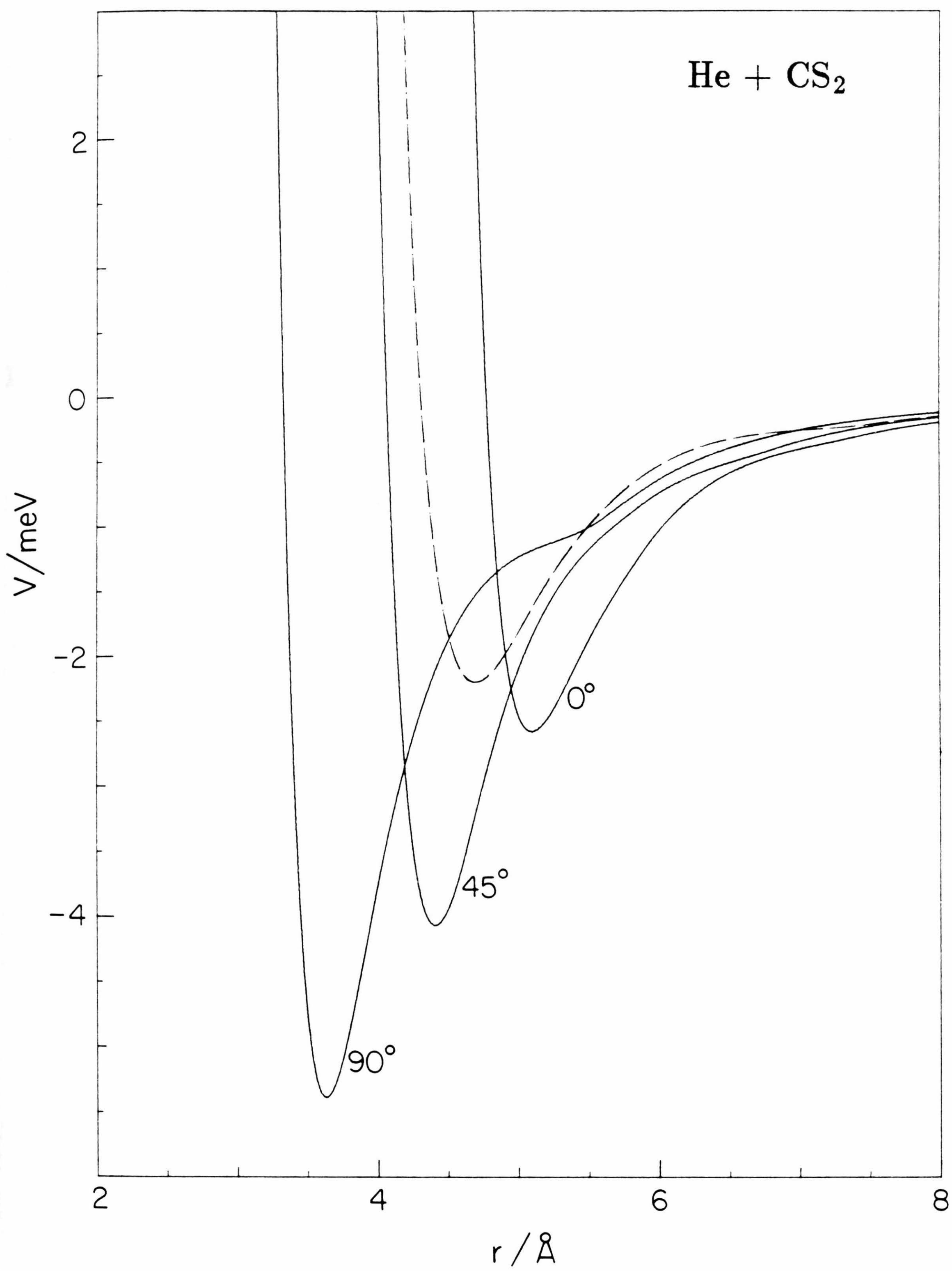

Figure 11.

Figure 12. Equipotential contours for the He + OCS MSV-m1 potential (see Tables X and XII). The indicated contour values are in meV, while the tick marks are in Ångstroms. The attractive region is indicated by solid curves, the repulsive by the small dashes, and the zero of the potential by the large dashes. The minimum of the potential is -4.6 meV at r = 3.76 Åand $\gamma = \pi/2$. One saddle point is at r = 5.2 Åγ = 0 with a value of -0.8 meV, the other saddle point is at r = 4.9 Å$\gamma = \pi$ with a value of -4.9 meV. The distance between the nuclei of the C and S atoms 1.560 Å, and the distance between the nuclei of the C and O atoms is 1.160 Å.

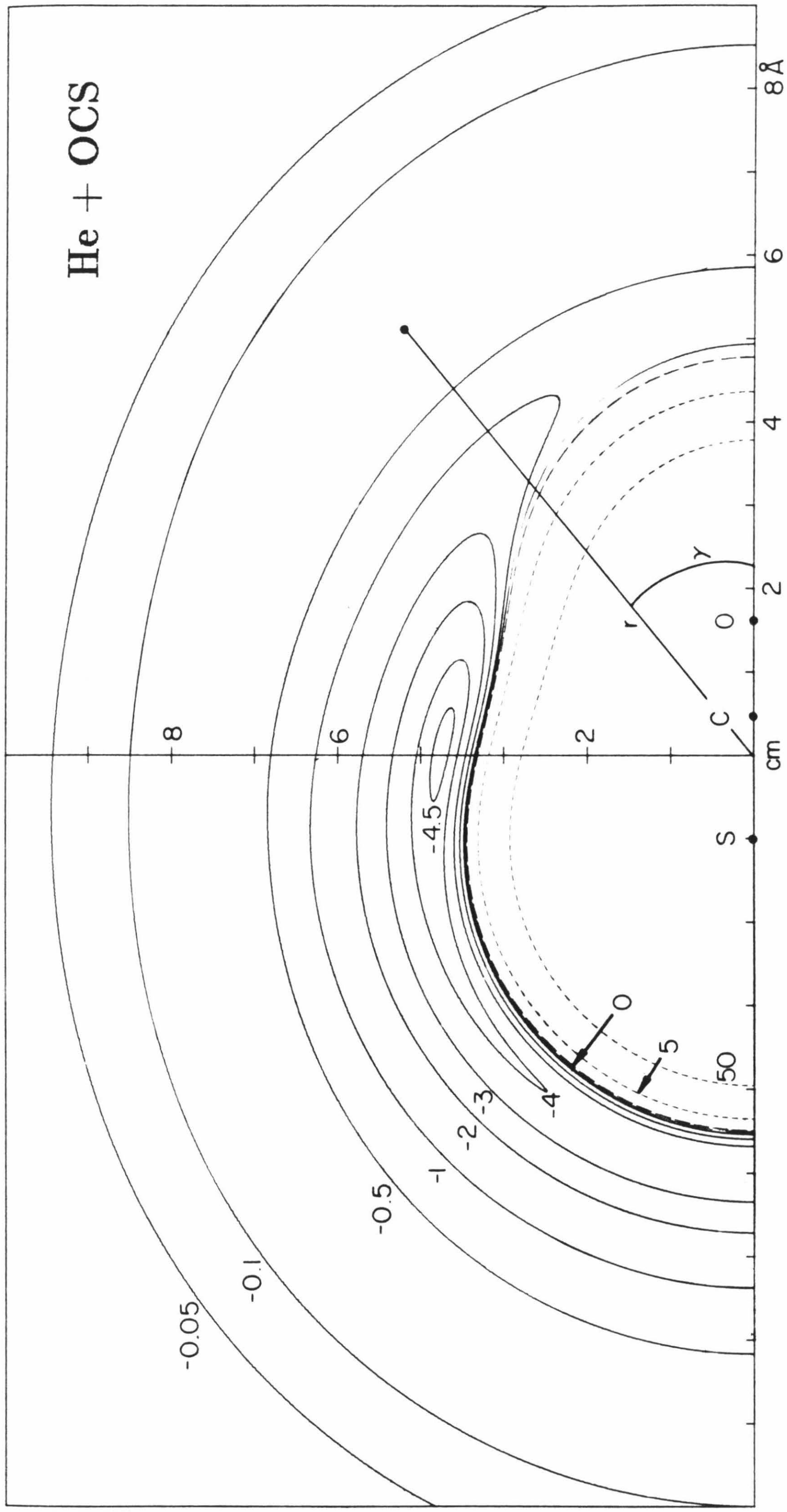

Figure 12.

Figure 13. He + CS_2 MMSV-m potential for three fixed approach angles γ, 0, 45, 90, 135, and 180 degrees and the spherical average of the potential (dashed curve). Please refer to Table XII for numerical details.

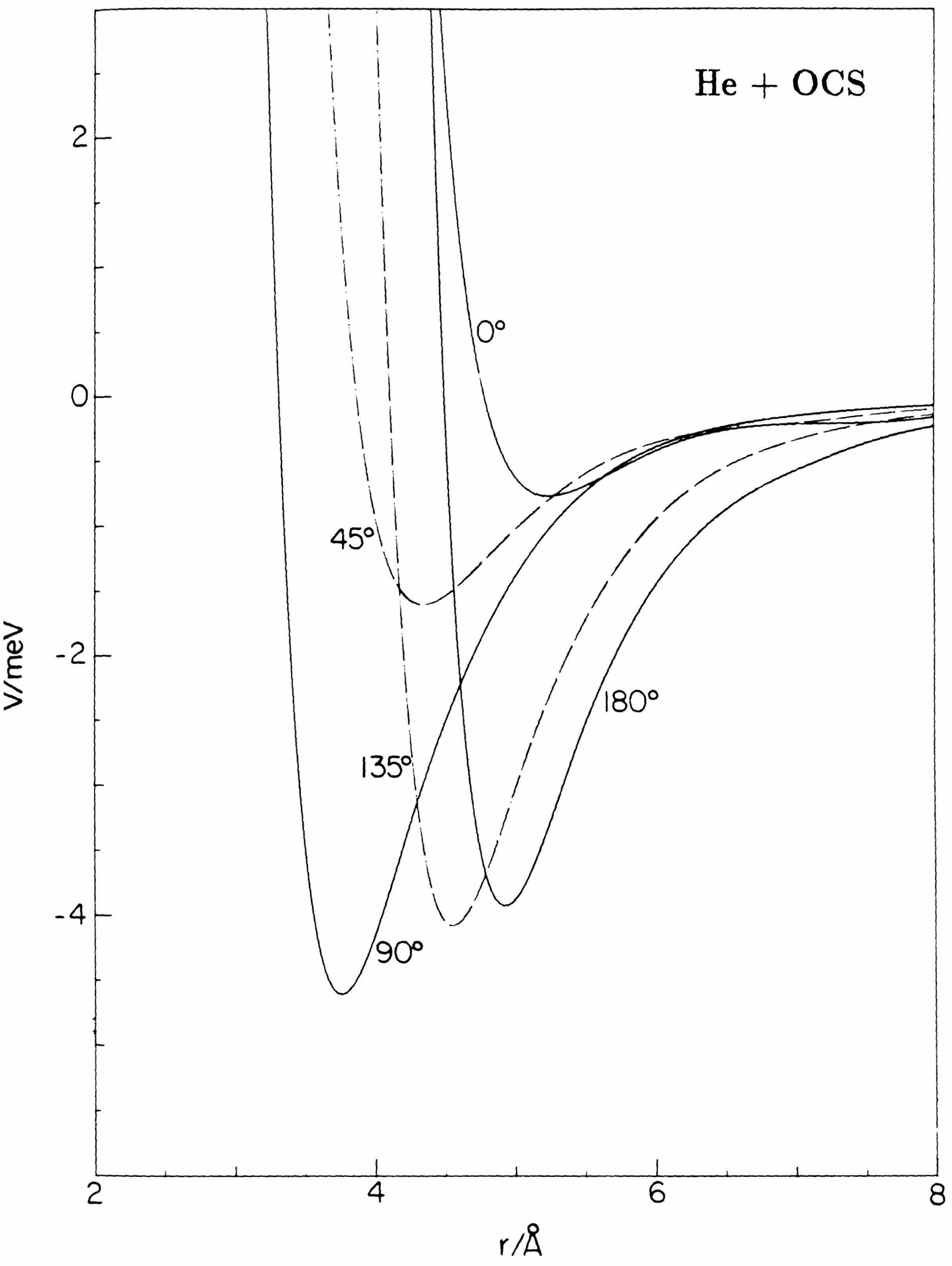

Figure 13.

Figure 14. Total integral cross sections as a function of the He beam velocity v_1. Points are from data of Butz et al. . The curve is a calculation for the He + CO_2 SPFD-e potential (Table IV). The ordinate scale is designed to exaggerate oscillatory behavior.

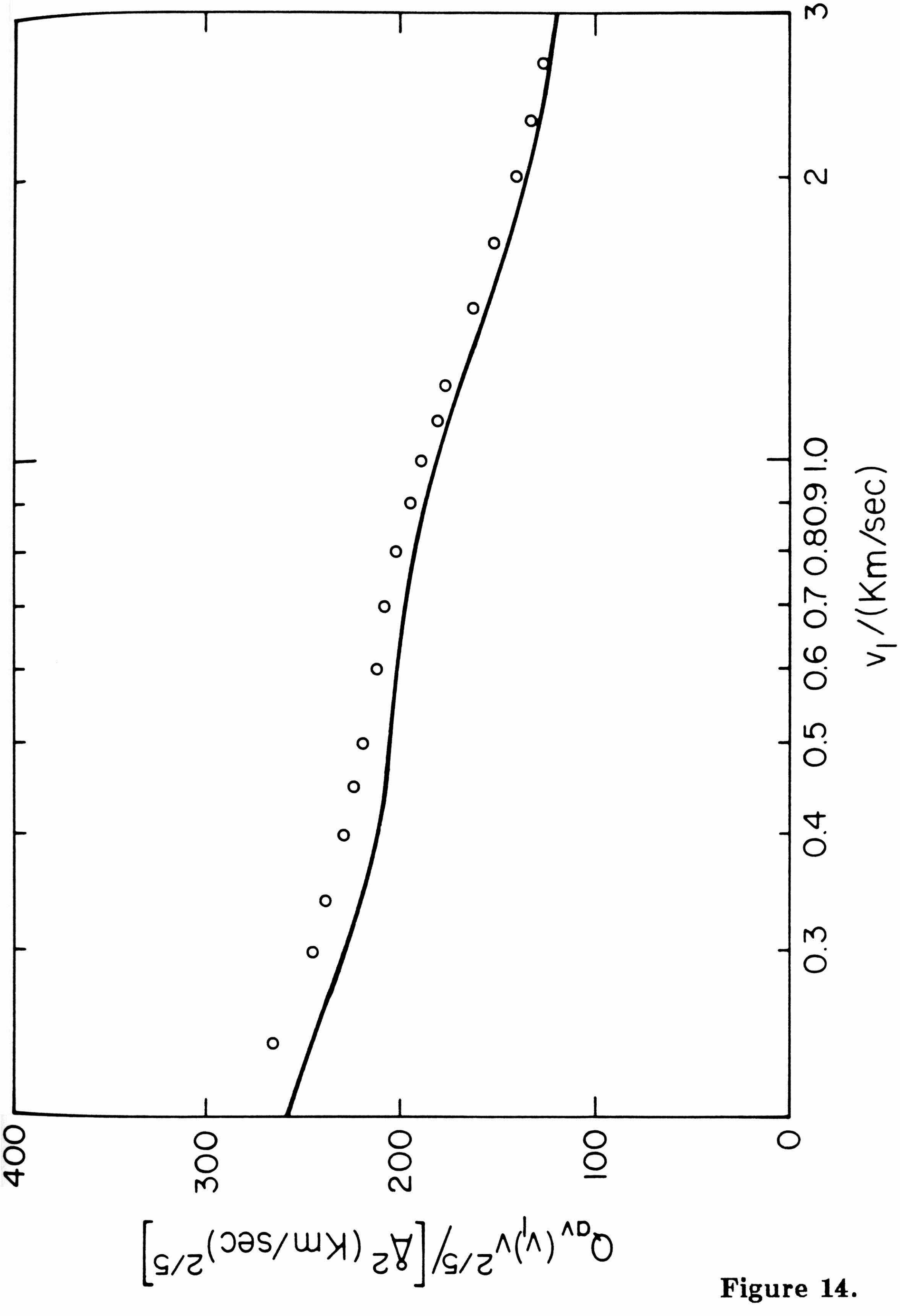
$Q_{av}(v_l)v^{2/5}/[Å^2 (Km/sec)^{2/5}]$
400
300
200
100
0
0.3
0.4
0.5
0.6
0.7
0.8
0.9
1.0
2
3
v_l/(Km/sec)

Figure 14.

Figure 15. Interaction diffusion coefficients as a function of temperature. Points are from various references (see text). The curve is a calculation for the He + CO_2 SPFD-e potential (Table IV).

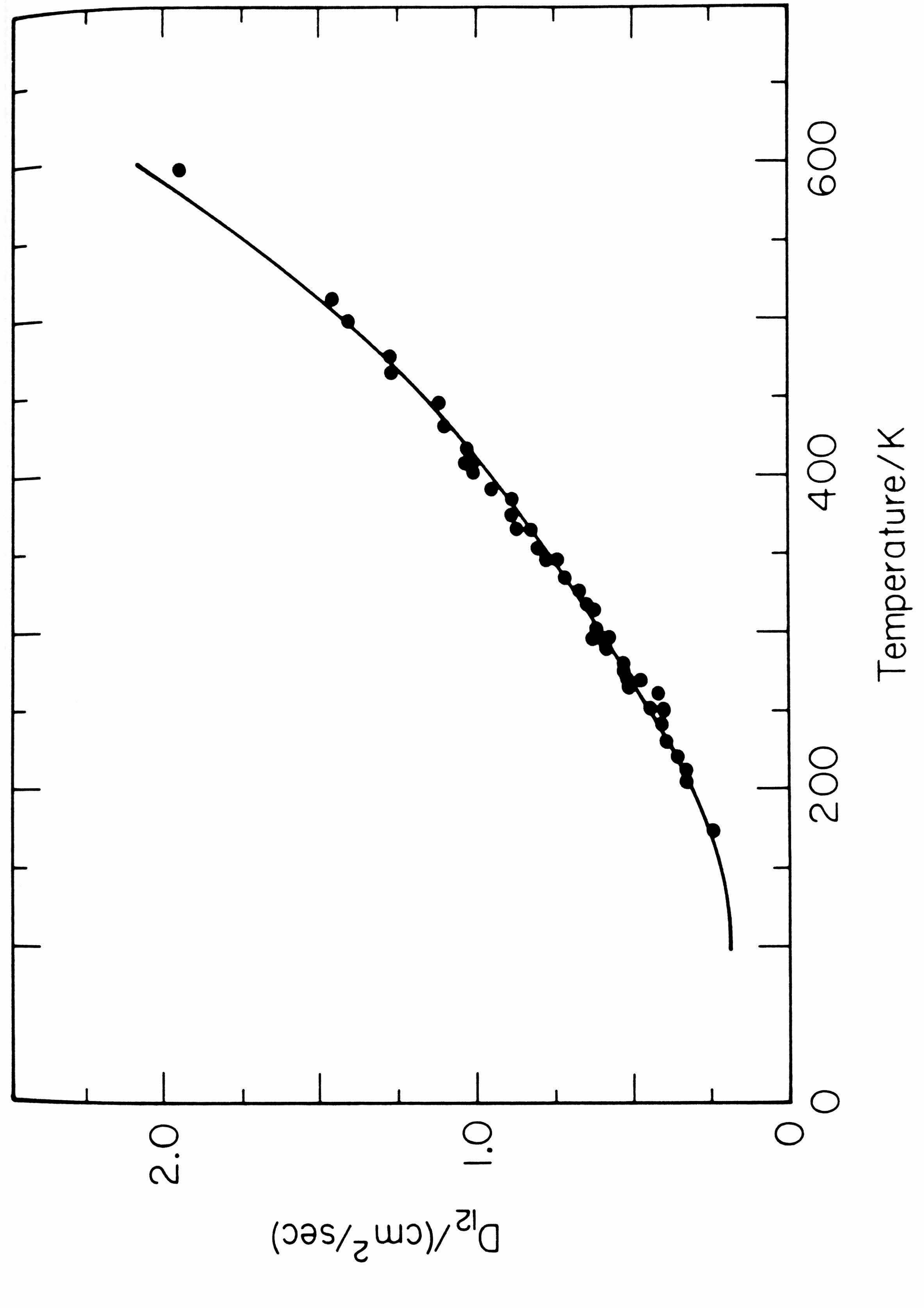

Figure 15.

Figure 16. Mixture viscosity coefficients as a function of temperature for two different mole fractions of CO$_2$: $x_{CO_2} = 0.0928$ (upper curve) and $x_{CO_2} = 0.6015$ (center curve). The lower curve is for the interaction viscosities η_{12}. See text for references on the points. The curves are calculations for the He + CO$_2$ SPFD-e potential (Table IV).

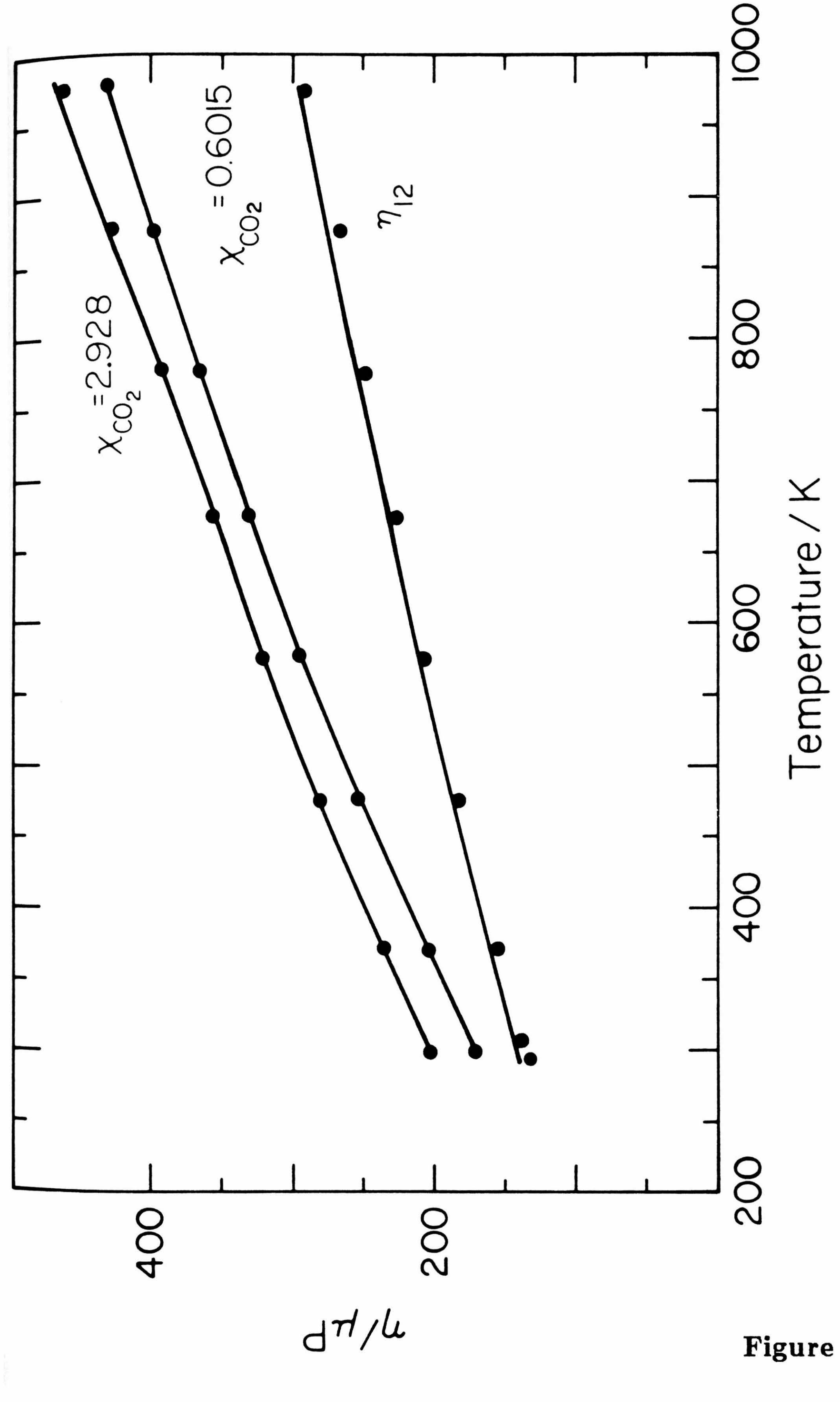
$\chi_{CO_2} = 2.928$
$\chi_{CO_2} = 0.6015$
η_{12}
400
200
$\eta/\mu P$
200
400
600
800
1000
Temperature / K

Figure 16.

Figure 17. Interaction second virial coefficients as a function of temperature. The curve is a calculation for the He + CO_2 SPFD-e potential (Table IV). See text for references on the points.

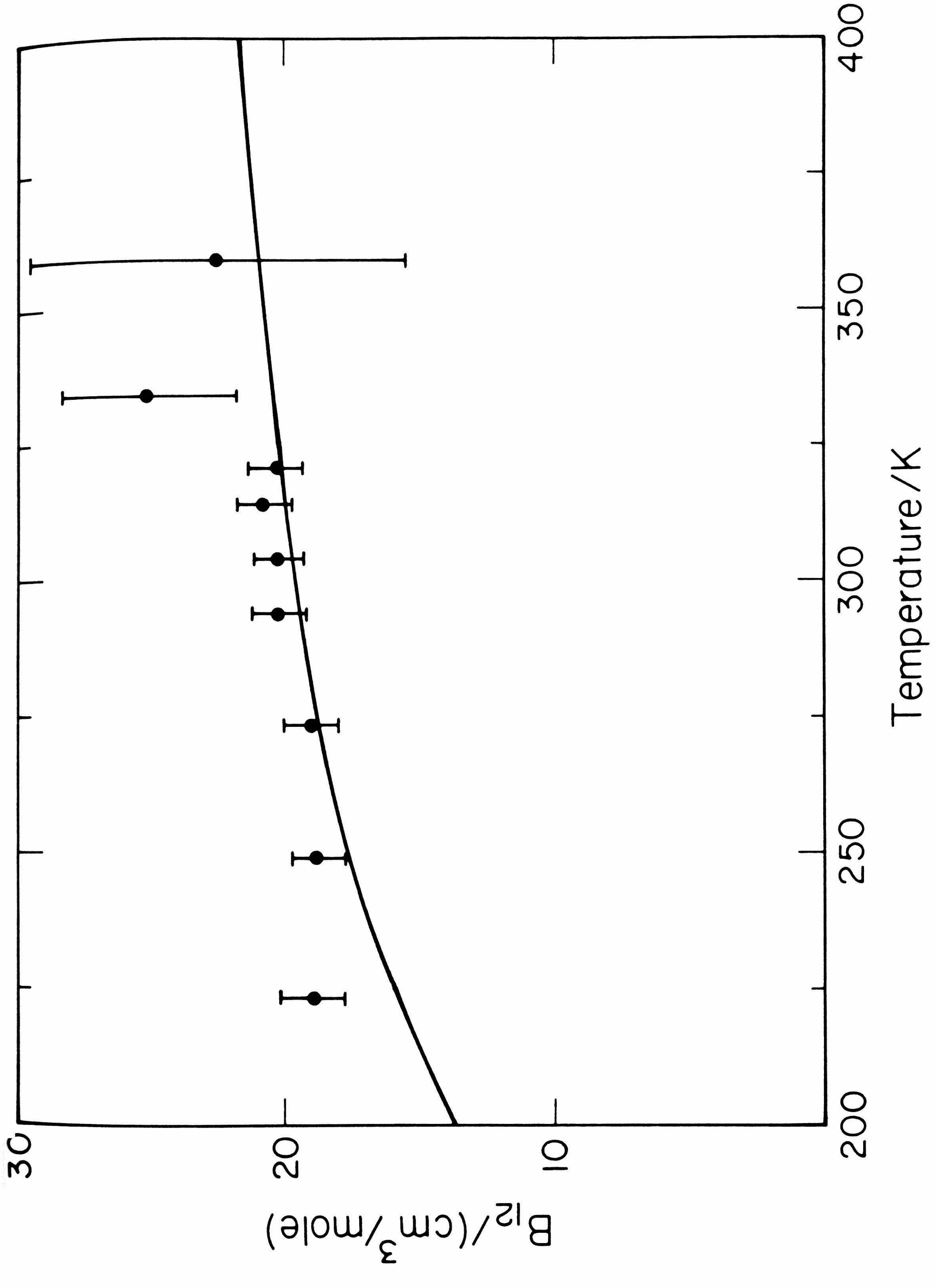

Figure 17.

CHAPTER 3

SENSITIVITY ANALYSIS FOR He + CO_2 SCATTERING

Sensitivity Analysis of the Differential Scattering Cross-Section to the He + CO_2 Interaction Potential [a]

Jarosław W. Winniczek [b] and Aron Kuppermann

Arthur Amos Noyes Laboratory of Chemical Physics [c]
California Institute of Technology, Pasadena, California 91125

(received)

A detailed sensitivity analysis of the total and rotational state-to-state differential cross-section (DCS) is performed on an empirical potential energy surface for He + CO_2. The infinite order sudden approximation is used to calculate the cross-sections. The sensitivity analysis consits of: 1) a large scale modification of the parameters that determine the anisotropic potential, and 2) an infinitesimal variation of these parameters to obtain a relative sensitivity function for the DCS. From these we demonstrate the effect each potential parameter has on the cross-sections. Despite the fact that this highly quantum system displays no classical effects such as rainbow scattering, we have

---

[a] This work was supported in part by the Air Force Office of Scientific Research (Contract No. F49620-79-C-0187).

[b] Work performed in partial fulfillment of the requirements for the Ph. D. degree in Chemistry at the California Institute of Technology.

[c] Contribution No. —-

shown that the quantal DCS oscillations contain significant information regarding the depth and width of the potential well and its anisotropy. Much of this information can be extracted from total-DCS scattering data. However the rotationally inelastic DCS contain a substantial amount of additional information regarding the shape of the potential energy surface.

1. INTRODUCTION

Interaction potentials between an atom and a molecule have been and continue to be subjects of significant theoretical as well as experimental analysis.[1–30] The experimentalists have sought ways to extract information on the shape of the potential from observed phenomena such as differential scattering cross-sections, integral cross-sections, transport phenomena, and relaxation spectroscopy.[9] The theorists have devised means for calculating and predicting the observed phenomena and associating them with various regions of the potential energy surface.[4–7,13,14,18–22] The anisotropy of these potentials results in the interconversion of translational and rotational energy during an encounter of the molecule with the atom. The most efficient theoretical tool for studing the outcome of such collisions is the infinite order sudden approximation (IOSA),[24] which we will use in the course of this paper, under conditions appropriate for its vadidity. The measurement of differential scattering cross sections in a crossed molecular beam apparatus is a very sensitive tool for the dermination of atom-molecule potentials. The region of the potential to which such data are most sensitive is the vicinity of the attractive well. Since this well results from the balance between the competing long-range atractive and the short range repulsive forces, its *ab-initio* evaluation is more difficult than for the adjacent regions. As a result, the experimental approach is the best one for the detrmination of the potential well characteristics.

The extraction of potentials from scattering data begins by proposing a physically reasonable model for the potential. The model is characterized by several parameters that define the specific shape of the potential, such as well depth, well minimum position, well width, repulsive wall steepness, and various features of the anisotropy. Initial values of these parameters are chosen judiciously, and are then used to simulate the observed scattering data. A least squares alogorithm is employed to adjust these parameters such that the best possible agreement is achieved between the observed and calculated cross-sections. As a result, the interpretation and analysis of scattering experiments is very dependent on theoretical considerations. In particular one wishes to know: a) how do various features of the potential effect the observed cross-section? b) how sensitive are the data to a given parameter and therefore how significant is this parameter?

These questions have been addressed by many investigators in a variety of ways. Cross[r4] used semiclassical theory to show that anisotropic potentials have differential cross-sections with dampened rainbow and quantal oscillations. Using the IOSA, Pack [25] has shown that the rainbow oscillation dampening is due to anisotropies in the potential well depth, while the quantal oscillation dampening is primarily caused by anisotropies in the position of the well depth minimum. In several instances computed IOSA integral rotational state-to-state cross-sections were found to be very sensitive to the anisotropic topography.[14,19–21] Rotationally inelastic rainbow structure has been related to details of the anisotropic potential energy surface.[5–7,] Numerous experimentalists have successfully fitted potentials to their data only if those potentials contained anisotropy.[3,9,10,15–17]

A potential that has received considerable attention is one for He + CO_2. The repulsive wall as well as its anisotropy have been calculated by several methods[21,22]. The anisotropic long-range dispersion coefficients were evaluated by Pack.[35,36] Parker et al.[10,9] measured the differential cross-section from which they obtained an anisotropic potential for the well region. Recently we remeasured the differential cross-sections for that system, and proposed a new potential which we believe to be more accurate.[3]

In this paper we wish to probe and answer the questions regarding the significance and sensitivity of the parameters which specify the He + CO_2 potential. Some of the above mentioned papers employed classical scattering theory in arriving at many of their conclusions. Classical mechanics is not applicable to this highly quantal system which shows no evidence of rainbow scattering. Some have used rather rigid and inflexible potentials, such as the Lennard-Jones, which was shown to be unsatisfactory for modeling real potentials.[18]

This study has been undertaken to establish a clearer connection between the observed differential cross-sections and the potential energy surface for He + CO_2. Although we have chosen a specific system for this analysis, we feel that the majority of the conclusions will apply to similar systems, *i.e.*, highly quantum systems with collision energies and rotational energy spacings analogous to those for He + CO_2. Our approach is two fold; a) We conduct a large scale sensitivity analysis by selectively modifing the parameters of our empirical potential to elucidate the effects they have on the scattering. b) We then conduct an infinitesimal sensitivity analysis by taking the partial derivatives of the cross-sections with respect to a given potential parameter; the sensitivities of all the parameters will be compared to each other and the relative significance of each parameter will be accessed.

The infinitesimal sensitivity analysis has been stimulated by the work of Rabitz and coworkers rf 11-14, allthough our approach is much less general and less elegant, it nonetheless is completely adequate in satisfing the goals of this paper.

Eno and Rabitz[11-14] have developed the formal theory of sensitivity analysis for collision process. The basic premise of the theory is to determine how variations in one quantity are affected by variations in an other quantity. The first application is obtaining the variations of cross-sections with variations in a feature of the interaction potential. The theory is highly generalizable to other applications, such as variation of one state-to-state cross-section with a different state-to-state cross-section, variations of one potential parameter with an other. All of these can be obtained from a single solution of the scattering problem, with relatively little additional computational effort.

Eno and Rabitz[13] have evaluated the parameter sensitivities for an assumed He + CO_2 anisotropic potential. This potential is an inflexible Lennard-Jones type, and hence does not fully resemble the empirical potential[3]. In addition they reported sensitivities for differential cross-sections with an initial ground rotational state ($j = 0$). If He + CO_2 sensitivity results are to be a useful guide for the experimentalist, one should present calculations that most closely model the conditions of the experiment. Under most experimental conditions it is not practical or possible to produce CO_2 molecules in their ground state.[3,10] Even if CO_2 molecules were prepared in their ground states the small energy loss by the helium in exciting the CO_2 to a higher rotational state could not be observed with current time-of-flight molecular beam apparati. The rotational constant for CO_2 is so much smaller than the collision energy, a transition from the ground rotational state would change the scattered He energy (and hence flight time to the detector) by such a small amount that the transition would be obscured by the spreads in energy of the He and CO_2 beams.

Schinke et al.[6] have pointed out that the rotational rainbow (not to be confused with the classical rainbow) is a structure highly sensitive to the potential anisotropy. Eno and Rabitz[13] have confirmed this with their sensitivity analysis. However both of these studies have been performed on the initial ground state of the target molecule. For higher ground states and larger changes in rotational quantum number the rotational rainbows become much less pronounced and move to higher scattering angles.[6,13] In fact Schinke et al.[6] recommend that experiments be conducted at the initial ground state of the target molecule and at higher scattering angles. As we stated before, for the case of CO_2 it is not practical to have it in its ground state. Also, large scattering angles are difficult to attain experimentally, since the signal is usually very low at high angles. For practical purposes it is best to concentrate on small scattering angles. We will then concentrate on conditions that best model experimental conditions, and as we will show the majority of significant information regarding the potential will be contained in the range of scattering angles easily observable.

In section 2 we briefly summarize the IOS approximation and present the needed expressions for the total and state-to-state differential cross-sections. In section 3 we review our model potential. In sections 4 and 5 we present the calculation methods. We demonstrate the inappropriateness of classical rainbow scattering analysis for our model system in section 6. Before considering anisotropic scattering we analyze a spherical analog of our model potential in section 7. The fully anisotropic potential sensitivities for the total differential cross-section are presented in section 8. In section 9 we discuss the rotational state-to-state differential cross-sections by way of the large scale sensitivity analysis, and employ the infinitesimal sensitivity analysis in section 10.

In section 11 we briefly discuss the results of a set of analyses at two collision energies above and below the 65 meV used in sections 4 thru 10. Finally we summarize our findings in section 12.

2. CROSS-SECTIONS

We have used the infinite order sudden approximation (IOSA) to calculate the total (elastic and inelastic) and rotational state-to-state differential scattering cross-sections (DCS). Since this formalism has been reviewed and outlined by many authors we will only present the salient points of the IOSA.

In the systems to be considered, the target molecules are essentially all in their ground vibrational states and the collision energies are well below the threshhold for producing vibrational excitations.[33] Therefore, it is reasonable to treat the target molecule as a rigid rotor of length R (the distance between the end atoms) having a moment of inertia I. Let $\underset{\sim}{r}$ be the position vector of the incident atom with respect to the center-of-mass of the molecule and γ be the angle between $\underset{\sim}{r}$ and the oriented molecular axis $\underset{\sim}{R}$. The nuclear motion Hamiltonian for this system is therefore

$$\hat{H} = -\frac{\hbar^2}{2\mu r}\frac{\partial^2}{\partial r^2}r + \frac{\hat{L}^2}{2\mu r^2} + \frac{\hat{J}^2}{2I} + V(r,\gamma) \tag{1}$$

where μ is the atom-molecule reduced mass, and $\hat{L}$ and $\hat{J}$ are the orbital angular momentum and molecular angular momentum operators, respectively.

The Schrödinger equation can be solved for the above Hamiltonian by expanding the wave function in eigenfunctions of the total angular momentum operator $\hat{\mathbf{J}} \equiv \hat{J} + \hat{L}$ and its projection $\hat{\mathbf{J}}_z$ about a space fixed axis z. This results in a set of coupled radial differential equations; the coupling being due to the matrix elements of $V(r, \gamma)$ obtained using these eigenfunctions. Under the conditions of our calculation it is valid to decouple these equations, by imposing the centrifugal sudden (CS)[29,30] and energy sudden (ES)[27,28] approximations, collectively known as the infinite order sudden approximation (IOSA).[24] The CS approximation is introduced by replacing the orbital angular momentum operator with its eigenvalue form[29,30]

$$\hat{L}^2 \simeq \hbar^2 \bar{l}(\bar{l}+1) \tag{2}$$

while to implement the ES approximation the molecular angular momentum operator is replaced with its eigenvalue form[27,28]

$$\hat{J}^2 \simeq \hbar^2 \bar{\jmath}(\bar{\jmath}+1) \tag{3}$$

where $\bar{l}$ and $\bar{\jmath}$ are appropriately chosen effective quantum numbers.

The resulting set of decoupled differential equations are

$$\left[\frac{d^2}{dr^2} + {k_{\bar{\jmath}}}^2 - \frac{\bar{l}(\bar{l}+1)}{r^2} - \frac{2\mu}{\hbar^2} V(r, \gamma)\right] \phi_{\bar{l}}(r; \gamma) = 0 \tag{4}$$

where the wave vector is

$$ {k_{\bar{\jmath}}}^2 = \frac{2\mu}{\hbar^2}\left[E - \frac{\hbar^2 \bar{\jmath}(\bar{\jmath}+1)}{2I}\right] \tag{5}$$

E being the total energy of the system and ϕ_l is an effective scattering wave function for a angle of incidence γ. These equations can be solved for a given $\bar{l}$ and γ in a manner analogous to a spherical problem, by requiring that the wave function must vanish at the origin, and at large r behave as

$$\phi_{\bar{l}} \xrightarrow[r\to\infty]{} k_{\bar{j}}^{-1/2}\left\{ e^{-i(k_{\bar{j}}r-\bar{l}\pi/2)} - e^{i[k_{\bar{j}}r-\bar{l}\pi/2+2i\eta_{\bar{l}}(\gamma)]}\right\} \qquad (6)$$

where $\eta_{\bar{l}}(\gamma)$ is the phase shift for a given fixed atom-molecule orientation, which is obtained in a manner identical to that for a spherical scattering problem[31,32], and the resulting scattering amplitude is given by

$$f^{k_{\bar{j}}}(\gamma \mid \theta) = \frac{i}{2k_{\bar{j}}}\sum_{l}(2l+1)\{1-e^{2i\eta_l(\gamma)}\}P_l(\cos\theta) \qquad (7)$$

It can be shown that the rotational state-to-state differential cross-section is given in this approximation by[24]

$$\sigma(j' \leftarrow j \mid \theta) = \frac{k_{\bar{j}}^2}{(2j+1)k_j{}^2}\sum_{m_j} \mid < j'm_j|f^{k_{\bar{j}}}(\gamma \mid \theta)|jm_j >_{\mathrm{BF}} \mid^2 \qquad (8)$$

where the matrix elements of $f(\gamma \mid \theta)$ are evaluated in the spherical harmonics of the body–fixed coordinates - BF.[23] It should be noted that this result is independent of the choice of $\bar{l}$.

Equation (8) can be simplified for calculational purposes by expanding $f^{k_{\bar{j}}}(\gamma \mid \theta)$ in Legendre polynomials

$$f^{k_{\bar{j}}}(\gamma \mid \theta) = \sum_{i} F_i^{k_{\bar{j}}}(\theta)P_l(\cos\gamma) \qquad (9)$$

where

$$F_i^{k_{\bar{j}}}(\theta) = (i + 1/2) \int_0^{\pi} P_i(\cos\gamma) f^{k_{\bar{j}}}(\gamma \mid \theta) \quad \sin\gamma \, d\gamma \qquad (10)$$

This then leads to the expression for the differential cross-section

$$\sigma(j' \leftarrow j \mid \theta) = \left(\frac{k_j}{k_{\bar{j}}}\right)^2 \sum_{j''} \frac{1}{2j''+1} C^2(j, j'', j'; 0, 0, 0) \mid F_{j''}^{k_{\bar{j}}}(\theta) \mid^2 \qquad (11)$$

The total differential cross-section is the sum of all state-to-state cross-sections $\sigma(j' \leftarrow j \mid \theta)$ from an initial state j over all energetically allowed final states j'. The cross-section in equation (11) can be summed and simplified if the effective IOSA rotational quantum number $\bar{j}$ is set equal to j (the initial rotational state). By way of the completeness of the spherical harmonics and the addition theorem for the spherical harmonics it can be shown that the total differential cross-section is

$$\sigma(\theta) = 1/2 \int_0^{\pi} |f^{k_j}(\gamma \mid \theta)|^2 \sin\gamma \, d\gamma \qquad (12)$$

This expression, for a given initial relative translational energy, is independent of the initial rotational state j, and hence represents the total differential cross-section for any initial state.

It has been demonstrated that the IOSA is valid in cases where the relative collision energy is much larger than the spacing between rotational levels and larger than the attractive part of the potential. Since we will consider collision energies of 35 to 95 meV we are well within the range validity for the He + CO_2 interaction where the typical CO_2 rotational spacings are less than 6 meV, and where the He + CO_2 well depth is less than 7 meV.

3. POTENTIALS

In order to obtain realistic results and fulfill the objectives of this paper we will use a realistic potential for our cross-section and sensitivity calculations. Our potential is based on one extracted from experimental crossed-beam data. We represent the anisotropy by giving an angular γ dependence to the parameters of an otherwise spherical potential,

$$V(r,\gamma) = V\left[r, \epsilon(\gamma), r_m(\gamma), \beta(\gamma)\right] \tag{13}$$

where ϵ is the well depth, r_m is the well minimum position, and β is a shape parameter which depends on the parameterization of V. Some parameterizations may have more than one shape parameter, all of which may have angular dependence. In this paper we will expand the well minimum position and the well depth to second order in Legendre polynomials

$$r_m(\gamma) = r_m^{(0)} + r_m^{(2)} P_2(\cos\gamma) \tag{14a}$$

$$= r_m^{(0)}[1 + qP_2(\cos\gamma)] \tag{14b}$$

and

$$\epsilon(\gamma) = \epsilon^{(0)} + \epsilon^{(2)} P_2(\cos\gamma) \tag{15a}$$

$$= \epsilon^{(0)}[1 + aP_2(\cos\gamma)] \tag{15b}$$

where we have defined the anisotropies of the well minimum position and depth as $q \equiv r_m^{(2)}/r_m^{(0)}$ and $a \equiv \epsilon^{(2)}/\epsilon^{(0)}$ respectively. Due to the symmetry of the CO_2 molecule the first order Legendre term is zero.

The shape of $V(r, r_m, \epsilon, \beta)$ is charterized by the highly flexible Morse-Morse-spline-van der Waals (MMSV) potential which may be written as

$$V(r) = \frac{\epsilon}{\omega}\left\{ \mathbf{e}^{2(\beta' - r\beta\omega/r_m)} - 2\mathbf{e}^{(\beta' - r\beta\omega/r_m)} \right\} \qquad (16a)$$

$$\text{for} \quad r < r_o$$

$$V(r) = \epsilon\left[\mathbf{e}^{2\beta(1-r/r_m)} - 2\mathbf{e}^{\beta(1-r/r_m)} \right] \qquad (16b)$$

$$\text{for} \quad r \leq r_i$$

$$\begin{aligned} V(r) = {} & \left[S_1(r_{sv} - r)^2 + S_3\right](r_{sv} - r) \\ + {} & \left[S_2(r - r_i)^2 + S_4\right](r - r_i) \end{aligned} \qquad (16c)$$

$$\text{for} \quad r_i < r < r_{sv}$$

$$V(r) = -\frac{C_6}{r^6} - \frac{C_8}{r^8} \qquad (16d)$$

$$\text{for} \quad r \geq r_{sv}$$

$$\text{with} \quad \omega = \frac{\beta' - \ln 2}{\beta - \ln 2}$$

where $r_o = r_m(1 - \ln 2/\beta)$ is the zero of both Morse funtions, and $r_i = r_m(1 + \ln 2/\beta)$ is the inflection point of the second Morse function. The spline coefficients S_1, S_2, S_3 and S_4 are determined by continuity conditions imposed on the potential and its derivative at r_i and r_{sv}. The Spline-van der Waals junction is maintained at $r_{sv}/r_m = 1.6$,[3,9,10,18] and the constant ω is used to impose a smooth transition between the two Morse functions.

This parameter-expansion MMSV potential is a good choice for this study since the various features of the potential are neatly segregated into specific parameters; the well minimum position ($r_m^{(0)}$), the well depth ($\epsilon^{(0)}$), their anisotropies (q and a), the well width (β),and the repulsive wall steepness (β'). Table I lists the values of these parameters as used in this study, obtained from an empirically derived potential,[3] the long range dispersion terms for this potential were computed by Pack[36]). In the course of this study we will change some of these values one by one to see what effect the change has on the cross-sections and the sensitivities.

4. SENSITIVITY CALCULATIONS

Extensive work has been done by Eno and Rabitz[11−14] on formal sensitivity analysis in quantum collison theory. However, since the aims of this study are less probing and less demanding, we can adopt a simpler and less general approach to analyzing the sensitivity of observable data, *i.e.*, cross-sections, to the interaction potential; one that will serve as a useful guide to interpreting experimental scattering data. We wish to know how sensitive the differential scattering cross-section is to a parameter specifing the corresponding potential? In other words, for a given potential and collision energy, by what fraction will the cross-section change for a small change in the parameter. If this change is small enough we can expand the cross-section σ in the potential parameter p_k as

$$\sigma = \sigma^0 + \left(\frac{\partial \sigma}{\partial p_k}\right)_{p_k} (p_k - p_k^0) \tag{17}$$

where σ can refer to a state-to-state or a total differential cross-section, and the super-scripted σ^0 and p_k^0 refer to a reference choice of parameters. In order to facilitate comparison between sensitivities for various parameters and for different scattering angles as well as different initial and final conditions, we define a reduced and unitless relative sensitivity

$$S(\sigma;p_k) \equiv \frac{p_k}{\sigma}\left(\frac{\partial\sigma}{\partial p_k}\right) \tag{18}$$

This quantity gives the fractional change in the cross-section for a fractional change in the parameter. This may be written as

$$\frac{\Delta\sigma}{\sigma} = S(\sigma;p_k)\left(\frac{\Delta p_k}{p_k}\right) \tag{19}$$

For a given potential and collision energy we calculated the phase shifts $\eta_l(\gamma)$ in equation (7), via Numerov integration[38] for low values of l and via the JWKB method[37,31] for higher values (the switch over taking place between $l = 15$ and 25). In general it is sufficient to use 48 approach angles γ in order to obtain good values for state-to-state cross-sections (total differential cross-sections are convergent with only 12 approach angles). Using equations (7) and (10) we determined the expansion scatttering amplitudes $F_j^{k_J}(\theta)$. These are then used to obtain all state-to-state differential cross-sections from equation (11).

The sensitivities are determined by the finite difference method, which from equation (19) is expressed as

$$S(\sigma;p_k) = \left(\frac{p_k}{\Delta p_k}\right)\frac{\sigma(p_k+\Delta p_k)-\sigma(p_k)}{\sigma(p_k)}$$

The Δp_k is $10^{-4}p_k$ and the cross-section is calculated at p_k and $p_k(1+10^{-4})$ for a collision energy of 65 meV. Collision energies of 35 and 95 meV are also considered in section 11. The masses of the He and CO_2 are 4.0026 and 44.0098 amu, respectively.[33] They are used along with the C-O bond distance[33] to determine the moment of inertia I (eq. 5).

The computational time for these sensitivities is rather small, 30 minutes on our VAX 11/780 computer for a given energy and a given potential with 10 parameter p_k varied.

5. THE METHOD

In order to investigate the effect the potential parameters have on the differential cross-section we have calculated the cross-sections and their sensitivities for several physically reasonable values of a given parameter. We start with the above mentioned parameter-expansion MMSV potential, the parameters for which are given in Table I. We then change one parameter and determine its effect on the cross-sections and sensitivities. Since there are ten parameters that specify this potential and since we wish to consider several initial values of each of these parameters above and below their actual values, we can easily generate well over several hundered figures representing the dependence of the differential cross-sections on these parameters. This is definately undesirable, nor is it very informative. Hence we will show only some of the figures and summarize the key features of the others in tabular form.

We have constructed various potentials based on the one in Table I, for which we give the designation M. In order to be able to refer to these modified potentials we will classify them by the symbols outlined in Tables II and III. The first table (II) lists the spherical potential constructed from the empirical anisotropic MMSV potential (M). This potential is generated by setting q, a, $C_6^{(2)}$,and $C_8^{(2)}$ equal to zero in Eqs. 14 and 15. The other table (III) lists variations in the anisotropic potential.

Various sensitivity features which are not plotted will be compared to those that are plotted, in Tables V thru IX. The two characteristics of the sensitivity functions which we will compare are: their overall magnitude, abbreviated as "mag.", and their oscillations with scattering angle, abbreviated as "osc.". A trend in either of these properties as a function of an increase of a parameter, energy or inelasticity is indicated with several adjectives. By "same" magnitude we mean that the magnitudes of the two sensitivities are within a factor of 1.2 of each other for all angles. Magnitudes that are "similar" (abbrev. "siml.") are within a factor of 1.2 at most angles with some larger variations up to factor of 1.5 for some ranges of angles. Changes in magnitude are marked as "increasing" ("incr.") or "decreasing" ("decr."). A "slight" ("sl.") increase or decrease is less than a factor of 2, and is usually over the entire range, unless marked otherwise; while "significant" ("sig.") change is a change by a factor of 10 or more.

Changes in oscillation control are more difficult to quantify. By "same" we mean that the sensitivity oscillations cross zero at the same angles for the two sensitivities being compared. "Similar" indicates the same number of zero crossings but with some at different angles. A "significant" increase or decrease in oscillation control means there was at least a factor of 2 change in the number of zero crossings; while a "slight" change is one for less than a factor of 1.2 or just a change in the positions of the crossings.

6. CLASSICAL BEHAVIOR

It is well known[3,9,10,15–18] that helium-molecule scattering data exhibit very pronounced quantum effects, as is evident by the broad oscillations in the differential cross-section. Let us nonetheless summarize the characteristcs of classical scattering using different central field potentials. To this effect we calculate the classical deflection function given by[2]

$$\Theta(b) = \pi - 2b \int_{r_c}^{\infty} dr \, \frac{1}{r^2\sqrt{1 - V(r)/E - b^2/r^2}} \tag{20}$$

where r_c is the classical turning point of the potential, and b is the classical impact parameter which can be expressed in terms of the partial wave angular momentum quantum number l

$$b = \frac{l + 1/2}{k} \tag{21}$$

The classical differential cross-section is given as[2]

$$\sigma(\theta) = \sum_i \frac{b_i}{\sin\theta \mid \frac{d\Theta}{db_i} \mid} \tag{22}$$

the sum is over all b_i for which $\Theta(b_i)$ exists such that $\theta = \mid \Theta(\mathrm{mod}\ \pi) \mid$.

It is clear that as $\frac{d\Theta}{db}$ approaches zero the cross-section approaches infinity. The scattering angle at which this occurs is known as the rainbow angle. In Figure 1 we plot the deflection function versus the reduced impact parameter (actually $bk - \frac{1}{2} = l$). The minimum of $\Theta(l)$

is indicative of the rainbow angle, while the inflection of $\Theta(l)$ will yield the pre-rainbow minimum of the cross-section.

Table IV summarizes the positions of the rainbow maxima and the corresponding oscillation minima for different spherical potentials. The rainbow angle is most strongly affected by the well depth and well width, and only slightly by the well minimum position. The well mimimum position does however, have a strong effect on the impact parameter (or l) at which the rainbow angle occurs. With behavior in mind let us analyze to quantum DCS for the SM potential given in Figure 2. The lowest scattering angle oscillation occurs at 4.5 degrees and it is very dampened. The next oscillation is much more pronounced having a well defined minimum at 7.7 degrees and a maximum at 9.8 degrees. Only this second oscillation is close enough to the rainbow to be considered as a vestige of that classical feature. If that is indeed the case it should not be strongly affected by changes in well minimum position (r_m), while its angular position should be shifted most by the well depth or well width. In order to verify whether this is or is not the case, we present in Figure 3 comparative plots for several different MMSV potentials. From Figure 3a we observe that increasing r_m shifts all of the oscillations closer together and modifies their relative intensities, while variations in ϵ or β have only a marginal influence on their positions (Figures 3a and 3b). Hence, we can conclude that there is no evidence of any rainbow structure in this highly quantum system. Despite the fact that this fingerprint of well depth is not observable, we will show that the quantal oscillations do contain significant well depth and width information.

7. DCS SENSITIVITIES FOR SPHERICAL POTENTIALS

Before we deal with the effects of potential anisotropy on the differential scattering cross-section (DCS), we will discuss the influence of the parameters of a spherical MMSV potential on the DCS. As mentioned in the previous section, the position of the DCS oscillations is most strongly influenced by the well position (r_m) with some small shifts due to changes in the well depth (ϵ) and width (β).

We draw attention to the intensity of the oscillations for various values of r_m, ϵ, and β in Figure 3. An increase in ϵ (Fig. 3a) tends to intensify most of the oscillations, even the low angle one becomes clearly visible at high ϵ. The only exception to this rule is the second oscillation (at $\sim 7.5°$) which decreases slightly in intensity with increasing ϵ. If the well is made narrower, i.e. β is increased (Fig. 3c) the high angle oscillations (above 15°) increase in intensity, while the intensity of the low angle oscillations decreases. The intensity of the oscillation at ~ 12 degrees does not change appreciably with β. The intensity behavior is less regular for variations in r_m (Fig.3a). The overall pattern is for the oscillation amplitude to decrease somewhat with increasing r_m - while the overall DCS increases as does the frequency of the oscillations. However, the lowest angle oscillation is first dampened as r_m increases, but as r_m becomes even larger it reappears.

It is clearly evident that despite no indication of rainbow scattering, the spherical potential DCS contains information pertaining to the well depth and width, and it is known that r_m has a greater influence over the cross-section than any of the other parameters. Since r_m effectively determines the size of the scattering target it will in turn determine the overall magnitude of the cross-section. The positions of the DCS oscillations will also be most influenced by the size of the scattering target. This may be visualized by analogy to the diffraction of light through a slit, where the slit width is analogous to the target size. As the slit width is decreased the diffraction pattern spacings increase and broaden out. The same is true for scattering; as r_m decreases the oscillations broaden out and decrease in frequency as a function of angle. However, it is unrealistic to expect *a priori* that the well depth and width have a small or negligible influence on the shape of the DCS. After all, they both deterime the shape and value of the potential at a given r. The value of the potential can in turn be related (in classical terms) to the degree of deflection the probe particle will be subject to for a given impact parameter.

In Figure 4 we plot the sensitivities for the six parameters of the MMSV-(SM) potential. The above mentioned observations and expectations are clearly evident in the plots. The r_m sensitivity is the greatest by an overall factor of 10 above that for ϵ or β. The overall sensitivities for ϵ and β are very similar, while the β' sensitivity is slightly smaller than that for β. The C_6 and C_8 sensitivities are lower by a factor of 100 and 1000, respectively, than that for r_m at angles below

25 degrees. Above 25 degrees, the C_6 sensitivity becomes similar to that for C_8, both being about 1000 times lower than for r_m. The most pronounced feature of all of these sensitivities is their oscillation between positive and negative values, such that an increase in a parameter will shift $\sigma(\theta)$ up at one angle and down at another. In other words, all the potential parameters have an influence on the DCS oscillations and magnitude.

Comparing the sensitivities $S(\theta;\epsilon)$ and $S(\theta;\beta)$ we observe that for θ less than 15 degrees they have in general opposite signs; while for θ between 15 and 35 degrees they usually have the same sign. Beyond 35 degrees their behavior is not well correlated. Even the small dampened DCS oscillation at 4.5 degrees shows strong sensitivity to both ϵ and β. However if this oscillation is dampened further by setting ϵ low and β high (potential SBEHL in Table II) the sensitivity in this region decreases and loses its oscillatory structure. In general many of the gross features of the sensitivities are preserved if a parameter is altered by a physically reasonable amount, as in Table II.

The β' sensitivity shows very similar structure to the β one in the range of 10 to 20 degrees. Beyond 20 degrees the overall magnitude of $S(\theta;\beta')$ remains relatively constant as the regularity of the oscillations decreases significantly; whereas at angles below 10 degrees overall magnitude of the sensitivity drops rapidly with angle. From classical scattering theory we would not expect a parameter that controls the close (low r) features of the potential to have any effect on small angle scattering. Since for $r \geq r_o$ (potential zero crossing) β' has no effect on the potential, we would not expect to see any β' sensitivity for those impact parameters which do not sample the potential in the region $r < r_o$. For the MMSV-SM potential these impact parameters correspond classically to scattering angles of less than 15 degrees, below which $S(\theta;\beta')$ starts to decrease, dropping to zero at 0 degrees. Yet because this is a highly quantum system the sensitivity does not drop to zero instantly at 15 degrees.

Similar classical scattering arguments can be used to explain why the C_6 and C_8 sensitivities are largest at small angles. Large impact parameters imply larger distances of closest approach, where the potential is weak and produces a small scattering angle. Hence the far reaches of the potential, as determined by C_6 and C_8, will have significant influence on small angle scattering. For scattering angles less than 7 degrees the C_6 sensitivity is within a factor of two of the r_m, ϵ, and β sensitivities. The C_8 sensitivity is much smaller then the one for C_6 at angles less than 25 degrees, and is not important in defining the shape of the DCS. Above 25 degrees both $S(\theta;C_6)$ and $S(\theta;C_8)$ have approximately the same small magnitude and should play a minor role in the appearance of the differential scattering cross-section.

The sensitivities described above have been calculated for specific values of the potential parameters. What happens to these sensitivities if one of the key parameters r_m, ϵ, or β is changed by a large although physically reasonable amount (as in Table II)? As we stated before, there is no benefit in plotting all of the sensitivities for every parameter change. Instead we have summarized, in Table V the changes that do occur in the sensitivities as each of these parameters is individually lowered or raised above its normal value (see also Section 5). Two key features of the sensitivities are the effects they imply on the overall magnitude and oscillations of the DCS. We will use the expression "oscillation control" as the effect of the parameter on the amplitude of the oscillations in the differential cross-section. This control manifests itself in the sensitivity versus angle curve as oscillations above and below zero. For example, we say that r_m exhibits strong oscillation control (Fig. 4a), while β' exhibits a poorer oscillation control (Fig. 4d), especially in ther range of 40 to 55 degrees.

Superficially, most of the sensitivities were not significantly affected by large, allthough physically reasonable, changes in a parameter. The most notable exceptions are the C_6 and C_8 sensitivites for changes in r_m and β. The increase of r_m moves both the Morse inflection point r_i and the spline-van der Waals junction to larger r where the van der Waals part of the potential is weaker. Therefore the van der Waals part makes up a smaller portions of the potential, and hence it has less less effect on the magnitude of the potential. Similarly, as β increases the well narrows, the inflection point r_i moves to smaller r, and the r_{sv} remains the same. This makes the spline region wider and results in a greater influence of the van der Waals region, giving the C_6 and C_8 coefficients a greater control of the DCS.

The other variations in sensitivities are more subtle and are not as readily predictable. However, a clue to understanding some of this behavior is realizing that β and β' are dimensionless parameters that govern the well and repulsive wall shapes, respectively. The actual slope of the potential, in the attractive and repulsive regions, is governed by ϵ and r_m. Hence any change of these parameters is expected to affect the sensitivity of parameters that also control the slope, i.e. β and β'.

8. TOTAL DCS SENSITIVITIES FOR ANISOTROPIC POTENTIALS

It is well known, as discussed in the introduction, that the anisotropy of r_m (q in eq. 14) has a much greater influence on the appearance of the DCS than does the anisotropy of ϵ (a in eq. 15). Yet it has been demonstrated[3] that a is essential in fitting potentials to experimental data; q as the only anisotropy term cannot adequately account for all the features of the observed DCS. Similar conclusions can be drawn from the total differential cross-sections (*i.e.*, summed over all final states) plotted in Figure 5. Variations of q from 0.1 to 0.5 show how significantly the oscillations can be dampened. For $q = 0.1$ the DCS is very similar to the one for a purely spherical potential (see Figure 2), despite the presence of ϵ anisitropy. However, both these values of q are physically unrealistic. The well minimum position anisotropy should follow the shape and size of the CO_2 molecule. Since the C-O bond distance is 1.16 Å, it then is expected that the difference between $r_m(\gamma = 0)$ and $r_m(\gamma = \pi/2)$ be approximately this distance. This is indeed the case for $q = 0.21$ (the experimentally fitted value) which results in a difference of 1.10 Å, whereas the difference is 0.53 Åfor $q = 0.1$ and 2.63 Åfor $q = 0.5$.

There are no easy clues that can be used to predict the well depth anisotropy (a), and as Figure 5b shows a has a much more subtle effect on the total DCS than q. An increase in a dampens some oscillations, i.e. at 5 and 9 degrees; while others become more pronounced, especially at 15 degrees. Hence, well depth anisotropy information is contained not in overall oscillation dampening but in relative dampening and relative intensities of the oscillation. Just as in the spherical potential case, the total DCS was determined mainly by r_m, with fine variations in oscillation intensity resulting from the well depth and shape. Consequently, for anisotropic potentials the angular dependent well minimum position $r_m(\gamma)$ determines the main features of the total DCS. The well depth anisotropy and shape parameters gives the oscillatory structure of the cross-section.

In Figure 6 we present the effects of varying the shape parameters β and β'. As was the case for the spherical potential, an increase of β increases the oscillation amplitudes above 10 degrees and reduces those below that angle. Also the magnitude of the DCS above 10 degrees remains about the same, while below it drops with increasing β. We know that classical low angle scattering is due to trajectories that sample regions of the potential for large distances of closest approach r_c. For this distance equal to 3.8 Å(the value of r_i for the SM potential) the resultant scattering angle is about 8 degrees (for the scattering energy of 65 meV considered in this paper). The deflection angle for $r_c = 5.6$ Å(the value of r_{sv}) is 1 degree. As β increases the well narrows and the spline region between r_i and r_{sv} becomes shallower, and a smaller fraction of the trajectories are scattered in to the region between 1 and 8 degrees. Similarly as the well narrows the DCS exhibits sharper quantum interference oscillations.

The repulsive wall shape parameter β' has little effect on scattering below about 16 degrees, the scattering angle corresponding to a classical closest approach distance radius of 3.1 Å, the value of r_o. Above 16 degrees, however, the increase of β' decreased the total DCS (Fig. 6b). The reason seems to be that as β' increases the wall becomes steeper and less likely to be penetrated, yielding a lower cross-section at the larger scattering angles.

In the framework of the above observations let us now consider the sensitivities for these parameters. The sensitivites to $r_m^{(0)}$, $\epsilon^{(0)}$, q, a, β and β' are presented in Figure 7, and to the van der Waals coefficients $C_6^{(0)}$, $C_8^{(0)}$, $C_6^{(2)}$, and $C_8^{(2)}$ in Figure 8. We can compare these sensitivities to those for the spherical limit of this potential (Fig. 4). The presence of anisotropy has significantly altered these sensitivites. Those for $r_m^{(0)}$, β and $C_6^{(0)}$ have increased in overall magnitude; while those for ϵ, β' and $C_8^{(0)}$ have decreased. The oscillation control has been reduced for ϵ and β', whereas for the other parameters it has remainded relatively the same in so far as the frequency of the sensitivity oscillations is concerned, with only some changes in their relative amplitudes. This is particularly true for $S(\theta; r_m^{(0)})$. The r_m sensitivity for the spherical potential has a progression of oscillations with alternating crests (postitive) and troughs (negative) of equal width and equal magnitude; whereas the $r_m^{(0)}$ sensitivity has large troughs (negative) and small and narrow peaks (postitive). An increase in $r_m^{(0)}$ tends to lower the DCS oscillation troughs much more than it raises the crests. This is effectively a decrease in oscillation control. The peak to trough height does not increase as much for the anisotropic potential as for the spherical one for an increase in $r_m^{(0)}$, since for the spherical potential the troughs move down as much as the peaks move up, while for the anisotropic potential the troughs move down, but the peaks move up only slightly.

The sensitivity to the spherical average of the well depth $\epsilon^{(0)}$ is reduced slightly by the introduction of anisotropy, as can be seen from a comparison of Figures 7b and 4b. There is also some reduction of oscillation control, especially for low scattering angles ($\theta < 20°$). The DCS oscillation at 4 degrees is still influenced by $\epsilon^{(0)}$ such that an increase will deepen the trough of the oscillation. In general, the inclusion of anisotropy has reduced the precision with which well depth information can be extracted from a measured DCS. However, this is not as unfortunate as it may seem, since the DCS also contains information pertaining to the anisotropy. Also, the presence of anisotropy permits CO_2 rotational energy transfer, which can be observed as inelastic scattering. This inelastic scattering, as we shall see later, contains additional information which can be used to extract the various potential parameters, as well as the well depth, more accurately and more precisely.

The DCS oscillation dampening properties of the well minimum position anisotropy q are clearly evident in Figure 7c. The sensitivity, $S(\theta; r_m^{(0)})$, is positive in regions of the DCS troughs, and negative in regions of DCS crests. The DCS dampening properties of a are very sinmilar to those of q, as is seen by comparing Figure 7d with Figure 7c. From 0 to 7.5 degrees the two sensitivites are of similar magnitude, while between 8 and 35 degrees the $S(\theta; q)$ magnitude rises up to 10 times that of $S(\theta; a)$. Therefore the scattering below 7.5 degrees should be most important in defining a, particularly since a has a greater oscillation control than q for the DCS oscillation at 4 degrees. Even in the range of 7.5 to 14 degrees $S(\theta; a)$ is one third of $S(\theta; q)$ indicating that a has a significant influence on the DCS. For low angle scattering ($\theta \leq 20°$) a provides much more oscillation control than $\epsilon^{(0)}$ and hence serves an indispensable function in modeling the real potential. In fact, it has been demonstrated[3] that a calculated DCS cannot be sucessfully fitted to experimental DCS scattering data with potential models that do not include well depth anisotropy.

The sensitivity to the well width parameter β has increased with the introduction of anisotropy, as indicated by comparing Figures 7e and 4c. The overall magnitude of this sensitivity has incresed, up to a factor of three, above 12 degrees; and oscillation control has also increased some (below 20 degrees). Indeed, the sensitivity to β is the second most intense one after $S(\theta; r_m^{(0)})$, greater than the $\epsilon^{(0)}$ sensitivity. Its importance should not be underemphasized, particularly for this anisiotropic potential, although it is not obvious why the sensitivity should increase with increased anisotropy. This sensitivity of the DCS to the β parameter has not been previously realized.

The sensitivity to β' (Figure 7f) shows essentially the same behavior as in Figure 6b; very little sensitivity at low angles with only very minor oscillation control, and a negative sensitivity at higher angles. As mentioned above, scattering below 15 degrees corresponds to classical trajectories that do not approach the repulsive wall, hence this region ($0 < \theta < 15°$) represents penetration into the classically forbidden region of the repulsive part of the potential. For the scattering angles above 15° oscillation control disappears and the sensitivity to β' demonstrates that a steeper wall (higher β') reduces the DCS magnitude.

The sensitivities to the dispersion coefficients are plotted in Figure 8. The only important coefficient, one with the largest magnitude by far, is $C_6^{(0)}$. The sensitivities to the other dispersion parameters is so low that they do not significantly affect the DCS. Since these coefficients are calculated theoretically, their sensitivities provide a guide as to how accurately those calculations must be performed. The sensitivities to the anisotropy terms $C_6^{(2)}$ and $C_8^{(2)}$ can be expected to be small because the van der Waals region extends ranging from r_{sv} to infinity and has some influence on the spline region. As the He atom traverses the van der Waals region the CO_2 molecule rotates thereby changing γ. The DCS then reflects the spherical averge of the dispersion terms. The well and wall regions will be traversed more quickly by the He atom, and hence the anisotropy of this part of the potential will not be severely averaged over γ.

Table VI summarizes the significant changes that occur in the sensitivities if q, a, or β are changed above or below their nominal values. In general the sensitivities are not substantially affected by these changes; most of the differences are subtle. Some sensitivites increase as a parameter is increased, and upon a further increase of the parameter they drop again in magnitude. Only $S(\theta; a)$ increases significantly in magnitiude as a is raised; it also gains oscillation control as q is increased. In addition, a narrowing of the well i.e., and increase in β makes the well a sharper target which in turn increases the sensitivity of the well minimum position $(r_m^{(0)})$. Other than these there are no regular or predictable trends in the small variations of these sensitivities.

9. STATE-TO-STATE DIFFERENTIAL CROSS-SECTIONS

The anisotropy of the He + CO_2 interaction potential allows for the coupling and transfer of energy between the rotation of the CO_2 molecule and the relative translational energy between it and the helium atom. The total differential cross-sections, discussed in the previous sections of this paper, are the sums of a large set of rotational state-to-state transitions (Equation 12), and therefore they are less sensitive to the details of the the potential then the individual cross-sections would be. In this section we will show these state-to-state cross-sections depend on the characteristics of the potential. We have chosen as an example an initial state $j = 12$, which lies in the range of rotational states that the CO_2 is likely to occupy at all but the lowest temperatures. The discussions and conclusions for $j = 12$ can be easily carried over to other initial states j, from $j = 4$ to $j = 30$.

In Figure 9 we plot the full range of rotational transitions from $j = 12$. For a given change in $\Delta j = j' - j$ (where j' is the final rotational state) the shapes of the DCS curves for the rotational gain ($\Delta j > 0$) are very similar to the one for rotational loss ($\Delta j < 0$), for the same $|\Delta j|$. The major difference is that the rotational $\Delta j > 0$ transitions have DCS's which in magnitude are greater than those for the corresponding $\Delta j < 0$ trasitions. We will therefore focus our attention on the former without compromising detail or completeness of conclusions.

Elastic scattering dominates at low scattering angles. Inelastic transitions for $\Delta j = 2$ become important for scattering angles θ above 10 degrees. Transitions for $\Delta j > 6$ are not significant for angles below 40 degrees. Beyond 40 degrees the $\Delta j = 8$ DCS has minor significance. Transitions with $\Delta j > 8$ although not shown in Figure 9, contribute very little to the total DCS, and are extremely small at all angles. We also do not show DCS's from initial states other than $j = 12$. These other transitions have virtually identical characteristics to those for $j = 12$. However, $j = 0$ is an exception in that DCS's for small Δj (2 and 4) are greater than those for the other inelastic ones and the elastic ones for angles above 10 or 15 degrees.

In Figure 10 we probe the effects of varying the potential well minimum position anisotropy q. The anisotropy parameter q elongates the potential along the CO_2 molecular axis (if it is positive). As this happens the torque about the center-of-mass of the CO_2 imparted by the He atom to the CO_2 molecule will increase, which increases the amount of translational to rotational energy exchange. We then expect a potential with a larger q to have greater inelastic cross-sections, as is borne out in Figures 10a and 10b. For $q = 0.5$ (high value) inelastic scattering is substantial even at 4 degrees (for Δj between 2 and 8). For $q = 0.1$ (low value) even $\Delta j = 4$ scattering has little effect on the total scattering. At 12 and 18 degrees (Fig. 10a) the DCS for the $\Delta j = 2$ transition is comparable in magnitude to that of the elastic DCS. The elastic DCS curve for $q = 0.1$ has oscillations of greater amplitude than the one for

$q = 0.21$. As q increases the elastic DCS oscillations dampen while those for inelastic transition DCS ($\Delta j > 2$) tend to increase. The elastic DCS decreases with q and so do the DCS's for small Δj transitions. The magnitude of the total DCS is unchanged by the value of q (Figure 5a), and since inelasticity increases with q, the elastic DCS should therefore decrease.

There are problems with potentials having large large values of q, and thereby relatively large differential cross-section for large Δj. The IOS approximation is only valid for cases where rotational transitions occur at small impact parameter and for relatively small changes in the rotational energy. A potential with a large q does not meet these criteria, and hence the results shown in Figure 10b, are not a good approximation to those the exact ones. Nonetheless, we can still use the results to show the trends that occur as q changes. Similar caution is required for low q potentials where the target molecule has a small moment of inertial I (a light diatom such as H_2, or even N_2 is an example). The small I is indicative of large spacings between rotational levels; a condition to which the IOSA is not applicable.

Variations in the well depth anisotropy a do not have as dramatic an effect on the DCS's as does q. Yet, as is evident from examining Figures 11a and 11b, the influence is significant. The differences in state-to-state DCS's are most apparent at low scattering angles, as a increases (in absolute value) from -0.2 to -0.9. We expect, based upon the discussion of spherical potentials, the well depth information to be concentrated at scattering angles in the range of greatest classical sampling of the well region, i.e. 4 to 20 degrees. An increase in a dampens the oscillations for all inelastic DCS's, particularly for larger Δj's, while the DCS's increase in magnitude especially at low angles.

To account for these observations, we probed further by making several modifications in the well depth and its anisotropy. First, we plot the state-to-state DCS's for two extreme values of the overall well depth $\epsilon^{(0)}$ (2.5 and 7.5 meV) with the anisotropy a unchanged at -0.5. For an increasing $\epsilon^{(0)}$ the trends, as shown in Figures 12a and 12b, are: the inelastic DCS amplitudes increases; the elastic DCS magnitude increases between 4 and 20 degrees; and the DCS oscillation magnitudes also increase somewhat abvove 25 degrees. For a negative a the well is deeper than the spherical average $\epsilon^{(0)}$ at angles greater than the zero point of the second order Legendre polynomial $P_2(\cos\gamma)$ ($\cos\gamma = 1/\sqrt{3}$ or $\gamma \approx 54.7°$). We can make this region shallower than $\epsilon^{(0)}$ and place the very minimum of the potential on the molecular axis ($\gamma = 0$, or π) rather than perpendicular to it ($\gamma = \pi/2$), by setting a to a positive value. Figures 13 show the DCS's for two different values of a positive: a +0.5 and +0.1. For scattering angles below 12 to 22 degrees (depending on the Δj of the transition) the inelastic DCS's increase in overall magnitude and decrease in oscillation amplitude as a is increased. Above these angles the DCS magnitude drops slightly and the oscillations intensify.

To complete the test we set the well depth anisotropy a to +0.3 and $\epsilon^{(0)}$ to 2.5 and 5.5 meV, Figures 13c and 13d respectively. Once again the deepening of the well produces an increase of the magnitude of the inelastic DCS for low scattering angles (12 to 22 degrees).

In summary, the increase of the well depth increases the inelastic DCS regardless of the anisotropy. The increase of the magnitude of the well depth anisotropy also increaes the inelastic DCS. An increase in the magnitude of a will deepen the well somewhere. Since the inelastic DCS's apparently sense a depth increase, regardless of the sign of a, they must be influenced by regions of the potential above and below the approach angle γ corresponding to the zero of $P_2(\cos\gamma)$. This is consistent with the arguments presented in the discussion of the well minimum anisotropy q: the most effective translational-rotational energy transfer will occur at approach angles γ for which the torque is greatest, i.e. somewhere away from both parallel and perpendicular approaches.

Figures 14a and 14b show elastic and inelastic DCS's for extreme values of the potential well width parameter β. As we demonstrated in the Sections 7 and 8, an increase in β results in an increase in the low angle scattering and an increase in DCS oscillation amplitudes. The same is observed for the state-to-state DCS's. An increase in β narrows the well so that the values of the potential in the well region decrease for all r other than r_m at a fixed γ. A narrower well will have a repulsive wall which starts at a larger r and has an initially steeper slope (before

β' becomes influential), and therefore the effective target size increases as does the cross-section. As β increases, the inelastic DCS increases at scattering angles which classically correspond to collisions with the repulsive wall of the potential, as can be seen by comparing Figures 14a, 9b and 14b for which β is 5.0, 7.2 12.0 respectively.

When we discussed the effects of the repulsive wall shape parameter on the total DCS, we observed that an increase in β' decreases the scattering intensity at higher angles with virtually no effect on the oscillations. A similar observation is made for state-to-state DCS's for small Δj (≤ 4). For the larger Δj (≥ 6) the reverse is true, i.e. the high angle state-to-state DCS's increase with increasing wall steepness. There is no discernable difference in the state-to-state DCS's for variations in β' at angles below 15 degrees, and only above 35 degrees is the difference reasonably significant. At 60 degrees the largest variation is for the $\Delta j = 8$ DCS, with less than a factor of 2 increarse in the DCS for a change in β' from 5.0 to 12.0.

10. STATE-TO-STATE DCS SENSITIVITIES

In the previous section we observed the response of the state-to-state differential cross-sections to relatively large changes in potential parameters. We now turn to the sensitivities of equation 18, to gauge the response of the state-to-state DCS to very small parameter changes. How do they compare to the total DCS sensitivities? How do they change as the inelasticity increases?

In Figure 15 we plot the sensitivities of the $j = 12$ to $j = 14$ DCS sensitivities to the parameters $r_m^{(0)}$, $\epsilon^{(0)}$, q, a, β and β'. We observe only one significant change over the total DCS sensitivities of Figure 7, otherwise the two sets of sensitivities are very similar. The change is in the q sensitivity $\mathrm{S}(\theta; q)$ which shows a very significant loss of oscillation control and an overall increase in magnitude. The sensitivities to the $C_6^{(0)}$ and $C_6^{(2)}$ coefficients do show some increase in magnitude over those for the total DCS. In Table VII we compare these sensitivities to the sensitivities for the total DCS, the elastic $j = 12$ DCS, and a variety of inelastic ($j = 12$ to $j = 4, 6, 8, 10, 14, 16, 18, 20$) DCS.

The difference between the total and state-to-state sensitivities for q is quite remarkable, compare Figures 7c and 15c respectively. The increase in magnitude was expected since the elongation of the potential should be and is the primary feature responsible for translational-rotational energy exchange. The significant loss of oscillation control indicates that the primary dampening mechanism of the total DCS oscillations is the fact that the phases of the inelastic DCS oscillations differ from each other and from those of the elastic DCS (see Figures 9 and 10). As q increases in magnitude the inelastic DCS's increase and therefore contribute more to the total DCS. Since the oscillation peaks of $j' \leftarrow j$ DCS occur roughly at the same angles as the troughs of the adjacent DCS for which the j' differ by 2, the oscillations of the total DCS will dampen. The state-to-state inelastic DCS oscillations are not dampened at all by q; actually, a large q tends to increase the large Δj oscillations (compare Figures 10a and 10b). The state-to-state elastic DCS oscillations, however, are dampened by an increasing q; and the $S(\theta; q)$ is very similar to the one for the total DCS with only minor decrease in oscillation control (we did not plot the elastic sensitivity since it is so similar to the total).

The q sensitivity in Figure 15d is positive for $\theta < 20$ degrees and negative for $\theta > 25°$. As Δj increases the sensitivity becomes positive for all angles and increases in magnitude up to 20 times for $j' = 4 \leftarrow j = 12$ over the $12 \leftarrow 12$ elastic process (Table VII). This effect was observed in Figure 10, where for small angles the DCS increases with q, while at larger angles ($\theta > 20°$) the DCS decreases for small Δj and increases for larger Δj. Classical trajectories with small values of the distance of closest approach correspond to small impact parameters and have large scattering angles. Large angle scattering is due to collisions that approach the repulsive wall, for which smaller Δj DCS decrease while larger Δj increase with increasing q. If a trajectory approaches the repulsive wall and scatters at large angles it will be able to transfer a greater amount of energy than at lower angles and therefore the total DCS will be dominated by larger Δj transitions.

The spherical average of the well depth minimum position $r_m^{(0)}$ has a very strong effect on the high inelasticity DCS. For $\Delta j = 8$ the sensitivity $S(\theta; r_m^{(0)})$ increases by a factor of 500 over the one for the total DCS (Table VII). The repulsive wall shape parameter β' sensitivity also shows a significant increase for larger Δj, up to a factor of 100. Since large Δj transitions occur at the wall, the parameters that control the position and shape of that wall ($r_m^{(0)}$ and β' respectively), should have the greatest influence on the corresponding inelstic DCS. A larger $r_m^{(0)}$ means a larger target and hence a greater DCS. A larger β' means a steeper wall and hence a more effective inelastic DCS (as we observed at the end of the previous section).

The sensitivity to the well depth anisotropy parameter a is rather strongly affected by large Δj transitions; the $\Delta j = 8$ sensitivity increases up to 30 times over the one for the total DCS. This confirms the observations and discussions of the previous section, according to which an increase in the magnitude of a increases the inelastic DCS.

The increase of sensitivities for the dispersion terms, particularly the anisotropy terms $C_6^{(2)}$ and $C_8^{(2)}$, with increasing inelasticity (Table VII), is unimportant because the corresponding state-to-state DCS is extremely small (Figures 9a and 9b), especially at low scattering angles where elastic transitions dominate.

Table VIII summarizes the effects of parameter changes on the $j = 12$ to $j' = 14$ DCS sensitivities. It is similar to the analogous table (VI) for the total DCS sensitivities. Many of the conclusions reached regarding Table VI are equally applicable to Table VIII. We include this table only for completeness sake, and refer the reader to previous discussions, since there is no additional insight that can be presented.

11. DIFFERENT SCATTERING ENERGIES

All of the above analyses were for a single relative kinetic energy of 65 meV. What happens to the DCS's and their sensitivities at energies above and below this value? We have made calculations at 35 meV and 95 meV and summarize their results below with emphasis on the differences between the studies at these energies and those at 65 meV. The IOS approximation is valid over this energy range.

The positions of the DCS oscillations depend not only upon the well minimum location but also on the kinetic energy and hence the wavelength. As the energy increases the wavelength decreases and hence the spacing of the oscillations decreases. The magnitudes of the total DCS and also the inelastic DCS decrease with increasing energy for scattering angles below 30 degrees. At scattering angles above 30 degrees kinetic energy has a negligible

effect on the magnitude of all the DCS's. Inelastic DCS's for small Δj also decrease with increasing energy; while for large Δj they increase. This is expected since the large Δj DCS's depend upon the repulsive wall collisions (see previous section); a larger energy makes the wall region more accessible.

Table XI list the changes in sensitivities for the total and $j = 12$ to $j = 14$ DCS's as the initial kinetic energy increases. Overall, the sensitivities were not very significantly altered. The well depth sensitivity showed a factor of 5 decrease only for scattering angles above

17 degrees (as the kinetic energy is raised from 35 to 95 meV). The sensitivities for β and $C_6^{(0)}$ were the virtually the same for 35 and 95 meV but much greater for 65 meV. The $C_8^{(2)}$ sensitivity showed a marked increase with energy.

Classically, one would expect that at a lower kinetic energy, the probing of the well region would be greater and the probing of the wall lesser. This is the case to a small extent for our system, but not significantly so. The β' sensitivity increases only slightly, indicating a slight increase in the probing of the repulsive wall. The minor decrease in the $\epsilon^{(0)}$ sensitivity indicates very little decrease in the probing of the well; most of the decrease in $S(\theta;\epsilon^{(0)})$ is for angles above the classical range of well sampling. The other well parameter β has the most sensitivity at an intermediate energy (65 meV); at the extreme energies (35 and 65 meV) the $S(\theta;\beta)$'s are identical.

The specific choice of a scattering energy to experimentally probe the He + CO_2 potential, or one for a similar system is not important. The higher energies in this range yield cross-sections with more classical behavior, and will sample more of the repulsive wall. At the lower energies the behavior is more quantal in nature, and hence the scattering will be less a function of how a trajectory samples the well region, than how a wave is distored by the total potential. It is not appropriate or very useful to invoke trajectory concepts in attempting to predict parameter sensitivities at low energies. Therefore, it is not very beneficial to measure cross-sections for quantal scattering systems at very low scattering energies, since similar information can be obtained at room temperature energies. The only advantage of lower energy studies is the increase in elastic cross-section at intermediate scattering angles; a factor of 2 increase is observed in the range of 5 to 15 degrees as the energy drops from 95 to 35 meV. The disadvantage is that the inelastic cross-sections decrease for these conditions. The best course of action is to measure the cross-sections at many energies, and use the combined data to extract a potential.

12. CONCLUDING REMARKS

In this paper we have investigated the effect of several anisotropic interaction potential parameters on observable differential cross-sections for the scattering of He by CO_2 at an energy of 65 meV. Relative sensitivity functions for the DCS were introduced to quantify the influence of each parameter. We also performed a large scale sensitivity analysis by calculating the cross-sections at several physically reasonable values of each of the potential parameters. The following conclusions were reached:

1. The DCS (total and inelastic) are most sensitive to the location of the potential well mimimum r_m, particularly the spherical average of $r_m(\gamma)$. It has, by far, the greatest effect on the overall magnitude of the DCS especially at low angles, and on the positions of the quantal oscillations.
2. The quantal oscillations of the total DCS versus scattering angle θ curves are dampened primarily by the presence of anisotropy in the position of the well minimum r_m. The dampening is due to the fact that the inelastic DCS's have oscillations with troughs and crests at different θ. The state-to-state DCS's are not dampened by the anisotropy of r_m, but their relative magnitudes are very dependent on this anisotropy.
3. Although the He + CO_2 system is highly quantal and therefore its DCS shows no classical rainbow behavior, it is still possible to

extract siginficant information regarding the depth and width of the well from DCS measurments. The sensitivities to these parameters extened well beyond what would be expected classically. The low angle DCS oscillations increase with the well depth. Increasing the well width increases the amplitude of low angle ($\theta < 12°$) oscillations and decreases the high angles ones. The increase of well depth also increases the inelasticity of the collision.

4. The elastic and inelastic DCS is highly sensitive to the width of the well. The sensitivity to it is actually somewhat greater than to the well depth. However the range in experimentally determied values for the reduced well width (parameterized by β for the MMSV potential, $\beta = 5.5$ to 8.2) is much smaller than the range of values of well depth (2.5 to 7.0 meV).
5. The anisotropy of the well depth ϵ is clearly discernable in the total DCS, primarily in the shape of the oscillations. It has little effect on the dampening of the oscillations. An increase in its absolute value increases the inelasticity.
6. There is little change in parameter sensitivities for scattering at energies other than 65 meV. At 35 meV the increase in sensitivity in the well depth is less than a factor 1.5 over that for 95 meV, indicating that classical arguments are not very useful in predicting sensitivities.

Although we considered a specific case, the above conclusions are valid for systems with similar characterstics: collision energy, reduced mass, and rotational energy spacing. The techniques outlined should prove beneficial in interpreting total and inelastic diffential cross-section data, and in assigning significance to the features of the potentials that are obtained from the data.

3.13 REFERENCES

1. *Atom-Molecule Collision Theory: A Guide for the Experimentalist* R. B. Bernstein ed. (Plenum, New York, 1979).
2. R. B. Bernstein, *Chemical Dynamics via Molecular and Laser Techniques*, (Clarendon Press, Oxford 1982)
3. J. W. Winniczek and A. Kuppermann, (to be submitted).
4. R. J. Cross, Jr., *J. Chem. Phys.* **52**, 5703 (1970).
5. (a) H. R. Mayne and M. Keil, *J. Phys. Chem.* **88**, 883 (1984); (b) M. Keil and H. R. Mayne, *Chem. Phys. Lett.* **85**, 456 (1982).
6. (a) R. Schinke, W. Müller, W. Meyer, and P. McGuire, *J. Chem. Phys.* **74**, 3916 (1981); (b) R. Schinke, H. J. Korsch, and D. Poppe, *J. Chem. Phys.* **77**, 6005 (1982).
7. F. Wolf and J. J. Korsch, *J. Chem. Phys.* **81**, 3127 (1984).
8. G. Scoles, *Ann. Rev. Phys. Chem.* **31**, 81 (1980).
9. M. Keil and G. A. Parker, *J. Chem. Phys.* **82**, 1947 (1985).
10. (a) G. A. Parker, M. Keil, and A. Kuppermann, *J. Chem. Phys.* **78**, 1145 (1983); (b) M. Keil, G. A. Parker, and A. Kuppermann, *Chem. Phys. Lett.* **59**, 443 (1978).
11. (a) J. T. Hwang and H. Rabitz, *J. Chem. Phys.* **70**, 4609 (1979); (b) L. Eno and H. Rabitz, *J. Chem. Phys.* **71**, 4824 (1979); (c) L. A. Elsava, L. Eno, and H. Rabitz, *J. Chem. Phys.* **73**, 4998 (1980).
12. L. Eno and H. Rabitz, *J. Chem. Phys.* **75**, 1728 (1981).
13. L. Eno and H. Rabitz, *J. Chem. Phys.* **74**, 3859 (1981).
14. L. Eno and H. Rabitz, *J. Chem. Phys.* **72**, 2314 (1980).
15. R.T Pack, G. A. Pfeffer, and J. P. Toennies, *J. Chem. Phys.* **80**, 4940 (1984).
16. M. Faubel, K. H. Kohl, J. P. Toennies, and F. A. Gianturco, *J. Chem. Phys.* **78**, 5629 (1984).
17. M. Faubel, K.-H. Kohl, and J. P. Toennies, *Faraday Discuss. Chem. Soc.* **73**, 205 (1982).
18. M. Keil and A. Kuppermann, *J. Chem. Phys.* **69**, 3917 (1978).
19. P. M. Agrawal and L. M. Raff, *J. Chem. Phys.* **74**, 3292 (1981)
20. P. M. Agrawal and L. M. Raff, *J. Chem. Phys.* **75**, 2163 (1981).
21. C. L. Stroud and L. M. Raff, *J. Chem. Phys.* **72**, 5479 (1980).

22. G. A. Parker, R. L. Snow, and R. T Pack, *J. Chem. Phys.* **64**, 1668 (1976)
23. R. T Pack, *J. Chem. Phys.* **60**, 633 (1974)
24. G. A. Parker and R. T Pack, *J. Chem. Phys.* **68**, 1585 (1978).
25. R. T Pack, *Chem. Phys. Lett.* **55**, 197 (1978).
26. G. Rotzoll and A. Lübbert, *J. Chem. Phys.* **71**, 2275 (1979).
27. V. Khare, *J. Chem. Phys.* **68**, 4631 (1978).
28. D. Secrest, *J. Chem. Phys.* **62**, 710 (1975).
29. P. McGuire and D. J. Kouri, *J. Chem. Phys.* **60**, 2488 (1974).
30. R. T Pack, *J. Chem. Phys.* **60**, 633 (1974).
31. D. S. Saxon, *Elementary Quantum Mechanics* (Holden-Day, San Francisco, 1968).
32. A. S. Davydov, *Quantum Mechanics* (Pergamon, Oxford 1976), 2nd edition, tr. D. ter Haar.
33. G.Herzeberg, *Molecular Spectra and Molecular Structure III. Electronic Spectra and Electronic Structure of Polyatomic Molecules*, (Van Nostrand Reinhold, New York, 1966).
34. The vibrational energies for the three vibrational modes of $CO2_2$ are given in ref. 22, and are 291.26 meV, 172.11 meV and 82.75 meV; at a temperature of 298 K these states have a ground state relative populations of 100.0%, 99.9% and 96.0%, respectively.
35. R. T Pack, *J. Chem. Phys.* **64**, 1659 (1976).
36. R. T Pack, *J. Chem. Phys.* **61**, 2091 (1974).
37. R. T Pack, *J. Chem. Phys.* **60**, 633 (1974).
38. K. Smith, *The Calculation of Atomic Collision Processes* (Wiley, New York 1971).

TABLE I. MMSV Anisotropic Parameter Expansion Potential[a] Parameters

Parameter	Symbol	Value
well minimum (spherical average)	$r_m^{(0)}$	3.5 Å
well minimum anisotropy	q	0.21
well depth (spherical average)	$\epsilon^{(0)}$	4.3 meV
well depth anisotropy	a	-0.50
well shape[b]	β	7.2
wall shape[b]	β'	7.2
Spline-van der Waals joint	$\rho_{sv} = r_{sv}/r_m$	1.6
van der Waals coefficients	$C_6^{(0)}$	9.98 meV Å^6
	$C_6^{(2)}$	2.31 meV Å^6
	$C_8^{(0)}$	46.4 meV Å^8
	$C_8^{(2)}$	48.4 meV Å^8

a) see equations 14, 15, and 16; this potential will be designated as M

b) in some cases these parameters will be expanded in Legendre polynomials (as in eqs. 14 or 15)

TABLE II. Modified Spherical Potentials

Characteristic	Parameter Value	Potential
unmodified potential[a]	-	SM
low r_m	$r_m = 2.5$ Å	SRL
high r_m	$r_m = 4.5$ Å	SRH
low ϵ	$\epsilon = 2.5$ meV	SEL
high ϵ	$\epsilon = 7.5$ meV	SEH
low β	$\beta = 4.0$	SBWL
high β	$\beta = 10.0$	SBWH
low β'	$\beta' = 4.0$	SBRL
high β'	$\beta' = 10.0$	SBRH
low β and β'	$\beta = \beta' = 4.0$	SBL
high β and β'	$\beta = \beta' = 10.0$	SBH
low ϵ and high β	$\epsilon = 2.5$ meV $\beta = 10.0$	SBEHL

a) Spherical limit of the MMSV anisotropic potential in Table I, i.e. $q = 0$ and $a = 0$ (also $C_6^{(2)}$ and $C_8^{(2)}$ are zero)

TABLE III. Modified Anisotropic Potentials

Characteristic	Parameter Value	Potential
unmodified potential[a]	-	M
zero q	$q = 0$	Q0
low q	$q = 0.1$	QL
high q	$q = 0.5$	QH
zero a	$a = 0$	A0
low a	$a = -0.2$	AL
high a	$a = -0.9$	AH
low β	$\beta = 5.0$	BWL
high β	$\beta = 12.0$	BWH
low β'	$\beta' = 5.0$	BRL
high β'	$\beta' = 12.0$	BRH
anisotropic β[b]	$\beta^{(2)}/\beta^{(0)} = 0.62$ $a = 0.0$	BA
low positive a	$a = 0.1$	PAL
high positive a	$a = 0.5$	PAH
low ϵ	$\epsilon = 2.5$ meV	EL
high ϵ	$\epsilon = 7.5$ meV	EH
positive a low ϵ	$a = 0.3$ $\epsilon = 2.5$ meV	PAEL
positive a high ϵ	$a = 0.3$ $\epsilon = 7.5$ meV	PAEH

a) the anisotropic MMSV potential of Table I

b) β ansiotropy is introduced by way of a Legendre expansion (eq. 14 or 15).

TABLE IV. Classical Rainbow Scattering Angles

Potential[a]	θ_r/deg	$l(\theta_r)$[b]	$\theta_{r\ min}/deg$[c]
SM	8.9	40	7.5
SRL	6.8 8.8	28 43	4.3 8.5
SRH	9.2	52	7.7
SEL	5.0	40	3.8
SEH	16.0	41	13.3
SBWL	7.0	43	2.9
SBWL	10.8	40	9.1
M			
$\gamma = 0$	4.5	48	4.0
$\gamma = \pi/4$	7.8	42	6.0
$\gamma = \pi/2$	11.0	36	9.1
A0			
$\gamma = 0$	9.1	48	7.1
$\gamma = \pi/4$	9.0	42	7.6
$\gamma = \pi/2$	8.7	37	7.6
Q0			
$\gamma = 0$	4.1	39	3.4
$\gamma = \pi/4$	7.7	40	6.7
$\gamma = \pi/2$	11.4	40	10.0

a) See tables II and III for potential symbols
b) The reduced impact parameter for the rainbow angle (eq. 21)
c) Location of the rainbow minimum

TABLE V. Sensitivity Variations as a Function of Parameter Increase for Spherical Potentials

Sensitivity[a] and characteristic	Parameter Increasing		
	r_m	ϵ	β
$S(\theta;r_m)$			
mag.	siml.	incr.	incr. ($\theta>20°$)
		($10\times$ $15°<\theta<20°$)	decr. ($\theta<20°$)
osc.	same	incr.	decr. ($\theta>30°$)
$S(\theta;\epsilon)$			
mag.	incr. (low r_m)	incr.	incr. ($\theta>25°$)
osc.	same	decr.	incr.
		($10°<\theta<15°$)	
$S(\theta;\beta)$			
mag.	sl. incr.	sl. decr.	same
osc.	same	decr. ($\theta>30°$)	incr.($\theta>25°$)
$S(\theta;\beta')$			
mag.	incr. (low r_m)	same	same
osc.	sig. incr.	sig. incr.[b]	incr. ($\theta>15°$)
$S(\theta;C_6)$			
mag.	decr. ($\times 10$)	same	incr.
			($\times 50$ $\theta>25°$)
osc.	simil.	var.[c]	same
$S(\theta;C_8)$			
mag.	decr. ($\times 10$)	same	same
osc.	simil.	var.[c]	same

a) See sec. 5 of text for a full description of this table and symbols

b) Especially small at low ϵ

c) Variable number of oscillations for different ranges of θ

TABLE VI. Sensitivity Variations as a Function of Parameter Increase for Anisotropic Potential Total DCS

Sensitivity[a] characteristic	Parameter Increasing		
	q	a	β
$S(\theta; r_m^{(0)})$			
mag.	simil.[b]	simil.[b]	sig. incr.[c]
osc.	simil.[b]	sl. decr.	same sig. incr.(θ>20°)[c]
$S(\theta; \epsilon^{(0)})$			
mag.	same	incr.	same
osc.	decr.	incr.	same
$S(\theta; q)$			
mag.	simil.[d]	simil.[d]	same
osc.	simil.[b]	same	simil.
$S(\theta; a)$			
mag.	same	sig. incr.	same
osc.	simil. incr. (5x θ<8°)	same	simil.
$S(\theta; \beta)$			
mag.	simil.[b]	simil.[b]	simil.[b]
osc.	simil.[b]	simil.[b]	simil.[b]
$S(\theta; \beta')$			
mag.	same	same	same
osc.	same	same	incr.

a) See sec. 5 of text for a full description of this table and symbols

b) Highest at intermediate value of the parameter and similar at extereme values

c) The increase is for value of β changing from 4.0 to 7.2 only

d) Increase only for higher value of parameter

TABLE VII. Comparison of Inelastic Sensitivities

Sensitivity[a] and characterisitc	increase in Δj for $j = 12$	Comparison with total DCS $S(\theta; p_k)$	
		elastic $j = 12$	inelastic $j = 12 \rightarrow 14$
$S(\theta; r_m^{(0)})$			
mag.	incr. (× 500)	same	incr. ($\theta<6°$)
osc.	same	same	same
$S(\theta; \epsilon^{(0)})$			
mag.	sl. incr.	same	simil.
osc.	decr.	sl. incr.	sl. incr.
$S(\theta; q)$			
mag.	incr. (×20)	simil.	incr.
osc.	sig. decr. $S(\theta;q)>0$	decr.	v. sig. decr.
$S(\theta; a)$			
mag.	incr.(×30)	simil.	incr.
osc.	decr.	simil.	sl. decr.
$S(\theta; \beta)$			
mag.	incr.	same	incr. (×10 $\theta<10°$)
osc.	same	same	same
$S(\theta; \beta')$			
mag.	incr. (×100 Δj=8)	same	sl. incr.
osc.	incr.	same	simil.

(continued)

TABLE VII. *(continuation)*

Sensitivity[a] and characterisitc	increase in Δj for $j = 12$	Comparison with total DCS $S(\theta;p_k)$	
		elastic $j = 12$	inelastic $j = 12 \rightarrow 14$
$S(\theta;C_6^{(0)})$			
mag.	incr.	simil.	incr.
osc.	same	same	simil.
$S(\theta;C_8^{(0)})$			
mag.	sl. incr.	decr. (×10)	sl. decr.
osc.	decr.	decr.	decr.
$S(\theta;C_6^{(2)})$			
mag.	incr. (×100 Δj=8)	simil.	incr. (×10 $\theta<5°$)
osc.	same	decr.	decr.
$S(\theta;C_8^{(2)})$			
mag.	incr. (×10 Δj=8)	same	simil.
osc.	decr.	decr.	simil.

a) See sec. 5 of text for a full description of this table and symbols

TABLE VIII. Sensitivity Variations as a Function of Parameter Increase for Anisotropic Potential $j = 12 \rightarrow j = 14$ DCS

Sensitivity[a] and characteristic	Parameter Increasing		
	q	a	β
$S(\theta; r_m^{(0)})$			
mag.	same	simil.[b]	incr.
osc.	sl. decr.	simil.	sl. incr.
$S(\theta; \epsilon^{(0)})$			
mag.	sl. decr.	incr.	same
osc.	sl. decr.	same	same
$S(\theta; q)$			
mag.	sl. incr.	same	same
osc.	sl. incr.	sl. incr.	sl. incr.
$S(\theta; a)$			
mag.	decr.	sig. incr.(×100)	sl. decr.
osc.	sl. decr.	sl. incr.	same
$S(\theta; \beta)$			
mag.	simil.[b]	sl. decr.	incr. ($\theta<6°$)
osc.	siml.[b]	sl. decr.	same
$S(\theta; \beta')$			
mag.	simil.	same	same
osc.	simil.	sl. decr.	sig. incr.

a) See sec. 5 of text for a full description of this table and symbols

b) Highest at an intermediate value of the parameter and similar at extreme values

TABLE IX. Variations in Sensitivities with Increasing Energy

Sensitivity[a] and characteristic	total DCS	$j = 12 \rightarrow j = 14$ DCS
$S(\theta; r_m^{(0)})$		
mag.	same	sl. decr. (@ 95 *meV*)
osc.	sl. incr.	same
$S(\theta; \epsilon^{(0)})$		
mag.	decr. (×5 θ>17°)	same
osc.	sl. incr.	same
$S(\theta; q)$		
mag.	incr. (×2 θ>25°)	same
osc.	same	simil.
$S(\theta; a)$		
mag.	same	same
osc.	same	same
$S(\theta; \beta)$		
mag.	simil.[b]	simil.[b]
osc.	simil.[b]	sl. incr.
$S(\theta; \beta')$		
mag.	incr.	sl. incr.
osc.	same	same

(continued)

TABLE IX. *(continuation)*

Sensitivity and characteristic	total DCS	$j = 12 \rightarrow j = 14$ DCS
$S(\theta; C_6^{(0)})$		
mag.	simil.^{c}	simil.^{c}
osc.	simil.^{c}	simil.^{c}
$S(\theta; C_8^{(0)})$		
mag.	same	same
osc.	same	same
$S(\theta; C_6^{(2)})$		
mag.	same	sl. decr.
osc.	same	simil.
$S(\theta; C_8^{(2)})$		
mag.	incr. (×10 95 *meV*)	sig. incr. (×100 95 *meV*)
osc.	same	sl. incr.

a) See sec. 5 of text for a full description of this table and symbols

b) Similar at 35 and 95 meV but 10 times greater at 65 meV, also the oscillations are increased at 65 meV

c) Similar at 35 and 95 meV but 100 times greater at 65 meV, also the oscillations are significantly increased at 65 meV

Figure 1. Deflection function for the spherical MMSV potential (SM Table II) at a collision energy of 65 meV.

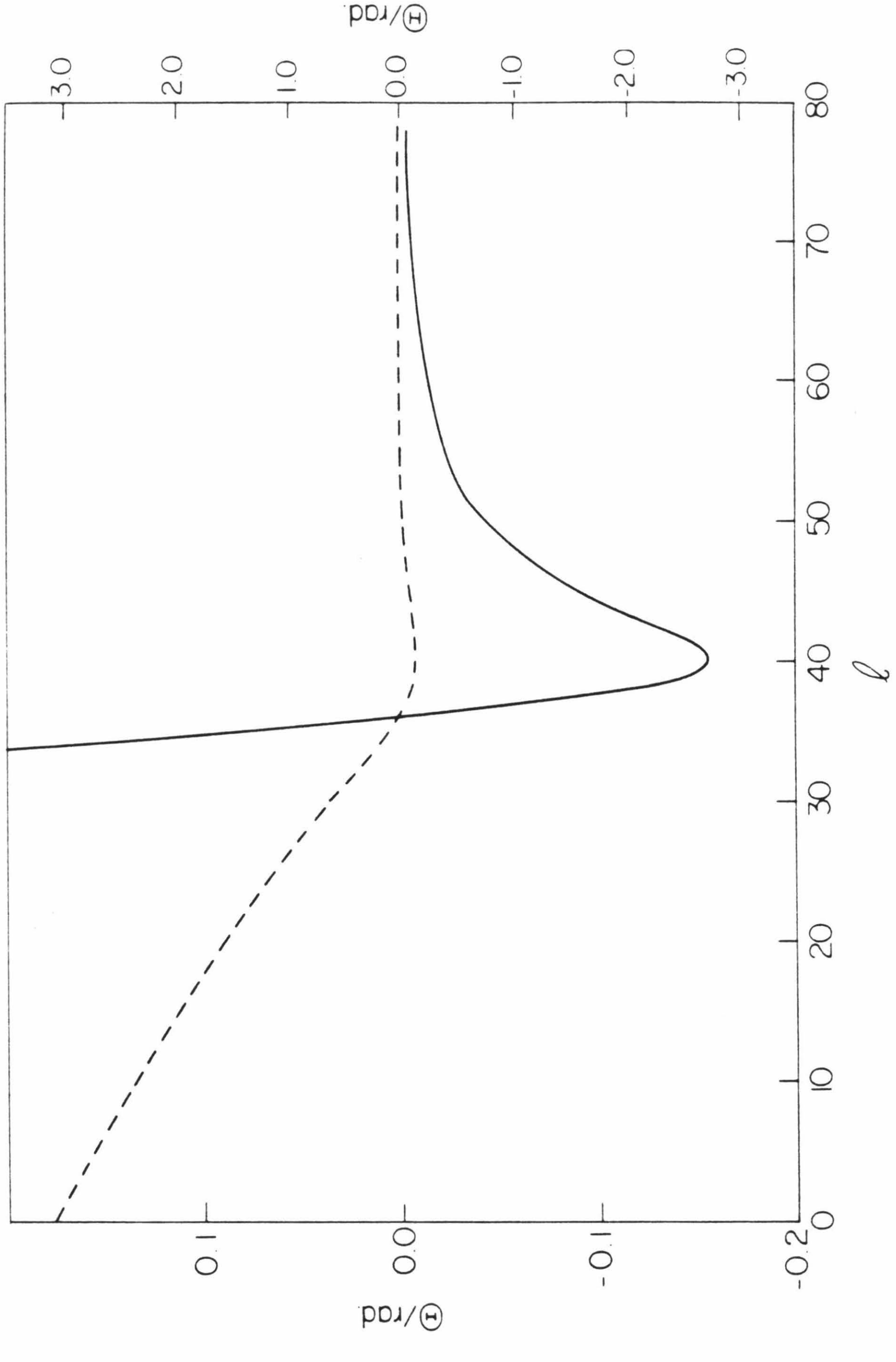

Figure 1.

Figure 2. Differential cross section (in the center-of-mass reference frame) for the spherical MMSV potential (SM Table II) at a collision energy of 65 meV.

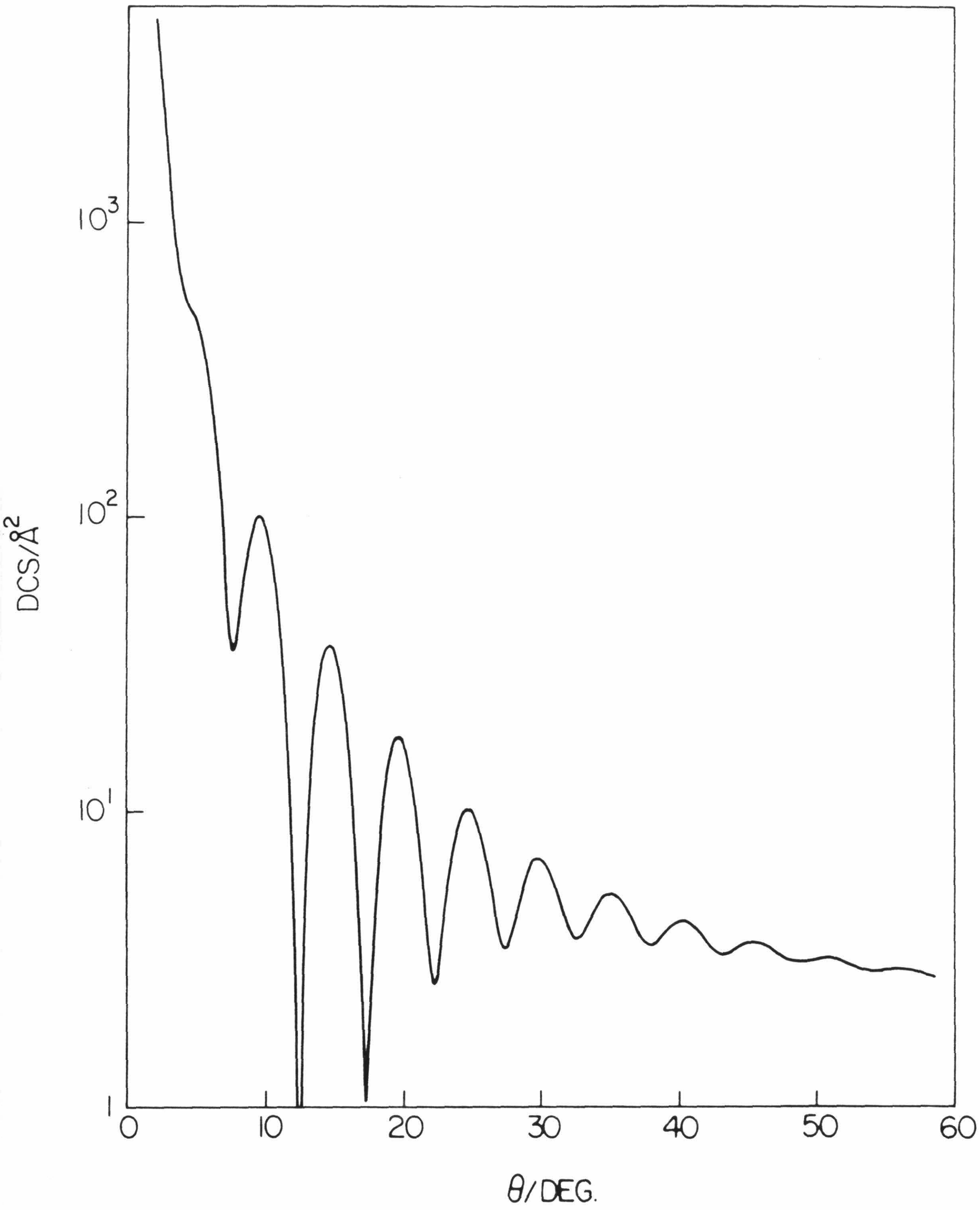

Figure 2.

Figure 3. Comparison of differential cross sections for variations of parameters r_m, ϵ, and β of the spherical MMSV potential. The center curve (in each of the three sets of curves) is for the SM potential (Table II). For clarity, the upper curves are shifted upwards by a factor of 10 while the lower curves are shifted downwards by the same factor. For panels a, b, and c the upper curves correspond to the SRH, SEH, and SBH potentials (Table II), respectively, and the lower curves correspond to the SRL, SEL, and SBL potentials, respectively.

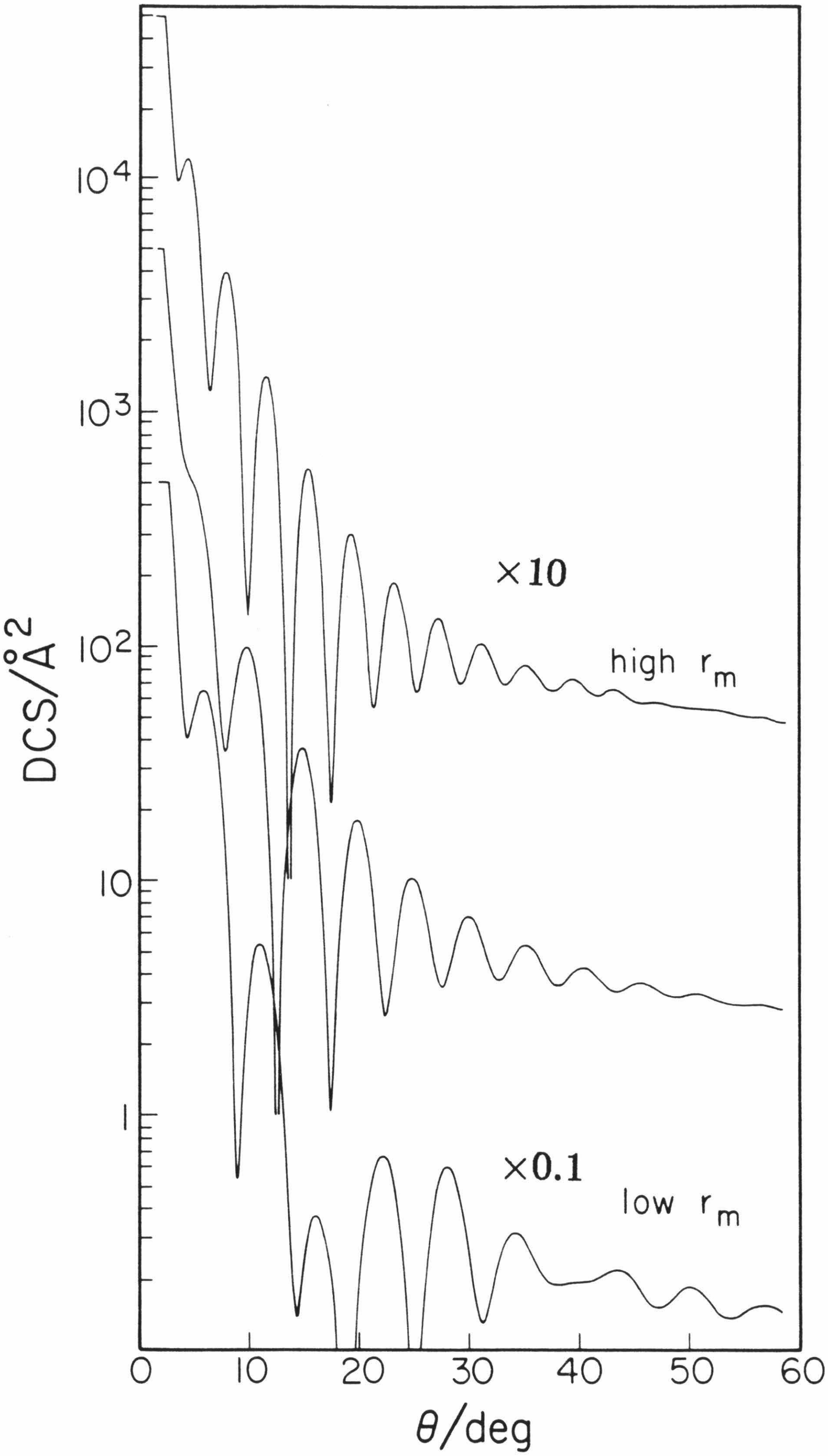

Figure 3a.

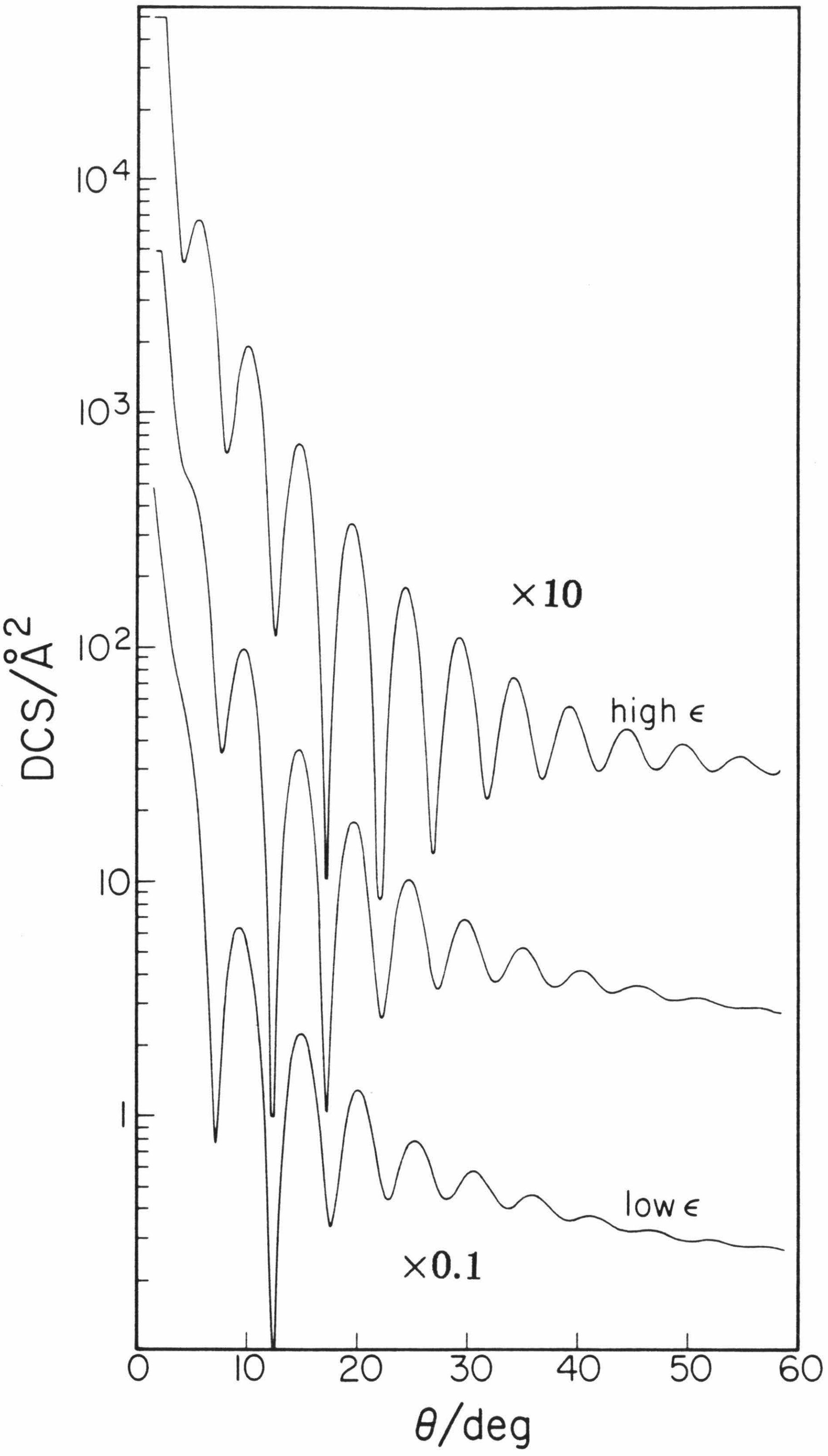

Figure 3b.

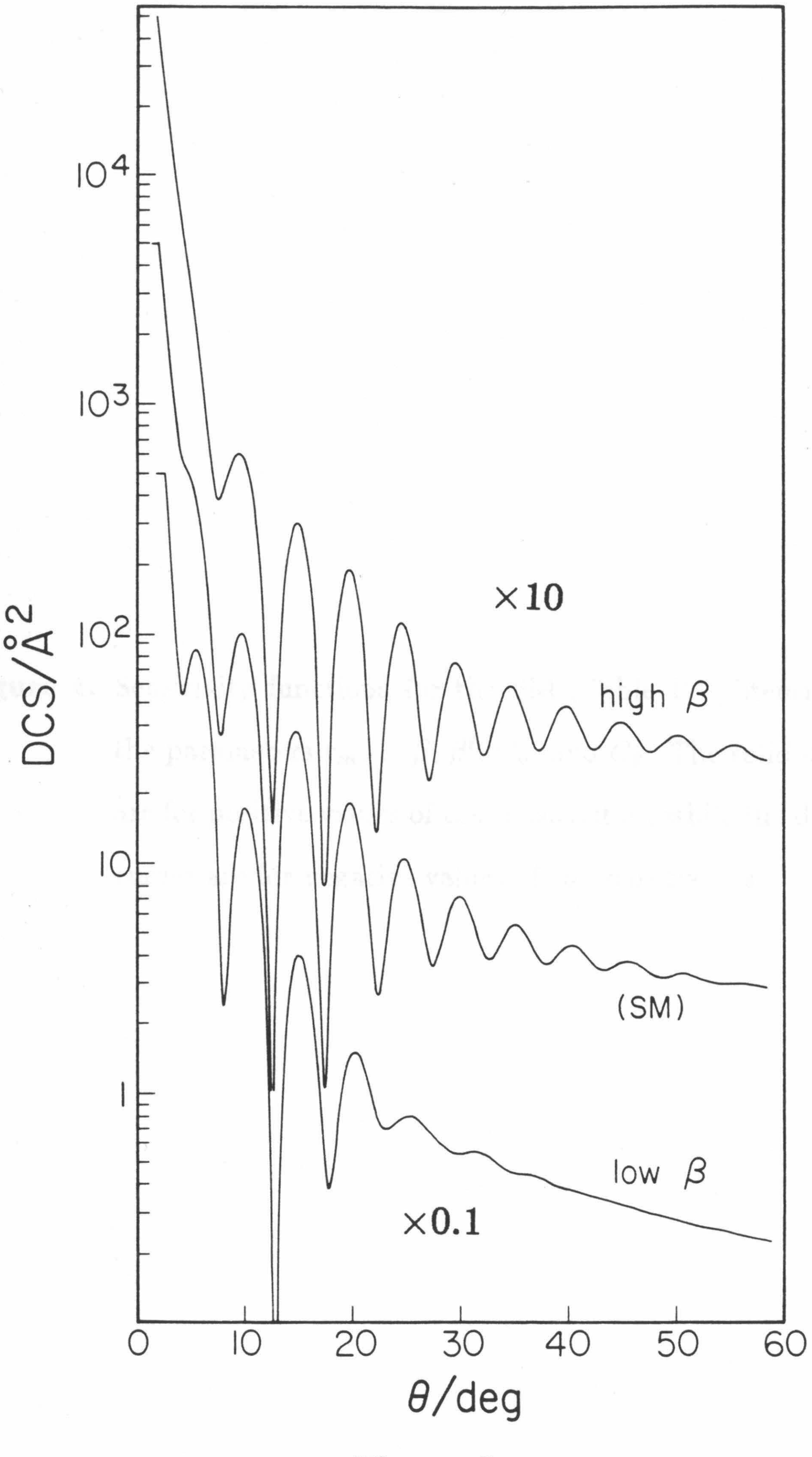

Figure 3c.

Figure 4. Sensitivity functions for the SM (Table II) potential for the parameters r_m, ϵ, β, β', C_6, and C_8. The solid curves are for positive values of the sensitivities, while the dashed curves are for negative values of the sensitivities.

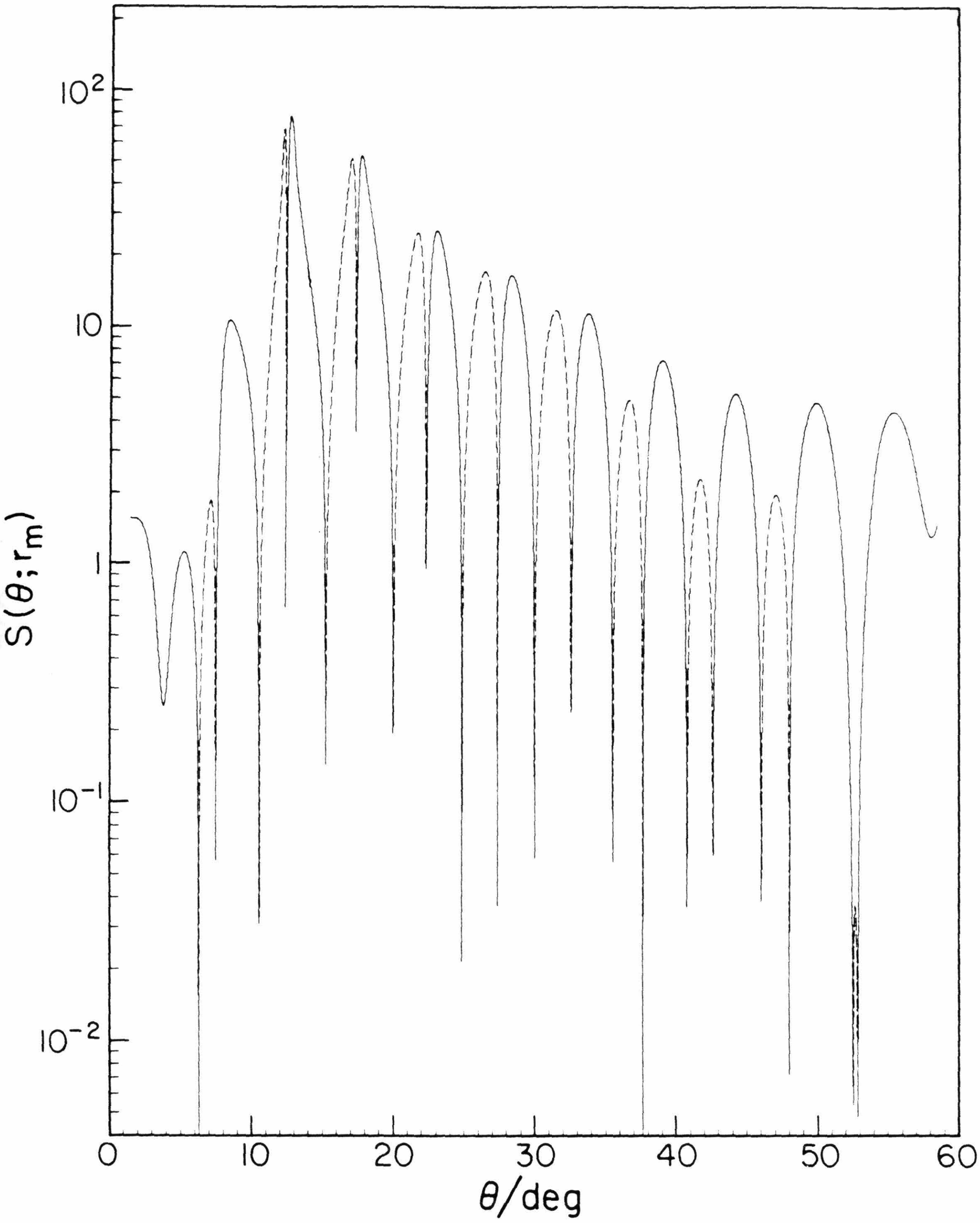

Figure 4a.

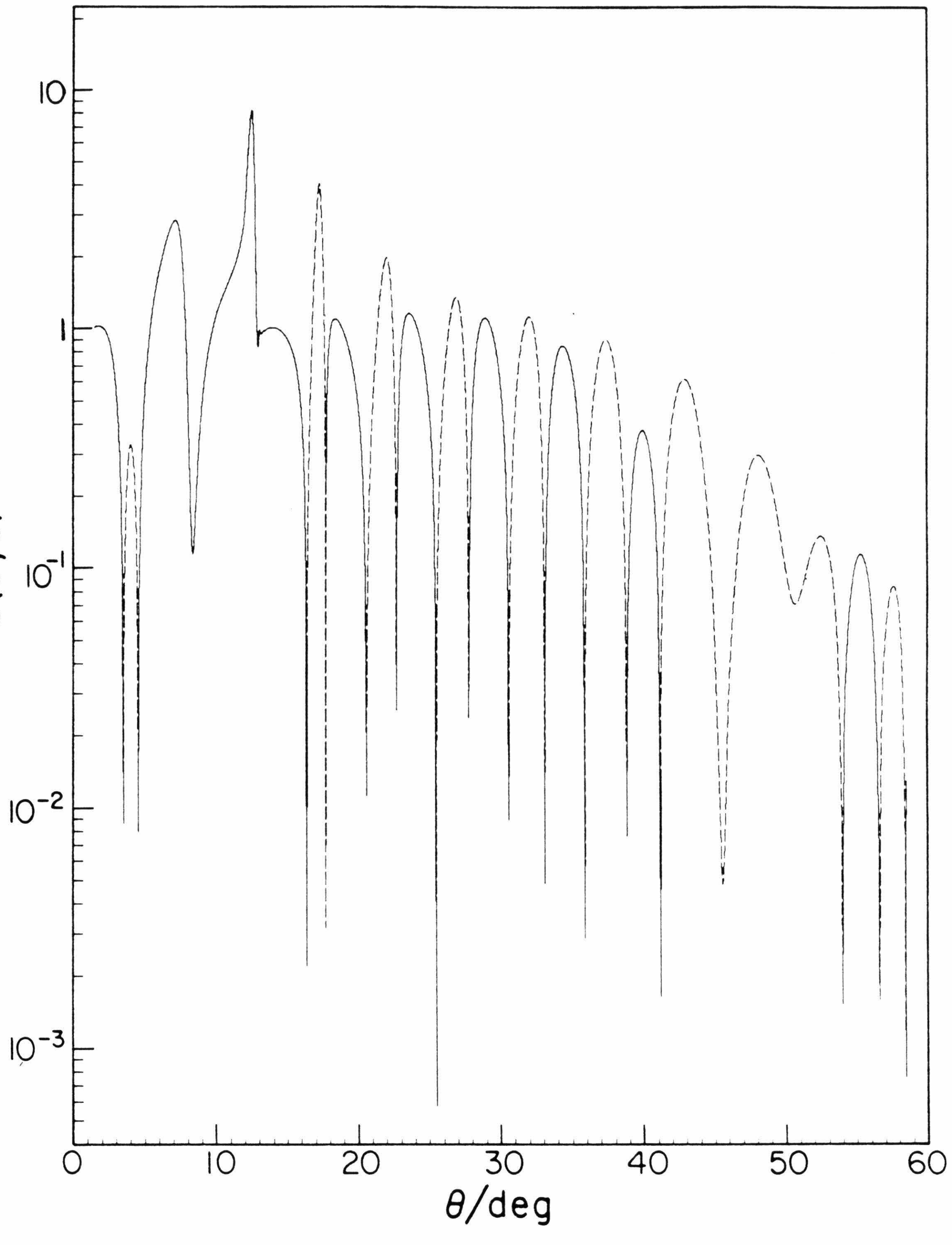

Figure 4b.

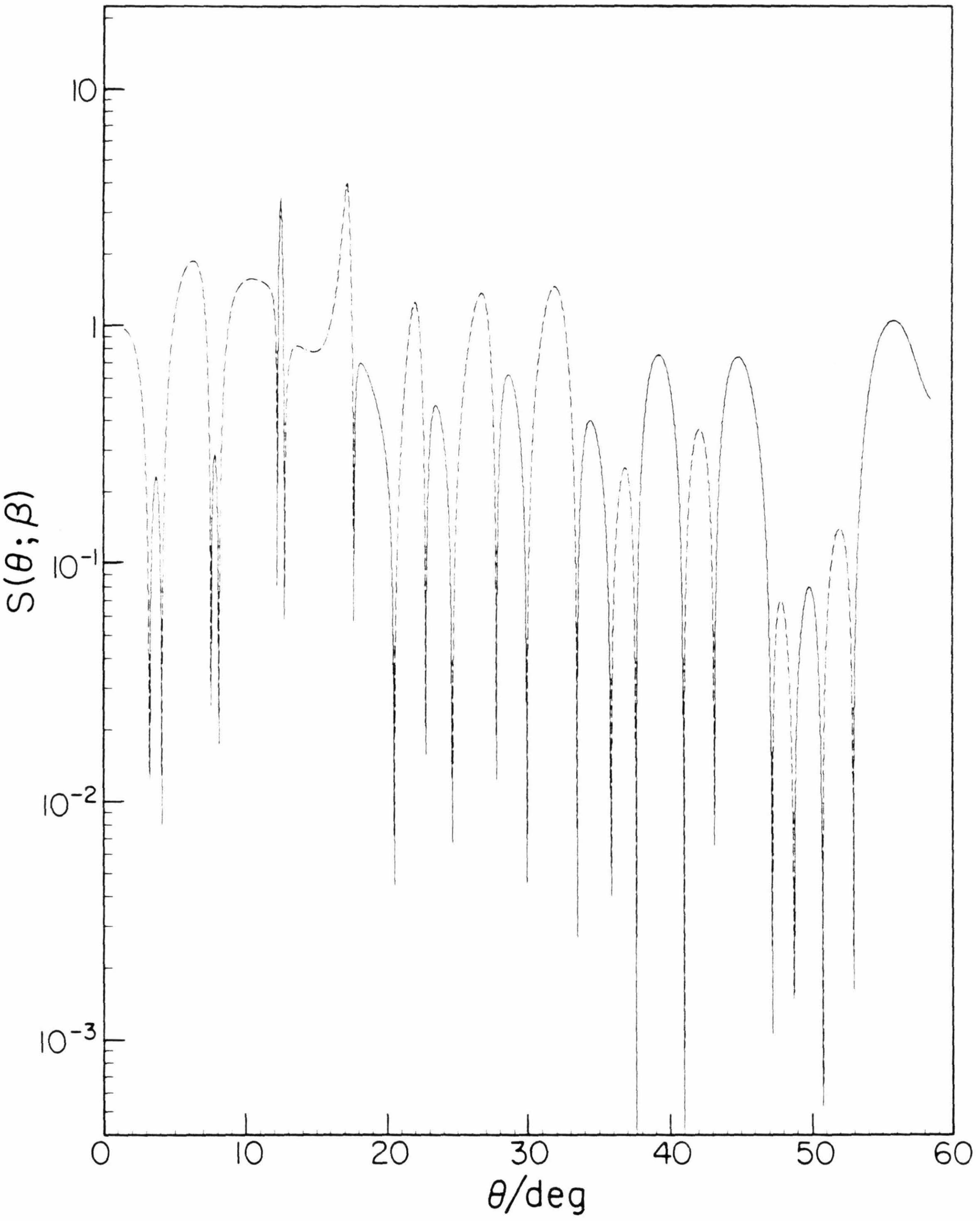

Figure 4c.

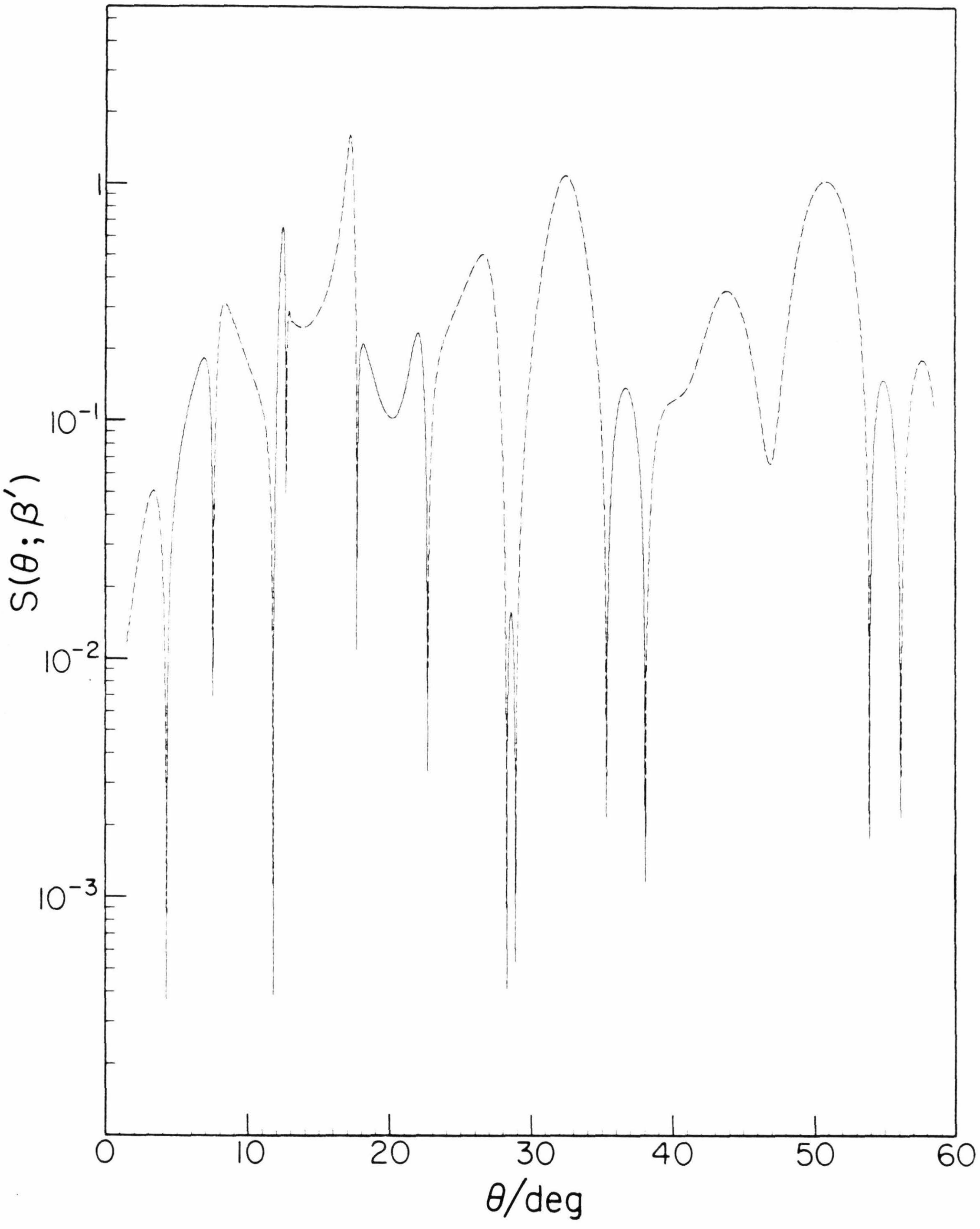

Figure 4d.

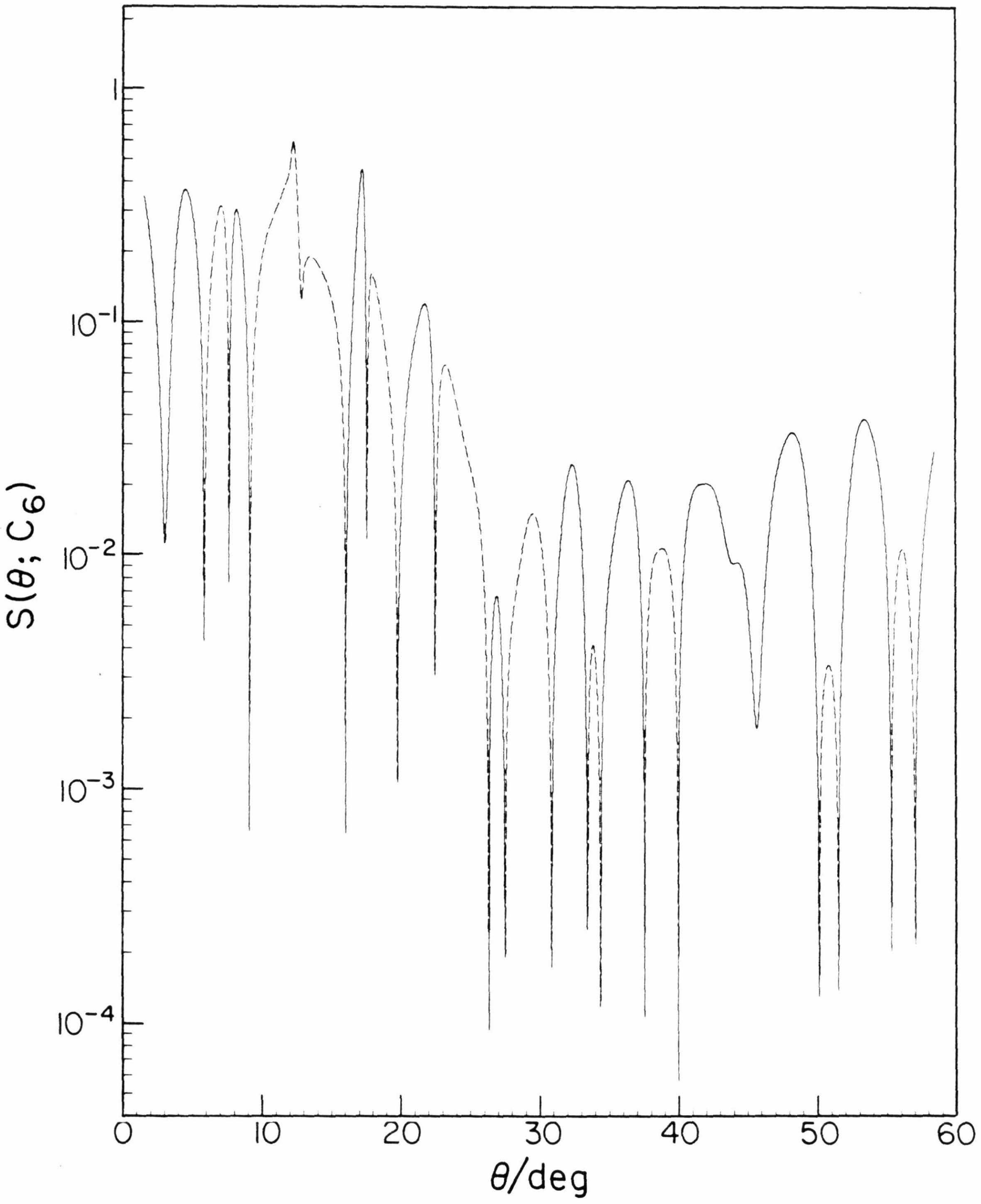

Figure 4e.

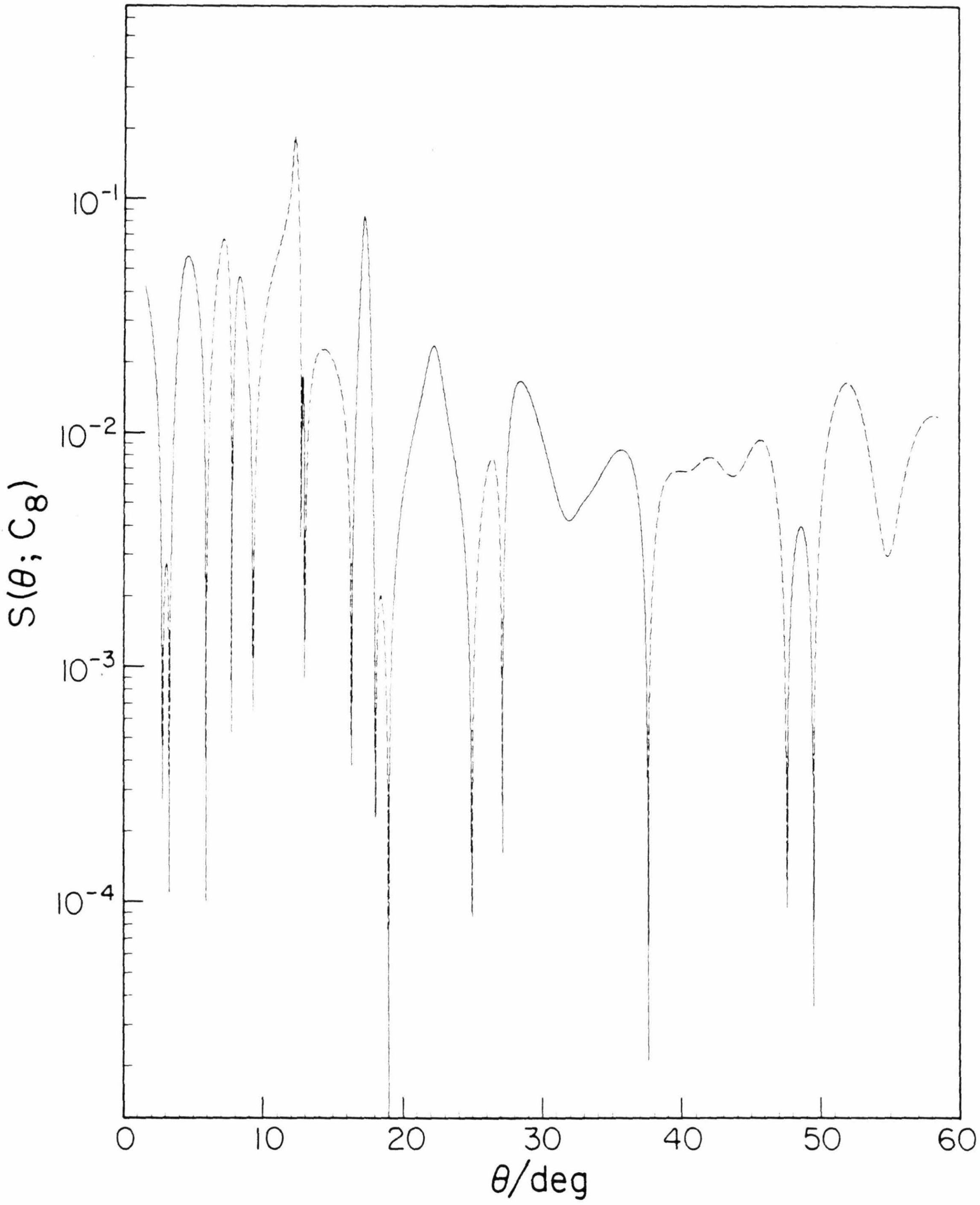

Figure 4f.

Figure 5. Comparison of differential cross sections for variations of the anisotropy parameters q, and a for the MMSV potential given in Table I and its variations given in Table III. The center curve (in the two set of curves) is for the M potential (Table III). For clarity, the upper curves are shifted upwards by a factor of two; while the lower curves are shifted downwards by the same factor. For panels a, and b the upper curves correspond to the QH and AH potentials, respectively, and the lower curves correspond to the QL and AL potentials, respectively.

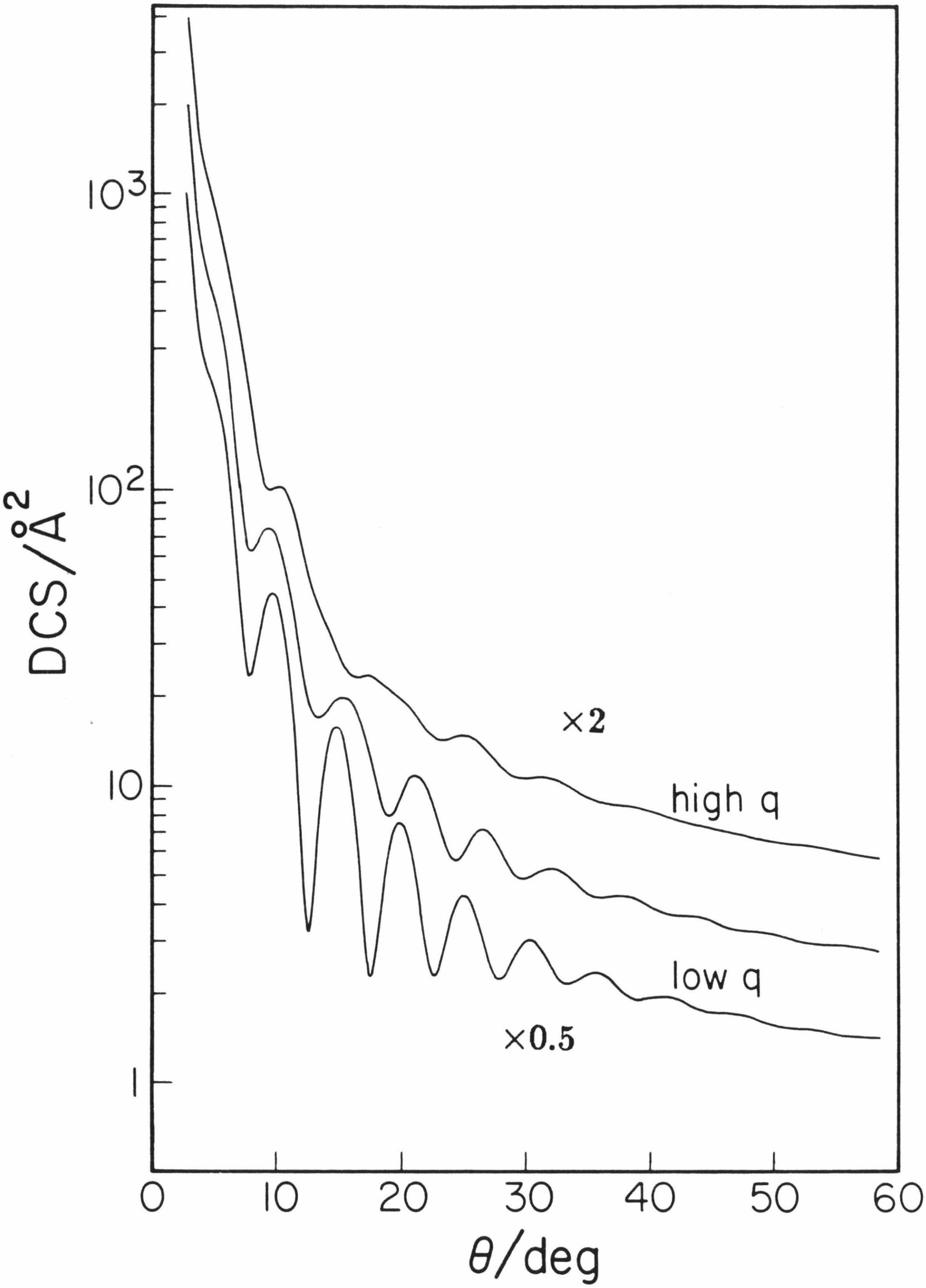

Figure 5a.

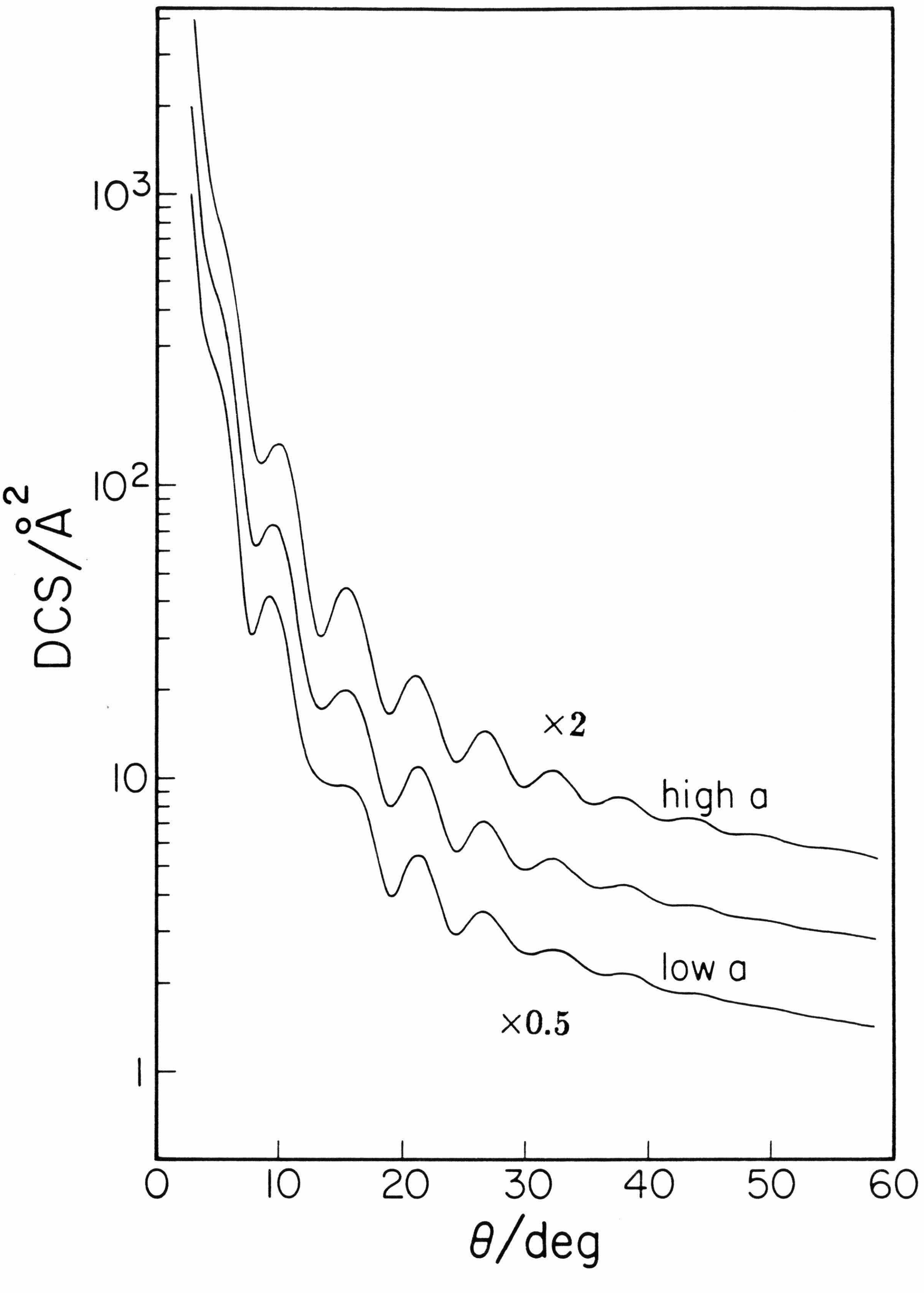

Figure 5b.

Figure 6. Comparison of differential cross sections for variations of the well shape parameter β and the repulsive wall shape parameter β' for the MMSV potential given in Table I and its variations given in Table III. The center curve (in the two set of curves) is for the M potential (Table III). For clarity, the upper curves are shifted upwards by a factor of two, while the lower curves are shifted downward by the same factor. For panels a and b the upper curves correspond to the BWH and BRH potentials, respectively, and the lower curves correspond to the BWL and BRL potentials, respectively.

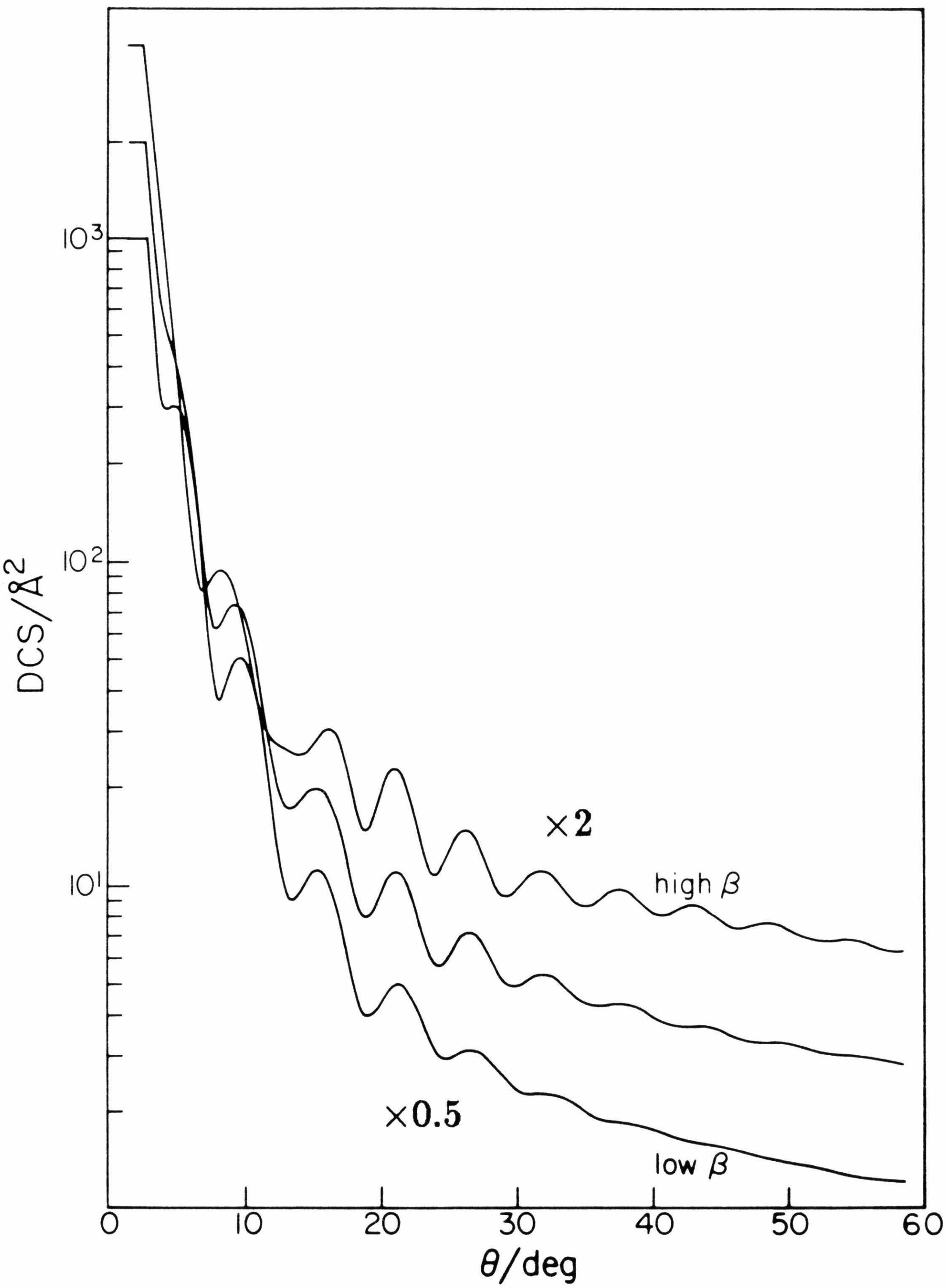

Figure 6a.

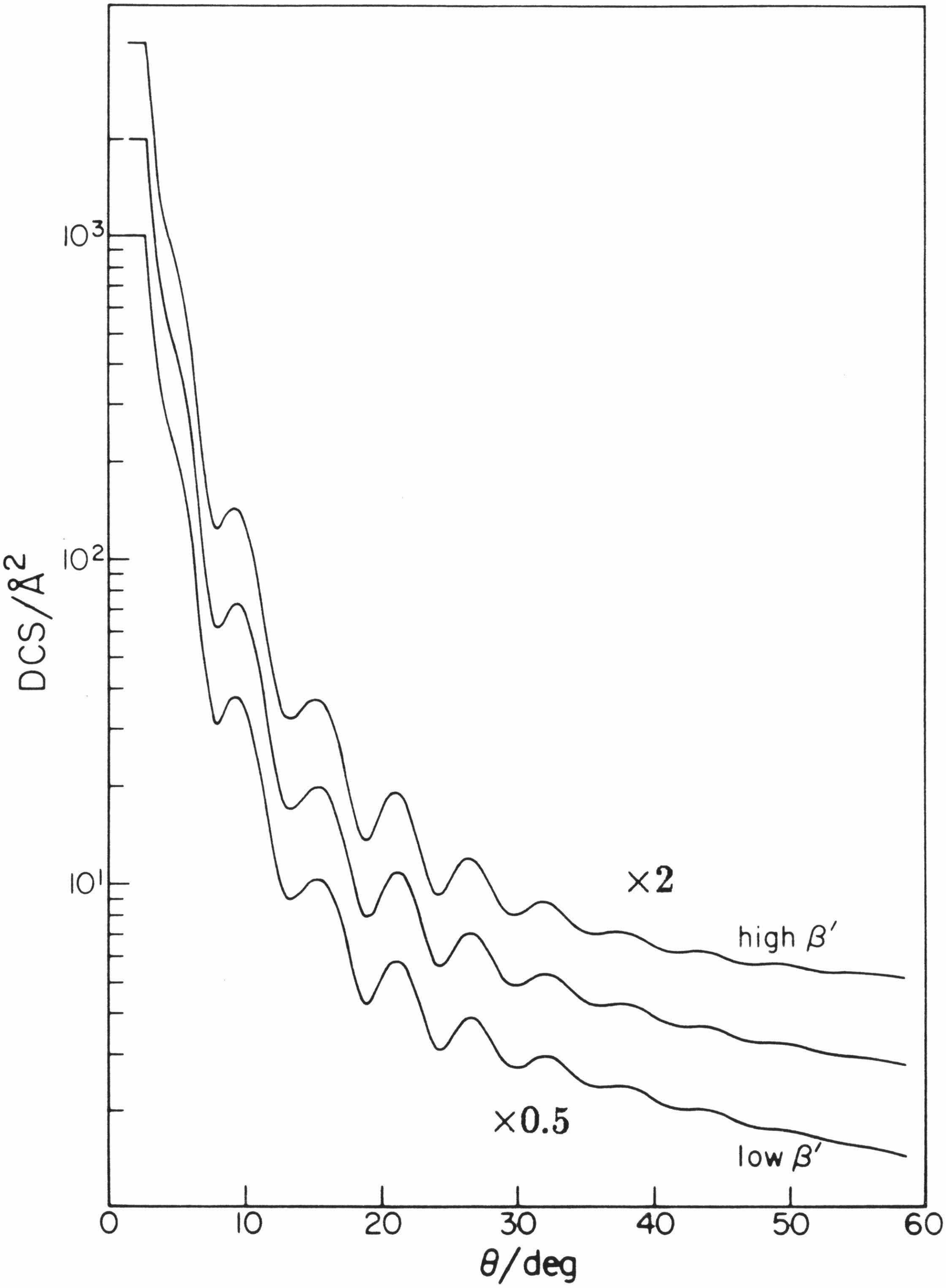

Figure 6b.

Figure 7. Total DCS sensitivity functions for the M (Table I) anisotropic potential for the parameters $r_m^{(0)}$, $\epsilon^{(0)}$, q, a, β and β'. The solid curves are for positive values of the sensitivities, while the dashed curves are for negative values of the sensitivites.

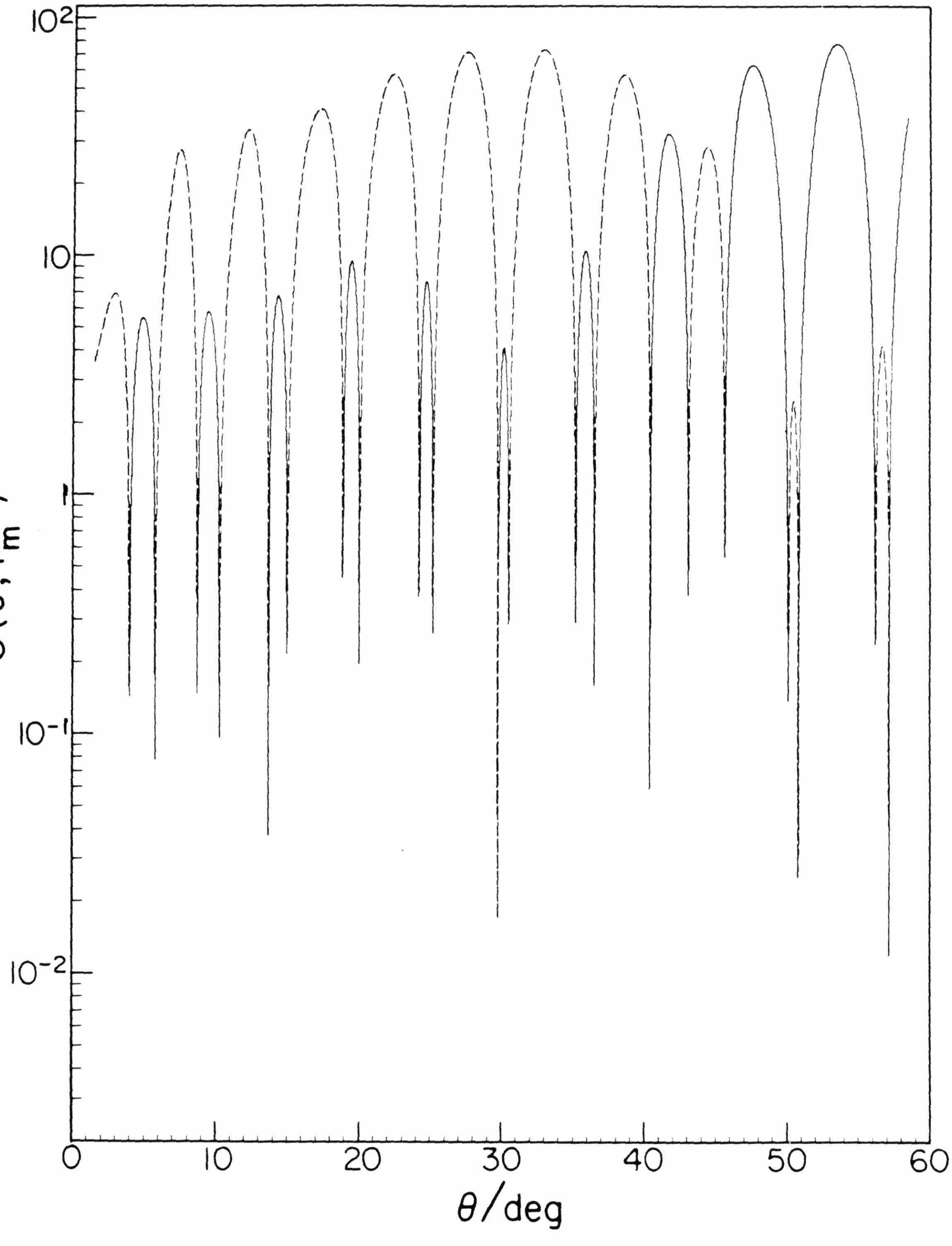

Figure 7a.

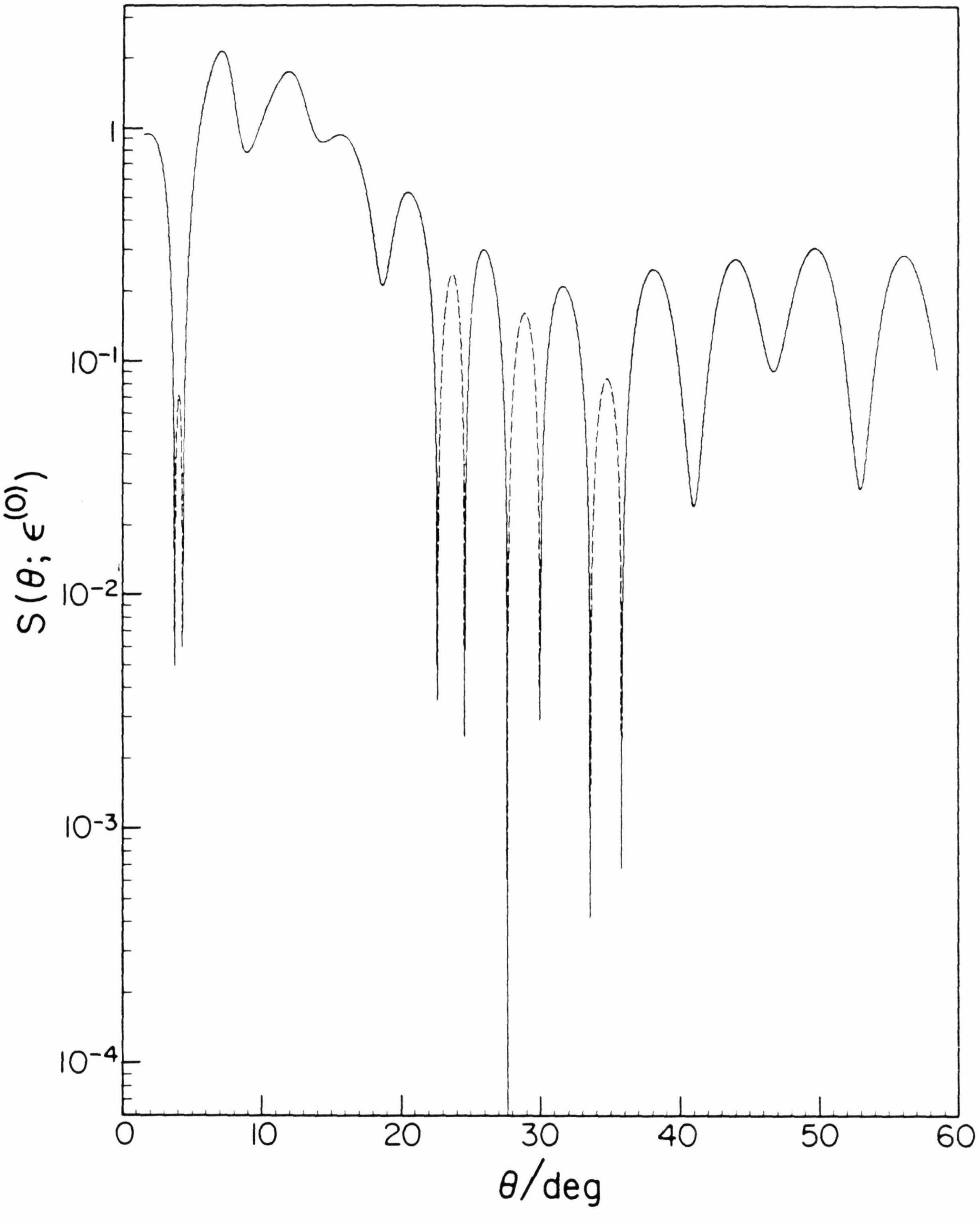

Figure 7b.

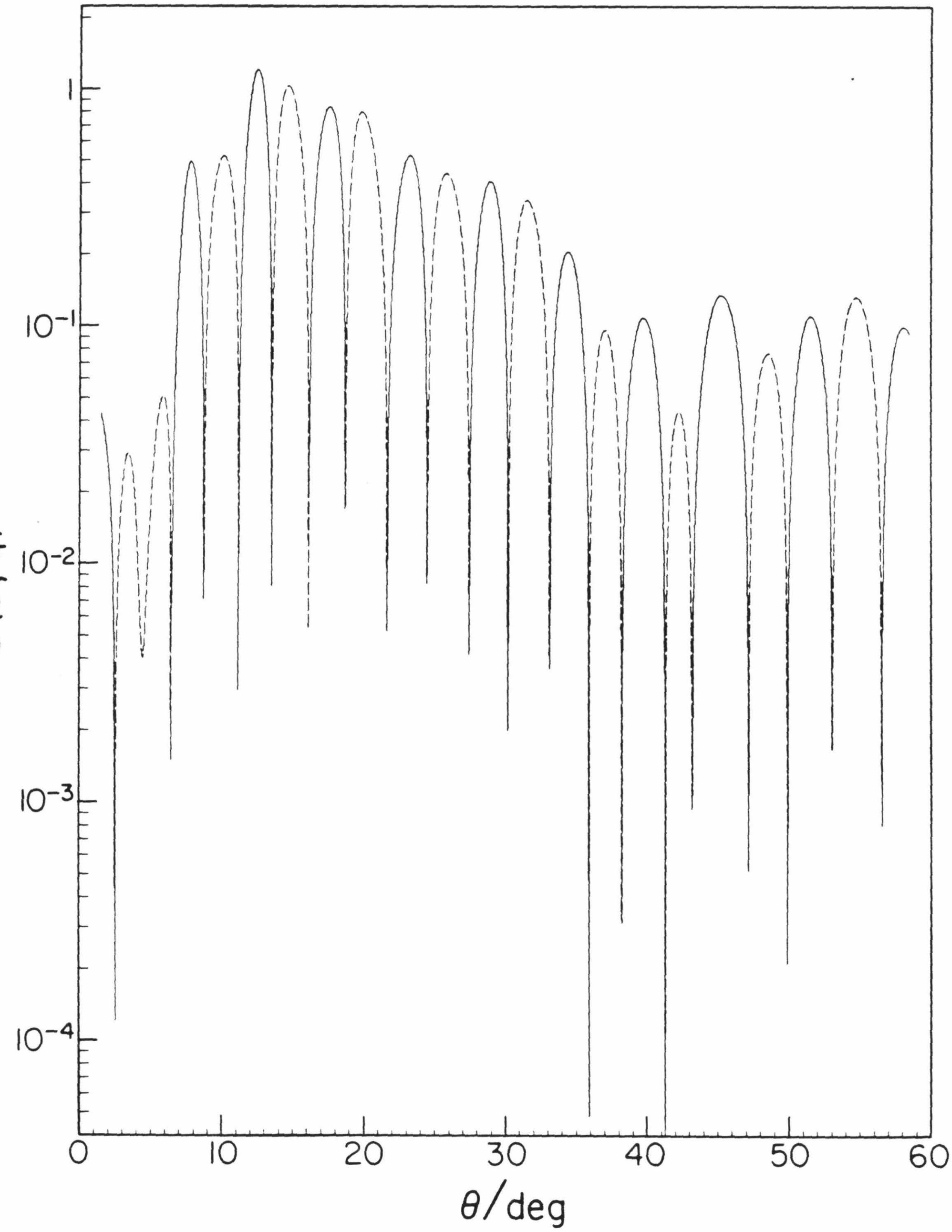

Figure 7c.

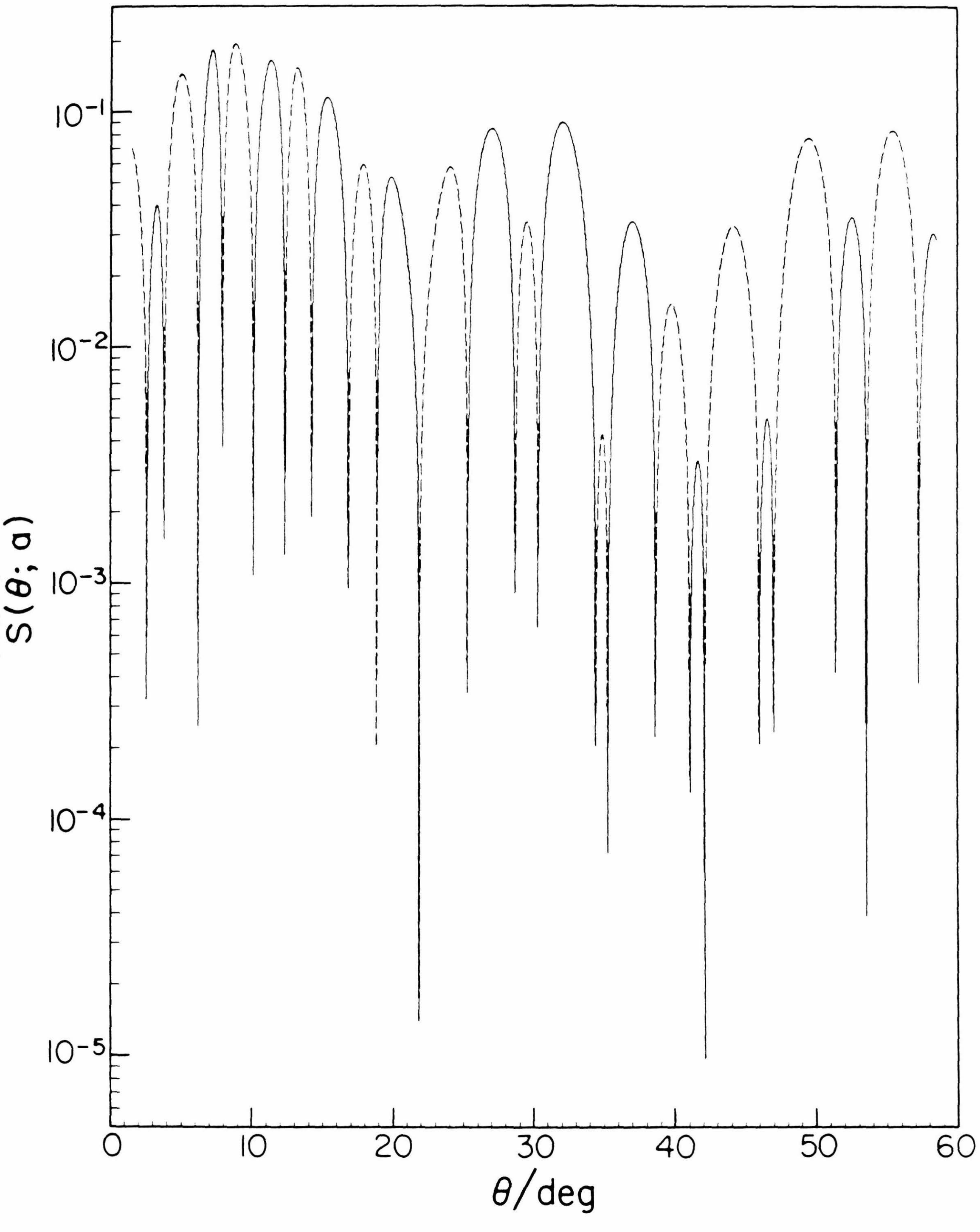

Figure 7d.

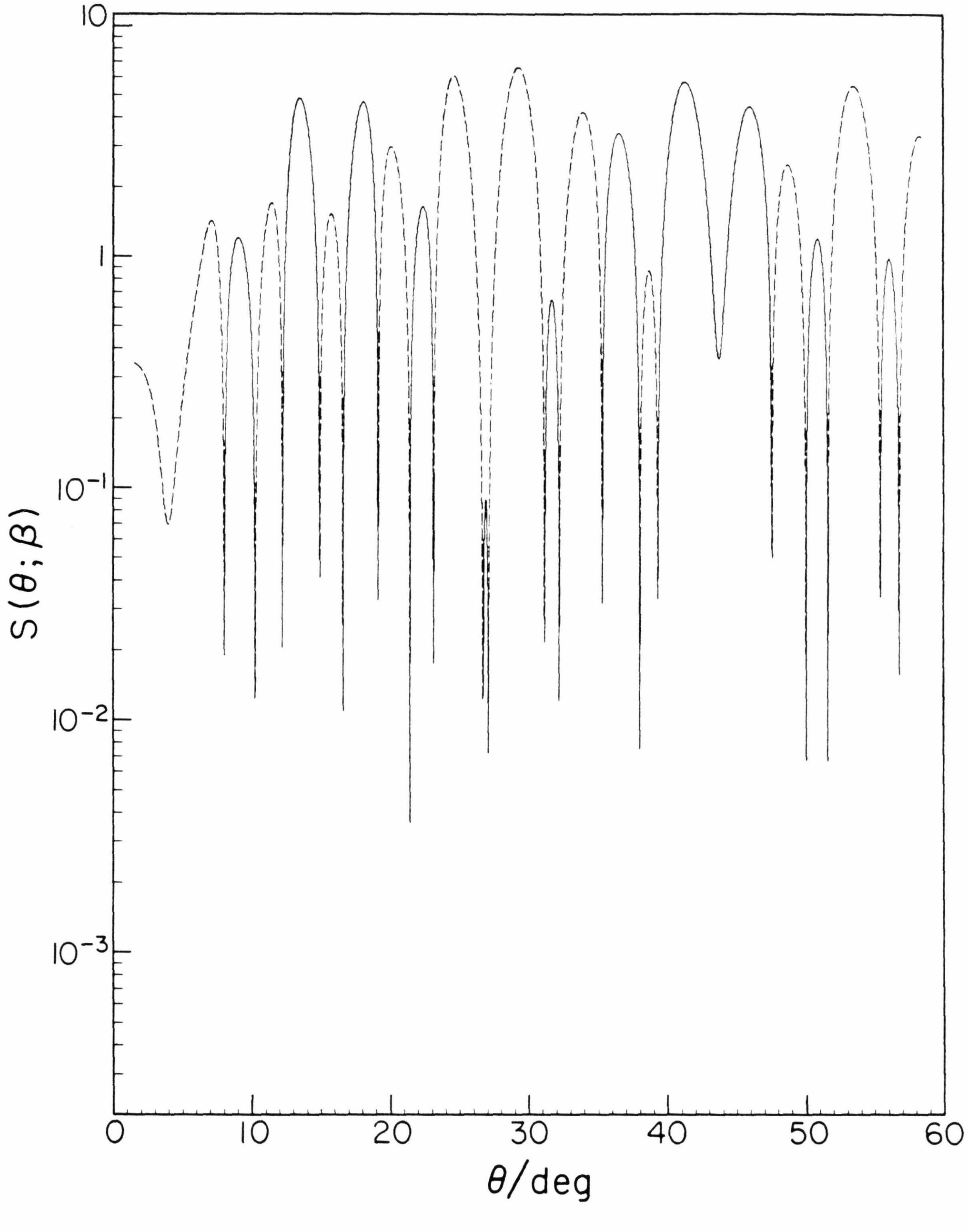

Figure 7e.

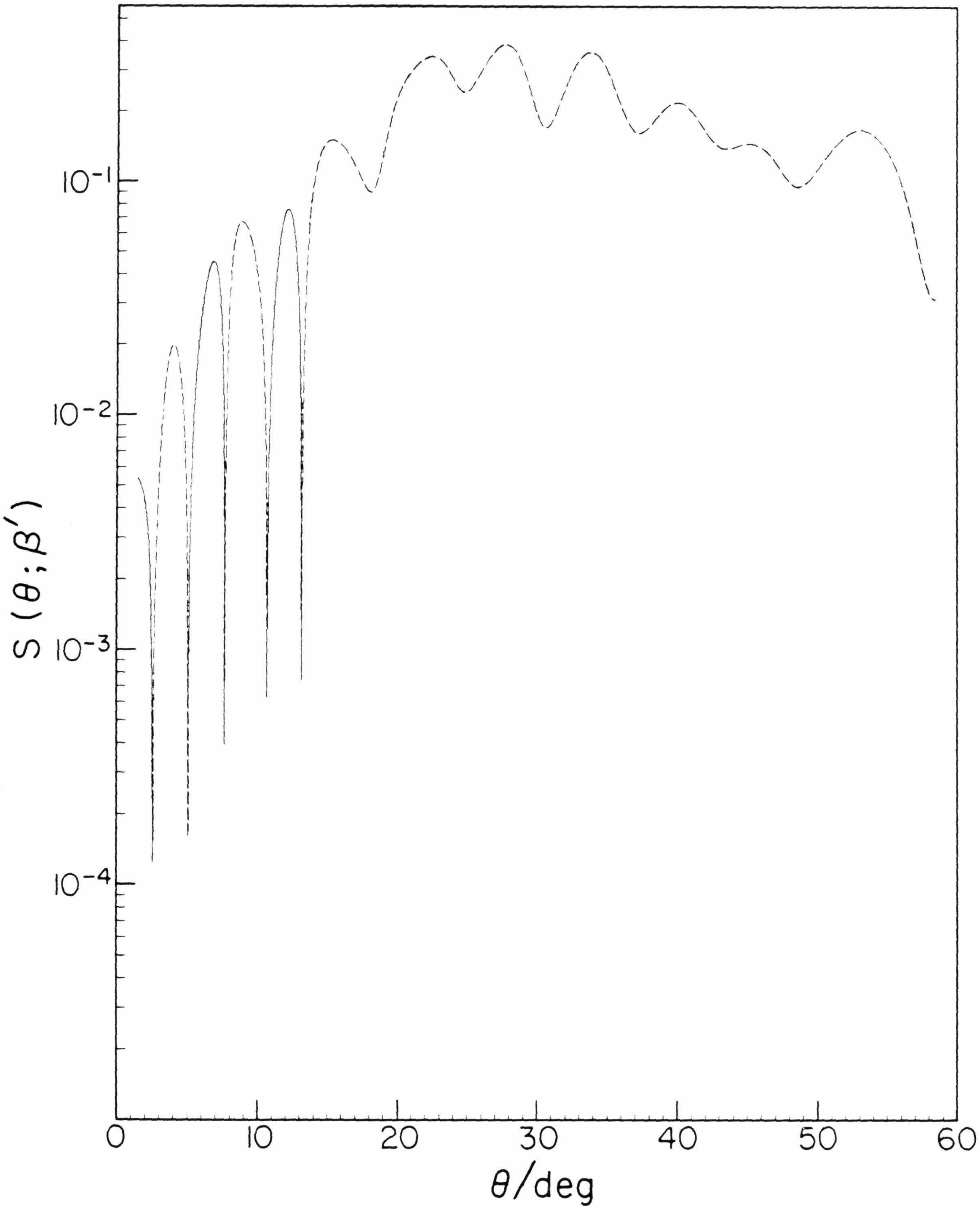

Figure 7f.

Figure 8. Total DCS sensitivity functions for the M (Table I) anisotropic potential for the long range dispersion coefficients $C_6^{0)}$, $C_6^{2)}$, $C_8^{0)}$ and $C_8^{2)}$. The solid curves are for positive values of the sensitivities, while the dashed curves are for negative values of the sensitivities.

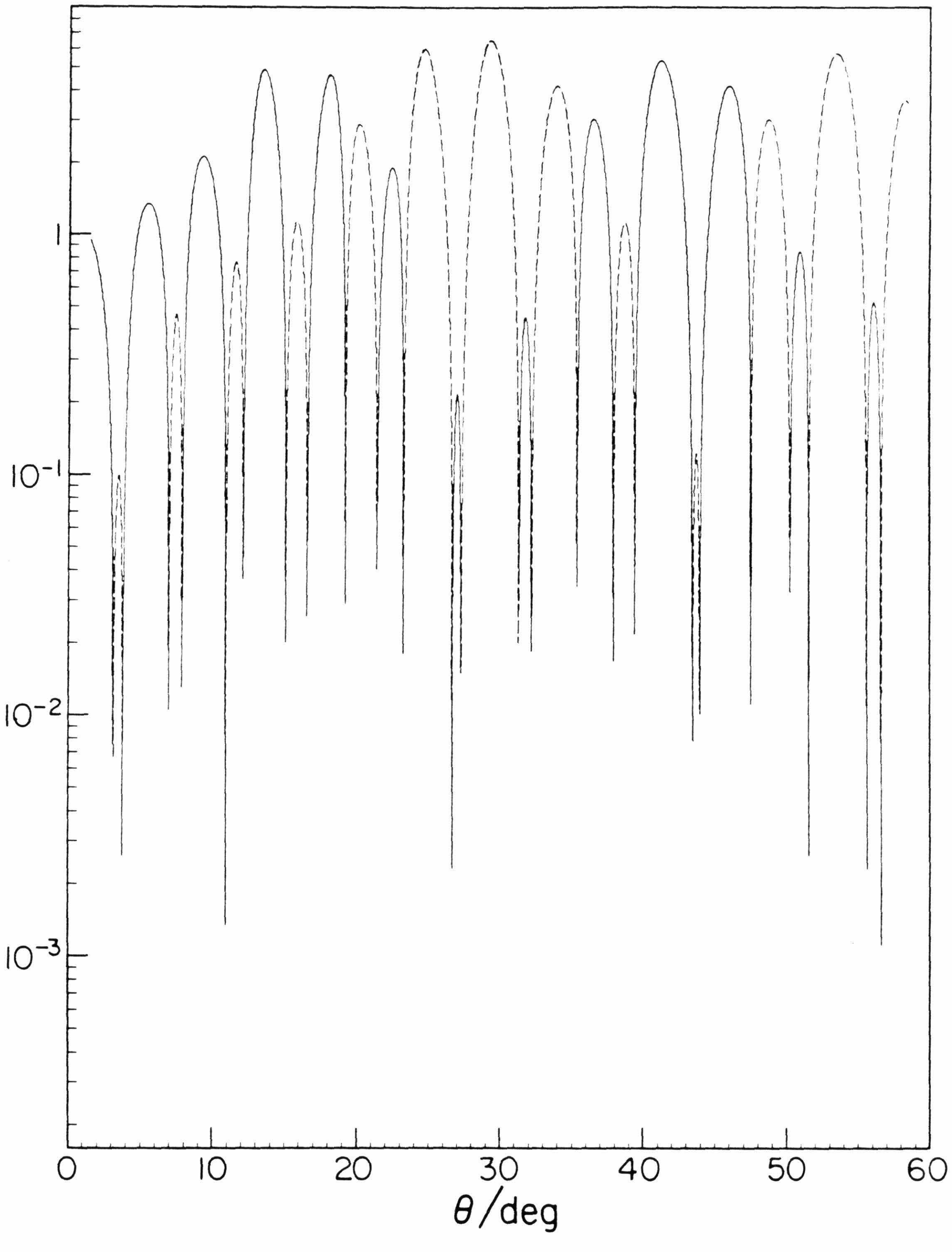

Figure 8a.

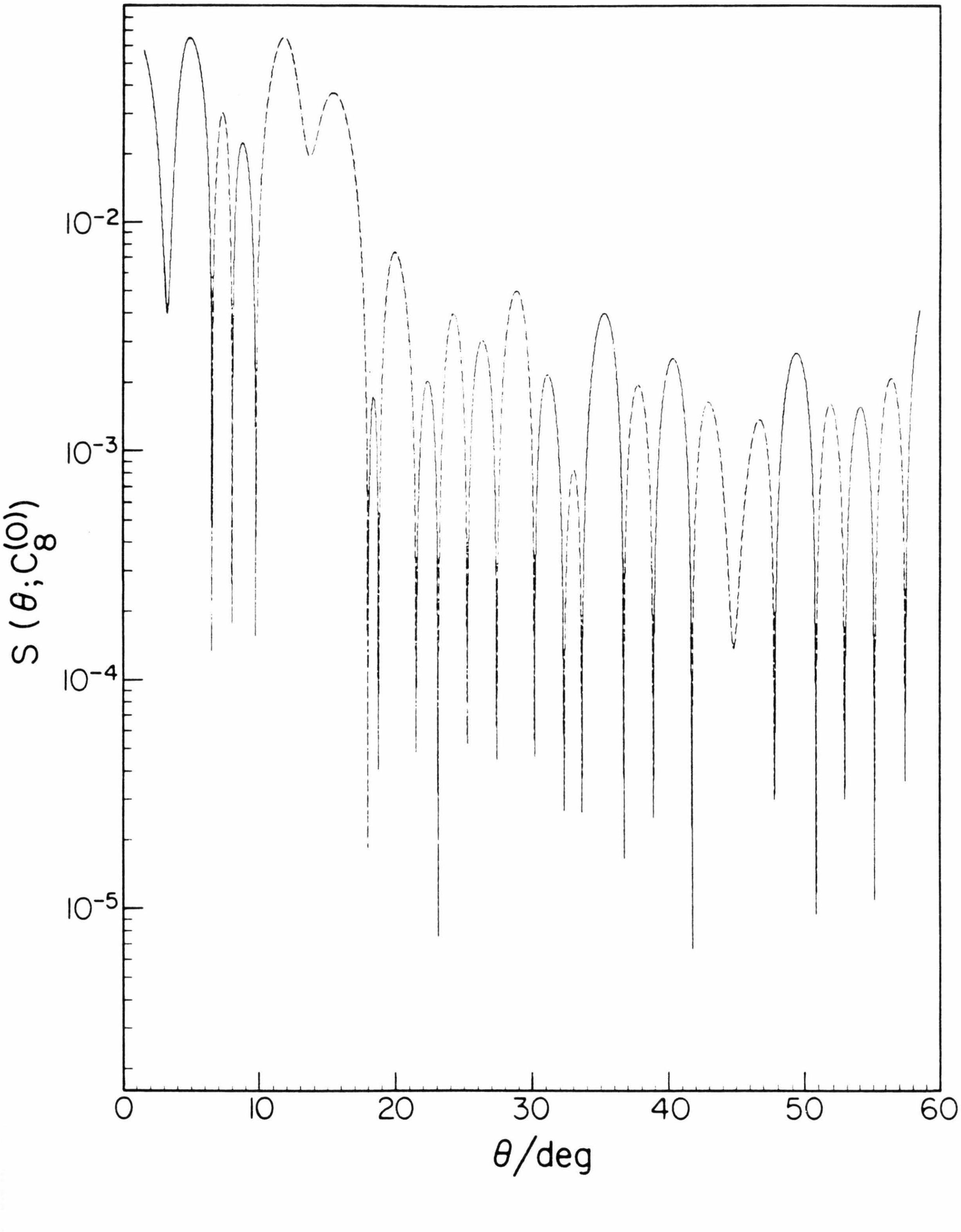

Figure 8b.

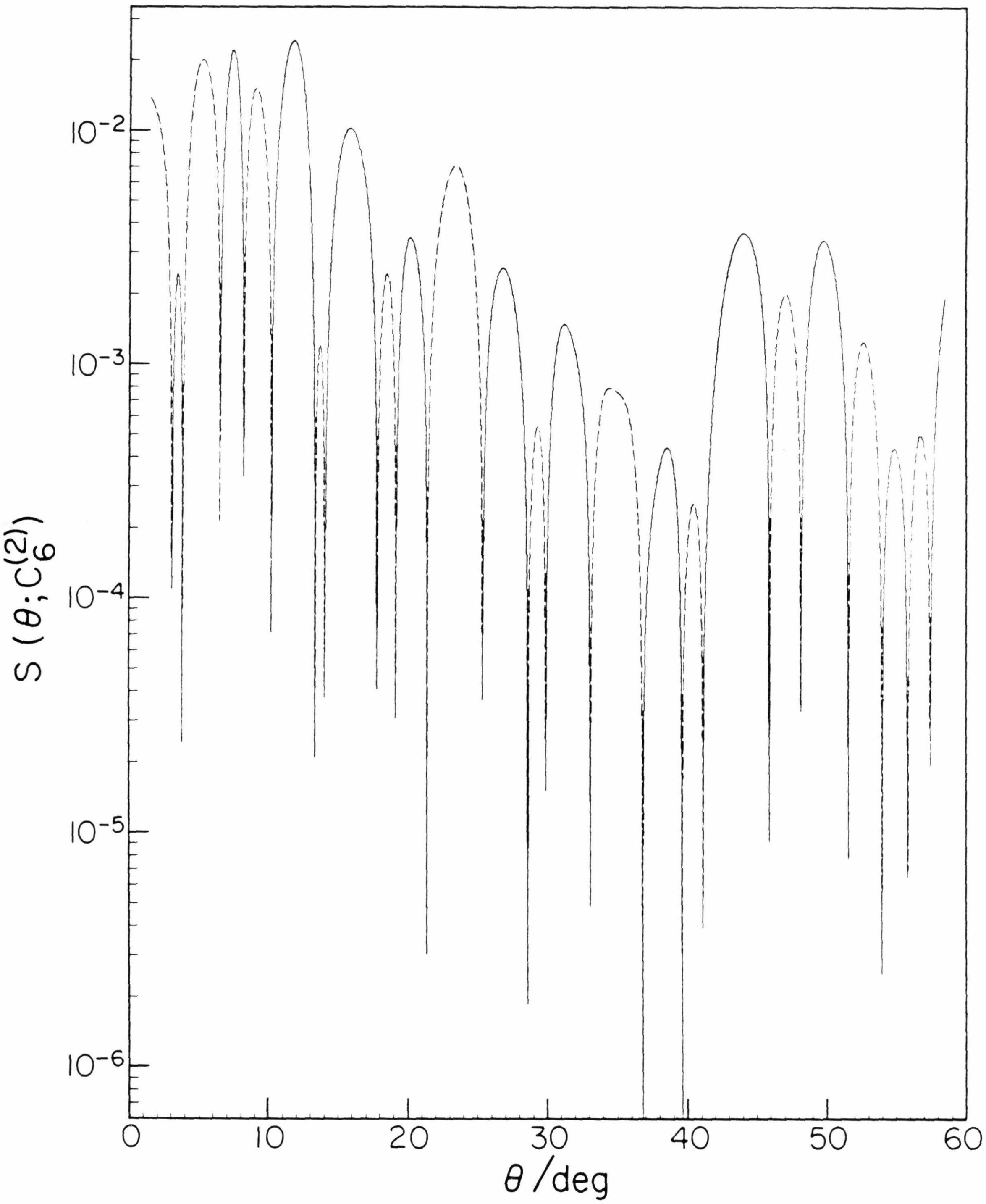

Figure 8c.

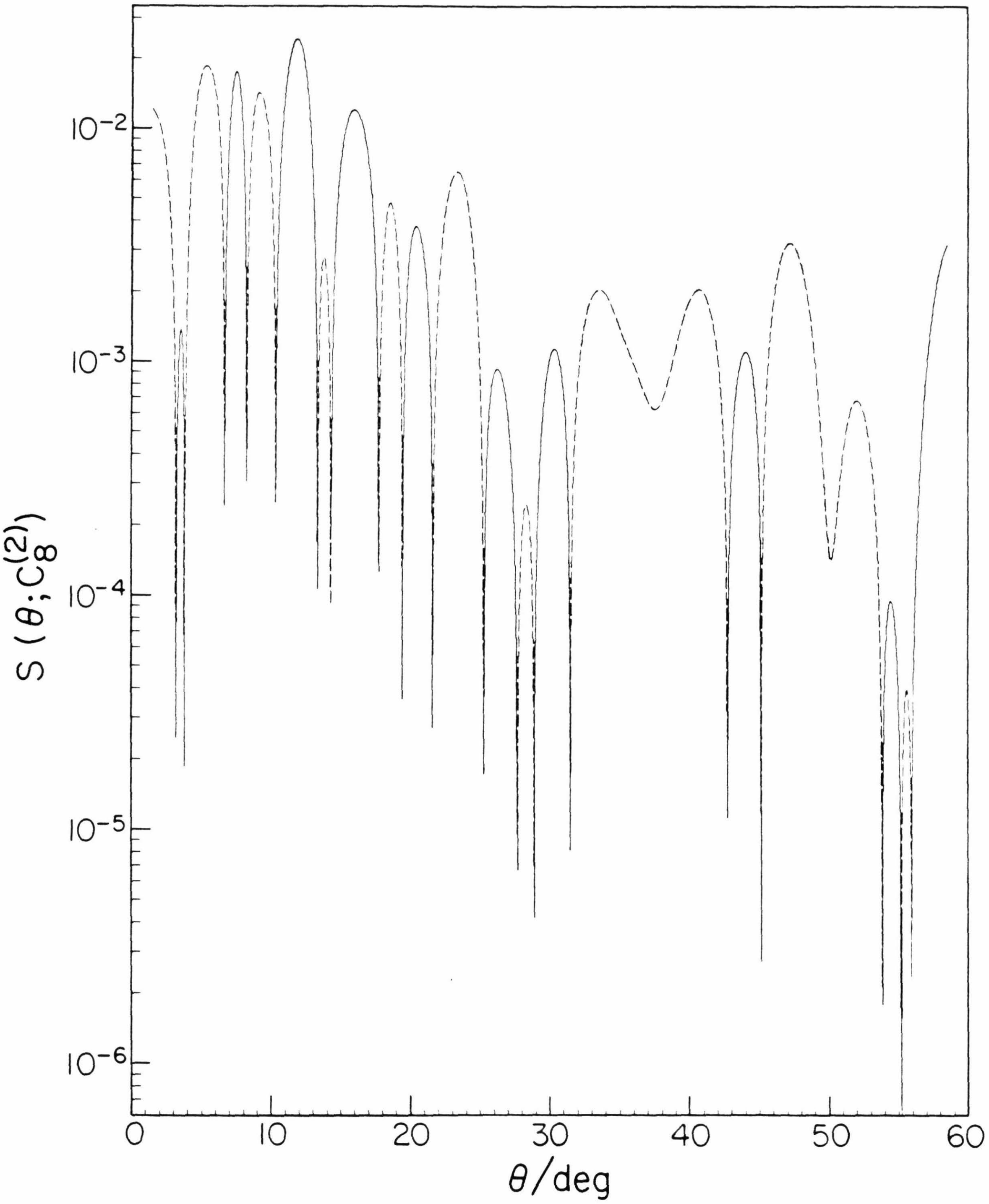

Figure 8d.

Figure 9. Rotational state-to-state differential cross sections for the anisotropic potential M (Table I) from initial state $j = 12$. Figure *a* shows the rotational energy loss cross sections final $j' = 12$, 10, 8, 6, and 4. While *b* shows the energy gain cross sections, final $j' = 12$, 14, 16, 18, and 20. The upper curve in both figures is for the elastic cross-section; the curves below it are progressively more inelastic. An increase in inelasticity corresponds to decrease in cross section, particularly at low scattering angles. The curves for alternating $j' \leftarrow j$ cross sections are plotted with dashes for distinguishability.

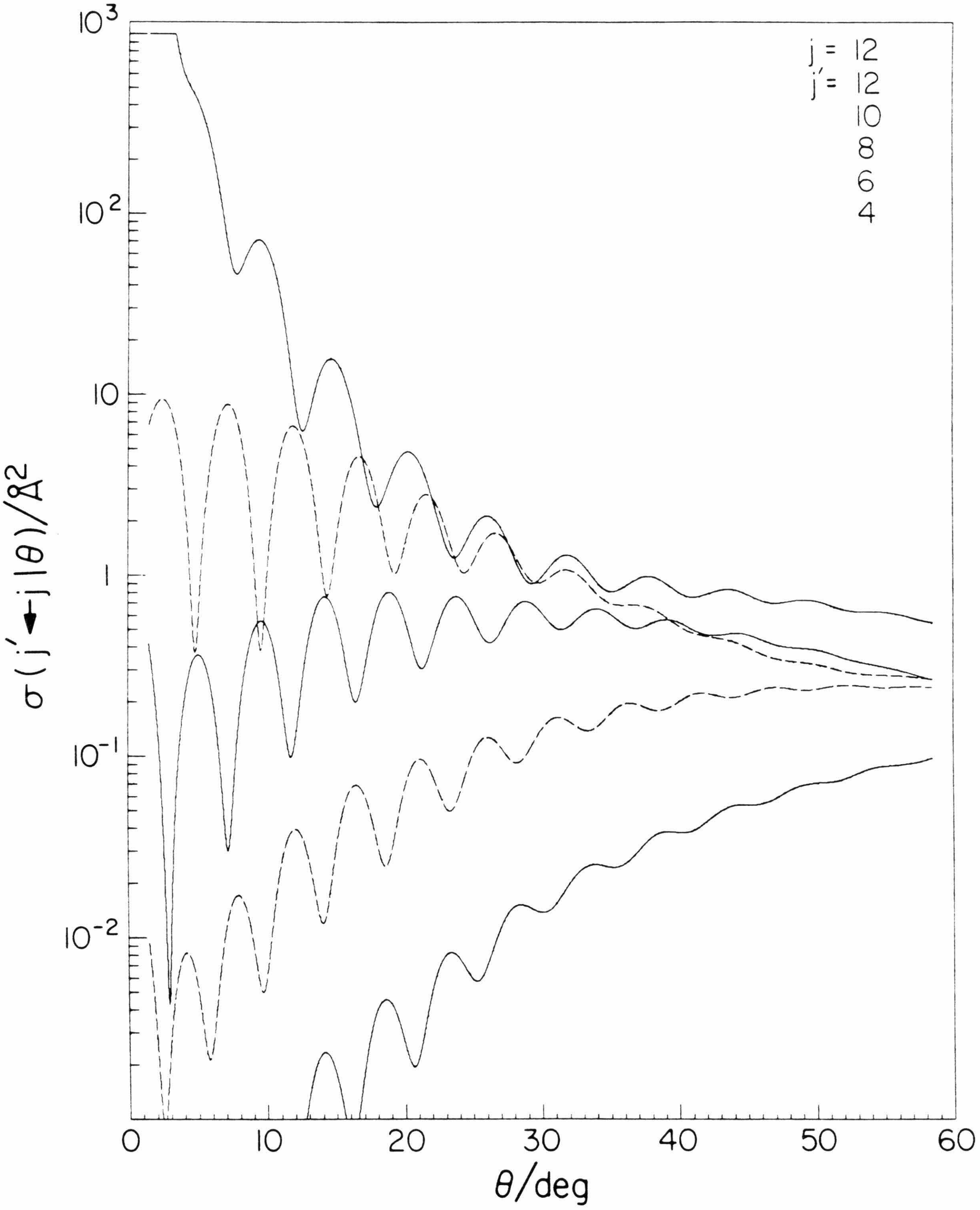
10^3
10^2
10
1
10^{-1}
10^{-2}
$\sigma(j' \leftarrow j\,|\,\theta)/\text{Å}^2$
0
10
20
30
40
50
60
θ/deg
j = 12
j′ = 12
10
8
6
4

Figure 9a.

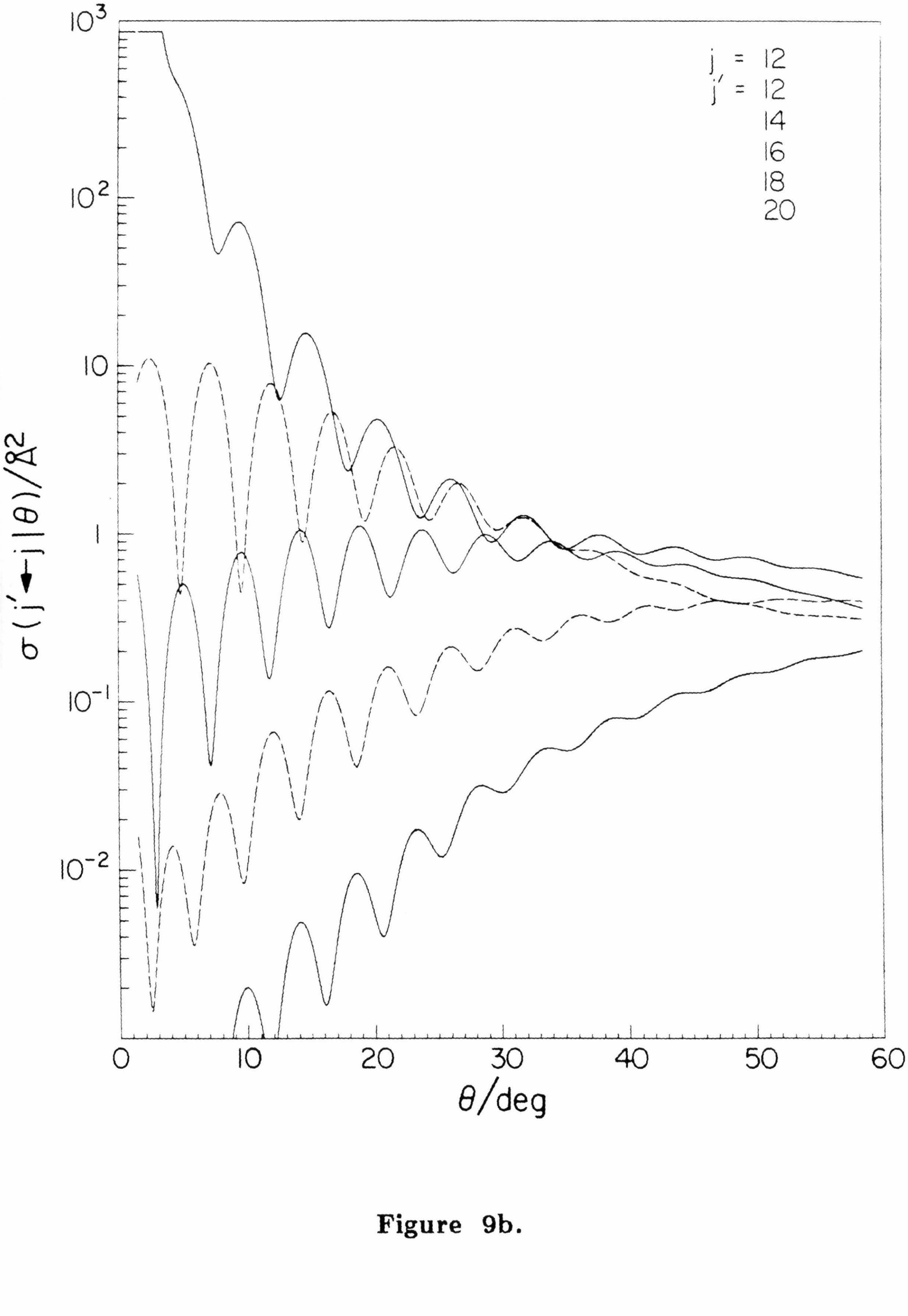
10^3
10^2
10
1
10^{-1}
10^{-2}
$\sigma(j' \leftarrow j|\theta)/\text{Å}^2$
0
10
20
30
40
50
60
θ/deg
j = 12
j′ = 12
14
16
18
20

Figure 9b.

Figure 10. Rotational state-to-state differential cross sections for high and low values of the parameter q (the well minimum position anisotropy). The values are given in Table III; Fig. 10a (low q) is for the QL potential, while 10b (high q) is for the QH. The same transitions are shown as in Figure 9b (rotational energy gain cross sections).

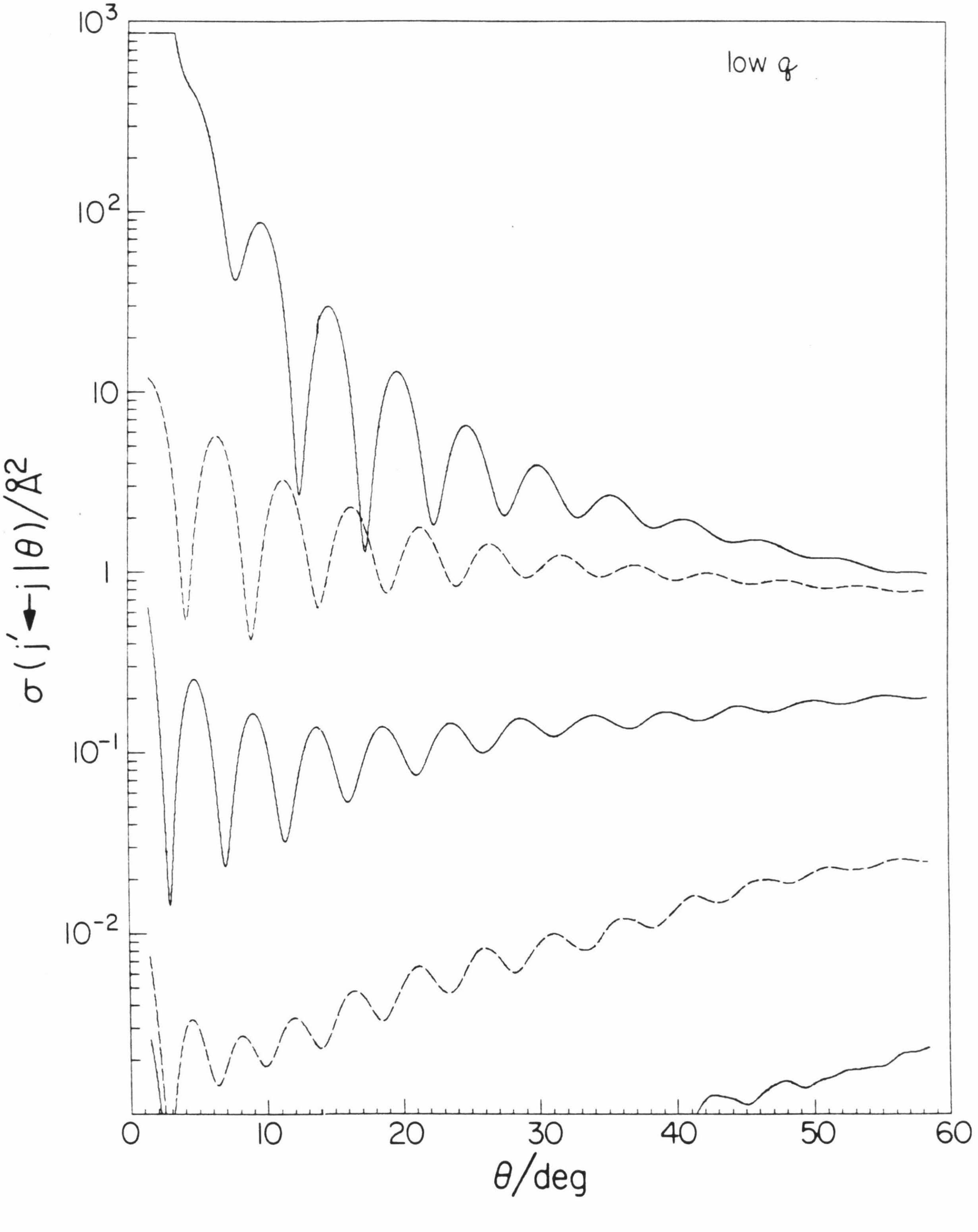

Figure 10a.

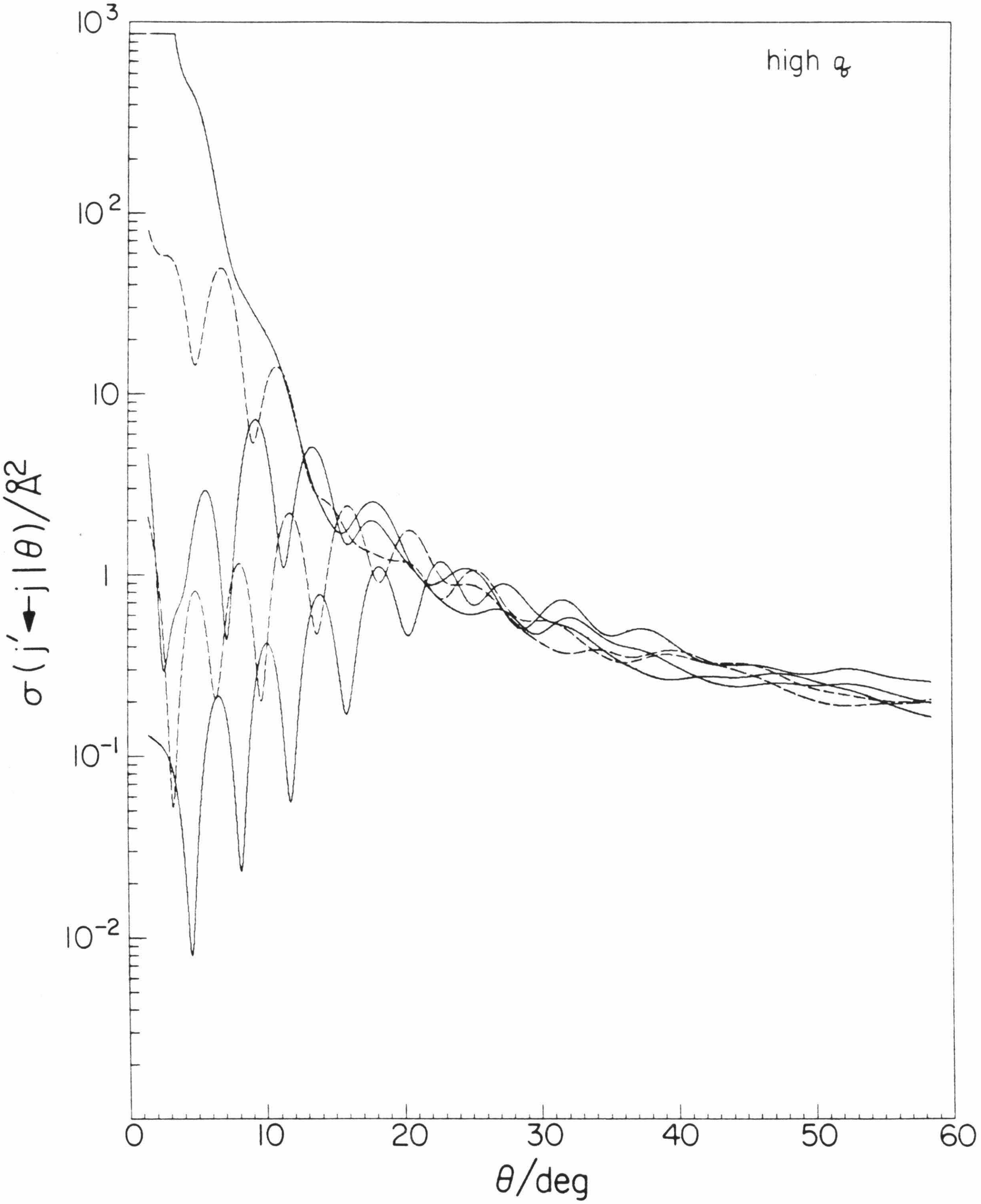
high q
10^3
10^2
10
1
10^{-1}
10^{-2}
0
10
20
30
40
50
60
θ/deg
$\sigma(j' \leftarrow j \mid \theta)/Å^2$

Figure 10b.

Figure 11. Rotational state-to-state differential cross sections for high and low values of the parameter *a* (the well depth anisotropy). The values are given in Table III; Fig. 11a (low *a*) is for the AL potential, while 11b (high *a*) is for the AH. The same transitions are shown as in Figure 9b (rotational energy gain cross sections).

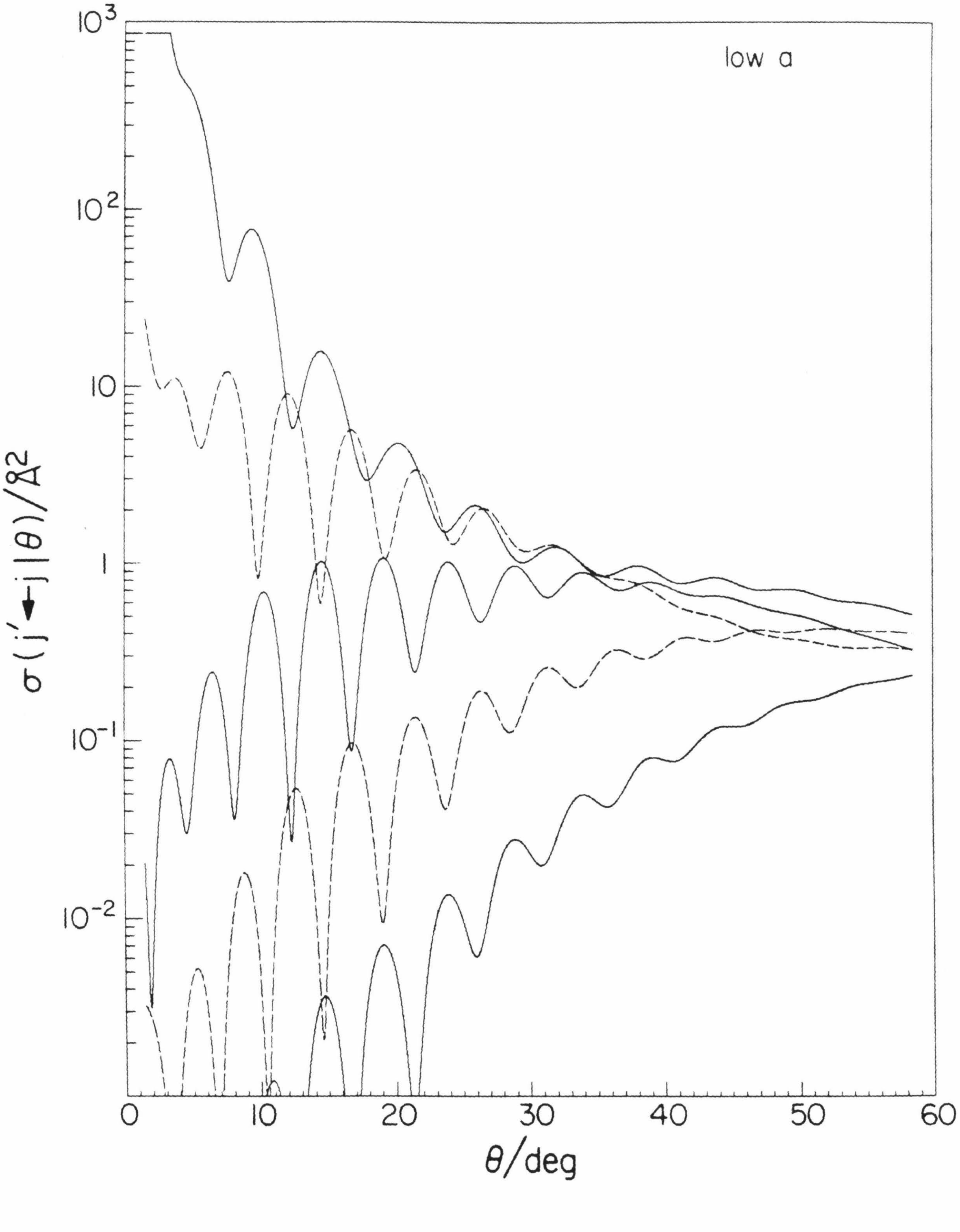
10^3
10^2
10
1
10^{-1}
10^{-2}
low a
$\sigma(j' \leftarrow j \mid \theta)/\text{Å}^2$
0
10
20
30
40
50
60
θ/deg

Figure 11a.

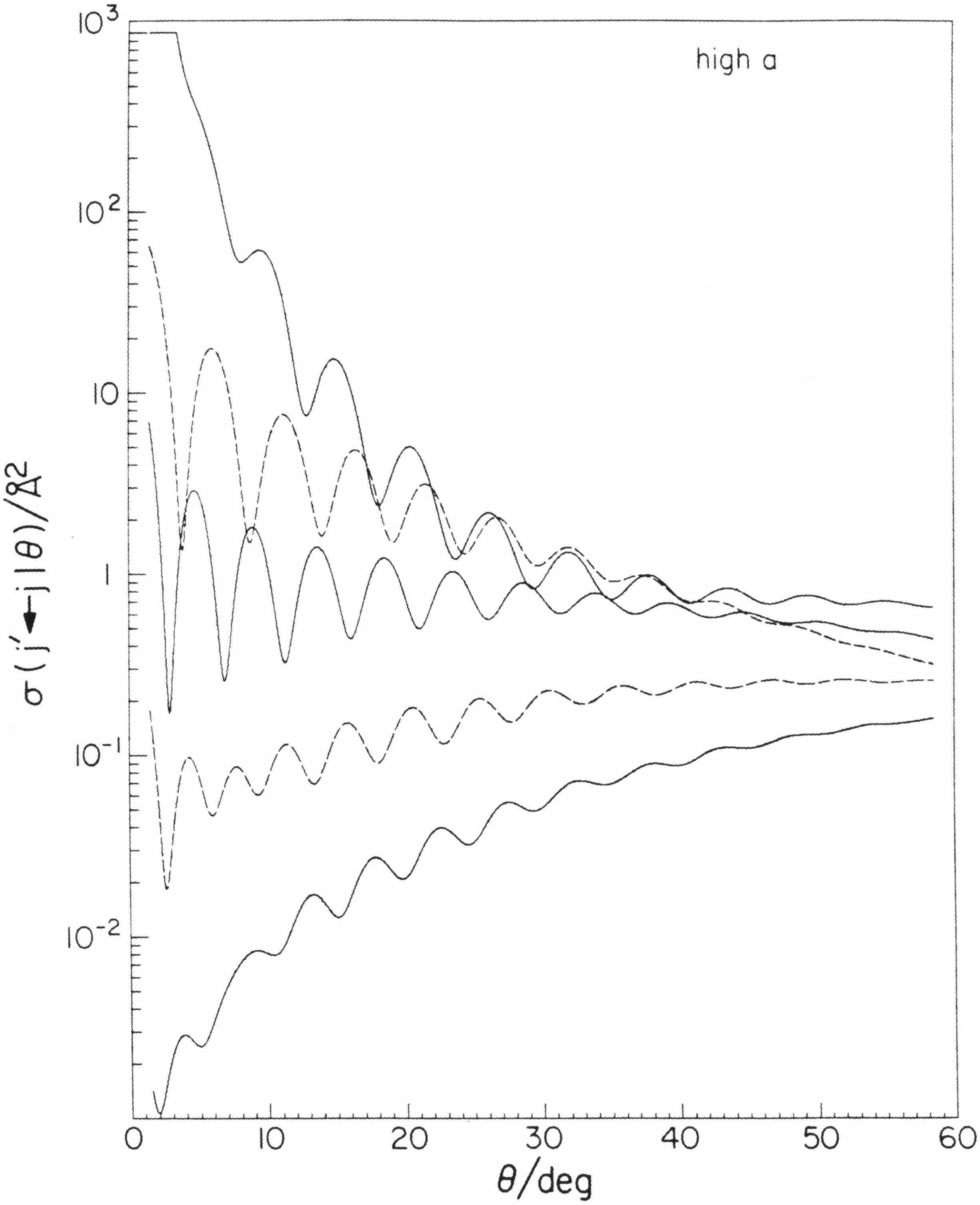
high a
10^3
10^2
10
1
10^{-1}
10^{-2}
$\sigma(j' \leftarrow j\,|\,\theta)/\text{Å}^2$
0
10
20
30
40
50
60
θ/deg

Figure 11b.

Figure 12. Rotational state-to-state differential cross sections for high and low values of the parameter $\epsilon^{(0)}$ (the spherical average of the well depth). The values are given in Table III; Fig. 12a (low $\epsilon^{(0)}$) is for the EL potential, while 12b (high $\epsilon^{(0)}$) is for the EH. The same transitions are shown as in Figure 9b (rotational energy gain cross sections).

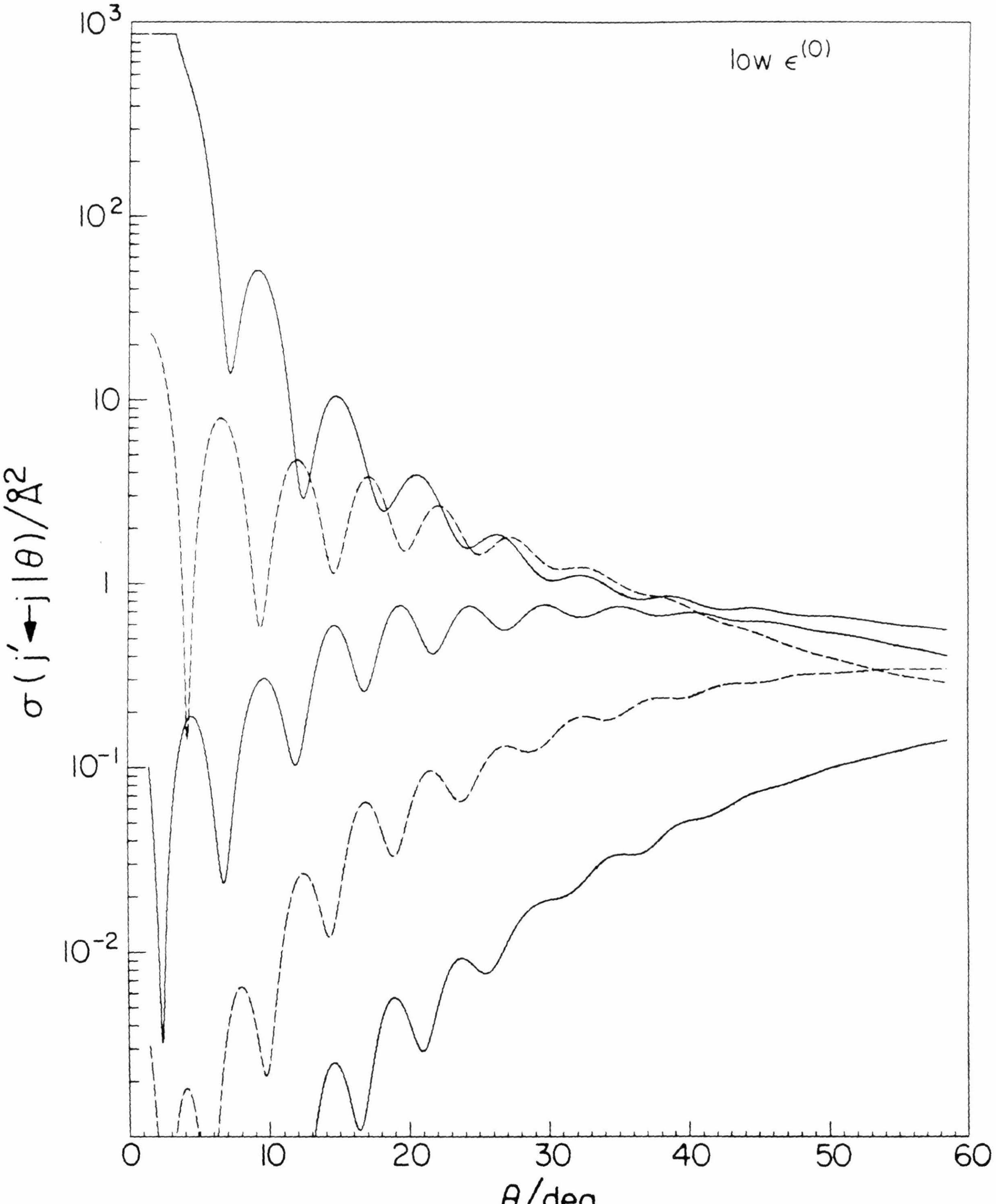
low $\epsilon^{(0)}$
$\sigma(j' \leftarrow j|\theta)/\text{Å}^2$
10^3
10^2
10
1
10^{-1}
10^{-2}
0
10
20
30
40
50
60
θ/deg

Figure 12a.

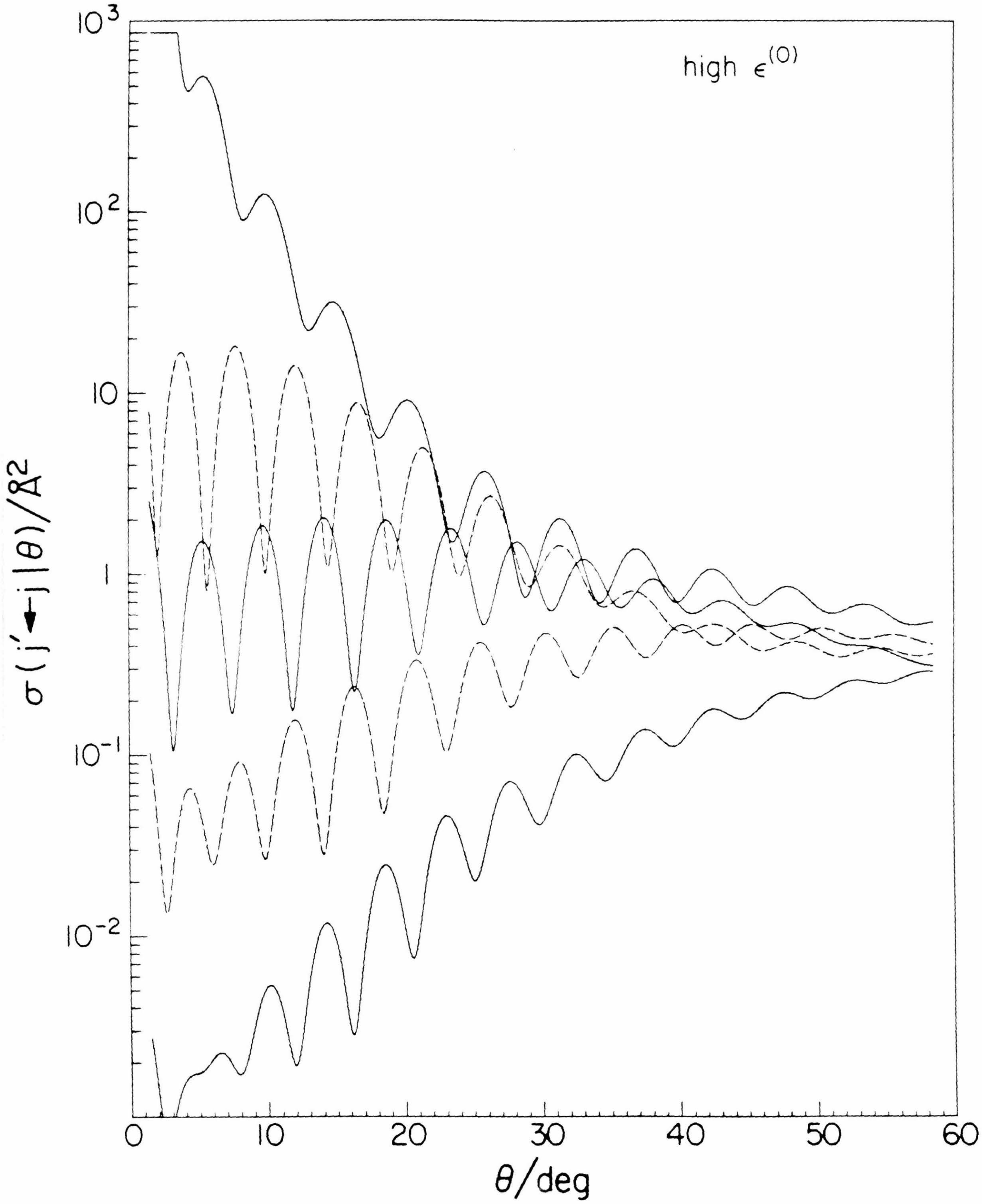
high $\epsilon^{(0)}$
10^3
10^2
10
1
10^{-1}
10^{-2}
$\sigma(j' \leftarrow j|\theta)/\text{Å}^2$
0
10
20
30
40
50
60
θ/deg

Figure 12b.

Figure 13. Rotational state-to-state differential cross sections for potentials with a "reversed" well depth anisotropy, i.e. a is a positive value. Figures 13a and 13b are for the PAL (low positive a) and PAH (high positive a) potential of Table III, respectively. Figures 13c and 13d are for potentials with an intermediate positive value of a $(+0.3)$ with low (PAEL) and high (PAEH) values of the spherical average of the well depth $\epsilon^{(0)}$, respectively. The same transitions are shown as in Figure 9b (rotational energy gain cross sections).

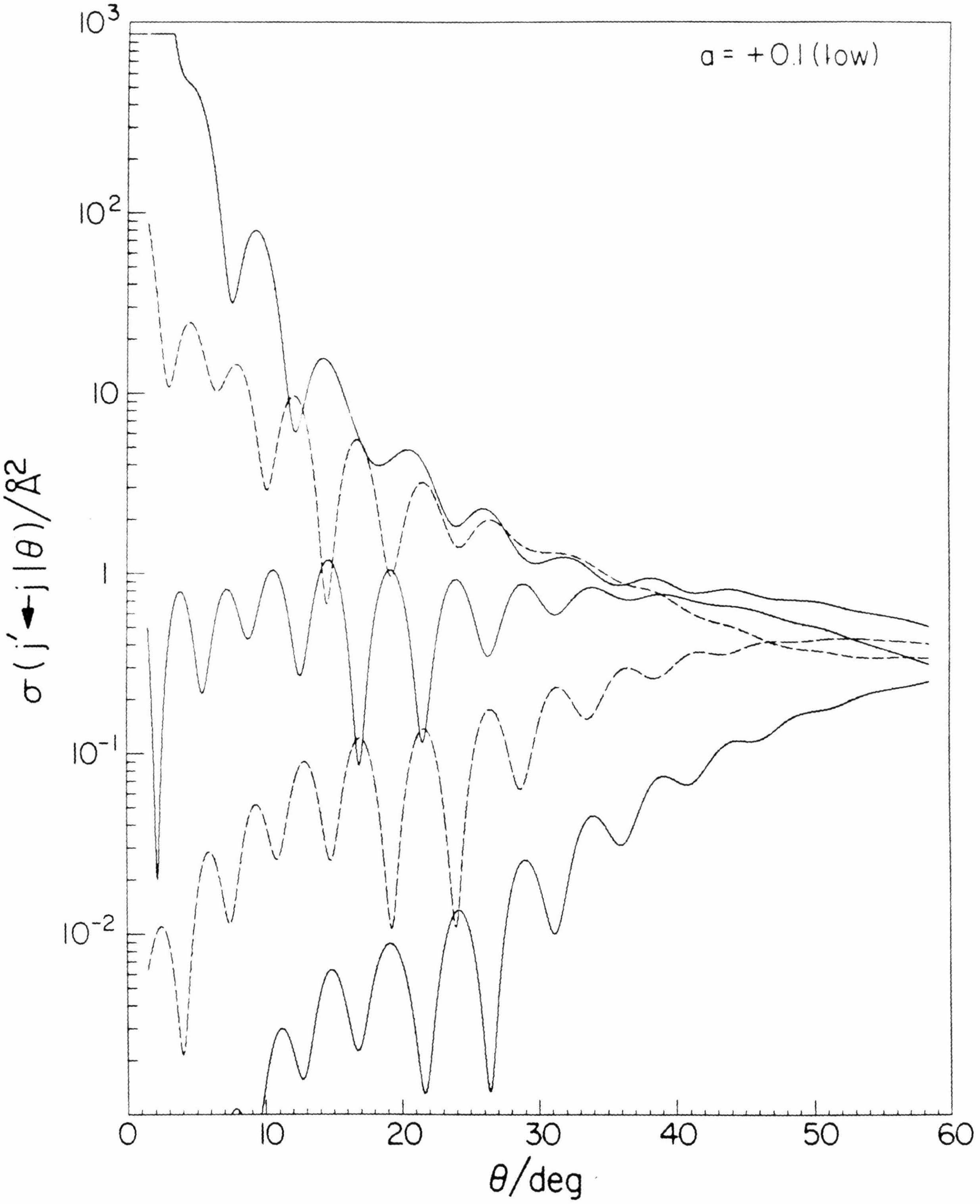
a = +0.1 (low)
$\sigma(j' \leftarrow j\,|\,\theta)/\text{Å}^2$
10^3
10^2
10
1
10^{-1}
10^{-2}
0
10
20
30
40
50
60
θ/deg

Figure 13a.

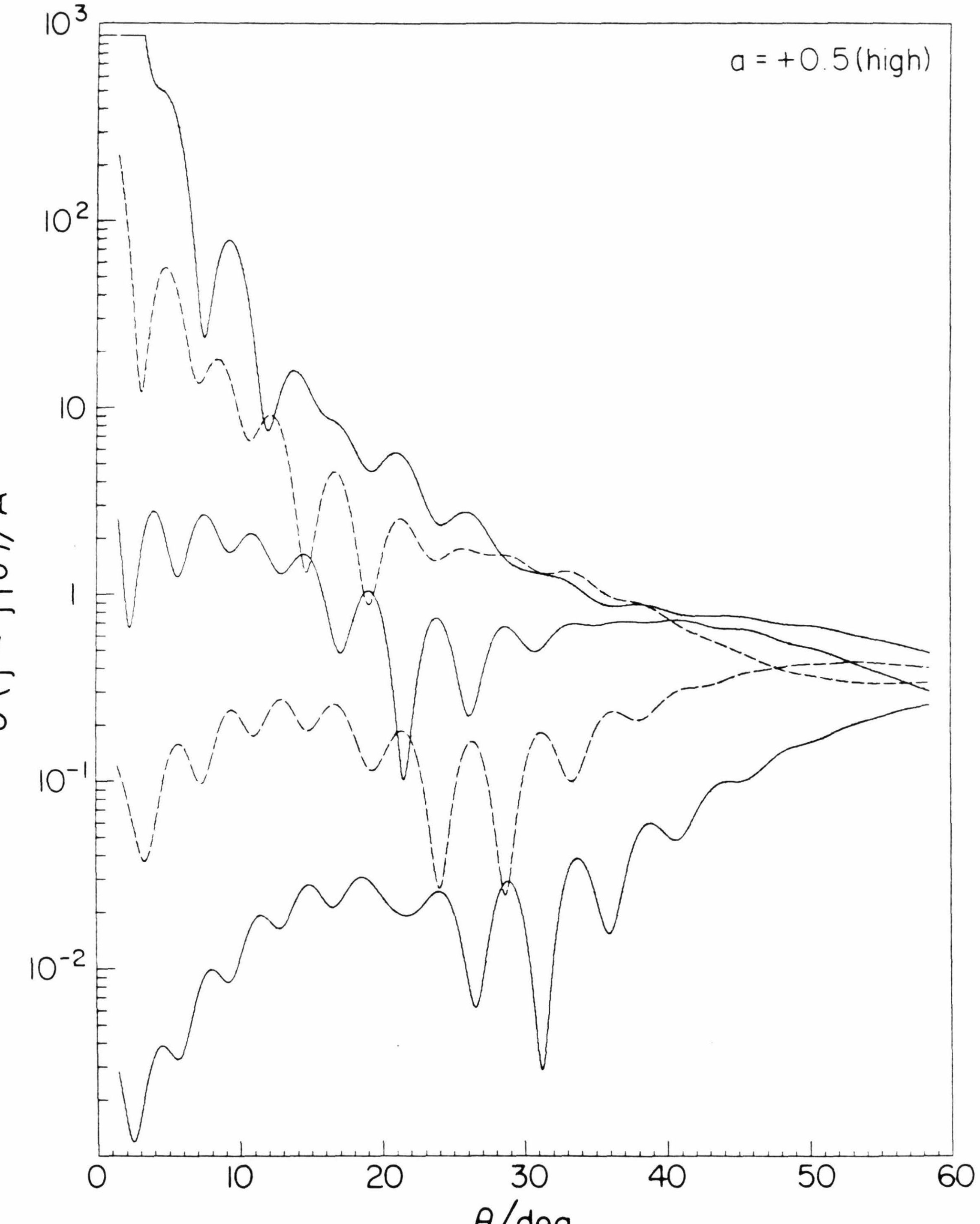
a = +0.5 (high)
10^3
10^2
10
1
10^{-1}
10^{-2}
0
10
20
30
40
50
60
$\sigma(j' \leftarrow j\,|\,\theta)/\text{Å}^2$
θ/deg

Figure 13b.

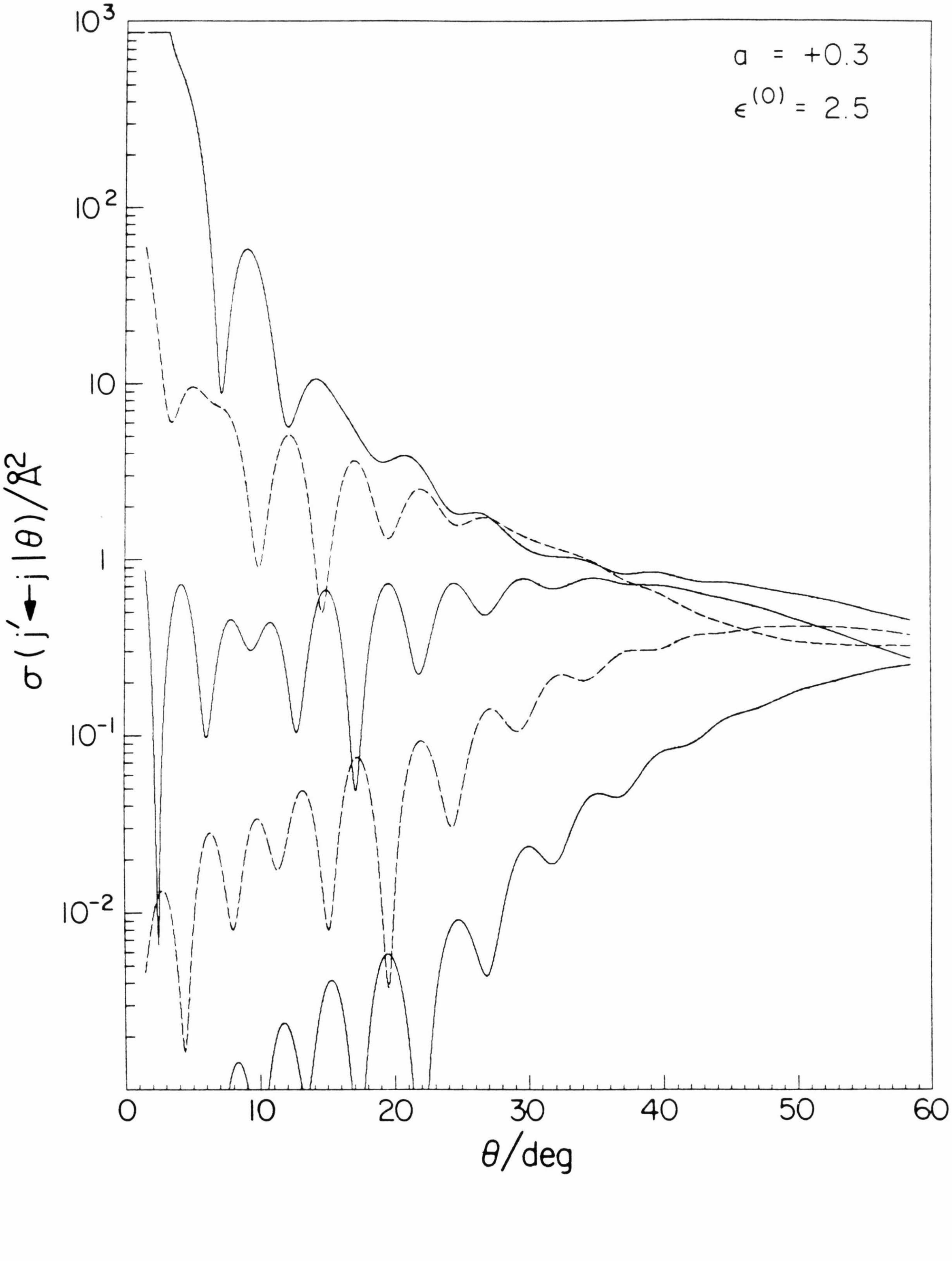
a = +0.3
$\epsilon^{(0)}$ = 2.5
10^3
10^2
10
1
10^{-1}
10^{-2}
$\sigma(j' \leftarrow j \mid \theta)/\text{Å}^2$
0
10
20
30
40
50
60
θ/deg

Figure 13c.

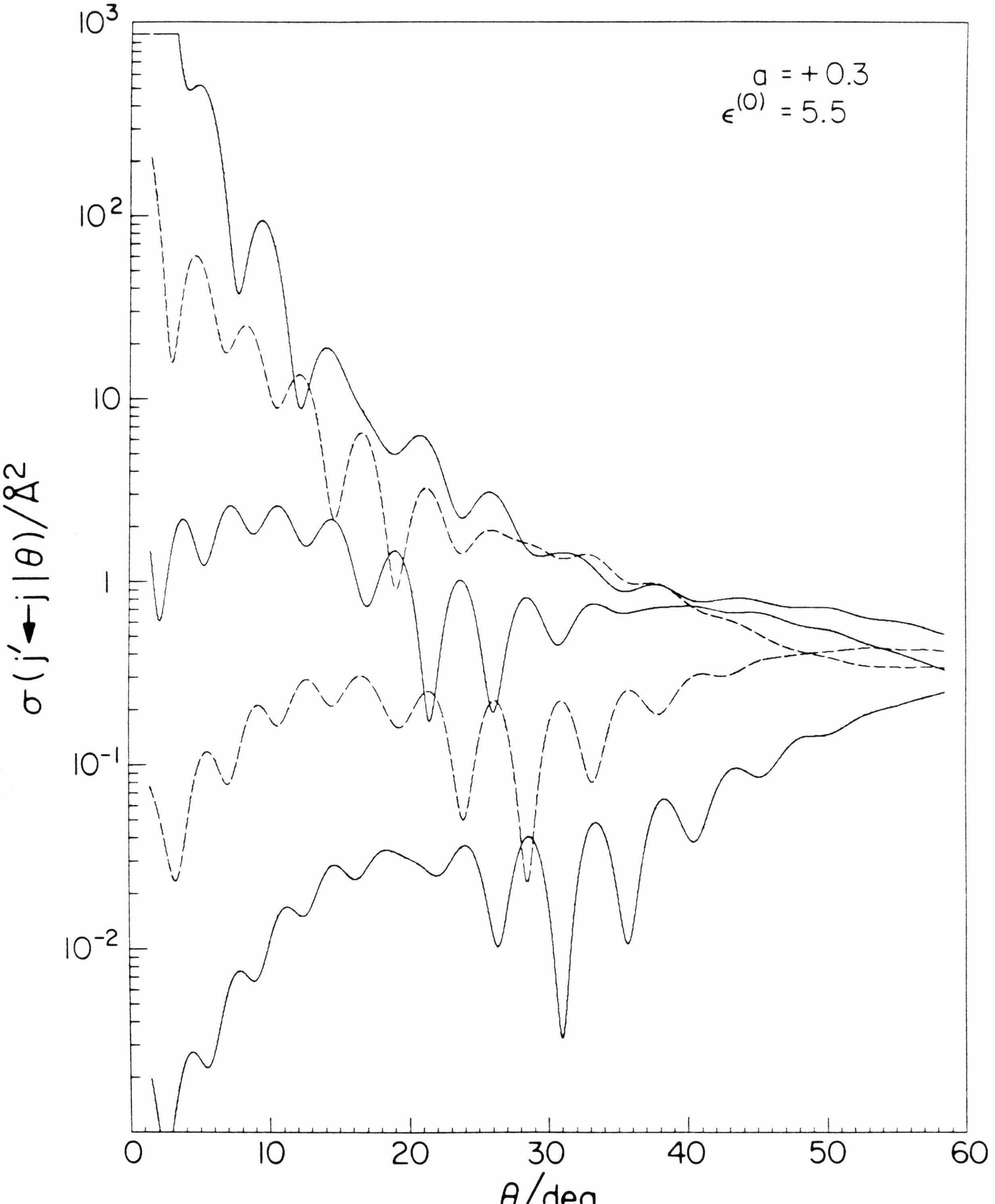
a = +0.3
$\epsilon^{(0)}$ = 5.5
10^3
10^2
10
1
10^{-1}
10^{-2}
σ(j′←j|θ)/Å²
0
10
20
30
40
50
60
θ/deg

Figure 13d.

Figure 14. Rotational state-to-state differential cross sections for high and low values of the well width parameter β. The values are given in Table III; Fig. 14a (low β) is for the BWL potential, Fig. 14b (high β) is for the BWH. The same transitions are shown as in Figure 9b (rotational energy gain cross sections).

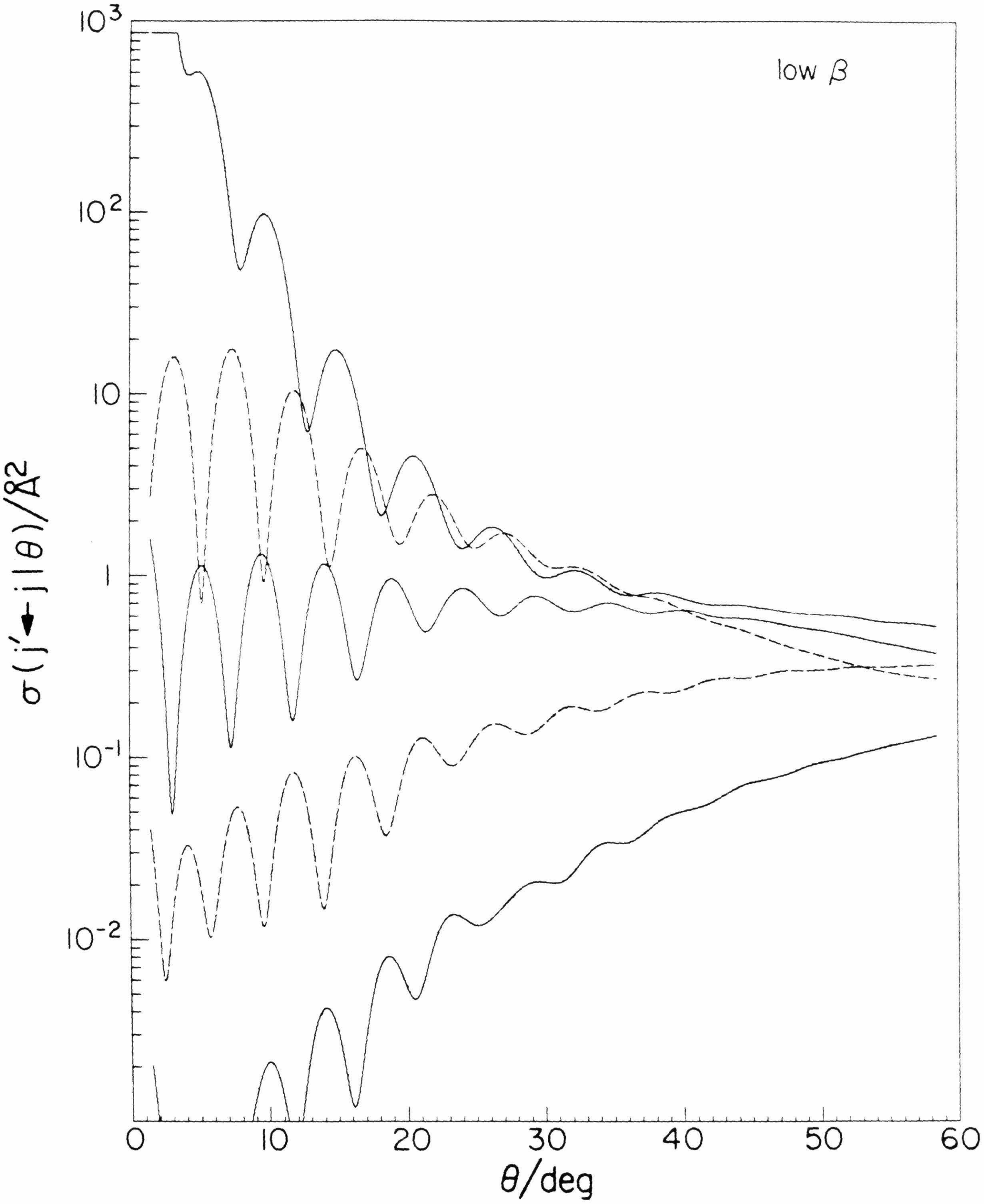
low β
$\sigma(j' \leftarrow j\,|\,\theta)/\text{Å}^2$
10^3
10^2
10
1
10^{-1}
10^{-2}
0
10
20
30
40
50
60
θ/deg

Figure 14a.

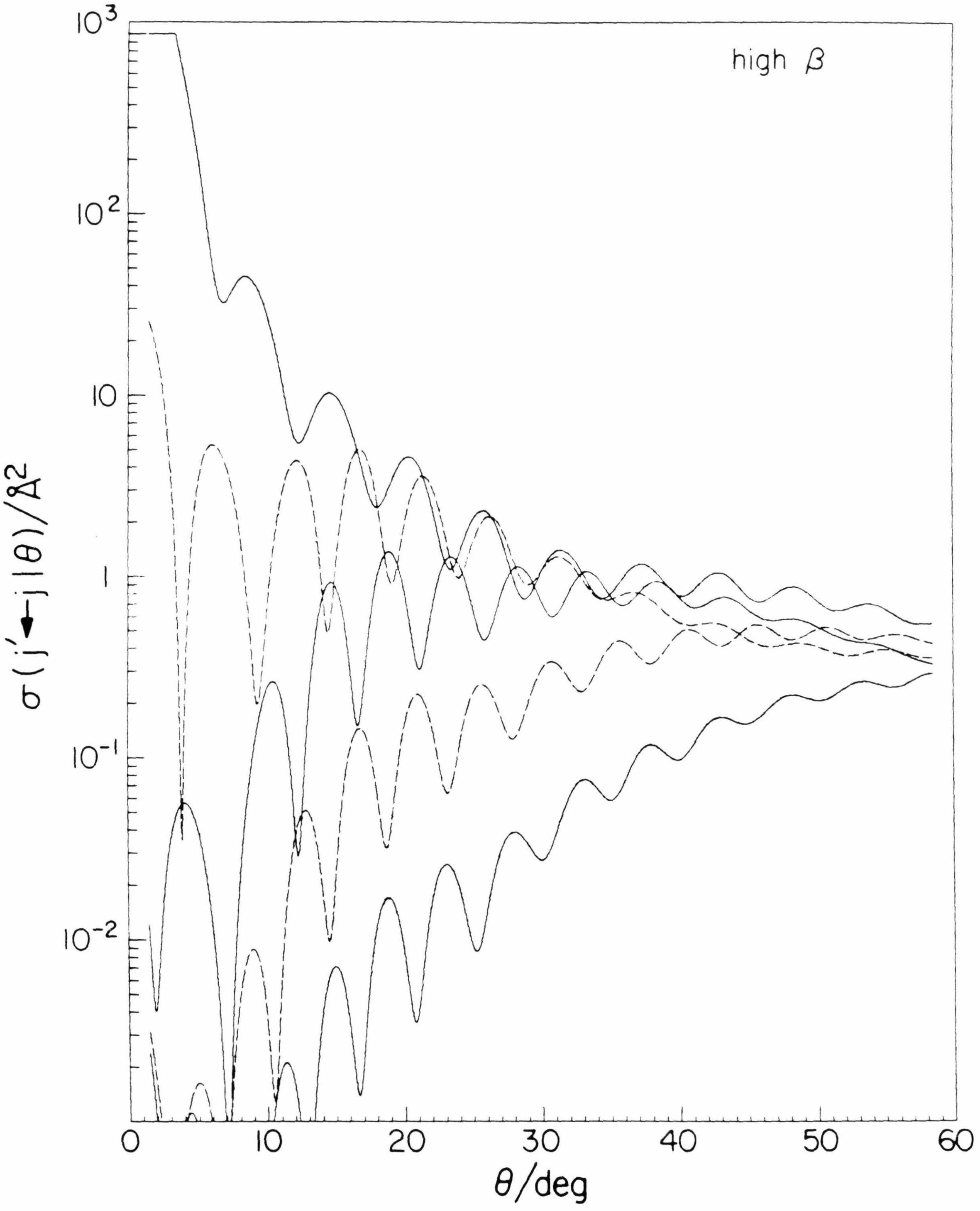
high β
$\sigma(j' \leftarrow j|\theta)/\text{Å}^2$
10^3
10^2
10
1
10^{-1}
10^{-2}
0
10
20
30
40
50
60
θ/deg

Figure 14b.

Figure 15. Rotational state-to-state $j = 12$ to $j = 14$ DCS sensitivity functions for the M (Table I) anisotropic potential for the parameters $r_m^{(0)}$, $\epsilon^{(0)}$, q, a, β and β'. The solid curves are for positive values of the sensitivities, while the dashed curves are for negative values of the sensitivities.

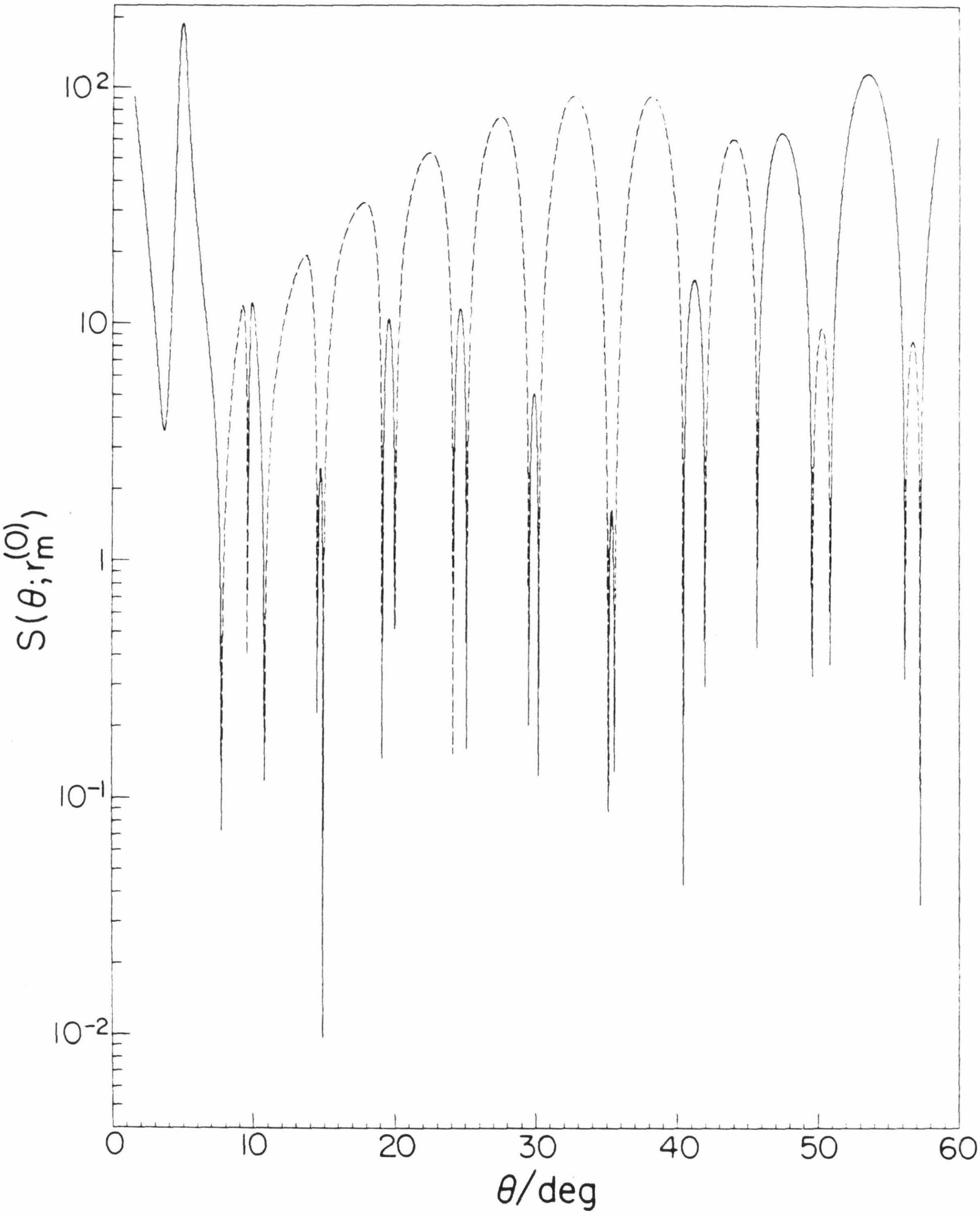

Figure 15a.

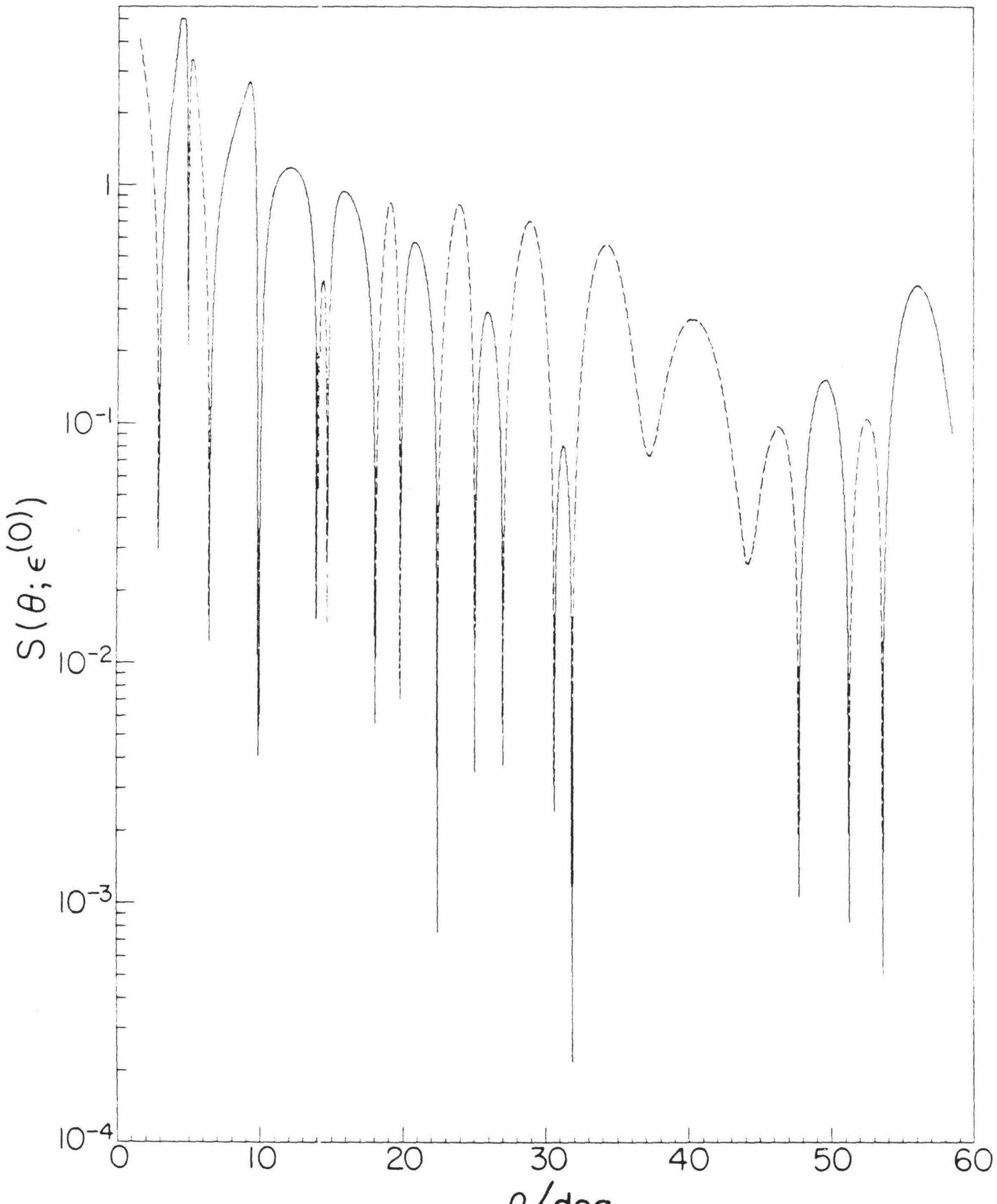

Figure 15b.

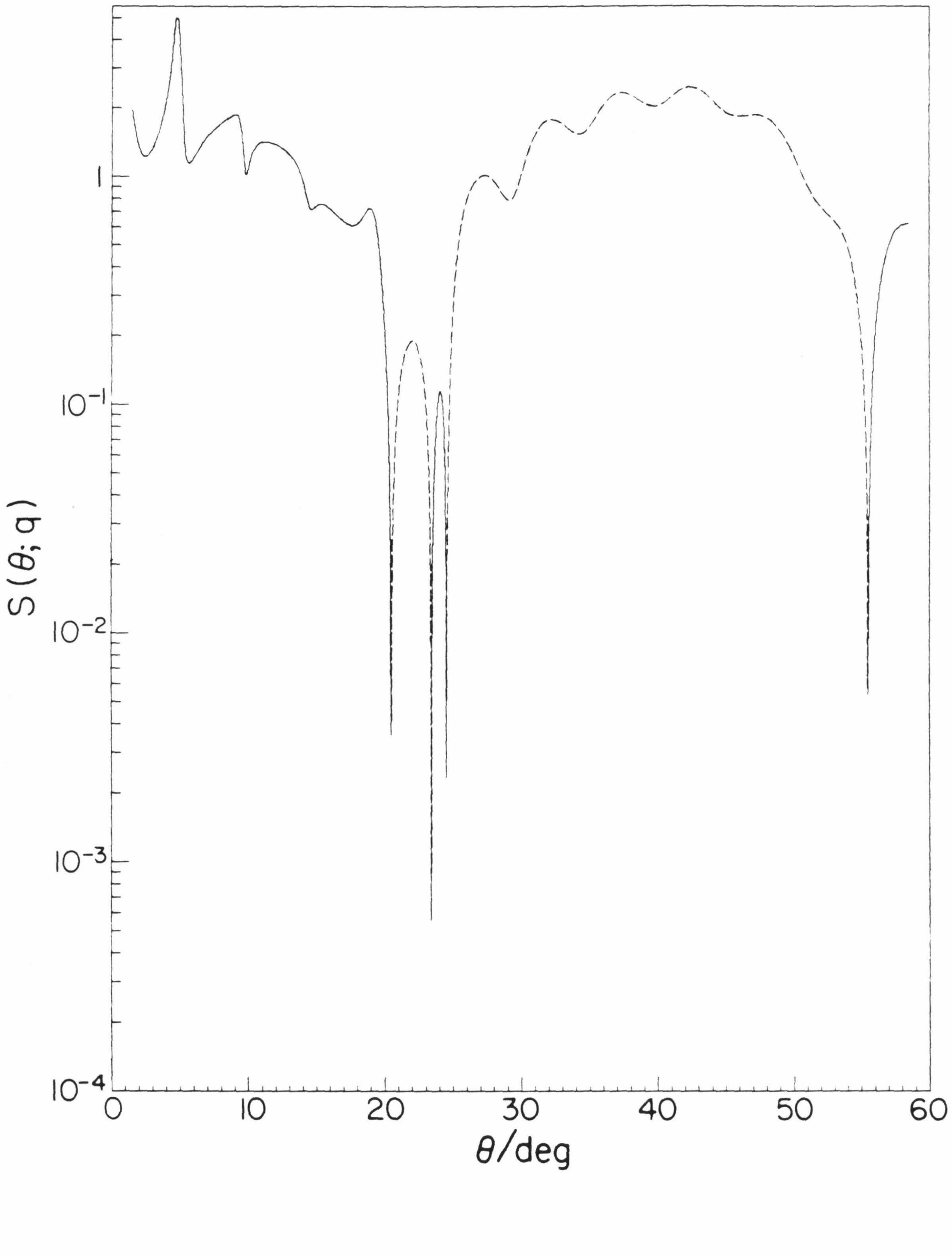

Figure 15c.

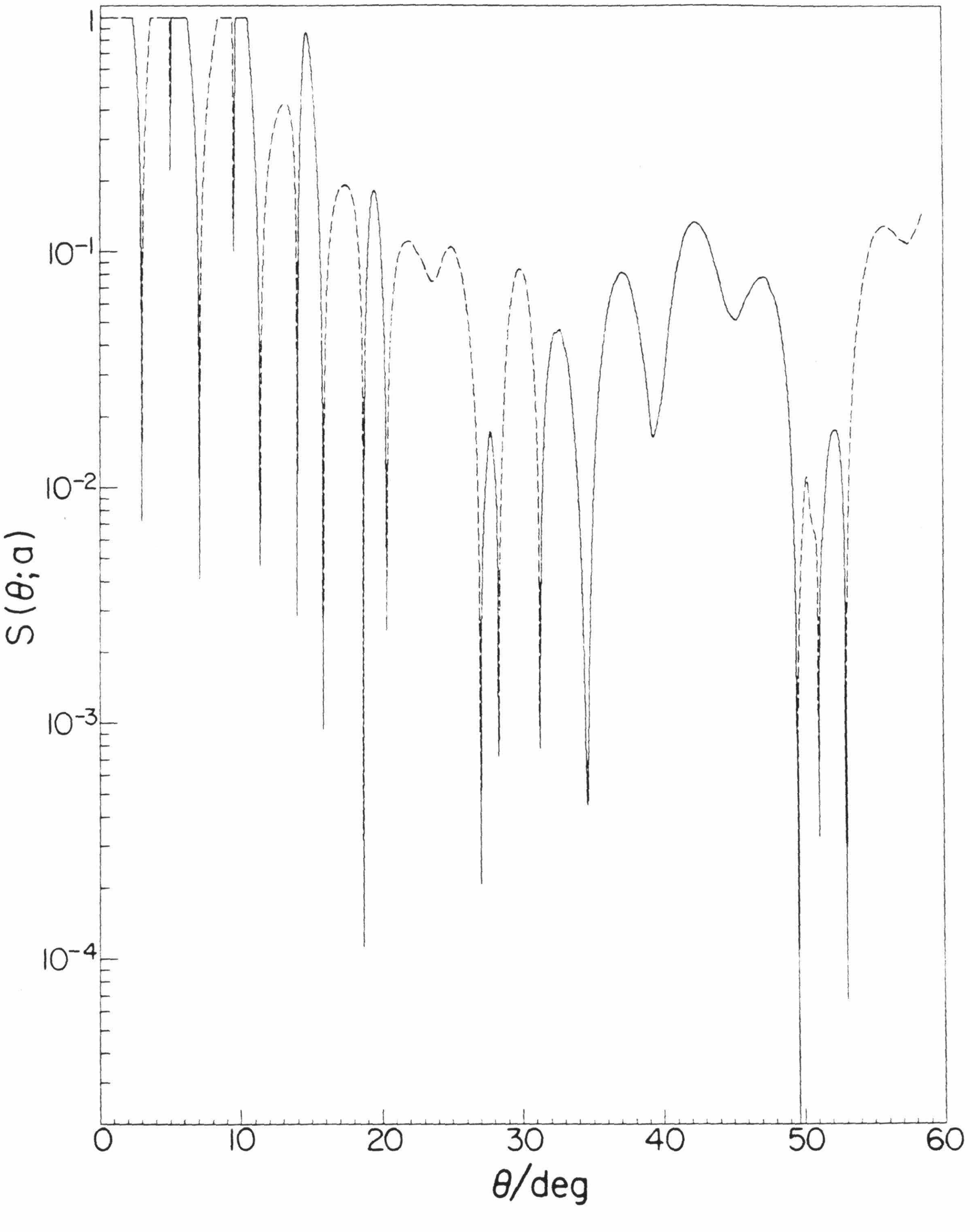

Figure 15d.

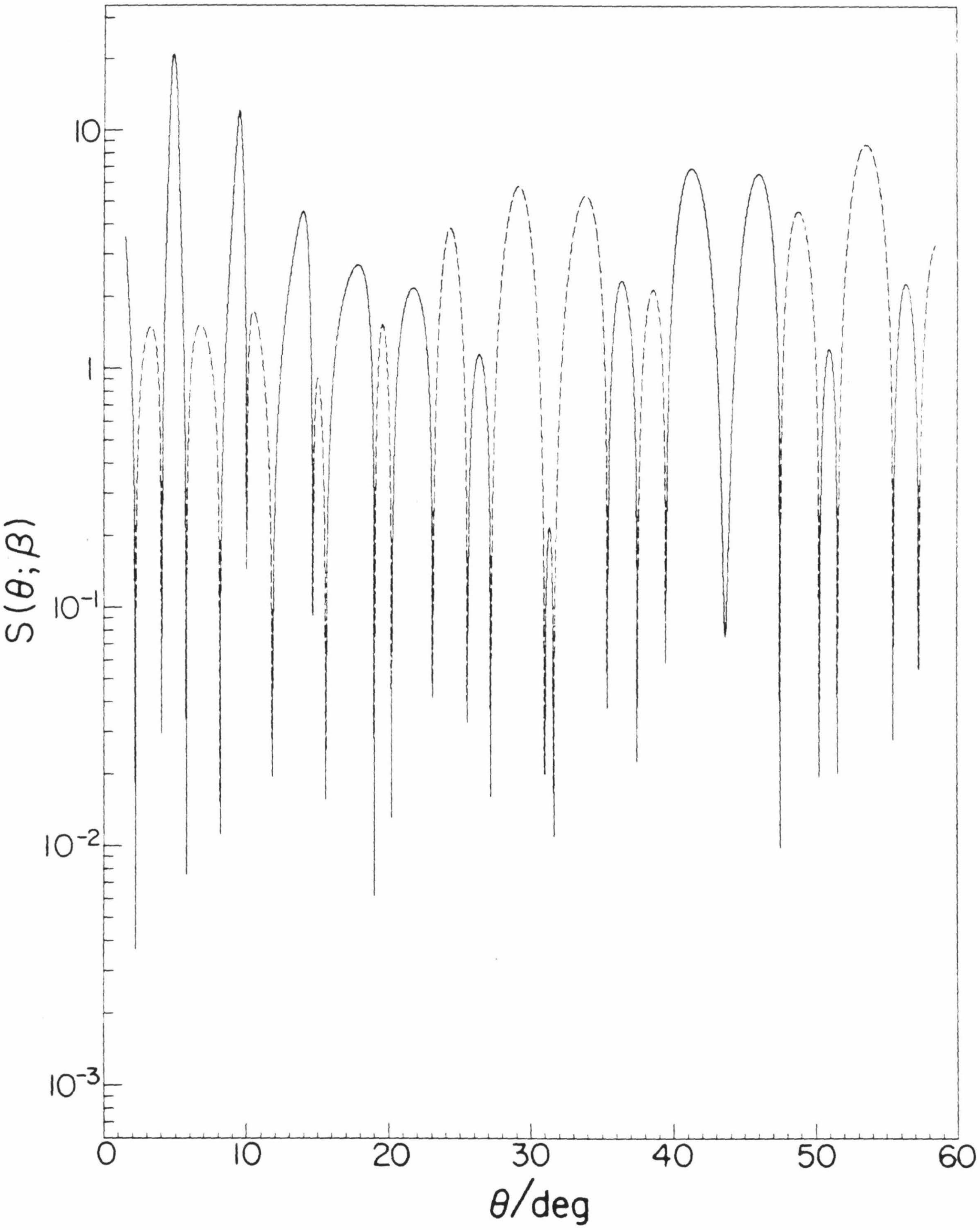

Figure 15e.

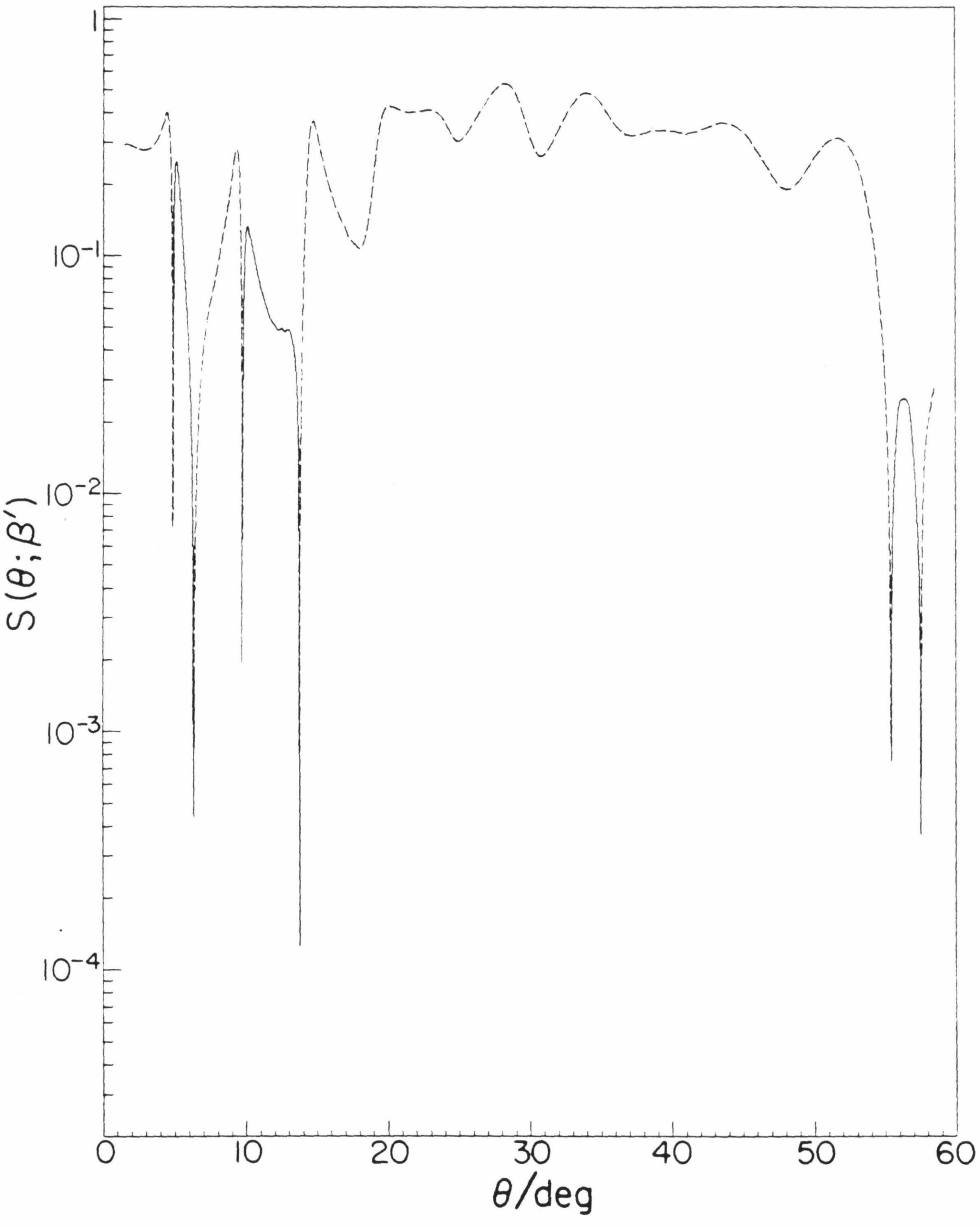

Figure 15f.

CHAPTER 4

SIMULATION OF INELASTIC SCATTERING

1.INTRODUCTION

Rotationally inelastic differential cross-sections (DCS) are the result of anisotropy in the interaction potential between an atom and a linear molecule. They have been measured together with the corresponding elastic DCS as a total DCS with no discrimination between elastic and inelastic processes.[1,3] Only an anisoptropic potential could accurately account for all the features of the total DCS for the scattering of He by CO_2, and other triatomic molecules.[1,3,10,11] However, the total DCS for the scattering of He by N_2 and O_2, was effectively predicted with an isotropic potential.[6] This does not indicate that the scattering process is insensitive to the anisotropy, only that the anisotropy is small and that it is possible to have a spherical potential that can account for the total DCS. The measurement of rotationally inelastic DCS for these systems confirms strongly that the potentials are anisotropic.[4,5] Although an aniostropic potential for He + CO_2 was extracted from total-DCS data, many of its features cannot be precisely determined from such a limited data set. A total-DCS curve depends on only one variable, the scattering angle; yet it is used to obtain the potential which is a function of two variables, the distance between the helium atom and the molecular center-of-mass and the angular orientation of the atom with respect to the molecular axis. The ability to measure rotational inelasticity will provide an additional dimension of information, which in turn will permit a more precise extraction of an anisotropic interaction potential.

Agrawal and Raff[8] have shown that total DCS's are much more sensitive to the topography of the potential energy surface than are the rotational state-to-state integral cross-sections. Eno and Rabitz[7] have computed sensitivity coefficients for a test anisotropic potential and have shown that the inelastic DCS's are highly sensitive to potential anisotropy. We have reached similar conclusions[2] for the empirical He + CO_2 potential, in addition to showing that inelastic-DCS are very sensitive to other features of the potential.

In order to obtain potentials from scattering data it is necessary to be able to simulate the data from a proposed potential for a fixed set of experimental conditions and compare the simulated to experimental data. The proposed potential is modified until the best agreement is attained between the simulation and experiment. In this chapter we present a technique for simulating this data by calculating the velocity distribution of the scattered particles for a given scattering angle. The inelasticity will be manifest as a loss or gain of velocity by the scattered particle over that for elastic scattering.

Section 2 summarizes the infinite order sudden approximation for calculating the rotational state-to-state differential cross-sections. This approximation is valid for the scattering of He from CO_2 and similar targets. Since these cross-sections are calculated in the center-of-mass frame, while the scattering is observed in the laboratory frame it is necessary to be able to transform the former to the latter. In Section 3 we derive a general set of coordinate transformations between the laboratory and center-of-mass reference frames. These transformations are completely general and are applicable to reactive scattering; they have been independently derived but are identical to those derived previously.[20] We also introduce a new set of coordinate transformations which we call "intermediate transformation relations." These relations are used in an apparatus averaging scheme which we call "source averaging" and describe in Section 4. This averaging is over a grid of all possible velocities of the center-of-mass frame with respect to the laboratory frame ($\vec{v}_g$). The grid is obtained from the velocity and angular spread distributions of the interacting beams. The source of scattered particles is the velocity space origin of the center-of-mass frame (G), hence the name of this averaging scheme. In Section 5 we present examples at serveral scattering angles for our empirical (total DCS) He + CO_2 potential.

2. THEORY

We have used the infinite order sudden approximation (IOSA) to calculate the total (elastic and inelastic) and rotational state-to-state differential scattering cross sections (DCS). Since this formalism has been reviewed and outlined by many authors we will only present the salient points of the IOSA. These cross sections were calculated on a highly flexibile anisotropic potential which we will present in section 2.2.

2. 1. CROSS SECTIONS

In the systems to be considered, the target molecules are essentially all in their ground vibrational states and the collision energies are well below the threshhold for producing vibrational excitations.[16] Therefore, it is reasonable to treat the target molecule as a rigid rotor of length R (the distance between the end atoms) having a moment of inertia I. Let $\underset{\sim}{r}$ be the position vector of the incident atom with respect to the center-of-mass of the molecule and γ be the angle between $\underset{\sim}{r}$ and the oriented molecular axis $\underset{\sim}{R}$. The nuclear motion Hamiltonian for this system is therefore

$$\hat{H} = -\frac{\hbar^2}{2\mu r}\frac{\partial^2}{\partial r^2}r + \frac{\hat{L}^2}{2\mu r^2} + \frac{\hat{J}^2}{2I} + V(r,\gamma) \tag{2.1}$$

where μ is the atom-molecule reduced mass, and $\hat{L}$ and $\hat{J}$ are the orbital angular momentum and molecular angular momentum operators, respectively.

The Schrödinger equation can be solved for the above Hamiltonian by expanding the wave function in eigenfunctions of the total angular momentum operator $\hat{\mathbf{J}} \equiv \hat{J} + \hat{L}$ and its projection $\hat{\mathbf{J}}_z$ about a space fixed axis z. This results in a set of coupled radial differential equations; the coupling being due to the matrix elements of $V(r, \gamma)$ obtained using these eigenfunctions. Under the conditions of our calculation it is valid to decouple these equations, by imposing the centrifugal sudden[12] (CS) and energy sudden[13] (ES) approximations, collectively known as the infinite order sudden approximation (IOSA).[10] The CS approximation is introduced by replacing the orbital angular momentum operator with its eigenvalue form

$$\hat{L}^2 \simeq \hbar^2 \bar{l}(\bar{l} + 1) \tag{2.2}$$

while to implement the ES approximation the molecular angular momentum operator is replaced with its eigenvalue form

$$\hat{J}^2 \simeq \hbar^2 \bar{\jmath}(\bar{\jmath} + 1) \tag{2.3}$$

where $\bar{l}$ and $\bar{\jmath}$ are appropriately chosen effective quantum numbers.

The resulting set of decoupled differential equations are

$$\left[\frac{d^2}{dr^2} + k_{\bar{\jmath}}{}^2 - \frac{\bar{l}(\bar{l}+1)}{r^2} - \frac{2\mu}{\hbar^2} V(r, \gamma)\right] \phi_{\bar{l}}(r; \gamma) = 0 \tag{2.4}$$

where the wave vector is

$$k_{\bar{j}}^{\,2} = \frac{2\mu}{\hbar^2}\left[E - \frac{\hbar^2 \bar{j}(\bar{j}+1)}{2I}\right] \tag{2.5}$$

E being the total energy of the system and $\phi_{\bar{l}}$ is an effective scattering wave function for a angle of incidence γ. These equations can be solved for a given $\bar{l}$ and γ in a manner analogous to a spherical problem, by requiring that the wave function must vanish at the origin, and at large r behave as

$$\phi_{\bar{l}} \quad \xrightarrow[r\to\infty]{} \quad k_{\bar{j}}^{\,-1/2}\left\{\mathrm{e}^{-i(k_{\bar{j}}r-\bar{l}\pi/2)} - \mathrm{e}^{i[k_{\bar{j}}r-\bar{l}\pi/2+2i\eta_{\bar{l}}(\gamma)]}\right\} \tag{2.6}$$

where $\eta_{\bar{l}}(\gamma)$ is the phase shift for a given fixed atom-molecule orientation, which is obtained in a manner identical to that for a spherical scattering problem[14], and the resulting scattering amplitude is given by

$$f^{k_{\bar{j}}}(\gamma \mid \theta) = \frac{i}{2k_{\bar{j}}}\sum_{l}(2l+1)\left\{1 - \mathrm{e}^{2i\eta_l(\gamma)}\right\}P_l(\cos\theta) \tag{2.7}$$

It can be shown that the rotational state-to-state differential cross-section is given in this approximation by[9]

$$\sigma(j' \leftarrow j \mid \theta) = \frac{k_{\bar{j}}^2}{(2j+1)k_j^{\,2}}\sum_{m_j} \left| < j'm_j|f^{k_{\bar{j}}}(\gamma \mid \theta)|jm_j >_{\mathrm{BF}} \right|^2 \tag{2.8}$$

where the matrix elements of $f(\gamma \mid \theta)$ are evaluated in the spherical harmonics of the body–fixed coordinates - BF.[9] It should be noted that this result is independent of the choice of $\bar{l}$.

Equation (2. 8) can be simplified for calculational purposes by expanding $f^{k_{\bar{\jmath}}}(\gamma \mid \theta)$ in Legendre polynomials

$$f^{k_{\bar{\jmath}}}(\gamma \mid \theta) = \sum_{i} F_i^{k_{\bar{\jmath}}}(\theta) P_l(\cos\gamma) \tag{2.9}$$

where

$$F_i^{k_{\bar{\jmath}}}(\theta) = (i + 1/2) \int_0^{\pi} P_i(\cos\gamma) f^{k_{\bar{\jmath}}}(\gamma \mid \theta) \quad \sin\gamma \, d\gamma \tag{2.10}$$

This then leads to the expression for the differential cross-section[9]

$$\sigma(j' \leftarrow j \mid \theta) = \left(\frac{k_j}{k_{\bar{\jmath}}}\right)^2 \sum_{j''} \frac{1}{2j'' + 1} C^2(j, j'', j'; 0, 0, 0) \mid F_{j''}^{k_{\bar{\jmath}}}(\theta) \mid^2 \tag{2.11}$$

The total differential cross-section is the sum of all state-to-state cross-sections $\sigma(j' \leftarrow j \mid \theta)$ from an initial state j over all energetically allowed final states j'. The cross-section in equation (2.11) can be summed and simplified if the effective IOSA rotational quantum number $\bar{\jmath}$ is set equal to j (the initial rotational state). By way of the completeness of the spherical harmonics and the addition theorem for the spherical harmonics it can be shown that the total differential cross section is

$$\sigma(\theta) = 1/2 \int_0^{\pi} |f^{k_j}(\gamma \mid \theta)|^2 \sin\gamma \, d\gamma \tag{2.12}$$

This expression, for a given initial relative translational energy, is independent of the initial rotational state j, and hence represents the total differential cross-section for any initial state.

It has been demonstrated that the IOSA is valid in cases where the relative collision energy is much larger than the spacing between rotational levels and larger than the attractive part of the potential. Since we will consider collision energies of 30 to 90 meV we are well within the range validity for the He + CO_2 interaction where the typical CO_2 rotational spacings are less than 6 meV, and where the He + CO_2 well depth is less than 7 meV.

2. 2. POTENTIALS

In order to obtain realistic results we will use a realistic potential for our cross-sections. Our potential is based on one obtained from experimental total differential cross-section crossed-beam data. We represent the anisotropy by giving an angular γ dependence to the parameters of an otherwise spherical potential,

$$V(r,\gamma) = V\left[r, \epsilon(\gamma), r_m(\gamma), \beta(\gamma)\right] \tag{2.13}$$

where ϵ is the well depth, r_m is the well minimum position, and β is a shape parameter which depends on the parameterization of V. Some parameterizations may have more than one shape parameter, all of which may have angular dependence. In this paper we will expand the well minimum position and the well depth to second order in Legendre polynomials

$$r_m(\gamma) = r_m^{(0)} + r_m^{(2)} P_2(\cos\gamma) \tag{2.14a}$$

$$= r_m^{(0)}[1 + qP_2(\cos\gamma)] \tag{2.14b}$$

and

$$\epsilon(\gamma) = \epsilon^{(0)} + \epsilon^{(2)} P_2(\cos\gamma) \tag{2.15a}$$

$$= \epsilon^{(0)}[1 + aP_2(\cos\gamma)] \tag{2.15b}$$

where we have defined the anisotropies of the well minimum position and depth as $q \equiv r_m^{(2)}/r_m^{(0)}$ and $a \equiv \epsilon^{(2)}/\epsilon^{(0)}$ respectively. Due to the symmetry of the CO_2 molecule the first order Legendre term is zero.

The shape of $V(r, r_m, \epsilon, \beta)$ is charterized by the highly flexible Morse-Morse-spline-van der Waals (MMSV) potential which may be written as

$$V(r) = \frac{\epsilon}{\omega}\left\{\mathrm{e}^{2(\beta' - r\beta\omega/r_m)} - 2\mathrm{e}^{(\beta' - r\beta\omega/r_m)}\right\} \tag{2.16a}$$

$$\text{for} \quad r < r_z$$

$$V(r) = \epsilon\left[\mathrm{e}^{2\beta(1 - r/r_m)} - 2\mathrm{e}^{\beta(1 - r/r_m)}\right] \tag{2.16b}$$

$$\text{for} \quad r \leq r_i$$

$$V(r) = \left[S_1(r_{SV} - r)^2 + S_3\right](r_{SV} - r)$$

$$+ \quad \left[S_2(r-r_i)^2 + S_4\right](r-r_i) \qquad (2.16c)$$

$$\text{for} \quad r_i < r < r_{SV}$$

$$V(r) = -\frac{C_6}{r^6} - \frac{C_8}{r^8} \qquad (2.16d)$$

$$\text{for} \quad r \geq r_{SV}$$

$$\text{with} \quad \omega = \frac{\beta' - \ln 2}{\beta - \ln 2}$$

where $r_z = r_m(1 - \ln 2/\beta)$ is the zero of both Morse funtions, and $r_i = r_m(1 + \ln 2/\beta)$ is the inflection point of the second Morse function. The spline coefficients S_1, S_2, S_3 and S_4 are determined by continuity conditions imposed on the potential and its derivative at r_i and r_{SV}. The Spline-van der Waals junction is maintained at $r_{SV}/r_m = 1.6$,[1] and the constant ω is used to impose a smooth transition between the two Morse functions.

This parameter-expansion MMSV potential is a good choice for this study since the various features of the potential are neatly segregated into specific parameters; the well minimum position ($r_m^{(0)}$), the well depth ($\epsilon^{(0)}$), their anisotropies (q and a), the well width (β),and the repulsive wall steepness (β'). The parameters for the potential used in this calculation are given in Table I; the long range dispersion terms for this potential were computed by Pack[17]). The masses of the He and CO_2 are 4.0026 and 44.0098 amu, respectively.[15] They are used along with the C-O bond distance[15] to determine the moment of inertia I (eq. 2.5).

TABLE I. MMSV Anisotropic Parameter Expansion Potential[a] Parameters

Parameter	Symbol	Value
well minimum (spherical average)	$r_m^{(0)}$	3.5 Å
well minimum anisotropy	q	0.21
well depth (spherical average)	$\epsilon^{(0)}$	4.3 meV
well depth anisotropy	a	-0.50
well shape	β	7.2
wall shape	β'	7.2
Spline-van der Waals joint	$\rho_{sv} = r_{sv}/r_m$	1.6
van der Waals coefficients	$C_6^{(0)}$	9.98 meV Å^6
	$C_6^{(2)}$	2.31 meV Å^6
	$C_8^{(0)}$	46.4 meV Å^8
	$C_8^{(2)}$	48.4 meV Å^8

a) see equations 2.14, 2.15 and 2.16.

3.TRANFORMATIONS BETWEEN LABORATORY AND CENTER-OF-MASS FRAMES

3.1. DEFINITIONS

Consider the reaction (or interaction) of molecule **A** with molecule **B** to produce molecules **C** and **D** accompanied with a net energy change ΔE. If the process is non-reactive than **C** and **D** will be just **A** and **B**, respectively.

$$\mathbf{A} + \mathbf{B} \rightarrow \mathbf{C} + \mathbf{D} + \Delta E \tag{3.1}$$

We wish to relate the velocities of the products in the center-of-mass reference frame (CM) to their velocities in the laboratory frame (LAB) and vice versa. For the purposes of this analysis we will only consider the case of the velocities of **C**; the equations that relate the CM and LAB velocities for **D** can easily be obtained from those for **C** by an interchange of indices.

Table I summarizes the symbols we will use; in all cases a prime on a variable refers to the products while unprimed variables refer to the pre-collision reactants. The subscripts 1, 2, $1'$ and $2'$ refer to **A**, **B**, **C** and **D**, respectively. For the scattering angles $\{\theta, \phi\}$ of **C** we will not use numerical subscripts, instead the subcript l will be used to denote $\{\theta, \phi\}$ in the LAB frame, while no subscript will indicate the CM frame. The subscript g denotes the position of the CM origin in the LAB frame.

TABLE I. Symbols for CM and LAB interconversion

	LAB		CM
velocity of **A**	$\vec{v}_1$		$\vec{w}_1$
velocity of **B**	$\vec{v}_2$		$\vec{w}_2$
velocity of **C**	$\vec{v}_1{}'$		$\vec{w}_1{}'$
velocity of **D**	$\vec{v}_2{}'$		$\vec{w}_2{}'$
scattering angles of **C**	$\{\theta_l, \phi_l\}$		$\{\theta, \phi\}$
initial relative velocity	$\vec{w}$		$\vec{w}$
final relative velocity	$\vec{w}\,'$		$\vec{w}\,'$
unit vectors	$\{\hat{\imath}, \hat{\jmath}, \hat{k}\}$		$\{\hat{I}, \hat{J}, \hat{K}\}$
origin	**O**		**G**
beam intersection angle		ς	
mass of **A,B,C,D**		$m_1, m_2, m_1{}', m_2{}'$	
total mass		$M = m_1 + m_2$ $= m_1{}' + m_2{}'$	
angle between v_1 and $\vec{w}_1$		α	
angle between $v_1{}'$ and $\vec{w}_1{}'$		ϵ	
velocity of center-of-mass		$\vec{v}_g$	
angle between v_1 and $\vec{v}_g$		θ_g	
angle between $v_1{}'$ and $\vec{v}_g$		η	

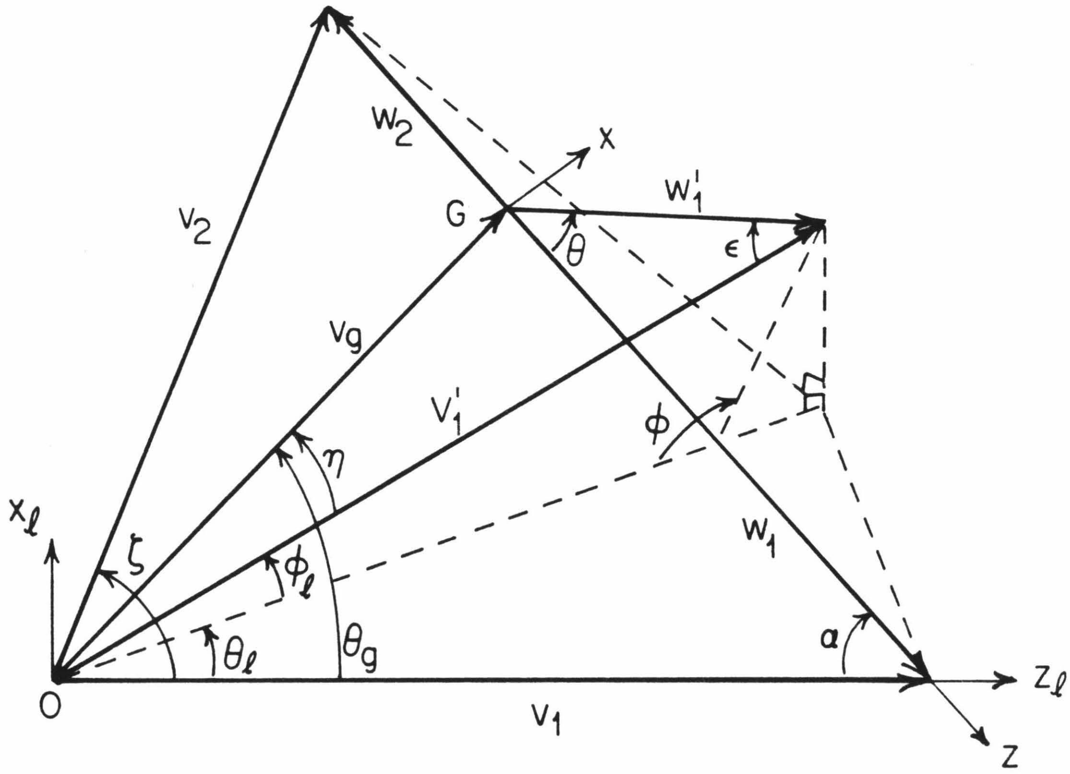

Figure A. Newton Diagram

Let us define the coordinates of the LAB frame such that $\vec{v}_1$ (the beam of **A**) is along the z_l-axis, while $\vec{v}_2$ (the beam of **B**) is in the $x_l z_l-$plane, with ς being the angle between the two, as shown in the Newton diagram in Figure A, and z_l, x_l and y_l are the cartesian axes in the laboratory frame. Then the initial beam velocities are

$$\vec{v}_1 = v_1 \hat{k} \tag{3.2a}$$

$$\vec{v}_2 = v_2(\hat{\imath}\sin\varsigma + \hat{k}\cos\varsigma) \tag{3.2b}$$

The initial relative velocity is defined as the difference between the inintial velocities of the interacting particles in either of the two frames;

$$\vec{w} = \vec{w}_1 - \vec{w}_2 \tag{3.3a}$$

$$= \vec{v}_1 - \vec{v}_2 \tag{3.3b}$$

$$= -\hat{\imath} v_2 \sin\varsigma + \hat{k}(v_1 - v_2\cos\varsigma) \tag{3.3c}$$

By the cosine rule the magnitude of the relative velocity is

$$w = \sqrt{{v_1}^2 + {v_2}^2 - 2v_1v_2\cos\varsigma} \tag{3.4}$$

The $z-$axis in the CM frame is defined to lie along the relative velocity vector $\vec{w}$, which is on the same axis as the CM initial velocities $\vec{w}_1$ and $\vec{w}_2$. The CM $y-$axis is parallel to the LAB y_l-axis, while the $x-$axis follows the right hand rule. The unit vectors of the CM frame may be transformed to those in the LAB frame as a rotation by angle α

$$\hat{I} = \hat{\imath}\cos\alpha + \hat{k}\sin\alpha \tag{3.5a}$$

$$\hat{J} = \hat{\jmath} \tag{3.5b}$$

$$\hat{K} = -\hat{\imath}\sin\alpha + \hat{k}\cos\alpha \tag{3.5c}$$

while the LAB unit vectors may be transformed to those in the CM frame by rotating by $-\alpha$

$$\hat{\imath} = \hat{I}\cos\alpha - \hat{K}\sin\alpha \tag{3.6a}$$

$$\hat{\jmath} = \hat{J} \tag{3.6b}$$

$$\hat{k} = \hat{I}\sin\alpha + \hat{K}\cos\alpha \tag{3.6c}$$

The cosine of α is merely given in terms of the dot product of $\vec{w}$ and $\vec{v}_1$

$$\begin{aligned}\cos\alpha &= \frac{\vec{w}\cdot\vec{v}_1}{wv_1}\\ &= \frac{v_1 - v_2\cos\varsigma}{w}\end{aligned} \tag{3.7}$$

The sine is given by the sine rule

$$\sin\alpha = \frac{v_2\sin\varsigma}{w} \tag{3.8}$$

3.2. CONSERVATION RELATIONS

Conservation of linear momentum in the LAB frame yields

$$M\vec{v}_g = m_1\vec{v}_1 + m_2\vec{v}_2 \tag{3.9}$$

Substituting in equation (3.2) we have an expression for the velocity of the center of mass:

$$\vec{v}_g = \frac{1}{M}\{\hat{\imath} m_2 v_2 \sin\varsigma + \hat{k}(m_1 v_1 + m_2 v_2 \cos\varsigma)\} \tag{3.10a}$$

$$= v_g\{\hat{\imath}\sin\theta_g + \hat{k}\cos\theta_g\} \tag{3.10b}$$

This may be written in polar coordinates:

$$v_g = \frac{1}{M}\sqrt{(m_1v_1)^2 + (m_2v_2)^2 + 2m_1v_1m_2v_2\cos\varsigma} \tag{3.11a}$$

$$\tan\theta_g = \frac{\sin\varsigma}{\frac{m_1v_1}{m_2v_2} + \cos\varsigma} \tag{3.11b}$$

The net linear momentum in the CM frame is by definition zero, which yields

$$m_1\vec{w}_1 + m_2\vec{w}_2 = 0 \tag{3.12}$$

By way of equation (3.3a) we also have

$$\vec{w}_1 = \frac{m_2}{M}\vec{w} \tag{3.13a}$$

$$\vec{w}_2 = -\frac{m_1}{M}\vec{w} \tag{3.13b}$$

In order to determine the velocities of the scattered products we must consider energy conservation. The total energy prior to the collision

E_T is the sum of the CM translational energy T and the internal energy E_ν for a given quantal state ν (the ν represents all of the internal states of **A** and **B**). This is equivalent to the final total energy $E_{T'}$, which is the sum of the final CM translational energy T', the internal energy $E_{\nu'}$ of **C** and **D**, plus the change in the ground state energies between reactants and products $\Delta E_\circ$. We then write

$$\begin{aligned} E_T &= E_{T'} \\ T + E_\nu &= T' + E_{\nu'} + \Delta E_\circ \end{aligned} \tag{3.14}$$

This can be rewritten if we define $\Delta E \equiv E_{\nu'} - E_\nu + \Delta E_\circ$ to be the net change in energy as in equation (3.1):

$$T = T' + \Delta E \tag{3.15}$$

The relative kinetic energies are

$$T = \frac{1}{2}\mu w^2 \tag{3.16a}$$

$$T' = \frac{1}{2}\mu' w'^2 \tag{3.16b}$$

where the reduced masses are

$$\mu = \frac{m_1 m_2}{M} \tag{3.17a}$$

$$\mu' = \frac{m_1' m_2'}{M} \tag{3.17b}$$

By combining equations (3.15) and (3.16) we obtain an expression for the magnitude of the final relative velocity vector

$$w' = \sqrt{w^2 \frac{m_1 m_2}{m_1' m_2'} - \frac{2}{\mu'} \Delta E} \tag{3.18}$$

Conservation of linear momentum in the CM frame yields the following equations for the final CM velocities:

$$\vec{w}\,' = \vec{w}_1' - \vec{w}_2' \tag{3.19}$$

$$\vec{w}_1' = \frac{m_2'}{M} \vec{w}\,' \tag{3.20a}$$

$$\vec{w}_2' = -\frac{m_1'}{M} \vec{w}\,' \tag{3.20b}$$

3.3. LAB TO CM TRANSFORMATIONS

In the LAB to CM transformation we want to express the final CM velocity vector of **C** (index 1') $\vec{w}_1'$ in terms of the LAB velocity vector $\vec{v}_1'$. These can be written in cartesian coordinates using the spherical coodinate angles ($\{\theta, \phi\}$ in the CM frame and $\{\theta_l, \phi_l\}$ in the LAB frame) to specify the magnitudes of the three cartesian vectors.

$$\vec{w}_1' = \frac{m_2'}{M} w' (\hat{I} \sin\theta \cos\phi + \hat{J} \sin\theta \sin\phi + \hat{K} \cos\theta) \tag{3.21}$$

$$\vec{v}_1{}' = v_1{}'(\hat{\imath}\sin\theta_l\cos\phi_l + \hat{\jmath}\sin\theta_l\sin\phi_l + \hat{k}\cos\theta_l) \tag{3.22}$$

The latter equation can be transformed to the CM frame by substituting in equation (3.6) for the LAB unit vectors. Upon rearranging and collecting terms we have

$$\begin{aligned}\vec{v}_1{}' = v_1{}'\{&\hat{I}(\sin\theta_l\cos\phi_l\cos\alpha + \cos\theta_l\sin\alpha)\\ &+\hat{J}\sin\theta_l\sin\phi_l\\ &+\hat{K}(-\sin\theta_l\cos\phi_l\sin\alpha + \cos\theta_l\cos\alpha)\}\end{aligned} \tag{3.23}$$

The LAB velocity $\vec{v}_1{}'$ is the vector sum of the velocity of the CM origin in the LAB frame $\vec{v}_g$ and the CM velocity $\vec{w}_1{}'$. We then can write $\vec{w}_1{}'$ as

$$\vec{w}_1{}' = \vec{v}_1{}' - \vec{v}_g \tag{3.24}$$

We can evaluate this further if we substitute equation (3.23) for $\vec{v}_1{}'$ and equation (3.10) for $\vec{v}_g$, but first we must transform equation (3.10) to CM frame cartesian coordinates. Substituting equations (3.6) into (3.10) and rearranging yields

$$\begin{aligned}\vec{v}_g = \frac{1}{M}\{&\hat{I}(m_2v_2\sin\varsigma\cos\alpha + m_1v_1\sin\alpha + m_2v_2\cos\varsigma\sin\alpha)\\ &+\hat{K}(-m_2v_2\sin\varsigma\sin\alpha + m_1v_1\cos\alpha + m_2v_2\cos\varsigma\cos\alpha)\}\end{aligned} \tag{3.25}$$

This can be simplified by use of angle addition formulas to give:

$$\begin{aligned}\vec{v}_g = \frac{1}{M}\{&\hat{I}(m_2v_2\sin(\varsigma+\alpha) + m_1v_1\sin\alpha)\\ &+\hat{J}(m_2v_2\cos(\varsigma+\alpha) + m_1v_1\cos\alpha)\}\end{aligned} \tag{3.26}$$

Substituting this into equation (3.24) we obtain

$$\begin{aligned}\vec{w}_1{}' = \{&\hat{I}[v_1{}'(\sin\theta_l\cos\phi_l\cos\alpha + \cos\theta_l\sin\alpha)\\ &\qquad - \frac{m_2v_2}{M}\sin(\varsigma+\alpha) - \frac{m_1v_1}{M}\sin\alpha]\\ &+\hat{J}v_1{}'\sin\theta_l\sin\phi_l \\ &+\hat{K}[v_1{}'(\cos\theta_l\cos\alpha - \sin\theta_l\cos\phi_l\sin\alpha)\\ &\qquad - \frac{m_2v_2}{M}\cos(\varsigma+\alpha) - \frac{m_1v_1}{M}\cos\alpha]\}\end{aligned} \tag{3.27}$$

We can obtain all the necessary tranformation relations by equating each of the three cartesian components in equation (3.27) with those in equation (3.21). Matching the $\hat{I}$ vectors we have

$$\begin{aligned}\cos\theta =& \frac{Mv_1{}'}{m_2{}'w'}(\cos\theta_l\cos\alpha - \sin\theta_l\cos\phi_l\sin\alpha)\\ &- \frac{m_2v_2}{m_2{}'w'}\cos(\varsigma+\alpha) - \frac{m_1v_1}{m_2{}'w'}\cos\alpha\end{aligned} \tag{3.28}$$

It is sufficient to know $\cos\theta$ to obtain θ since the range of θ is 0 to π. However, the range of ϕ is 0 to 2π; therefore we must know both the sine and cosine. Hence we match the $\hat{I}$ and $\hat{J}$ components to yield

$$\sin\phi = \frac{Mv_1{}'}{m_2{}'w'}\frac{\sin\theta_l\sin\phi_l}{\sin\theta} \tag{3.29}$$

$$\begin{aligned}\cos\phi =& \frac{Mv_1{}'(\sin\theta_l\cos\phi_l\cos\alpha + \cos\theta_l\sin\alpha)}{m_2{}'w'\sin\theta}\\ &- \frac{m_2v_2\sin(\varsigma+\alpha) - m_1v_1\sin\alpha}{m_2{}'w'\sin\theta}\end{aligned} \tag{3.30}$$

3.4. CM TO LAB TRANSFORMATIONS

For the CM to LAB coordinate transformation we want to express the final LAB velocity vector of **C** ($\vec{v}_1{}'$) in terms of the CM velocity vector $\vec{w}_1{}'$. These can be written in cartesian coordinates using the spherical coordinate angles ($\{\theta_l, \phi_l\}$ in the LAB frame and $\{\theta, \phi\}$ in the CM frame) to specify the magnitudes of the cartesian coordinates, as was done in equations (3.21) and (3.22). This time we transform equation (3.21) to the LAB frame using equations (3.5), to obtain

$$\begin{aligned} \vec{w}_1{}' = \frac{m_2{}'}{M} w' \{ &+\hat{\imath}(\sin\theta\cos\phi\cos\alpha - \cos\theta\sin\alpha) \\ &+\hat{\jmath}\sin\theta\sin\phi \\ &+\hat{k}(\sin\theta\cos\phi\sin\alpha + \cos\theta\cos\alpha)\} \end{aligned} \tag{3.31}$$

Recall that $\vec{v}_1{}'$ is the vector sum of $\vec{v}_g$ and $\vec{w}_1{}'$

$$\vec{v}_1{}' = \vec{v}_g + \vec{w}_1{}' \tag{3.32}$$

Substituting in equations (3.10) and (3.31) gives

$$\begin{aligned} \vec{v}_1{}' = \frac{1}{M}\{ &+\hat{\imath}[m_2{}'w'(\sin\theta\cos\phi\cos\alpha - \cos\theta\sin\alpha) + m_2 v_2 \sin\varsigma] \\ &+\hat{\jmath}\, m_2{}'w'\sin\theta\sin\phi \\ &+\hat{k}[m_2{}'w'(\sin\theta\cos\phi\sin\alpha + \cos\theta\cos\alpha) + m_1 v_1 + m_2 v_2 \cos\varsigma]\} \end{aligned} \tag{3.33}$$

The magnitude of $\vec{v}_1{}'$ may be found by taking the square root of the dot product, which after much algebra yields

$$\begin{aligned} v_1{}' &= (\vec{v}_1{}' \cdot \vec{v}_1{}')^{1/2} \\ &= \frac{1}{M}\{(m_2{}'w')^2 + (m_2v_2)^2 + (m_1v_1)^2 + 2m_1v_1m_2v_2\cos\varsigma \\ &+ \quad 2m_2{}'w'm_2v_2(\sin(\varsigma+\alpha)\sin\theta\cos\phi + \cos(\varsigma+\alpha)\cos\theta) \\ &+ \quad 2m_2{}'w'm_1v_1(\sin\alpha\sin\theta\cos\phi + \cos\alpha\cos\theta)\}^{1/2} \end{aligned} \tag{3.34}$$

The angular postion of $\vec{v}_1{}'$ can be found by matching the cartesian components of equations (3.22) and (3.31). Matching the $\hat{k}$ vectors we have

$$\cos\theta_l = \frac{1}{v_1{}'M}\{m_2{}'w'(\sin\theta\cos\phi\sin\alpha + \cos\theta\cos\alpha) + m_1v_1 + m_2v_2\cos\varsigma\} \tag{3.35}$$

As we stated before, it is sufficient to know the $\cos\theta_l$ to obtain θ since the range of θ is 0 to π. However, the range of ϕ is 0 to 2π and therefore we need $\sin\phi_l$ and $\cos\phi_l$. If we match the $\hat{\jmath}$ and $\hat{\imath}$ components we obtain

$$\sin\phi_l = \frac{m_2{}'w'}{Mv_1{}'}\frac{\sin\theta\sin\phi}{\sin\theta_l} \tag{3.36}$$

and

$$\cos\phi_l = \frac{m_2{}'w'(\sin\theta\cos\phi\cos\alpha - \cos\theta\sin\alpha) + m_2v_2\sin\varsigma}{Mv_1{}'\sin\theta_l} \tag{3.37}$$

3.5. EVALUATION OF ϵ

The angle between $\vec{v}_1{}'$ and $\vec{w}_1{}'$ is important for converting of cross sections between the two reference frames,ϵ. Equations (3.21) and (3.22) may be used to find $\cos\epsilon$ which is

$$\cos\epsilon = \frac{\vec{v}_1{}' \cdot \vec{w}_1{}'}{v_1{}' w_1{}'} \tag{3.38}$$

We can use equations (3.5) or (3.6) to evaluate the dot products between the CM and LAB unit vectors to give

$$\begin{aligned}\cos\epsilon = {} & \sin\theta_l \cos\phi_l(\sin\theta\cos\phi\cos\alpha - \cos\theta\sin\alpha) + \sin\theta_l \sin\phi_l \sin\theta \sin\phi \\ & + \cos\theta_l(\sin\theta\cos\phi\sin\alpha + \cos\theta\cos\alpha)\end{aligned} \tag{3.39}$$

For the case of in-plane scattering ϕ_l is zero and as a consequence ϕ is also zero (or π). If we use three angle addition formulas we find

$$\epsilon = \theta_l - \theta + \alpha \tag{3.40}$$

It can be easily shown that the case of $\phi = \pi$ can be accommodated by giving θ the range of $-\pi$ to π, i.e. θ is negative if $\phi = \pi$.

3.6. INTERMENDIATE TRANSFORMATION RELATIONS

The above equations are useful for direct interconversion between the two reference frames. However, for certain applications it is more useful to have a different set of initially known conditions. For instance if we have a given LAB angle and velocity and we know ΔE we wish to find the initial and final CM conditions which can be used to evaluate the appropriate cross-sections. We do need more initial conditions before we can solve the problem. A very useful intitial condition is knowing the the position of the CM orign **G** in relation to the LAB origin **O**, i.e. $\vec{v}_g$. Once $\vec{v}_g$ is given along with $\{\theta_l, \phi_l\}$,v_1',and ΔE all the other quantities needed to make the transformation can be evaluated.

The problem then is to find $\vec{w}_1'$,w', and w for given $\vec{v}_g$ and $\vec{v}_1'$ (i.e. v_1' and $\{\theta_l, \phi_l\}$). We first note that $\vec{v}_g$,$\vec{v}_1'$, and $\vec{w}_1'$ form a triangle, with ξ being the angle between $\vec{v}_g$ and $\vec{v}_1'$. Then w_1' is given by the cosine rule as

$$w_1' = \sqrt{{v_g}^2 + {v_1'}^2 - 2v_g v_1' \cos\xi} \tag{3.41}$$

We can find ξ from the dot product of $\vec{v}_g$ and $\vec{v}_1'$, using equations (3.10b) and (3.22)

$$\begin{aligned}\cos\xi &= \frac{\vec{v}_g \cdot \vec{v}_1'}{v_g v_1'} \\ &= \sin\theta_g \sin\theta_l \cos\phi_l + \cos\theta_g \cos\theta_l\end{aligned} \tag{3.42a}$$

For the in-plane case this gives

$$\cos\xi = \cos(\theta_l - \theta_g) \tag{3.42b}$$

Using equation (3.20a) we find w', and using equation (3.18) we find w:

$$w' = \frac{M}{m_2{}'} w_1{}' \tag{3.43}$$

and

$$w = \sqrt{\frac{m_1{}' m_2{}'}{m_1 m_2}(w' + \frac{2}{\mu'}\Delta E)} \tag{3.44}$$

Once w is evaluated we can find with simple trigonometric relations the initial LAB velocities and the angle α. Using the sine and cosine rules we have the following equations:

$$\sin\alpha = \frac{v_g}{w_1}\sin\theta_l \tag{3.45a}$$

$$\cos\alpha = \cos[\sin^{-1}(\sin\alpha)] \tag{3.45b}$$

$$w_1 = \frac{m_2}{M} w \tag{3.46}$$

$$v_1 = w_1 \frac{\sin(\pi - \theta_g - \alpha)}{\sin\theta_g} \tag{3.47}$$

$$v_2 = \sqrt{w^2 v_1^2 - 2 w v_1 \cos\alpha} \tag{3.48}$$

$$\cos\varsigma = \frac{v_1^2 + v_2^2 - w^2}{2 v_1 v_2} \tag{3.49}$$

These quantities can be used in conjunction with equations (3.28),(3.29) and (3.30) to obtain the CM angles $\{\theta, \phi\}$, which can then be used for calculating differential cross-sections.

A quantity that will prove to be useful later on is the angle between the center-of-mass origin **G** velocity vector $\vec{v}_g$ and the velocity of **C** $\vec{v}_1{}'$, which can be evaulated using the dot product of both vectors (equations 3.10b and 3.22) and dividing it by the vector magnitudes, and is given by

$$\cos\eta = \sin\theta_g \sin\theta_l \cos\phi_l + \cos\theta_g \cos\theta_l \tag{3.50}$$

For a given $\vec{v}_g$ and the scattering angles $\{\theta_l, \phi_l\}$ (the direction of $\vec{v}_1{}'$) the minimum $w_1{}'$ which will intersect the line passing through the origin **O** in the direction $\{\theta_l, \phi_l\}$ will be perpendicular to that line, and by inspection can be written as

$$w_1{}'_{min} = v_g|\sin\eta| \tag{3.51}$$

Similarly, the corresponding $v_1{}'$ is given in as

$$v_1{}'_{(w_1{}'_{min})} = v_g|\cos\eta| \tag{3.52}$$

3.7. TRANSFORMATION OF CROSS-SECTIONS

We wish to relate the diffential cross-section $\sigma(\theta, \phi)$ in CM frame to that in the LAB frame $\sigma(\theta_l, \phi_l)$. The first consideration is that the flux per unit of solid angle $d\Omega$ should be the same in either frame for coresponding cross-sections, hence we write

$$\sigma(\theta_l, \phi_l)d\Omega_l = \sigma(\theta, \phi)d\Omega \tag{3.53}$$

where

$$d\Omega = \sin\theta d\theta d\phi$$

and

$$d\Omega_l = \sin\theta_l d\theta_l d\phi_l$$

This can also be seen in another way: the total cross-section should be invariant to the coordinates used, hence we have

$$Q = \int \sigma(\theta, \phi)d\Omega = \int \sigma(\theta_l, \phi_l)d\Omega_l$$

equation (3.53) follows from this since the integrands must be be equal in order for the integrals to be equal.

We now must relate $d\Omega$ to $d\Omega_l$. One way is to consider an element of surface in velocity space for both frames:

$$d\mathbf{S}_l = {v_1'}^2 d\Omega_l$$

$$d\mathbf{S} = {w_1'}^2 d\Omega$$

where $d\mathbf{S}_l$ is normal to $\vec{v}_1{}'$ while $d\mathbf{S}$ is normal to $\vec{w}_1{}'$. Therefore the LAB cross-section may be written in terms of the CM cross-section

$$\sigma(\theta_l, \phi_l) = \sigma(\theta, \phi) \frac{{v_1'}^2}{{w_1'}^2} \left[\frac{d\mathbf{S}}{d\mathbf{S}_l} \right] \tag{3.54}$$

The ratio of the surface area elements is easily evaluated by taking into account the angle between the two infinitesimal planes passing through $d\mathbf{S}$ and $d\mathbf{S}_l$. We already know the normals to these planes $\vec{w}_1{}'$ and $\vec{v}_1{}'$ respectively and the angle between them as in equations (3.38) thru (3.40). Then the projection of $d\mathbf{S}$ onto $d\mathbf{S}_l$ gives

$$d\mathbf{S}_p = d\mathbf{S} |\cos\epsilon| \tag{3.55}$$

This is the portion of the CM surface area that is observed by a given unit surface area in the LAB frame. As the angle ϵ increases the amount of CM surface area that is subtended by a unit of LAB surface area increases, as would be expected. The absolute value insures no negative areas. This then gives the transformation relation

$$\sigma(\theta_l, \phi_l) = \sigma(\theta, \phi) \frac{{v_1'}^2}{{w_1'}^2} \frac{1}{|\cos\epsilon|} \tag{3.56}$$

The reason we project the CM area on to the LAB and not vice versa is that the final state of the system is specified by the initial conditions and $\vec{w}_1{}'$ which is a dynamic constant of motion for the overall reaction, while $\vec{v}_1{}'$ is not a constant of motion. Rather it is dependent upon the scattering angles in both reference frames (see equations (3.33) and (3.34)). Hence it is better to view in the LAB frame the amount of flux coming from the CM frame for a given unit LAB area, since the CM flux is only descriptive of the processes involved in the reaction (equation (3.1)) and is independent of any peculiarities of the LAB frame.

3.8. DETECTION OF SCATTERING

Two basic type of detection schemes can be employed to measure the number of scattered molecules **C**: a) flux detection (particles per area), and b) number-density detection (particles per volume). Both of these are related in different ways to the differential cross-section.

The cross-section σ is defined as the ratio of the scattered probability flux density $\mathbf{j}_s$ to the incident probability flux density $\mathbf{j}_i$

$$\sigma = \frac{|\mathbf{j}_s|\, d^2}{|\mathbf{j}_i|}$$

where d is the distance from the scattering center to the point at which the flux $\mathbf{j}_s$ is measured. The incident probability flux density $\mathbf{j}_i$ is for an incoming plane wave and represents the total incoming flux, the scattered probability flux density $\mathbf{j}_s$ is for an outgoing spherical wave and represent the flux scattered into into an element of surface area subtended by the solid angle $d\Omega$ (or in the LAB frame $d\Omega_l$). As the distance from the scattering center increases the outgoing flux will decrease in inverse proportion to the surface area of a sphere (d^{-2}); hence it is multiplied by d^2 to obatain a quantity independent of d. This definition for the cross-section may be rearanged to given an expression for the scattering flux

$$\mathrm{j}_s = \sigma \frac{\mathrm{j}_i}{d^2} \tag{3.57}$$

where we have replaced the absolute values of the vector quantities $|\mathbf{j}_s|$ and $|\mathbf{j}_i|$ with the symbols j_s and j_i, respectively. This expression is valid in the CM frame as well as in the LAB frame; it is for a collisional encounter of one particle **A** with one particle **B**. The scattered flux $\mathbf{J_C}$ of particles **C** for a number of single collision encounters between **A** and **B** (in a crossed-beam of **A** and **B**, particle **A** will encounter only one particle **B**, and vice versa), is the product of the scattered flux j_s (for particle **C**) and the number of scattering centers. If we pick j_i to be the flux of particle **A** then the number of scattering centers this flux encounters will be equal to the number density of particles **B** ($n_\mathbf{B}$) times the volume of interaction V. Since the particles **B** are in motion with velocity v_2, the density that will actually be encountered by $\mathrm{j}_\mathbf{A}$ will be different than the densitity measured in the laboratory frame. This density $n'_\mathbf{B}$ can be obtained by considering a stationary particle **B** with density $n_\mathbf{B}$ with a flux of particles **A** impinging on it; the velocity of this flux is just the relative velocity between the two particles w. The flux of particles **A** as measured in the laboratory frame has a velocity v_1, hence the density $n'_\mathbf{B}$ is the product of the laboratory density $n_\mathbf{B}$ and the ratio of the velocities w/v_1. Then the total flux of **C** scattered into solid angle $d\Omega_l$ at distanance d is

$$\mathbf{J}_C = \mathrm{j}_{\mathbf{A}} n'_{\mathbf{B}} \frac{V}{d^2}\, \sigma(\theta_l, \phi_l) \tag{3.58a}$$

$$= \mathrm{j}_{\mathbf{A}} \left(\frac{w}{v_1}\right) n_{\mathbf{B}} \frac{V}{d^2}\, \sigma(\theta_l, \phi_l) \tag{3.58b}$$

Since flux is the product of the number density and velocity, we can write

$$\mathbf{J}_C = n_{\mathbf{A}} n_{\mathbf{B}} \frac{V}{d^2} w\; \sigma(\theta_l, \phi_l) \tag{3.58c}$$

This same result could have been obtained by considering a flux of **B** impinging on a number density of paritcles **A**.

The output signal of many detectors, such as electron impact spectrometers, is proportional to the number of particles in a given volume, and not the number passing though one end of this volume. Particles with a greater speed will pass through the volume faster than slower ones and hence have a smaller chance of being detected. Hence the number density $I(\theta_l, \phi_l)$ of particles **C** scattered into $d\Omega_l$ in the direction $\{\theta_l, \phi_l\}$ per unit time is the product of equation (3.58) and the reciprocal of the final LAB velocity $v_1{}'$

$$I(\theta_l, \phi_l) = n_{\mathbf{A}} n_{\mathbf{B}} \frac{V}{d^2} \frac{w}{v_1{}'} \sigma(\theta_l, \phi_l) \tag{3.59}$$

We may combine the above equation with equation (3.56) to obtain a general center-of-mass to laboratory transformation

$$I(\theta_l, \phi_l) = \sigma(\theta, \phi) \frac{w v_1{}'}{w_1{}'^2} \frac{1}{|\cos \epsilon|} \left(\frac{n_{\mathbf{A}} n_{\mathbf{B}} V}{d^2} \right) \tag{3.60}$$

The number densities of the initial particles **A** and **B** and the interaction volume V are useful in the process of averaging over instrumental parameters. These parameters include the velocity distributions of the particles and the angular spreads of the particle beams. The velocitiy distributions are proportional to the number densities; while angular spreads of the beams define the scattering volume.

4. VELOCITY RESOLVED LABORATORY SCATTERING

The simulation of a velocity resolved signal from a crossed beam scattering experiment consists of two basic steps: 1) the calculation of cross sections in the center-of-mass frame at appropriate energies and scattering angles, 2) transformation of these quantities to the laboratory reference frame while averaging over the characteristics of the experiment. In order to perform the center-of-mass calculations the conditions of the experiment being simulated must be known. For computational convenience it is useful to first determine the characteristics of the experiment and obtain several quantities that will be needed in the actual calculation. We therefore break up our simulation into three parts: 1) preliminary calculations, 2) cross section calculations, and 3) center-of-mass to laboratory transformations and apparatus averaging.

The apparatus averaging is over a range of $\vec{v}_g$. The vector $\vec{v}_g$ defines the location of the CM origin in the LAB frame. This origin is the source of the scattered particles, hence we call this averaging scheme: "source averaging." The range of $\vec{v}_g$ is determined by velocity distributions and angular divergences of the beams.

4.1. Preliminary Calculations

For a specific molecular beam apparatus we are given the following:

(1) Velocity distribution of the primary beam $f(v_1)$

(2) Angular spread of the primary beam $\Gamma_1(\delta_1)$

(3) Velocity distribution of the secondary beam $f(v_2)$

(4) Angular spread of the secondary beam $\Gamma_2(\delta_2)$

(5) The intersection angle between the two beams ς.

(6) The set of scattering angles to be simulated $\{\theta_l, \phi_l\}_{[a]}$ (the $[a]$ is an index).

The beam velocity distributions are characterized by the function[21]

$$f(v) = cv^3\mathbf{e}^{-\frac{m}{2kT_s}(v-v_s)^2} \tag{4.1}$$

where m is the mass of the beam atom or molecule. In this expression there are two variable parameters T_s and v_s. The constant c is determined be requiring $f(v)$ to be normalized over v. The gas stream temperature T_s and stream velocity v_s are related to the effective nozzle stagnation temperature T_0, a Mach number M, and the heat capacity ratio $\gamma = C_p/C_v$ [21]

$$T_s = \frac{T_0}{1 + \frac{\gamma-1}{2}M^2} \tag{4.2}$$

and

$${v_s}^2 = \frac{kT_s\gamma M^2}{m} \tag{4.3}$$

The beam angular distributions are characterized by

$$\begin{aligned} \Gamma(\delta) &= A\cos\Big[\delta\frac{\pi}{2\delta_w}\Big]^2 && \text{for } -\delta_w \le \delta \le +\delta_w \\ &= 0 && \text{for } |\delta| > \delta_w \end{aligned} \tag{4.4}$$

where ς_w is the half width of the distribution at the base.

The range of the beam velocities to be considered is truncated by specified distribution cut offs, which are chosen to include a significant portion of the distribution and exclude velocities of low probability which contribute negligibly to the final result.

From the given distributions and cut offs we calculate:

(1) a convolution of beam angular divergences as a single function, represented as a distribution of beam intersection angles ς and characterized by

$$\begin{aligned} Z(\varsigma) &= A\cos\Big[(\varsigma - \varsigma_o)\frac{\pi}{2\varsigma_w}\Big]^2 && \text{for } -\varsigma_w \le \varsigma \le +\varsigma_w \\ &= 0 && \text{for } |\varsigma| > \varsigma_w \end{aligned} \tag{4.5}$$

where ς_w is the half width of the convoluted ditribution, while ς_0 is the most probable beam intersection angle

(2) range of relative velocities $w_{[b]}$ for the cross-section calculations, (see eq. 3.3 for w)

(3) range of velocities of the center-of-mass frame with respect to the laboratory frame $\vec{v}_g$. These are determined by constructing a grid of $\vec{v}_g$ points within a trapezoid; the corners of the trapezoid are obtained from the limits of the beam velocity and angular spread distributions. The grid is constructed by dividing each edge of the

trapezoid into a given number of points and connecting the points on one edge to those of the oposite edge (oposite edges are divided into the same number of points). The intersections of the connecting line segments make up the grid points $(\vec{v}_g)_{[i,j]}$.

The center-of-mass scattering angles $\{\theta,\phi\}_{[c]}$ are determined for the entire scattering range. Since the cross-sections for the system under consideration are independent of ϕ, the range of ϕ is not important. The range of θ is from 0 to π.

4.2. Cross Section Calculations

For a given potential and collision energy we calculated the phase shifts $\eta_l(\gamma)$ in equation (2.7), via Numerov integration[19] for low values of l and via the JWKB method[18,14] for higher values (the switch over taking place between $l = 15$ and 25). In general it is sufficient to use 48 approach angles γ in order to obtain good values for state-to-state cross-sections (total differential cross-sections are convergent with only 12 approach angles). Using equations (2.7) and (2.10) we determined the expansion scatttering amplitudes $F_j^{k_J}(\theta)$. These are computed at energies corresponding to the initial relative collision velocity $w_{[b]}$ and scattering angles $\theta_{[c]}$ for all b and c, and are then used to calculate state-to-state differential cross sections $\sigma(j' \leftarrow j \mid \theta)$ using equation (2.11).

4.3. Transformation and Averaging

For each laboratory scattering angle $\{\theta_l, \phi_l\}_{[a]}$ and each $j' \leftarrow j$ transition we calculate the laboratory signal as a function of velocity of particle **C** (equation 3.1) $I\big(j' \leftarrow j, \{\theta_l, \phi_l\}_{[a]}, {v_1}'\big)$. These are calculated as follows:

(1.) The limits at which the laboratory velocities ${v_1}'$ are to be calculated are given by

$$ {v_1}'_{lim} = {v_1}'_{{w_1}'_{min}} \pm \sqrt{{w_1}'^2 - {w_1}'^{2}_{min}} \qquad (4.6) $$

${w_1}'_{min}$ and ${v_1}'_{{w_1}'_{min}}$ are obtained from equations (3.50) thru (3.52); ${w_1}'$ is obtained from equations (3.18) and (3.20a) which are dependent on the inelasticity of the transitions. The actual limits are determined by selecting v_g and w from the extreme limits of v_1, v_2, and ς; v_g and w are given by equations (3.10a) and (3.3b), respectively. Since there are eight possible combinations of extremes for v_1, v_2, and ς, the upper limit is picked as the maximum ${v_1}'_{lim}$ and the lower limit as the minimum. The $\pm$ refers to the possibility of two ranges of ${v_1}'_{lim}$. The plus sign applies to all cases; while the negative sign applies only when ${v_1}'_{lim}$ is positive, which for inelastic scattering occurs only when ${w_1}' < w_1$.

(2.) For each ${v_1}'$ we integrate (Gaussian) over $\vec{v}_g$ the contributions of each $(\vec{v}_g)_{[i,j]}$. This technique is called: "source averaging."

(a.) Using equations (3.41) thru (3.49) we determine: the final CM velocity ${w_1}'$, the corresponding initial relative velocity w, the angle α, and the laboratory beam velocities v_1 and v_2 along with the beam intersection angle ς.

(b.) From v_1, v_2 and ς we determine the relative number density for this configuration of beam velocities and intersection angle using equations (4.4) and (4.5) which will be proportional to $(n_A n_B V)$ in equation (3.60). This is the product $f(v_1) \cdot f(v_1) \cdot Z(\varsigma)$.

(c.) Using equation (3.39) (or 3.40) we find $\cos \epsilon$.

(d.) The center-of-mass scattering angle θ is obatined from equation (3.28). The azimuthal scattering angle ϕ can be obtained from equations (3.29) and (3.30), but since the cross-sections are independent of this angle we do not need to calculate it.

(e.) The cross sections $\sigma(\theta, w)$ are interpolated from those calculated on the grid $\{\theta_{[c]}, w_{[b]}\}$.

(f.) These above quantities are combined as in equation (3.60) and are multiplied by the relative thermal population at temperature T of the initial rotational state

$$P_j(T) = \frac{(2j+1)\mathbf{e}^{-E_j/k_b T}}{Q_r(T)} \tag{4.7}$$

to obtain the final result. (Where, k_b is Boltzmann's constant, and $Q_r(T)$ is the rotational partition function.) The rotational energy E_j is given by equation (2.5) (it is the second term on the left).

In summary, this $\vec{v}_g$ grid integration process is expressed as

$$I(j' \leftarrow j, \theta_l, v_1{}') = \frac{1}{N_g} \int_{grid} d\vec{v}_g \; P_j(T) f(v_1) f(v_2) Z(\varsigma) \frac{w v_1'}{w_1{}'^2 |\cos\epsilon|} \sigma(j' \leftarrow j|\theta, w) \tag{4.8}$$

where v_1, v_2, ς, w, v_1', $w_1{}'$, ϵ, and θ are dependent on $\vec{v}_g$, θ_l, $v_1{}'$, j and j'. The integral is normalized over the grid, with the factor $N_{grid} \equiv \int d\vec{v}_g$. The factor of $1/d^2$ (Eq. 3.59) was excluded since it is a constant for a given experimental configuration.

Usually all possible transitions $j' \leftarrow j$ are summed for a given scattering angle to simulate an actual experimentally observable signal.

The beam parameters used for this simulation are the same as those for our He + CO_2 scattering experiments[1]. The cut-offs for the beam velocities v_1 and v_2 are at 0.05 of the peak of both distributions $f(v_1)$ and $f(v_2)$. The cut-offs for the convoluted distribution of beam intersection angles ς are at 0.05 of the peak of the distribution $Z(\varsigma)$.

We use 8 CM velocities $w_{[c]}$ which are equally spread over an interval between the cut-offs of the w probability distribution. The cut-offs are at 0.005 of the peak of the w distribution. The cross sections are calculated at each of these $w_{[c]}$ and CM angles θ from 0 to 180 degrees (every 1/3 deg. for 0 to 20 deg., every 1 deg. for 20 to 40 deg., and 2 deg. for 40 to 180 deg.) .

A grid of 64 (8 by 8) $\vec{v}_g$ integration points is perfectly adequate for this application.

At a temperature of 298 K 99.3 % of the CO_2 molecules are in states below $j = 50$ (the most probable rotational state for the CO_2 is $j = 16$). Hence we will consider all initial rotational states up to $j = 50$. Final states will depend upon the cross sections. As we will show in the next section, transitions for a change in rotational quantum number $\Delta j > 8$ are virtually insignificant, and need not be considered. For low scattering angles ($\theta < 10$ deg.) only $\Delta j = 2$ transitions need be calculated; for 10 deg. $< \theta < 18$ deg. only $\Delta j \leq 4$ need be calculated; for 18 deg. $< \theta <$ 25 deg. only $\Delta j \leq 6$ need be calculated.

5. RESULTS AND DISCUSSION

In Figure 1 we plot the center-of-mass differential cross-section (DCS) for the He + CO_2 potential at 65 meV, the most probable energy for the conditions of the simulation outlined in the previous section. All of the five curves are for an initial rotational state $j = 12$; curve for other initial states from $j = 4$ thru $j = 30$ are very similar to these. The lowest curve is for the elastic cross-section (the change in rotational quantum number for the CO_2 molecule $\Delta j = 0$); the curve above it is a sum of all state-to-state cross sections with $|\Delta j| \leq 2$; the center curve is for $|\Delta j| \leq 4$; the curve above it is for $|\Delta j| \leq 8$; the upper curve (dashed) is barely visible and it is for the total DCS from $j = 12$ (eq. 2.12). It is clear from this figure that to calculate the laboratory cross-sections it is sufficient to include only a small fraction of all the possible state-to-state DCS's.

This figure can also serve as a guide in selecting scattering angles for which the observed scattering signal will contain the greatest rotational inelasticity. We can use the CM cross-section as a guide to understanding the LAB cross-section because the difference between θ (the CM scattering angle) and the corresponding θ_l (the LAB scattering angle) is small for scattering angles less than 90 degrees.[11,2] At low scattering angles elastic transitions should predominate. At 13, 18 and 23 degrees the elastic DCS is at a minimum and the inelastic DCS's contribute significantly to the total DCS. From 30 to 60 degrees the elastic DCS is only 1/3 to 1/4 of the total.

Four angles were chosen for simulation of laboratory velocity resolved cross-sections: 5, 13, 18 and 40 degrees. At 5 degrees the inelasticity will be minimal. At 13 and 18 degrees there should be enough inelasticity to be observed experimentally. These angles are relatively small and the cross-section is high enough that they should be easily distinguished from the background in a crossed molecular beam apparatus. At 40 degrees the inelasticity is somewhat higher than at 18, but not significantly (as will be shown below), while the expected signal is lower by about a factor of three. There is also another reason why there is no significant advantage in measuring inelasticity at 40 degrees versus 18 (or 23); it will be discussed later.

The velocity resolved cross-sections for 5 degrees are shown in Figure 2. The inelastic cross-section makes up 1.74% of the total cross-section, compare Figure 2a (the total) to Figure 2b (the inelastic). This is not a negligible contribution, although it is quite small, and hence it becomes difficult to distinguish the inelastic and purely elastic contributions to the observed signal. The peaks of both the total and elastic signals are shifted to a slightly higher most probable velocity v_{max} over the velocity of the He beam, 1.76 km/sec. The width (full-width-at-half-maximum, v_{fwhm}) of the total peak is 0.185 km/sec which is narrower than the He beam width of 0.210 km/sec. This peak shift and narrowing are primarily a consequence of the CM to LAB transformation. The range of LAB velocities for Figure 2 correspond to a 1 degree range of CM velocities; the lower velocities correspond to lower CM angles, and the higher velocities to higher CM angles. Hence the velocity distribution is modified by the sloping CM DCS.

At 13 degrees the inelastic contribution increases to 25% of the total cross-section, compare Fig. 3a and 3b. The total cross-section peak is wider than the elastic, and is shifted to a slighly higher velocity.

At 18 degrees the inelastic contribution to the total cross-section is 60%, compare Fig. 4a and 4b. The total (Fig. 4a) cross-section peak is about 25% wider than the elastic (Fig. 4b). The shoulder on the inelastic cross-section peak (Fig. 4c) is due to the $\Delta j > 0$ transitions (Fig. 4e) which shows the source of this structure. This shoulder is due to the fact that a range of CM scattering angles is transformed to the LAB frame for a given LAB angle. The slight indentation at 1.82 km/sec (Fig. 4e) corresponds to a trough in the inelastic DCS oscillations, which in general are much sharper than elastic ones. The sum of the $\Delta j < 0$ transitions (Fig. 4d) does not show a similar shoulder, indicating that no trough was sampled in the LAB frame for these cross-sections.

Inelastic cross-sections contribute 75% to the total cross-section at 40 degrees, compare Figs. 5a and 5b. However, the relative broadening of the total over the pure elastic velocity distribution peaks is 17%, compared 25% for 18 degrees. The elastic peak is significantly wider than elastic peaks for the lower angles. This widening is caused by the velocity distribution of the CO_2 beam, which has a FWHM of 0.38 km/sec for a most-probable velocity of 0.49 km/sec. At larger LAB angles the CO_2 beam velocity distribution has a greater effect on the velocity distribution of the scattered He, which at low angles is primarily affected by the incoming He beam distribution. The advantages of greater inelasticity at 40 degrees are compromised by this broadening and the lower scattering intensity.

From the above observations, it is evident that the velocity distribution of the scattered signal contains enough information to permit one to distinguish inelastic processes from purely elastic ones. The inelasticity is present as a widening and a distortion of the velocity distribution peak from what would be expected for an elastic process. The actual inelasticity cannot be observed as a distinct and isolated peak, but it can be obtained in conjunction with a potential fitting algorithm. The algorithm would simulate the observed velocity distributions according to the procedure outlined above using a potential which can be extracted from total-DCS experiments. The potential can then be adjusted via a least-squares algorithm untill it provides calculated "data" that is in best agreement with the experimental data.

6. REFERENCES

1. J. W. Winniczek, Ph.D. Thesis, California Institute of Technology, Chapter 2 (1985); J. W. Winniczek and A. Kuppermann, (to be submitted).
2. J. W. Winniczek, Ph.D. Thesis, California Institute of Technology, Chapter 3 (1985); J. W. Winniczek and A. Kuppermann, (to be submitted).
3. M. Keil and G. A. Parker, *J. Chem. Phys.* **82**, 1947 (1985);
   G. A. Parker, M. Keil, and A. Kuppermann,
   J. Chem. Phys. **78**, 1145 (1983);
   M. Keil, G. A. Parker, and A. Kuppermann,
   Chem. Phys. Lett. **59**, 443 (1978).
4. M. Faubel, K. H. Kohl, J. P. Toennies, and F. A. Gianturco,
   J. Chem. Phys. **78**, 5629 (1984).
5. M. Faubel, K.-H. Kohl, and J. P. Toennies,
   Faraday Discuss. Chem. Soc. **73**, 205 (1982).
6. M. Keil, J. T. Slankas, and A. Kuppermann,
   J. Chem. Phys. **70**, 482 (1979).
7. L. Eno and H. Rabitz, *J. Chem. Phys.* **74**, 3859 (1981).
8. P. M. Agrawal and L. M. Raff, *J. Chem. Phys.* **75**, 2163 (1981).
9. G. A. Parker and R. T Pack, *J. Chem. Phys.* **68**, 1585 (1978).
10. R. T Pack, *Chem. Phys. Lett.* **55**, 197 (1978).
11. G. Rotzoll and A. Lubbert, *J. Chem. Phys.* **71**, 2275 (1979).
12. P. McGuire and D. J. Kouri, *J. Chem. Phys.* **60**, 2488 (1974);
    R. T Pack, *J. Chem. Phys.* **60**, 633 (1974).
13. V. Khare, *J. Chem. Phys.* **68**, 4631 (1978);
    D. Secrest, *J. Chem. Phys.* **62**, 710 (1975).
14. D. S. Saxon, *Elementary Quantum Mechanics* (Holden-Day, San Francisco, 1968); A. S. Davydov, *Quantum Mechanics* (Pergamon, Oxford 1976), 2nd edition, tr. D. ter Haar.
15. G.Herzeberg, *Molecular Spectra and Molecular Structure III. Electronic Spectra and Electronic Structure of Polyatomic Molecules*, (Van Nostrand Reinhold, New York, 1966).
16. The vibrational energies for the three vibrational modes of $CO2_2$ are given in ref. 22, and are 291.26 meV, 172.11 meV and 82.75 meV; at a temperature of 298 K these states have a ground state relative popula-

tions of 100.0%, 99.9% and 96.0%, respectively.

17. R. T Pack, *J. Chem. Phys.* **64**, 1659 (1976).
18. R. T Pack, *J. Chem. Phys.* **60**, 633 (1974).
19. K. Smith, *The Calculation of Atomic Collision Processes* (Wiley, New York 1971).
20. T. T. Warncock and R. B. Bernstein, *J. Chem. Phys.* **49**, 1878 (1966).
21. J. B. Anderson and J. B. Fenn, *Phys. Fluids* **8**, 780 (1965).

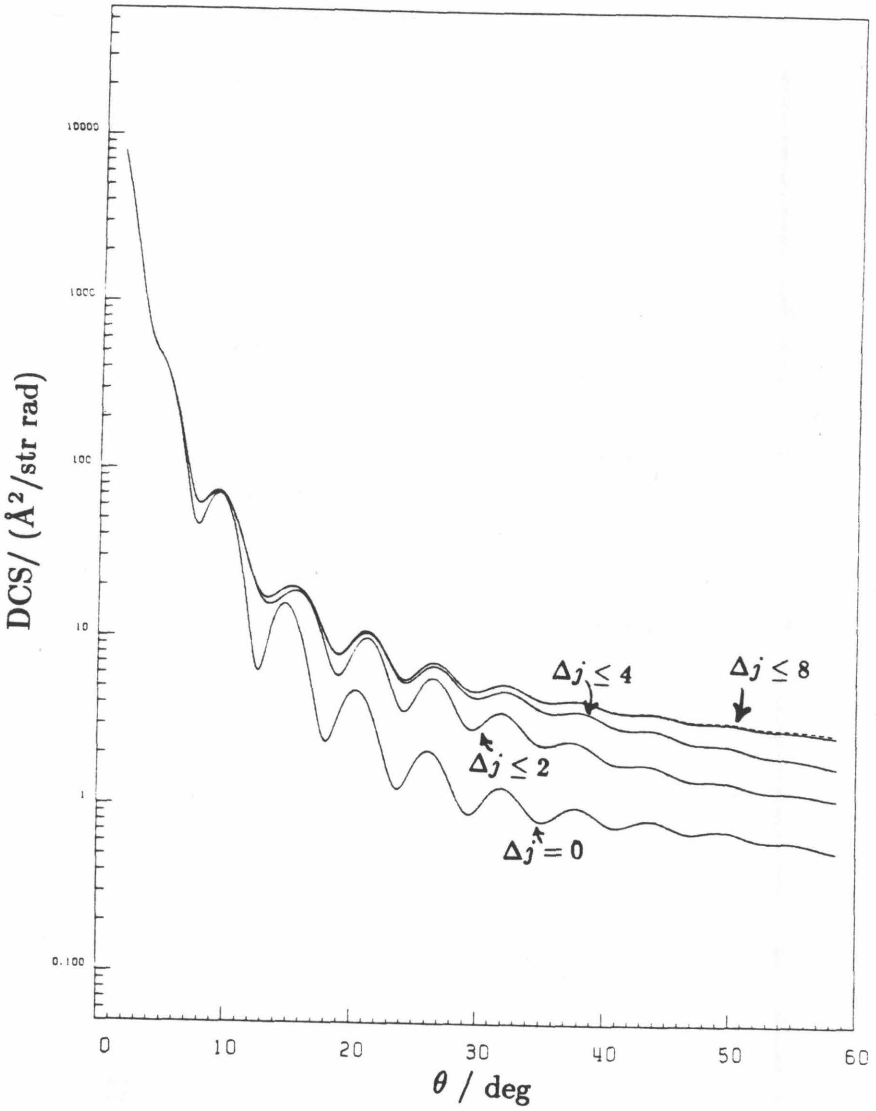

Figure 1. Center-of-mass $j = 12$ differential cross-sections (DCS) for the MMSV potential at a scattering energy of 65 meV. The bottom curve is for the elastic DCS ($\Delta j = 0$). The curves above it progressively include more anisotropy, as indicated by Δj. The upper dashed curve (barely visible) is the total DCS from $j = 12$.

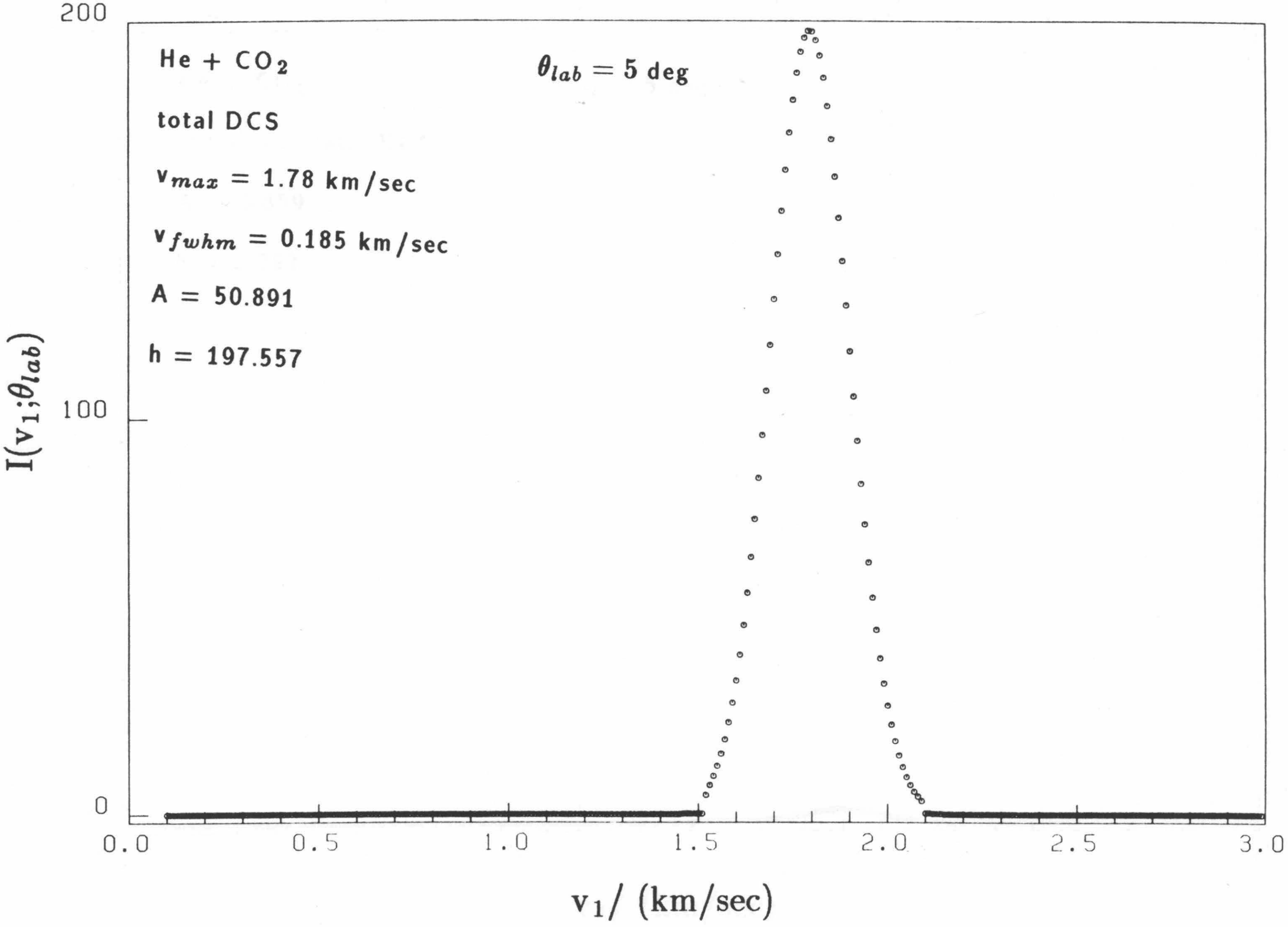

Figure 2a. Velocity resolved laboratory scattering signal for He.

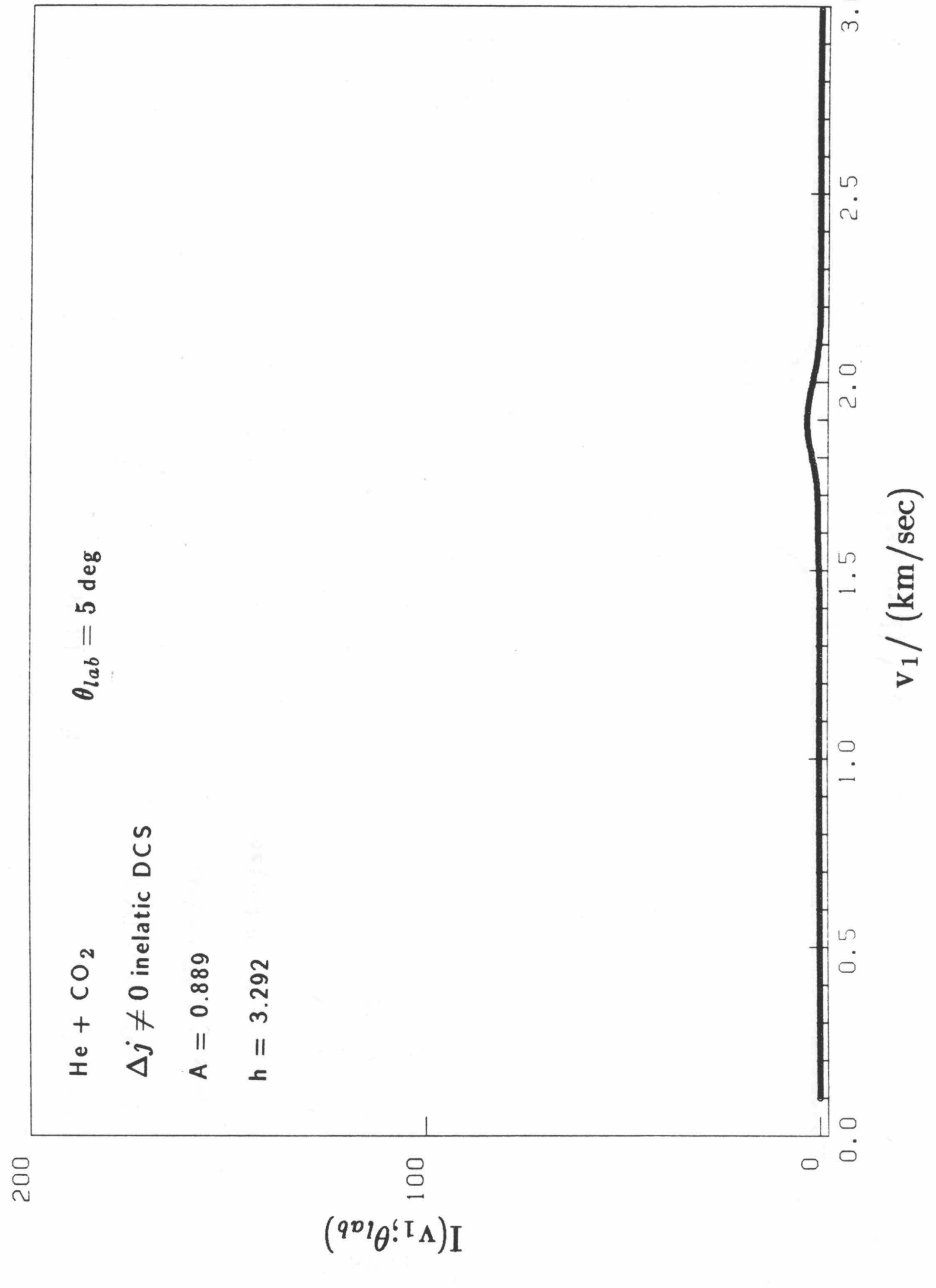

Figure 2b. Velocity resolved laboratory scattering signal for He.

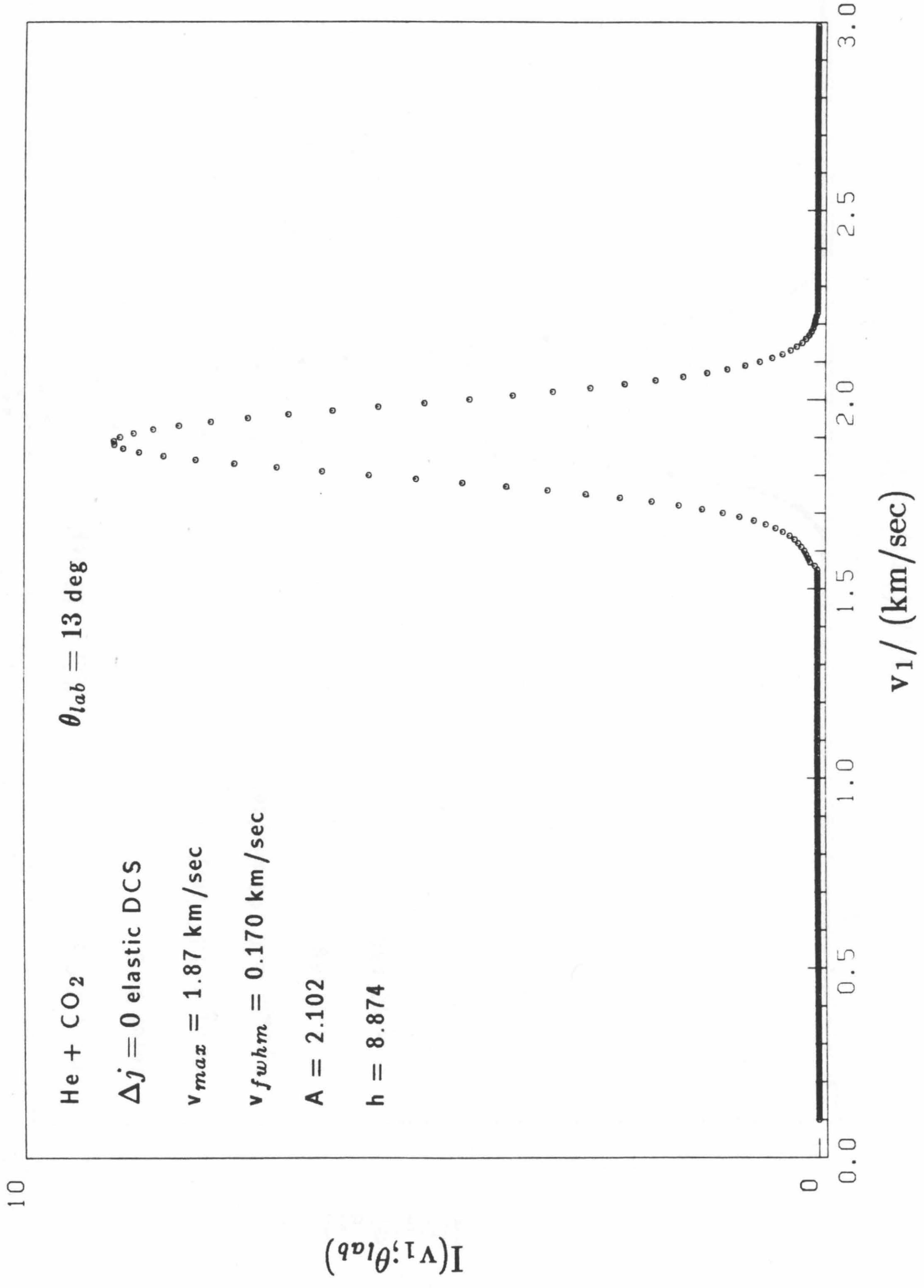

Figure 3a. Velocity resolved laboratory scattering signal for He.

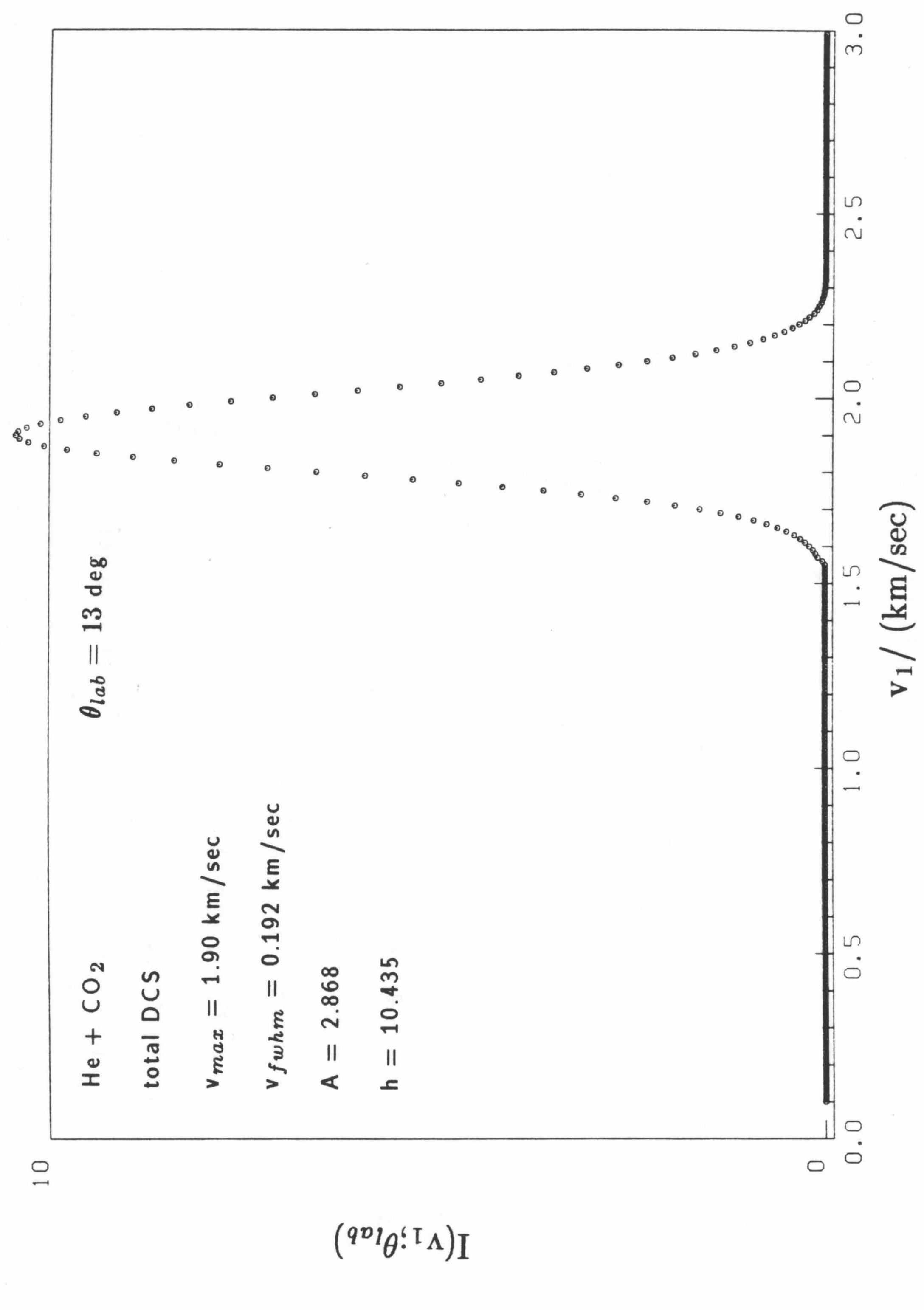

Figure 3b. Velocity resolved laboratory scattering signal for He.

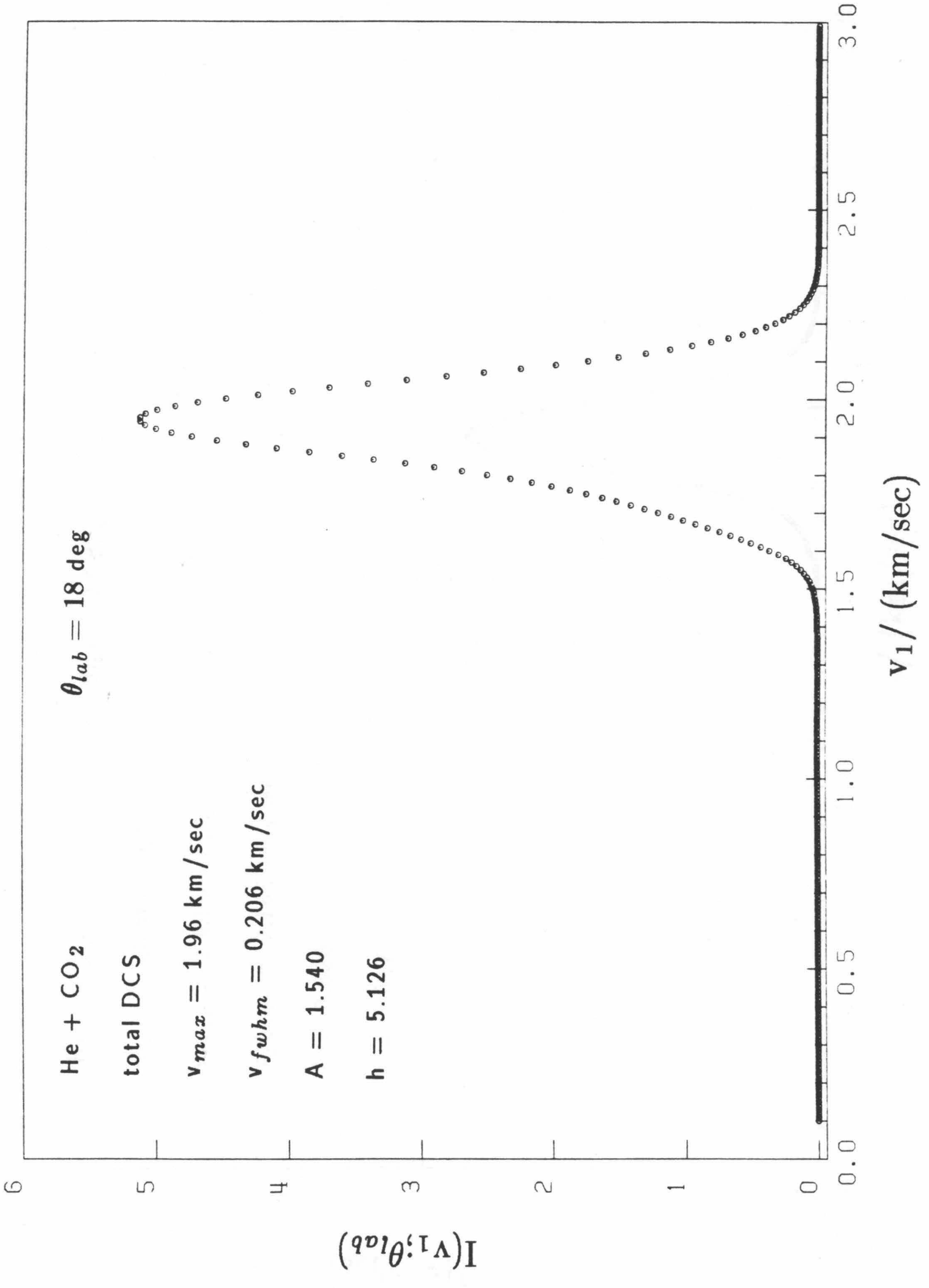

Figure 4a. Velocity resolved laboratory scattering signal for He.

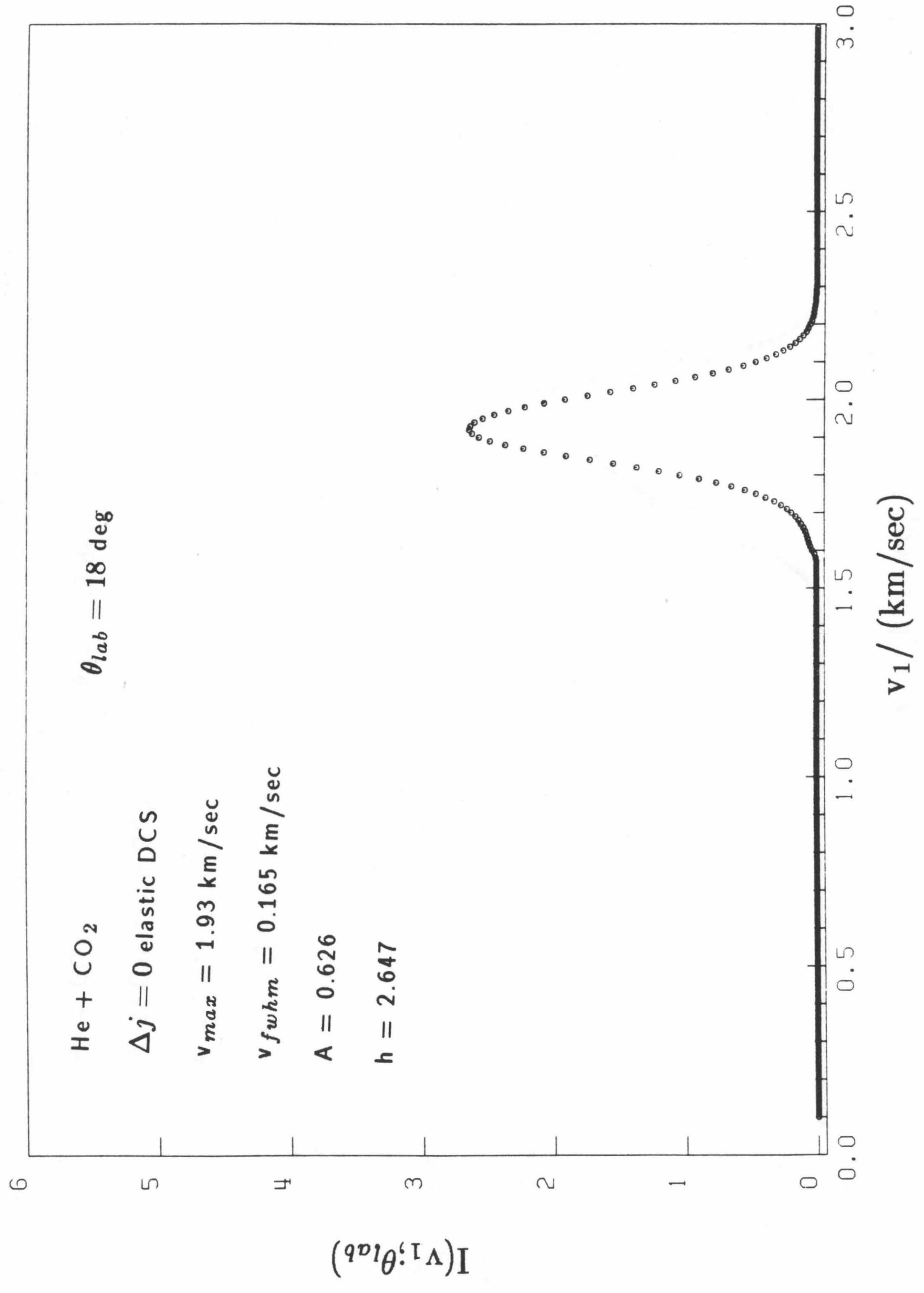

Figure 4b. Velocity resolved laboratory scattering signal for He.

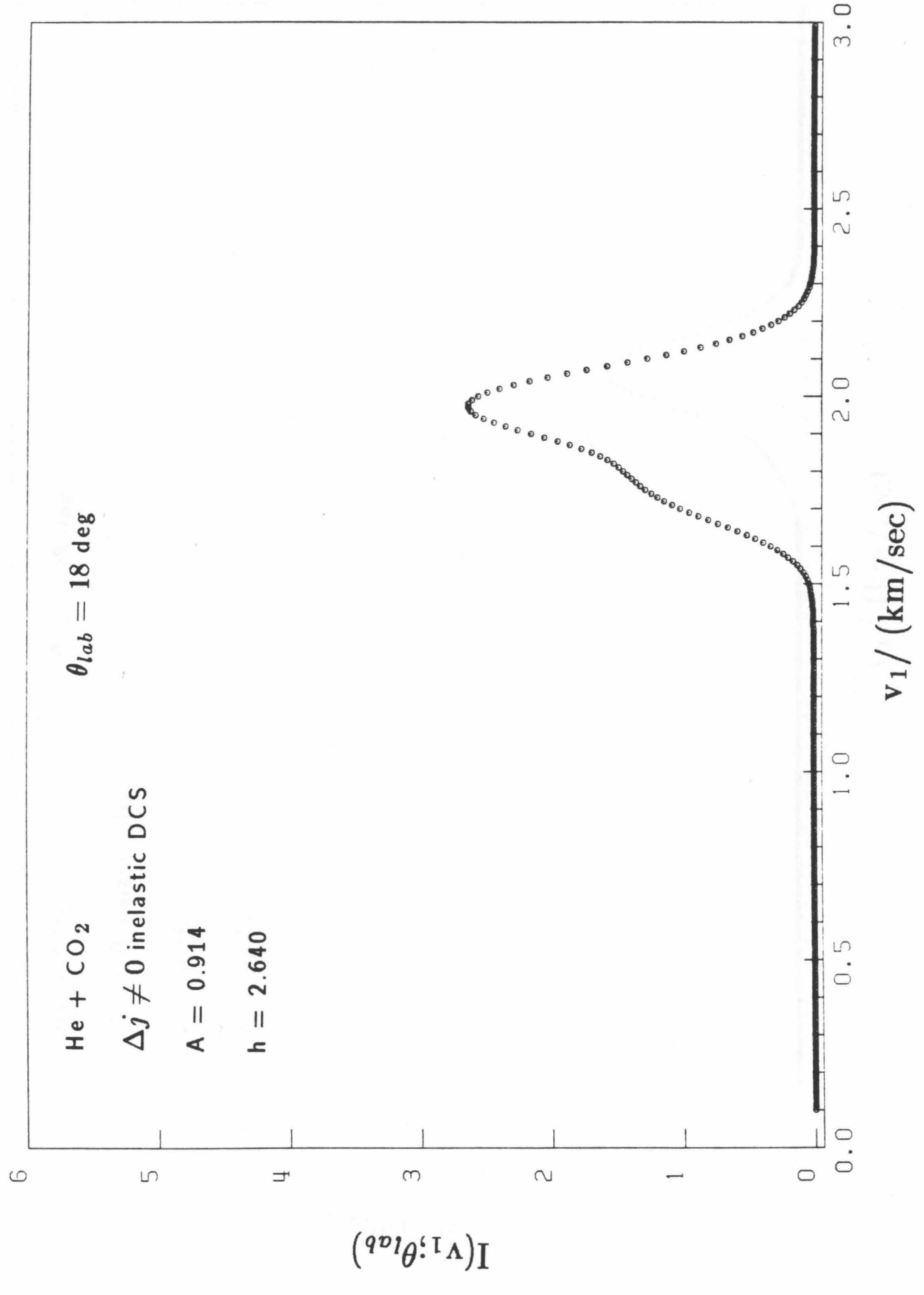

Figure 4c. Velocity resolved laboratory scattering signal for He.

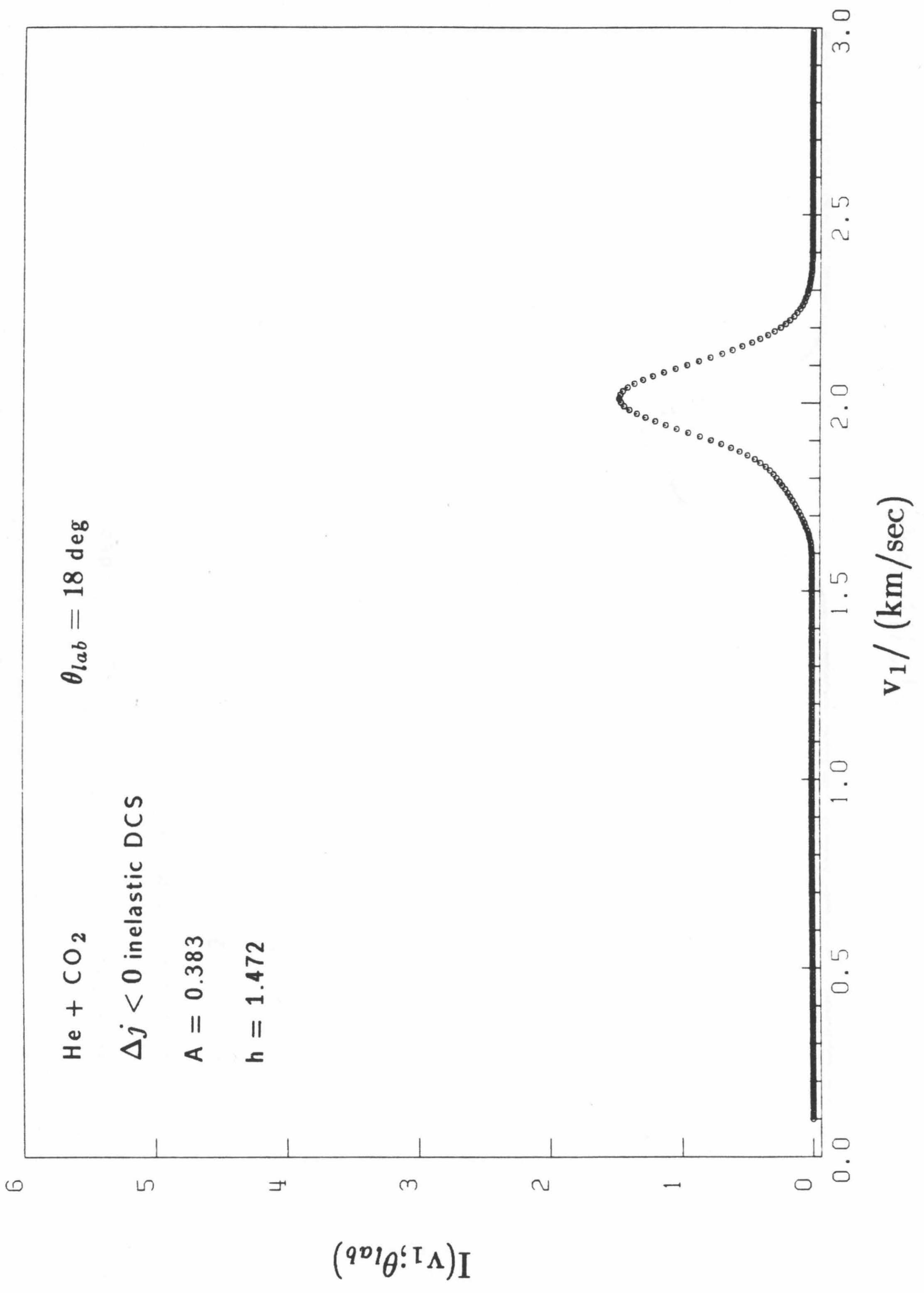

Figure 4d. Velocity resolved laboratory scattering signal for He.

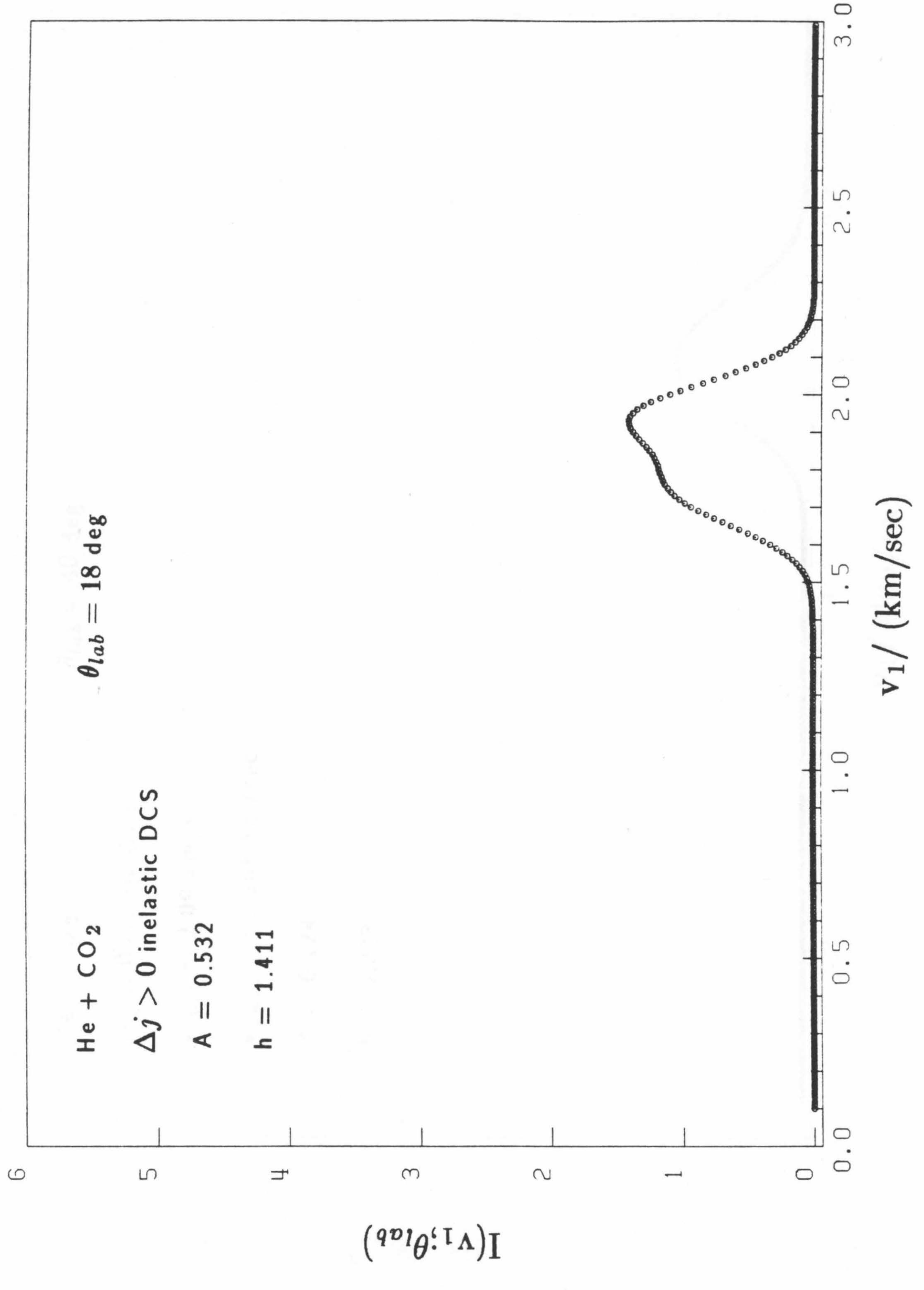

Figure 4e. Velocity resolved laboratory scattering signal for He.

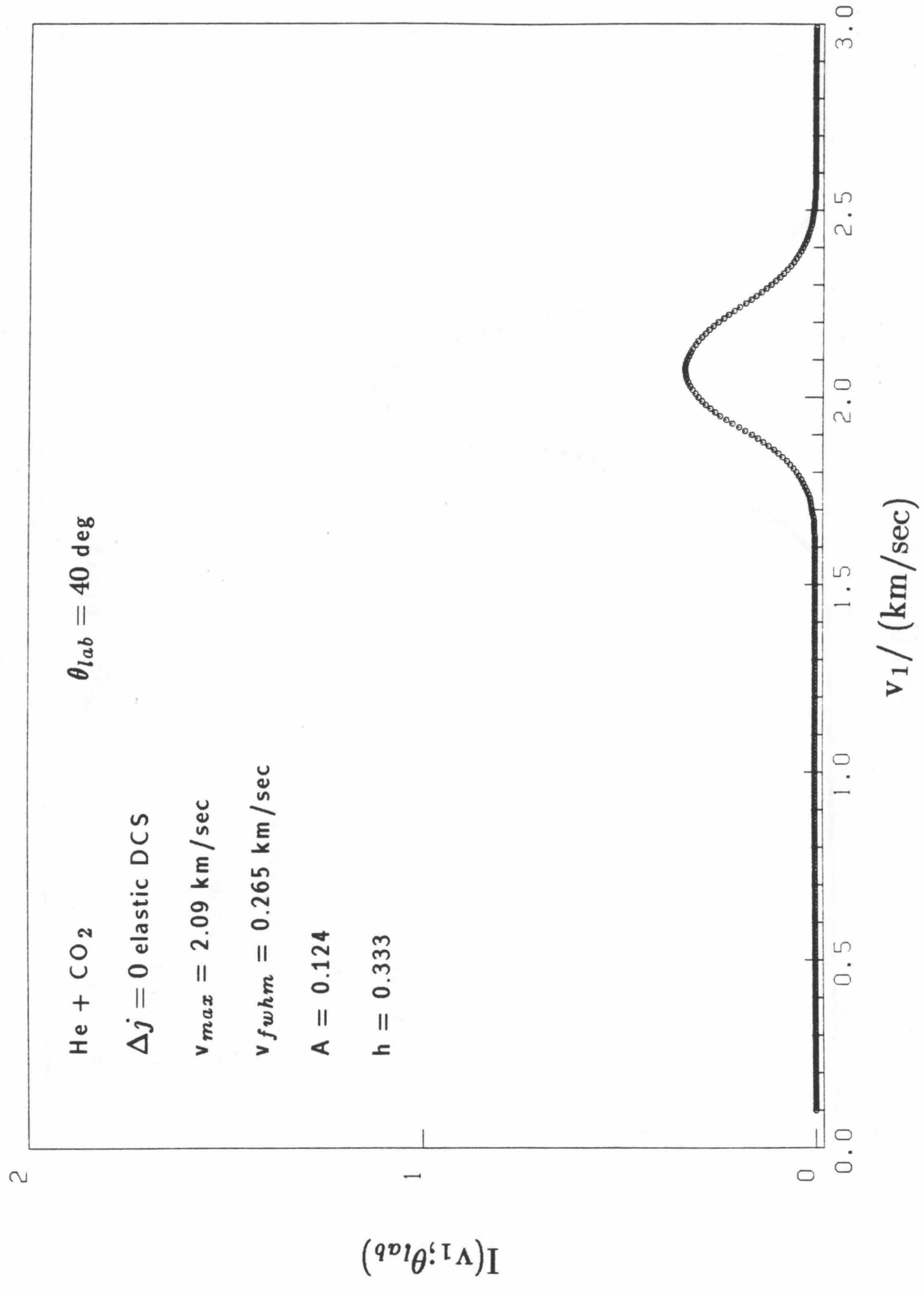

Figure 5a. Velocity resolved laboratory scattering signal for He.

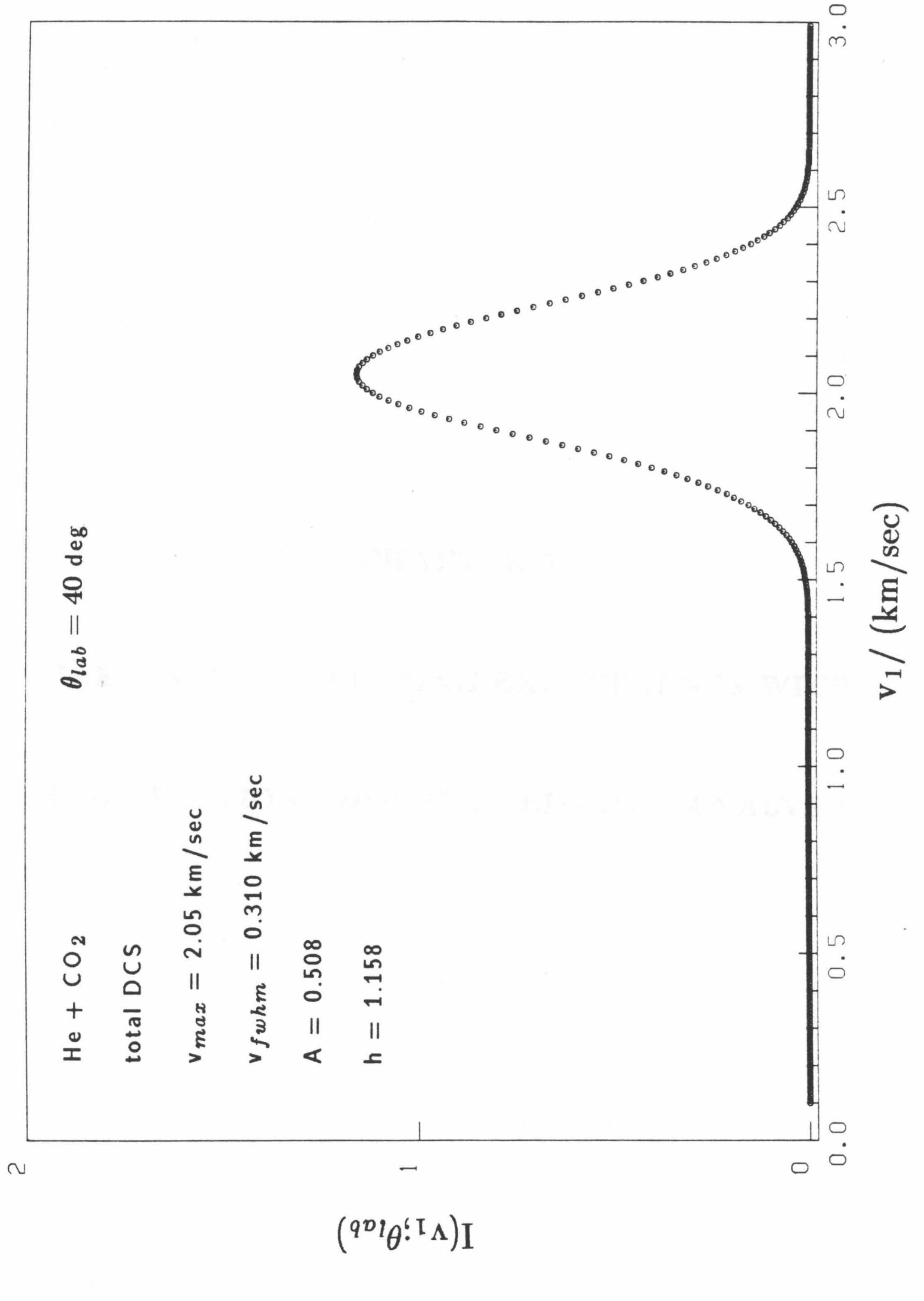

Figure 5b. Velocity resolved laboratory scattering signal for He.

CHAPTER 5

INELASTIC SCATTERING EXPERIMENTS WITH CORRELATION CHOPPER VELOCITY ANALYSIS

1.INTRODUCTION

In the previous chapter we described a method for simulating velocity resolved laboratory DCS data for an assumed interaction potential. From these simulations for He + CO_2 we showed that the velocity distribution of the scattered He contains rotationally inelastic contributions that can be related to potential anisotropy. In this chapter we describe experimental techniques for measuring these velocity distributions and present results of preliminary experiments for He + CO_2.

In Section 2 we review the theoretical background behind the correlation chopper technique for measuring the time-of-flight distributions (which are easily converted to velocity distributions) of the scattered particles. The primary advantage of the correlation chopper technique is its high duty cycle of almost 50%, over alternate time-of-flight and velocity analysis techniques. For instance the velocity selector described in Chapter 2, has a duty cycle of 0.5%, while a single slot chopper with a resolution of the correlation chopper described in this chapter will have a duty cycle of about 1%. Thus, the correlation chopper offers at least a factor of 50 advantage over the other techniques, meaning that the data collection time will be appropriately reduced for the same quality of data.

In Section 3 we present a simulation of the performance of our chopper. In Section 4 we outline the modifications to the molecular beam apparatus described in Chapter 2, in order to facilitate correlation chopper experiments. In Section 4 we discuss the results for preliminary experiments for He + CO_2. In the final section we mention suggestions for improvements to the apparatus to facilitate further experiments.

2.CORRELATION CHOPPER THEORY

The correlation chopper was initially developed to measure velocity distributions of cold neutrons. Von Jan and Scherm[1] along with Price and Sköld[2,3] have presented the theory and means of application to neutron spectrometry. The technique was naturaly adaptable to measuring velocity distributions of scattered atoms and molecules, and numerous descriptions of the theory and apparati have been presented.[4-6] This section will most closely follow the outline and notation of von Jahn and Scherm[1], and hence, individual references will be omitted.

2.1. THE TECHNIQUE

In an experiment utilizing a correlation chopper, particles along a given direction (determined by their source and the point of detection) are modulated according to the modulation function $M(t)$ by a correlation chopper located near their source, and are then detected as a function of time by a detector at a distance d from the chopper. The modulation function $M(t)$ basically determines how much scattered beam is passed to the detector at a given time t and has values ranging from 0 to 1. The quantity we wish to measure is the time-of-flight distribution $S(t)$ of the scattered beam, and is assumed to be non-zero for a finite range $0 \leq t \leq T$. The signal $z(t)$ at the detector is given by

$$z(t) = \int_0^T S(t')M(t-t')\mathrm{d}t' + B \tag{2.1}$$

where B is the time-independent background intentsity.

The modulation function $M(t)$ can be described as

$$M(t) = \sum_{i=1}^{N} x_i f(t - t_i) \tag{2.2}$$

where the chopper has been divided into N equally spaced intervals i of a time duration ϑ. Therefore one chopper rotation occurs in a period of $N\vartheta$. Each interval i is specified by $x_i = \{0, 1\}$ indicating the presence ($x_i = 1$) or absence ($x_i = 0$) of an open slot. The function $f(t - t_i)$ specifies the shape of the pulse produced by an individual chopper interval lasting from $t = t_i - \vartheta$ to $t = t_i$.

An ideal modulation $M(t)$ is one characterized by a δ-function autocorrelation

$$\begin{aligned} A^{MM}(\tau) &= \frac{1}{T}\int_0^T M(t)M(t-t')\mathrm{d}t \\ &= a\delta(\tau) + b \end{aligned} \tag{2.3}$$

if the time T is sufficiently large. The constants a and b depend upon the exact form of $M(t)$.

For this correlation $M(t)$ it is possible to reconstruct the time-of-flight distribution $S(t)$ from the detected signal $z(t)$ by way of the cross correlation $P(\tau)$, which is defined by

$$P(\tau) \equiv \frac{1}{T}\int_0^T z(t)M(t-\tau)\mathrm{d}t \tag{2.4}$$

which from equation (2.3) can be written as

$$\begin{aligned} P(\tau) &= a\int_0^T S(t')\delta(\tau - t')\mathrm{d}t + b\int_0^T S(t')\mathrm{d}t + B\frac{1}{T}\int_0^T M(t-t')\mathrm{d}t' \\ &= aS(\tau) + b\int_0^T S(t')\mathrm{d}t + B\frac{1}{T}\int_0^T M(t-t')\mathrm{d}t' \end{aligned} \tag{2.5}$$

It is quite evident that $P(\tau)$ is indeed proportional to the desired distribution $S(\tau)$. We now need to establish the constants a and b so as to minimize the background distribution.

2.2. PROPERTIES OF THE MODULATION FUNCTION

In order for the modulation function $M(t)$ (equation (2.2)) to meet the requirements of equation (2.3) it must meet several criteria, which will be imposed on the functions x_i and $f(t-t_i)$. First the pulse shape function must obey the relation

$$\sum_i f(t-t_i) = 1 \tag{2.6}$$

where rigorously, the sum is over N, but in practice it includes at most $i-1$, i and $i+1$. All this relation makes sure of is that when neighbouring pulses overlap they should add up to a plateau. The ideal form for $f(t-t_i)$ is a pure step pulse such that it is non-zero only for

$t_i - \vartheta \le t \le t_i$. Since real choppers cannot instantanously block and unblock a beam of particles, the process of blocking and unblocking will show up as a gradual fall and rise in the modulation, with $f(t - t_i)$ reflecting this property. If two or more consecutive intervals are open to beam transmission then the region between the rise and fall must be a flat plateau; equation (2.6) ensures this.

The autocorrelation of the discrete sequence x_i must be of the δ-function type such that

$$A_k \equiv \sum_{i=1}^{N} x_i x_{i+k} = \begin{cases} A_0 & k{=}0,N,2N,3N\ \ldots \\ A & \text{otherwise} \end{cases} \tag{2.7}$$

where the constants A_0 and A are integers because the $x_i = \{0,1\}$.

Sequences which have autocorrelations of the above type are called pseudorandom sequences.[7,8] The autocorrelation function can be solved in terms of the constants A_0 and A for a modulation with m pulses per period of chopper rotation, i.e. in one rotation m slots out of N will be open. This then give by inspection

$$A_0 = \sum_{i=1}^{N} x_i^2 = m \tag{2.8}$$

We can easily show that

$$\sum_{i=1}^{N} A_k = \left[\sum_{i=1}^{N} x_i\right]^2 = m^2$$

and from equation (2.7)

$$\sum_{i=1}^{N} = A_0 + (N-1)A$$

combining these two equation we obtain an expression for A

$$A = \frac{m(m-1)}{N-1} \tag{2.9}$$

Since A must be an integer several other conditions must be satisfied before equation (2.9) is met. A set of sequences called minimum length sequences or shift register sequences fulfill all the above requirements. The number of intervals N is

$$N = 2^n - 1 \tag{2.10a}$$

where n is an integer. The number of open intervals is

$$m = (N+1)/2 \tag{2.10b}$$

The sequence is generated with a binary shift register having n digits d_l. The register is shifted to the right, where the rightmost digit d_n determines x_i for the i-th shift of the register. The new leftmost digit d_1 is obtained by taking the exclusive-or (modulo two addition) of the rightmost digit d_n with a set of digits $\{d_{l1}, d_{l2}, d_{l3}, \ . \ . \ . \ \}$[7,8,4]

$$d_1^{i+1} = d_{l1}^i \oplus d_{l2}^i \oplus d_{l3}^i \oplus \ . \ . \ . \ \oplus d_n^i \tag{2.11a}$$

$$d_l^{i+1} = d_{l-1}^i \qquad l \neq 1 \tag{2.11b}$$

$$x_i = d_n^i \tag{2.11c}$$

The number of digits $\{d_{l1}, d_{l2}, d_{l3}, ...\}$ varies upon the sequence required. A useful starting shift register is one where all the d_n^1 are set to 1. For a set of digits to be modulo-two added the resulting sequence must be verified so that it does indeed meet all the criteria; not all sequences generated by this method meet the criteria.

2.3. CROSSCORRELATION

In equation (2.4) we crosscorrelated the signal $z(t)$ with the modulation function $M(t - \tau)$ and showed that the time-of-flight distribution $S(t)$ can be recovered from the crosscorrelation $P(\tau)$ in equation (2.5). It would be simpler if one could crosscorrelate from the discrete sequence x_i. The crosscorrelation is

$$\begin{aligned} P(\tau) &= \int_0^{T_r} z(t)x(t-\tau)dt \\ &= \sum_{i=1}^{rN} x_i \int_{t_i - \vartheta}^{t_i} z(\tau + t)dt \end{aligned} \tag{2.12}$$

where T_r is the total data collection time $T_r = rN\vartheta$ for r revolutions of the chopper.

Subsitituting equation (2.1) for $z(\tau + t)$ gives

$$P(\tau) = r\left[\sum_{i,j}^{N} x_i x_j \int_0^{N\vartheta} \int_{t_j-\vartheta}^{t_j} f(\tau + t - t' - t_i) S(t') dt \ \ dt' + \bar{B}\sum_i^N x_i\right] \tag{2.13}$$

where $\bar{B} = \vartheta B$ is the background per interval. The double integral involving $S(t)$ is merely a convolution over the pulse shape function and the the width of one interval (ϑ). We can redefine this integral to be

$$\bar{S}(\tau + \tau') \equiv \int_0^{N\vartheta} \int_{\tau'-\vartheta}^{\tau'} f(\tau + t - t') S(t') dt \ \ dt' \tag{2.14}$$

From equation (2.7) we have

$$P(\tau) = r\left[\sum_{k=1}^{N} A_k \int_0^{N\vartheta} \int_{t_k-\vartheta}^{t_k} f(\tau + t - t') S(t') dt \ \ dt' + \bar{B}\sum_i^N x_i\right] \tag{2.15}$$

where $t_k = t_j - t_i$ (and hence $k = j - i$) .

By taking into account equations (2.6), (2.7), and the following trivial relations

$$\int_0^T f(t) dt = \vartheta \qquad \text{for large } T$$

$$\int_0^T \bar{S}(t) dt = \vartheta \int_0^T S(t) dt$$

we obtain

$$P(\tau) = rm\left[(1-D)\bar{S}(\tau) + \frac{D}{\vartheta}\int_0^{N\vartheta} \bar{S}(t)dt + \bar{B}\right] \tag{2.16a}$$

the integral can easily be converted into a sum by considering the inner integral of equation (2.14), this yields

$$P(\tau) = rm\left[(1-D)\bar{S}(\tau) + D\sum_{i=1}^{N} \bar{S}(t_i) + \bar{B}\right] \tag{2.16b}$$

where D is the duty cycle of the chopper and is given by $D = A/m$ (A is defined by equation (2.9)).

The above equation provides the means for solving for the pulse-shape- and interval-width-convoluted distribution $S(t)$. If $S(t)$ is significantly wider than $f(t)$ or ϑ then $\bar{S}(t)$ will for all practical purposes be identical to the true distribution.

2.4. CHANNELS OF FINITE WIDTH

Under experimental conditions data are collected into channels of finite width such that data $z(t)$ are integrated over the width of the channel ϑ. An integral of this type appears in equation (2.12) for the crosscorrelation of $z(t)$ with x_i. We can define a discrete form for $z(t)$ such that

$$z[\tau + t_i] \equiv \int_{t_i-\vartheta}^{t_i} z(\tau + t)dt \tag{2.17}$$

We can also define similar discrete forms for the deconvolution $P(t)$ and the distribution $\bar{S}(t)$. Where a "τ" in square brackets is now discrete $\tau = k\vartheta$ for $k = 0, 1, 2, 3, \ \ldots \ , N$.

Rearranging equation (2.16b) for discrete τ and solving for $S[\tau]$ we obtain

$$\bar{S}[\tau] = \frac{1}{1-D}\left[\frac{1}{rm}\sum_{i=1}^{rN} x_i z[\tau + t_i] - D\sum_{i=1}^{N} \bar{S}[t] - \bar{B}\right] \tag{2.18}$$

The sum over $\bar{S}[t]$ is a constant and can be related to the total signal and background which permits us to write

$$\bar{S}[\tau] = \frac{1}{mr}\sum_{i=1}^{rN} \frac{x_i - D}{1-D} z[\tau + t_i] - \bar{B} \tag{2.19}$$

In general the most efficient correlation-choppers have a duty cylce of $D \equiv A/m = 1/2$, see equations (2.9) and (2.10b). We can sum all the $z[\tau + t_i]$ for all the revolution to obtain

$$Z[\tau + t_i] = \sum_{l=0}^{r} z[\tau + t_i + l\vartheta N] \tag{2.20}$$

We also can define a new correlation sequence

$$\begin{aligned} a_i &\equiv \frac{x_i - D}{1 - D} \\ &= \{-1, 1\} \qquad \text{for} \quad D = 1/2 \end{aligned} \tag{2.21}$$

yielding

$$\bar{S}[\tau] = \frac{1}{mr} \sum_{i=1}^{N} a_i Z[\tau + t_i] - \bar{B} \tag{2.22}$$

This is the most useful form for computational purposes and will be employed in all analyses and data reduction described below.

2.5. VELOCITY DISTRIBUTIONS

A velocity distribuition $F(v)dv$ measures the number of particles having velocities v in the range v to $v + dv$. This must equal the number of particles specified by the time-of-flight distribution $S(t)dt$

$$F(v)dv = S(t)dt$$

then

$$F(v) = S(t)\frac{dt}{dv}$$

since for a given constant velocity the flight time over distance R is

$$t = \frac{R}{v}$$

then

$$F(v) = \left(-\frac{R}{t^2}\right) S(t) \tag{2.23}$$

Therefore to convert a time-of-flight distribution to a velocity distribution one must divide by the square of the flight time.

3.CORRELATION CHOPPER SIMULATION

The correlation chopper which was used for the experiments to be described in the next section, consists of 255 intervals $(2^8 - 1)$. The sequence that specifies the chopper may be generated according to equation 2.11, which we repeat for this particular case

$$d_1^{i+1} = d_2^i \oplus d_3^i \oplus d_8^i \tag{3.1a}$$

$$d_l^{i+1} = d_{l-1}^i \qquad l \neq 1 \tag{3.1b}$$

$$x_i = d_8^i \tag{3.1c}$$

where d_l^i is the l-th digit of an a 8-digit shift register after i shifts to the right of that register, the 8-th digit is the rightmost one. The left-most digit is constructed by modulo two addition of bits 2, 3, and 8. (The digits are binary quantities with values of either 0 or 1). Figure 1 shows the resultant correlation sequence. Since the sequence is periodic for every 255 interval the starting position can be chosen arbitrarily. For the experiments to be described below, the chopper is installed such that the sequence begins with a value of 143_8 for the initial shift register (the octal representation of the shift registers is such that the least significant digit of the binary equivalent corresponds to the 8-th register digit).

Prior to presenting experimental details it is worthwhile to perform simulations of the correlation chopper operation. In Figure 2 we plot a Gaussian veleocity distribution of the form

$$G(v) = Ae^{-\alpha(v-v_o)^2} \tag{3.2a}$$

where v_o is the most probable velocity, A is a normalization factor, α is the width parameter and is related to the velocity full-width-at-half--maximum v_{fwhm} by

$$\alpha = \frac{v_{fwhm}^2}{4\ \ln 2} \tag{3.2b}$$

This particular Gaussian is centered at $v_o = 1.5$ km/sec with a $v_{fwhm} = 0.4$ km/sec. What does the signal $Z[t_k]$ look like when this Gaussian velocity distribution is convoluted by our chopper with a detector at 13 cm from it (an actual representation of the experimental apparatus described below)?

Figures 3 thru 5 show $Z[t_k]$ for three different v_o with various widths v_{fwhm}. The predominant trait of these plots is the smoothing of sharp structure with an increase of probability of lower velocities; this is evident if we compare plots for one value of v_o with an increase in width, or if we compare plots for one value of v_{fwhm} with a decrease in v_o. The very narrow and high velocity peak (Fig. 3a, $v_o = 2.0$ km/sec, $v_{fwhm} = 0.1$ km/sec) bears a very strong resemblance to the chopper correlation sequence (Fig. 1). There is very little smoothing of the sequence, only prior to and after a change from open to closed (or vice versa) does $Z[t_k]$ show some smoothing. A decrease in velocity $v_o = 1.5$ km/sec for the same width shows greater smoothing and also an upward shift in time t_k, as would be expected since the lower velocities will have a longer chopper-detector flight time than higher ones. This type of behavior can be seen in the other plots. The reason that $Z[t_k]$ is smoothed with a decrease in v_o for an equal width v_{fwhm} is that this technique measures time-of-flight distributions $S(t)$; at higher flight times (lower velocities) the flight-time density dt increases for a fixed velocity density dv: $dt \propto v^2 dv$. Basically, lower velocities (longer flight times) shift $Z[t_k]$ to the left. A greater density of flight-times produces broadening of $Z[t_k]$, since each flight time individually results in a different shift in $Z[t_k]$.

4. EXPERIMENTAL APPARATUS

The crossed beam apparatus has been described previously in Chapter 2 (Sec. 4), and hence only changes from this will be presented here. These changes can be classified as improvements in the apparatus or modifications to accommodate the correlation chopper, and are shown in Figure 7.

In order to improve the signal to noise ratio for the correlation chopper experiments the pumping speed in the mass-spectrometer has been increased by substituting the ion pumps with turbo-molecular pumps TMP_b and TMP. The TMP_b[11] pumps helium at 60 liters/sec (air at 55 liters/sec), which is a dramatic improvement over the ion pump pumping speed of 0.3 l/sec for He (5 l/sec for air). Since this pump is in the differential buffer chamber between the scattering region and the ionizer (I) of the mass-spectrometer, it limits the number of atoms and molecules in the scattering chamber which are not in collimation with the detector apertures, from entering the ionization region. For a He + CO_2 scattering experiment (see Chapter 2) the background signal for helium (the CO_2 beam entering into the scattering chamber but not crossed with the He) at a scattering angle of 10 degrees was 9×10^3 counts/sec. If the ion (5 l/sec) pump was turned off the background signal increased to 18×10^2 cnts/sec. Under otherwise identical conditions, but with the 60/l pump in place of the ion pump, this background is reduced to about 250 cnts/sec. In both cases the background is relatively constant for scattering angles greater than (and equal to) 10 degrees.

The other turbo-molecular pump (TMP)[12] has a pumping speed of 350 liters/sec. It essentially replaces the liquid-helium cryo-pump (CP). Although the cryo-pump has an estimated pumping speed of 300 l/sec, it makes a negligible contribution to reducing the He background signal level when the turbo pump is operational. The reason for this could be related to how the cryo-pump functions. Helium atoms at a partial pressure in the 10^{-10} torr range can not condense on a surface which is at liquid helium temperatures (at 1 atmosphere). Rather, they are occluded in crystals of other gases which do condense and freeze on the cryo-surface. Since the turbo pump removes most of these gases the cryo-pump is not able to effectively pump helium. The major advantage of the turbo-molecular pump over the cryo-pump is the convenience of operation and the indefinte running time (the cryo-pump hold liquid helium for 4 hours). Also the turbo-pump is able to maintain a pressure of 4×10^{-10} torr for stand-by mode, and 8×10^{-10} during experiments.

The position of the correlation chopper is shown in Figure 7. It is located 13.0 cm before the center of the ionization region. For visual clarity the gate valve which covers the entrance aperture of the detector, has been omitted from the figure; nonetheless it is present. For the time-of-flight experiments the primary beam modulator (descibed in Chapter 2, not shown in the figure) is still in place but is not rotating, rather, it is held in a fixed position so as to pass the entire primary beam.

The chopper is rotated by a hysteresis synchronous motor[9] at frequencies ranging from 400 to 650 Hz. In order to operate at the higher frequencies it is necessary to periodically replace the bearings[10]. Frequencies up to 950 Hz can be achieved but the chopper rotation is not stable for a long time and bearing wear is severe. Cooling is very important for the motor which may heat up above the safe operating temperature of 85 C in less than 8 hours, causing premature bearing wear and potential damage to the motor windings.

Figure 8 show a functional schematic of the correlation chopper drive and data collection system, the heart of which is the multi-channel scaler (MCS). It generates the signal that drive the chopper motor, collects the data, and transmits it to a PDP 11/03 computer. In order to drive the drive the chopper motor the MCS generates two pulses for the duration ϑ of one channel (corresponding to $Z[t_k]$, see equation 2.20), these are then divided by the number of chopper intervals N $(2^8 - 1 = 255_{10} = 377_8)$ to produce a square wave. The square wave is filtered and amplified to yield a sine wave, which is input into a power amplifier[13]. The output of the amplifier is impedence matched and stepped up with a transformer[18] for use with the motor. The phase matching capacitor (C) mantains a 90 degree phase delay between the two motor windings; its value has been optimized at 0.22 μf for 400 Hz and 0.06 μf for 650 Hz. As the chopper completes one revolution its large slit passes between a light emitting diode (not shown) and a photo diode which generates a trigger signal in the MCS. The "chopped" atoms (or molecules) enter the ionization (I) region of the detector. The resulting ions are mass filtered (quadrupole mass filter QMF) and impinge on the Channeltron electron multiplier (CEM). The CEM current is converted to pulses via a pulse amplifier and discriminator. The pulses a counted by the MCS and are stored in memory.

The MCS is a virturally identical copy of one developed by Brian Reid and Randal Sparks[17], which is a modification of a model designed at the University of California[19]. A schematic of the basis functions is shown in Figure 9. The unit is designed in conjuction with a CAMAC crate[14,15], which interfaces easily with any computer via the CAMAC dataway and a computer specific controler[16]. A 20 MHz clock signal is divided to a lower frequency to provide the data channel interval ϑ, the increment for the memory, and the drive pulses for the motor (as described in the previous paragraph). The channel interval can be set by computer at any value from 1 to 999 μsec. The memory is incremented untill a preset memory address is reach, the unit the waits for the trigger pulse from the chopper before continuing to collect more data. The trigger pulse is the signal that initiates data collection; if the memory counter does not reach the preset value before the trigger signal it is reset to zero and data collection resumes for a chopper revolution. The data collection stops after a given number (set by the computer) of trigger signals (chopper revolutions). At this time the computer may read the data from the MCS memory, it may also clear the memory, and then proceed with more accumulation of data. A sweep counter is also provided to count down each time the trigger counter reaches zero; it primarily functions as an aid to the users (the value is displayed on the front panel of the MCS). The unit is equiped with dual data counters; as one is counting the incoming data, the other is added to a memory location for a given channel. The memory increment signal switches the function of the counters. This dual counter system has a very short "dead" time between channels (time during which no pulse are counted) of 60 $n$sec, which is almost insignificant compared to the 80 $n$sec width of the data pulses.

For the He + CO_2 velocity resolved experiments the beam operating conditions are identical to those for the total DCS experiments (see Chapter 2). The chopper is operated 653.59 Hz, which corresponds to 6 μsec per MCS channel. Data are collected with the MCS for 6500 chopper revolutions (triggers) before the computer reads and clears the MCS memory and restarts the data collection. This gives the computer time to add this data to an array, deconvolute the data to a velocity distribution, and plot it on a display, before it is time to read in the next set of data. The scattering signal is measured with the beams crossed for about 10 minutes (60 sweeps), the beams are uncrossed and the background signal is measured for the same time period. Both measurments are necessary, since the background signal has a thermal velocity distribution which contributes to the total signal. Measurement times range from about 1 to 2 hours for low scattering angles (below 7 degrees) to 120 hours for large scattering angles (40 degrees).

5.PRELIMINARY RESULTS

Figure 10a shows the deconvoluted velocity distribution for a He beam entering the mass spectrometer at 0.75 degrees; Figure 10b shows the "raw" data from which the deconvolution was made. In order to reduce the pumping load on the mass-spectrometer chamber, the measurement was made at this small angle rather than with the beam going directly into the detector. Also to reduce gain degradation on the Channeltron electron multiplier (CEM) the mass-spectrometer ionizer was operated at a reduced ionization efficiency. The resultant velocity spectrum compares favorably with the one obtained using the velocity selector, as described in Chapter 2 (Sec. 2.4). The position of the most probable velocity is at 1.76 km/sec, in both cases. The width of the peak is 12.4%, which is slightly higher than the 12.0% which was measured with the velocity selector. Also, the peak is somewhat broader near the baseline, this is most likely attributable to the fact that the deconvoluted signal does not give the actual time-of-flight (or velocity) distribution but rather a distribution which is the convolution of the actual distribution of the He atoms with the width of the individual chopper channel and the chopper shape function (Eq. 2.14). This verifies the choppers ability to resolve velocity distributions of similar characteristics.

The velocity resolved scattering signal for He + CO_2 was measured at several angles from 5 to 40 degrees. In Figures 11 thru 13 we present the deconvoluted velocity distributions (and the "raw" data - Fig. 11b for 5 deg.) for only three of these angles: 5, 13, and 18 degrees. In all three cases we do observe an outline of a distribution. However, these distributions are much wider than and are peaked at lower velocities than those predicted for these angles in Chapter 4. Also, they are very noisy. These problems are evident in the "raw" data plot for 5 degrees in Figure 11b; the "raw" data plots for the other angles are similar. There is much more noise in the "raw" plot than would be expected on the basis of Poisson statistics, which gives error bars of about 3% for Figure 11b (the full scale of the plot is for the range of Z_k from maximum to minimum, the range is 5.3% of the maximum signal Z_k). The small details that were pointed out in Section 3 as being indicative of higher velocities are completely obscured by this noise. The convoluted signal should resemble the one in Figure 10b; it, instead, has a very broad structure which implies a broad velocity distribution. The situation is similar for the other angles.

The above results give an indication of a velocity distribution for He scattered by CO_2 at several scattering angles. If the beams are uncrossed the resultant distribution is even broader and much weaker. However, the widths of these distributions are much too large for indentifying rotationally inelastic processes, and therefore these results are inconclusive.

There are several causes of broadening of the correlation chopper signal. The first one was mentioned before, i.e. the technique measures a distribution that is a convolution of the actual distribution and the chopper function. This is most unlikely to be the cause of the extreme broading of the measured distributions for the scattered signal, since the He beam distribution was only slightly broadened. The three most likely causes are: 1) jitter of the chopper blade, 2) insufficient pumping in the ionization region, and 3) the ionization region of the mass spectrometer has a high density of electrons such that ions that are formed there are trapped for a period of time before moving to the mass filter.

The jitter problem has been mentioned before.[6] It arises from the inherent friction of the bearings which gives rise to stick and slip effects and thus a jerky rotation of the blade. This problem is particularly prevalent at high rotation speeds and prolonged operation times. Our experience indicates that bearings will have a longer running life if they are operated for shorter periods of time (less than 2 hours) rather than one extended period. The accurate balance of the blade and the rotor (of the motor) has a strong effect on bearing life as well as vibration of the motor unit. Slight errors in balance cause such excessive vibrations that mounting screws will be removed.

Insufficient pumping in the ionization region will of course cause a high background count level, which makes it more difficult to distinguish the signal from that background. The introduction of the turbo-molecular pump TMP_b in the buffer chamber has reduced the background level by a factor of 50 for angles above 15 degrees. Also, the total signal with the beams crossed is much greater than the background (the beams uncrossed) at 5 degrees. Nonetheless the 5 degree velocity distribution is as broad as that at 13 or 18 degrees. Hence, it is unlikely that insufficient pumping is a major cause of the broadening.

The high density of electrons in the ionization region is probably the most likely cause of the broadening. The measurement of the velocity distribution for the He beam was performed with an electron emission current of 0.5 mA, while the measurements of the scattered signal were performed with an emission current of 15 mA. This is the only operational difference between the two cases. Unfortunately, the signal at angles above 15 degrees is so low that it it is unlikely that is can be observed at the low emission currents.

6. SUGGESTIONS FOR FUTURE EXPERIMENTS

The He + CO_2 velocity resolved experiments cannot be conducted any further under the above conditions, because the results are inconclusive. However, since we were able to diagnose several very probable causes of this inconclusiveness, we then propose several modifications to the molecular beam apparatus which will most likely remedy these problems for the rotationally inelastic experiments as well as for the planned H-atom reactive scattering experiments.[20]

A relatively straightforward modification is the increase of the distance between the correlation chopper and the ionization region from 13 to 19 cm. This can be done by rebuliding the support which holds the mass-spectrometer to the flange (the entire mass-spectrometer is contained on this flange permitting it to be remove from the chamber). This change will not alter the ionizer or the quadrupole mass filter in any way; only the distance between the exit aperture of the quadrupole and the electron multiplier needs to be decreased. Increasing the chopper-ionizer distance increase the flight time for particles with a given velocity, which in turn increases the number of deconvoluted channels for the width of a velocity distribution peak (see Eqs. 2.22 & 2.23), which effectively increases the resolution of the velocity peak. The same resolution can be obatined with an 19 cm distance as with the 13 cm one by lowering the chopper rotation frequency by a factor of 13/19.

The major advantage of the longer flight time is that the ion trapping mechanism, mentioned at the end of the previous section, will be less significant. The consequece of this mechanism is to smooth out (in time) the "raw" data, but with increasing chopper-ionizer distances the convoluted data ($Z[t_k]$ of Eq. 2.20) becomes smoother for the same velocity distribution.

Increasing of pumping speed in the mass spectrometer chamber, particularly in the ionization region, will decrease the background signal, permitting the measurement of lower scattering intensities. This in turn, will permit the lowering of the electron emission current of the ionizer. Currently the lowest level of background He (m/e = 4) is 200 counts per second at angles above 20 degrees, while the scattered signal at these angles can be as low 5 counts per second. A turbo-molecluar pump directly over the ionizer should reduce this background. The cryo-pump currently over the ionizer does not pump effectively with a fast turbomolecular pump in the same chamber for reasons discussed in Section 4. Additional backgound reduction can be achieved if the ionization region is isolated from the rest of the mass spectrometer, except for an aperture between the last ion lens and the quadrupole mass filter This way two chambers are formed, and atoms or molecules which are not ionized when they pass the ionizer will be pumped by the pump over the quadrupole region and will not be able to return to the ionization region.

If the ionizer is moved further away from the scattering region, space will be provided to insert another level of differential pumping on the entrance slits of the mass spectrometer chamber. This should further reduce background from the scattering chamber.

The correlation chopper bearings tend to wear out very quickly at frequencies of 650 Hz. They also produce a jerkey motion of the chopper blade. Comsa *et al.*[6] have observed a similar problem, which they solved very sucessfully by magnetically suspending the motor shaft. This is a highly recommended course of action for the chopper system described herein.

6. REFERENCES

1. R. von Jan and R. Scherm, *Nucl. Instr. and Meth.* **80**, 69 (1970).
2. K. Sköld, *Nucl. Instr. and Meth.* **63**, 114 (1968).
3. D. L. Price and K. Sköld, *Nucl. Instr. and Meth.* **82**, 208 (1970).
4. L. D. F. Allen, *Velocity Distributions by Correlation Techniques*, Los Alamos Scientific Laboratory Technical Report LA-5187, (1973).
5. C. V. Nowikow and R. Grice, *J. Phys. E: Sci. Instrum.* **12**, 515 (1979).
6. G. Comsa, R. David, and B. J. Schumacher, *Rev. Sci. Instrum.* **52**, 789 (1981).
7. W. D. T. Davies, *Control* **10**, 302 (1966).
8. K. R. Godfrey, *Control* **10**, 305 (1966).
9. TRW Globe Motors, Div. of TRW Inc., Dayton, Ohio;
   Model FC 751003-2.
10. Hamilton-Avnet Inc., Culver City, California; part number for bearings 15D023Z066 (with Krytox lubricant).
11. Balzers Inc., Hudson, New Hampshire; model TPU 50.
12. Leybold-Heraeus Vacuum Products Inc., Export, Pennsylvania;
    model TURBOVAC 360.
13. We use a standard audio power amplifier with a power rating of 120 watts for an 8 Ohm input. (Our amplifier is a NAD model 2140 stereo amplifier with 40 watts of power into 8 Ohms per channel; it is operated as a monophonic amplifier in bridged mode delivering 120 watts per channel).
14. D. Horelick and R. S. Larsen, *IEEE Spectrum*, **April**, 50 (1976);
    H. J. Stuckenberg, *CAMAC Bulletin* **13A**, 1 (1975).
15. Kinetic-Systems Corp., Lockport Illinois;
    CAMAC crate model 1500-P1K.
16. Standard Engineering Corp., Fremont, California; CAMAC crate interface to a Q-bus (PDP 11) model CCLSI-11.

17. Division of Chemistry and Chemical Engineering, Department of Chemistry, California Institute of Technology; Electronic Support Group reference no. ESG 4821.
18. Universal Transformer Corp., New York, New York; model GVP-4.
19. R. K. Sparks, Ph.D. Thesis, University of California, Berkeley (1979).
20. J. F. Garvery, Ph.D. Thesis, California Institute of Technology (1985).

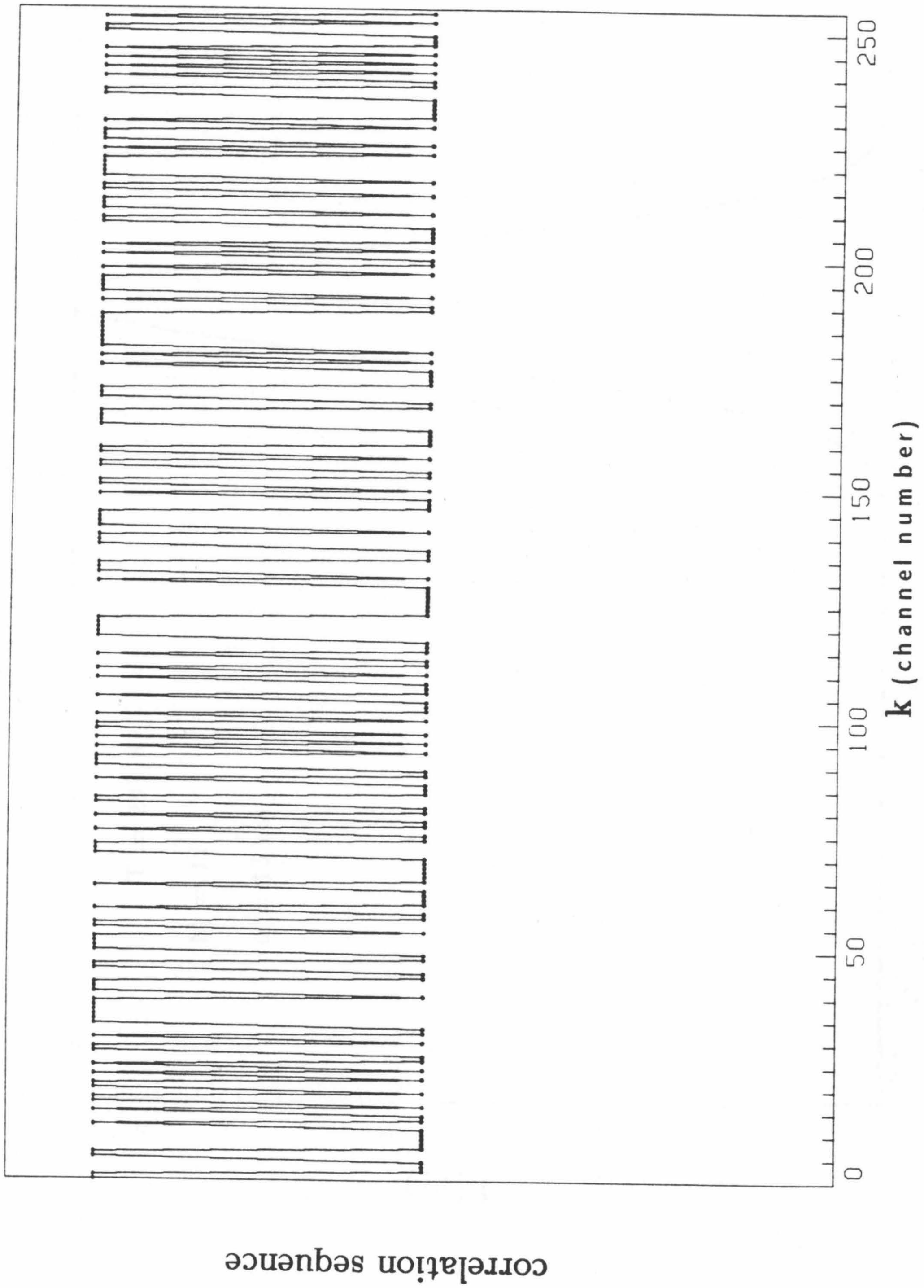

Figure 1. Correlation chopper sequence.

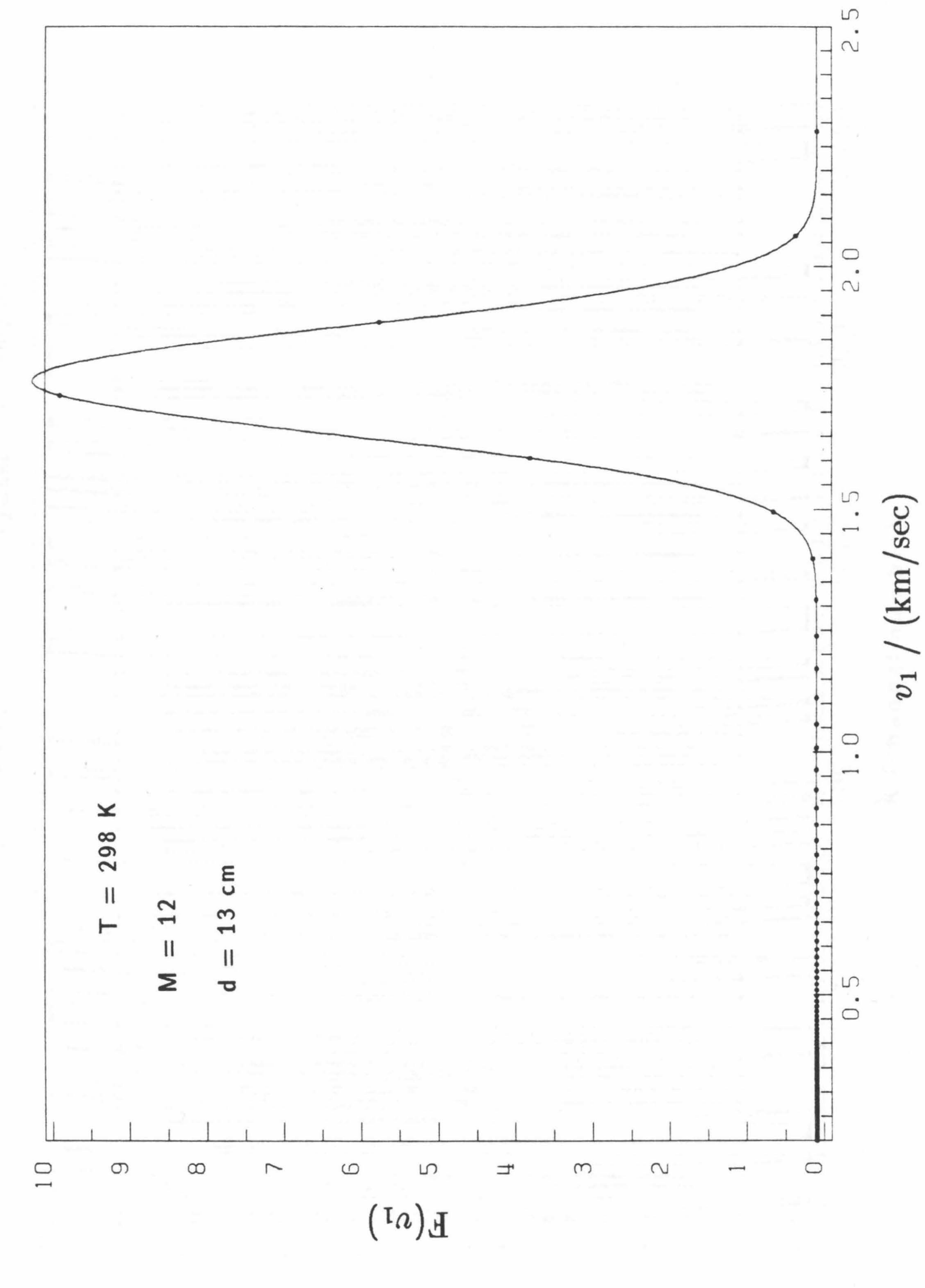

Figure 2. Gaussian velocity distribution. The points are for a deconvolution of the convoluted signal in Fig. 4c.

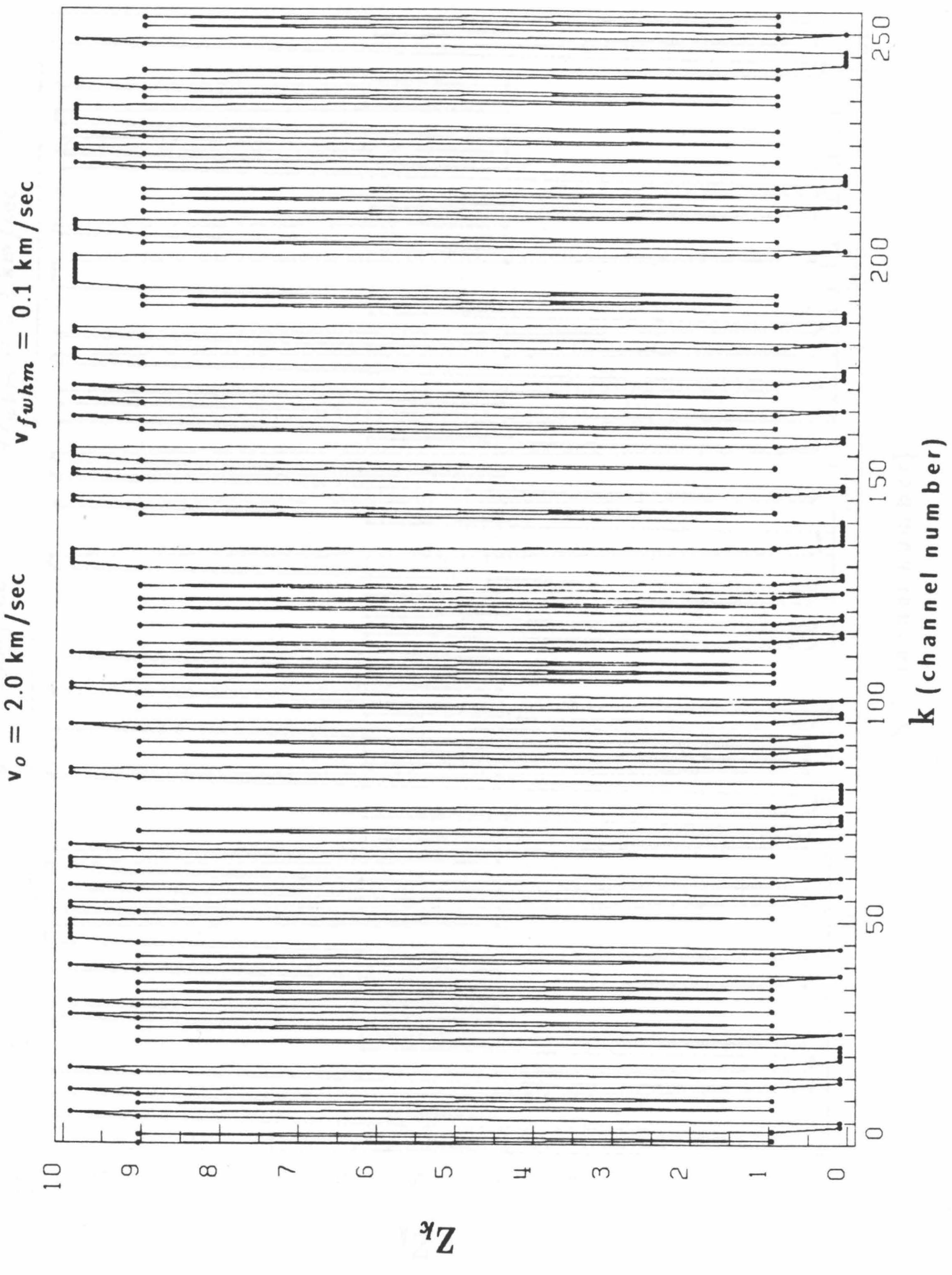

Figure 3a. Convolution of a Gaussian velocity distribution.

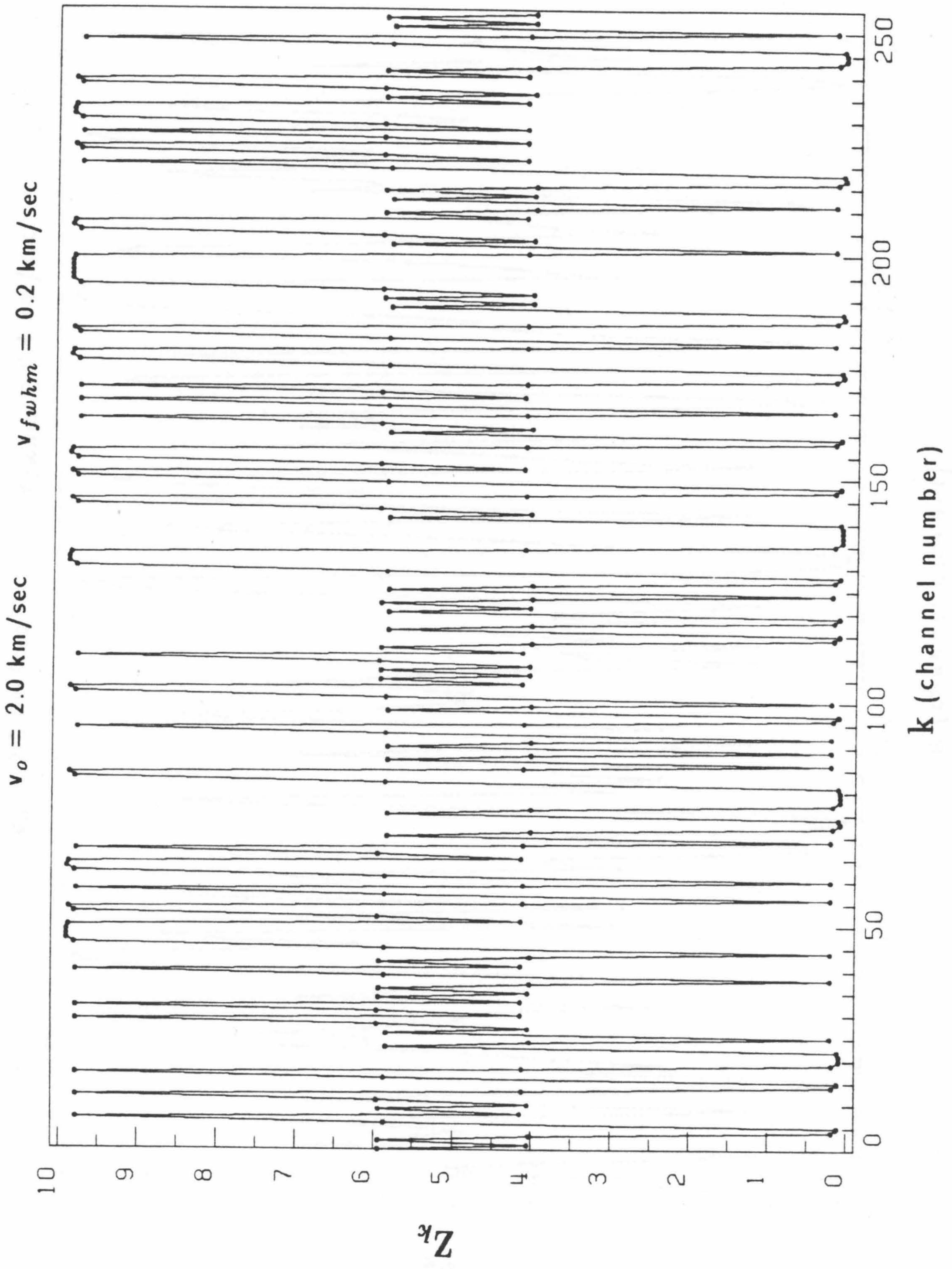

Figure 3b. Convolution of a Gaussian velocity distribution.

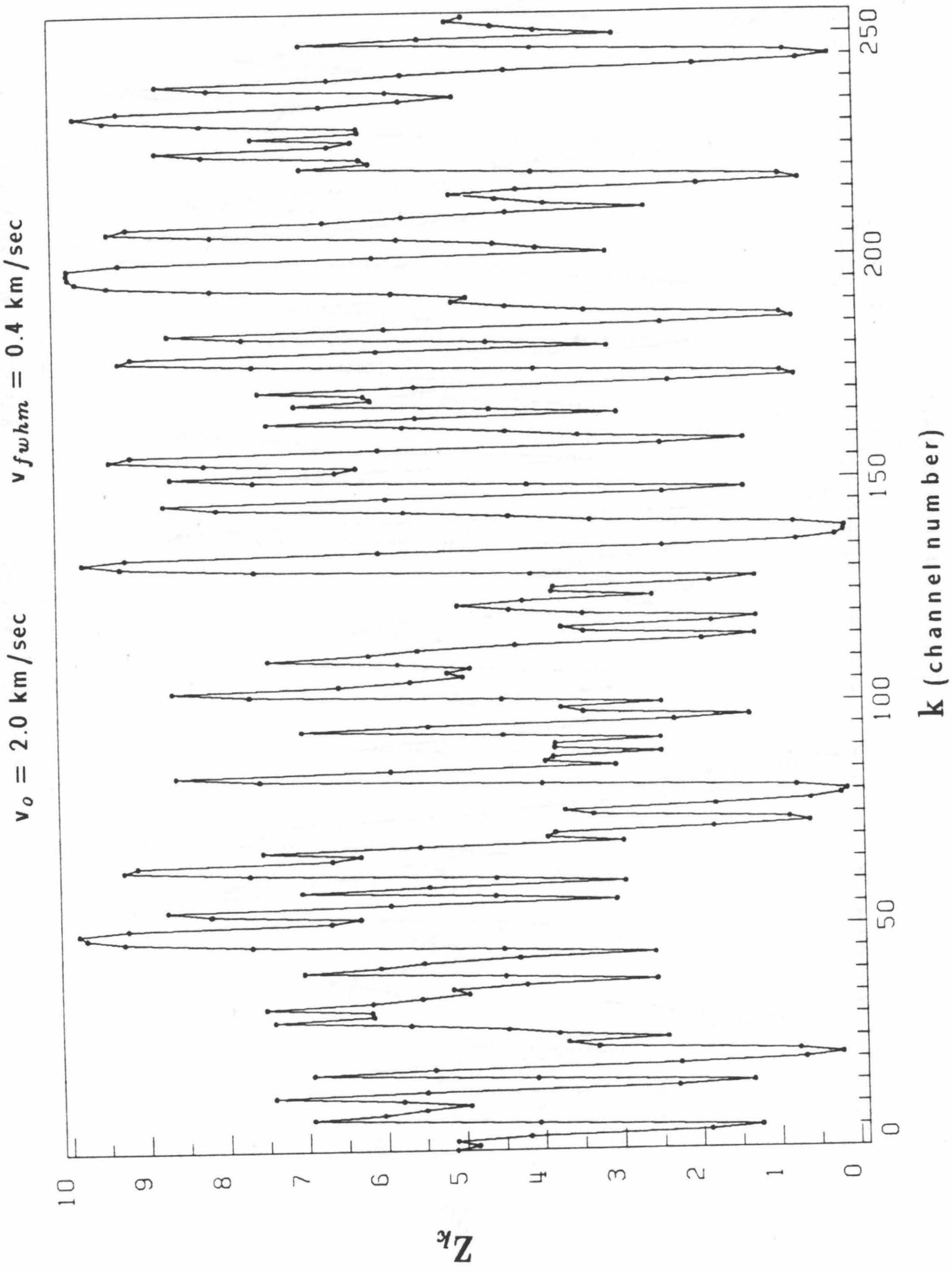

Figure 3c. Convolution of a Gaussian velocity distribution.

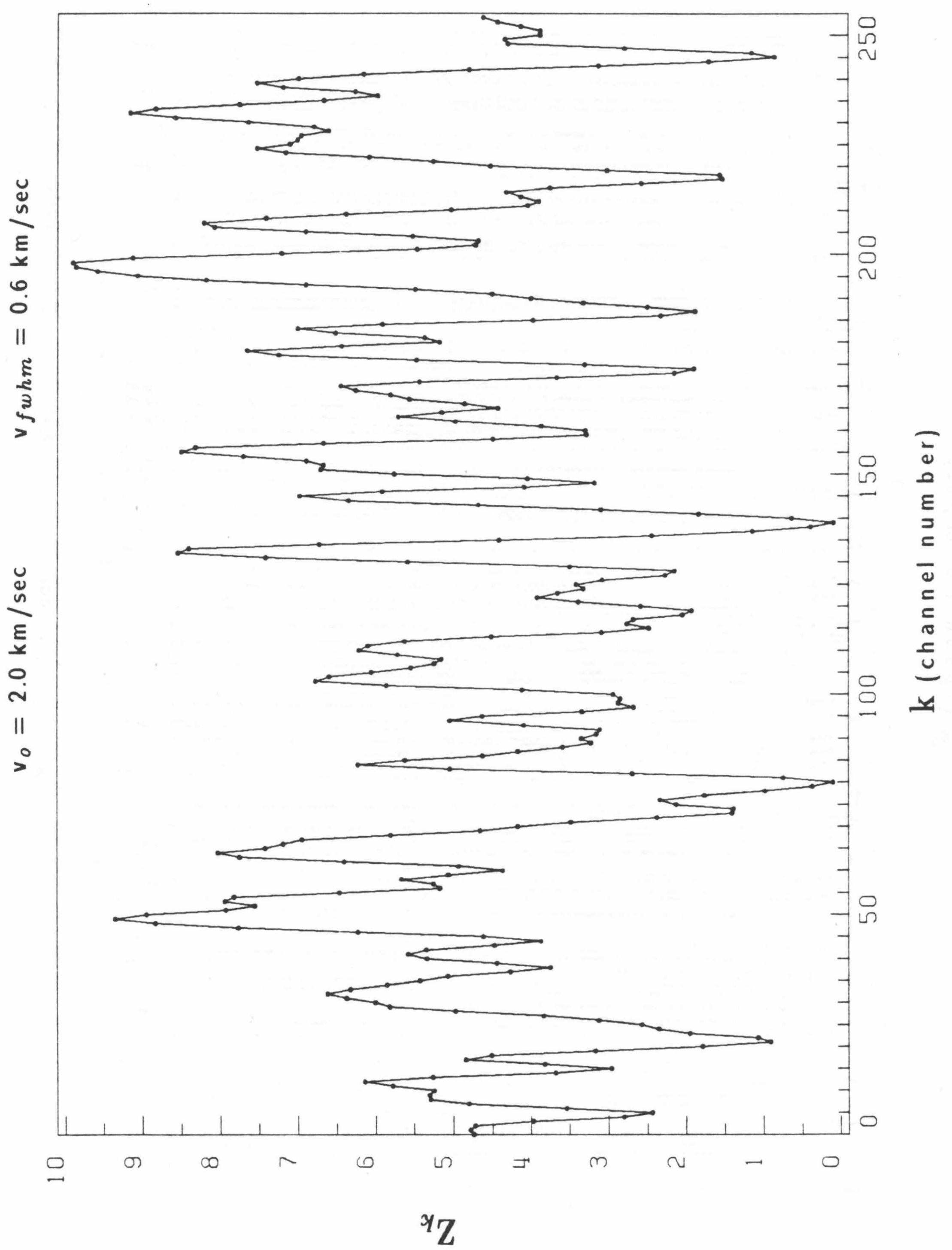

Figure 3d. Convolution of a Gaussian velocity distribution.

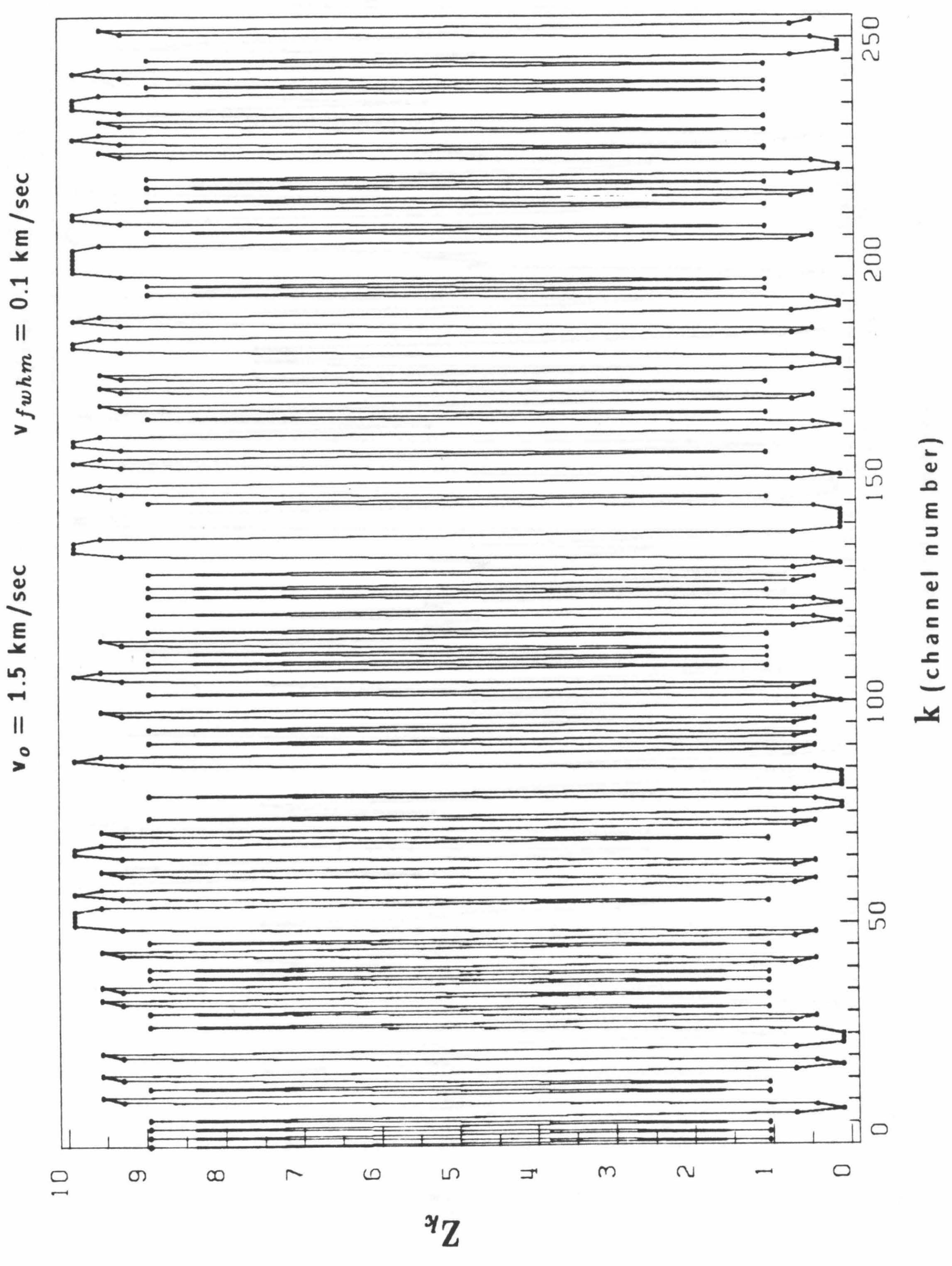

Figure 4a. Convolution of a Gaussian velocity distribution.

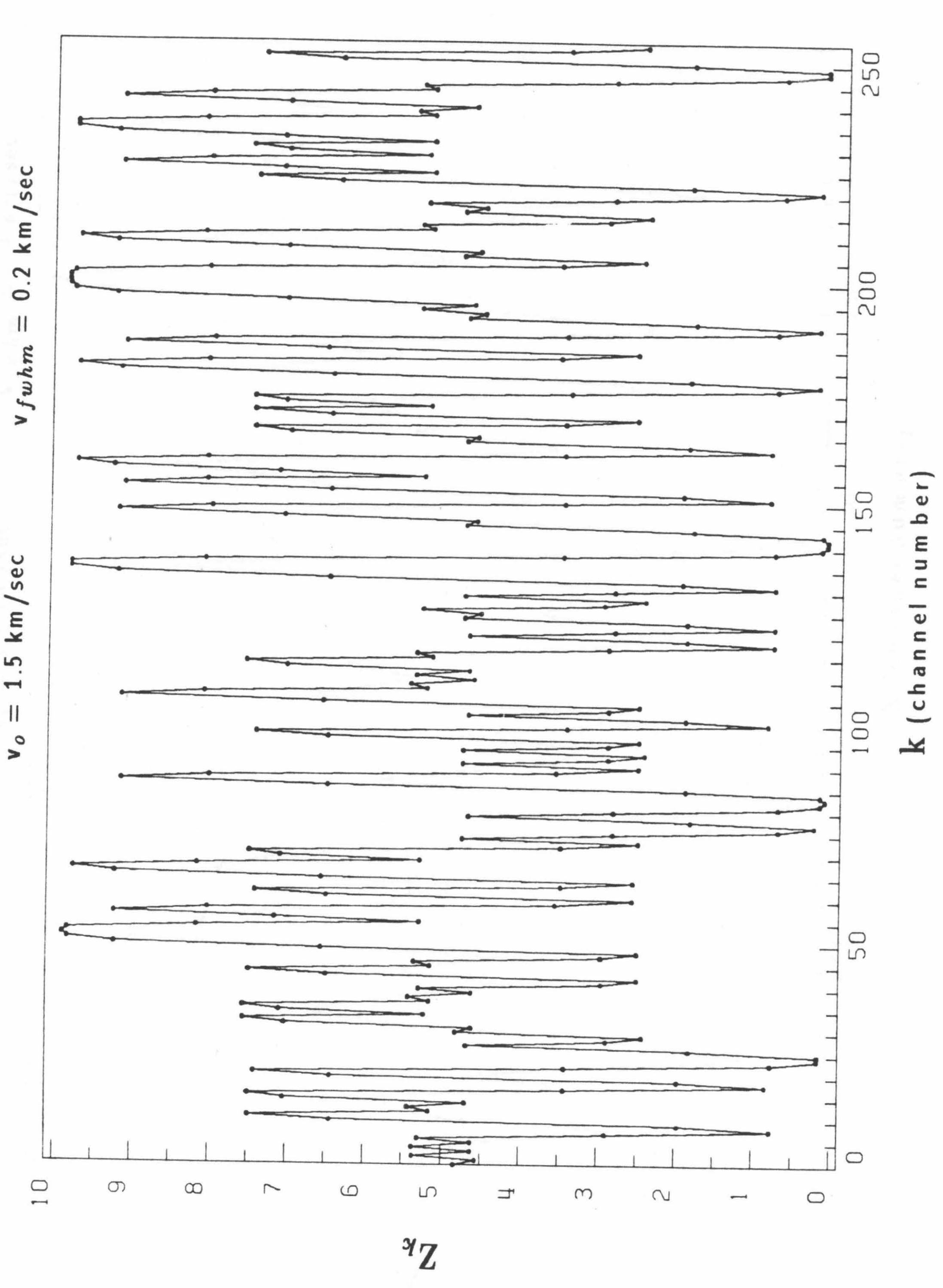

Figure 4b. Convolution of a Gaussian velocity distribution.

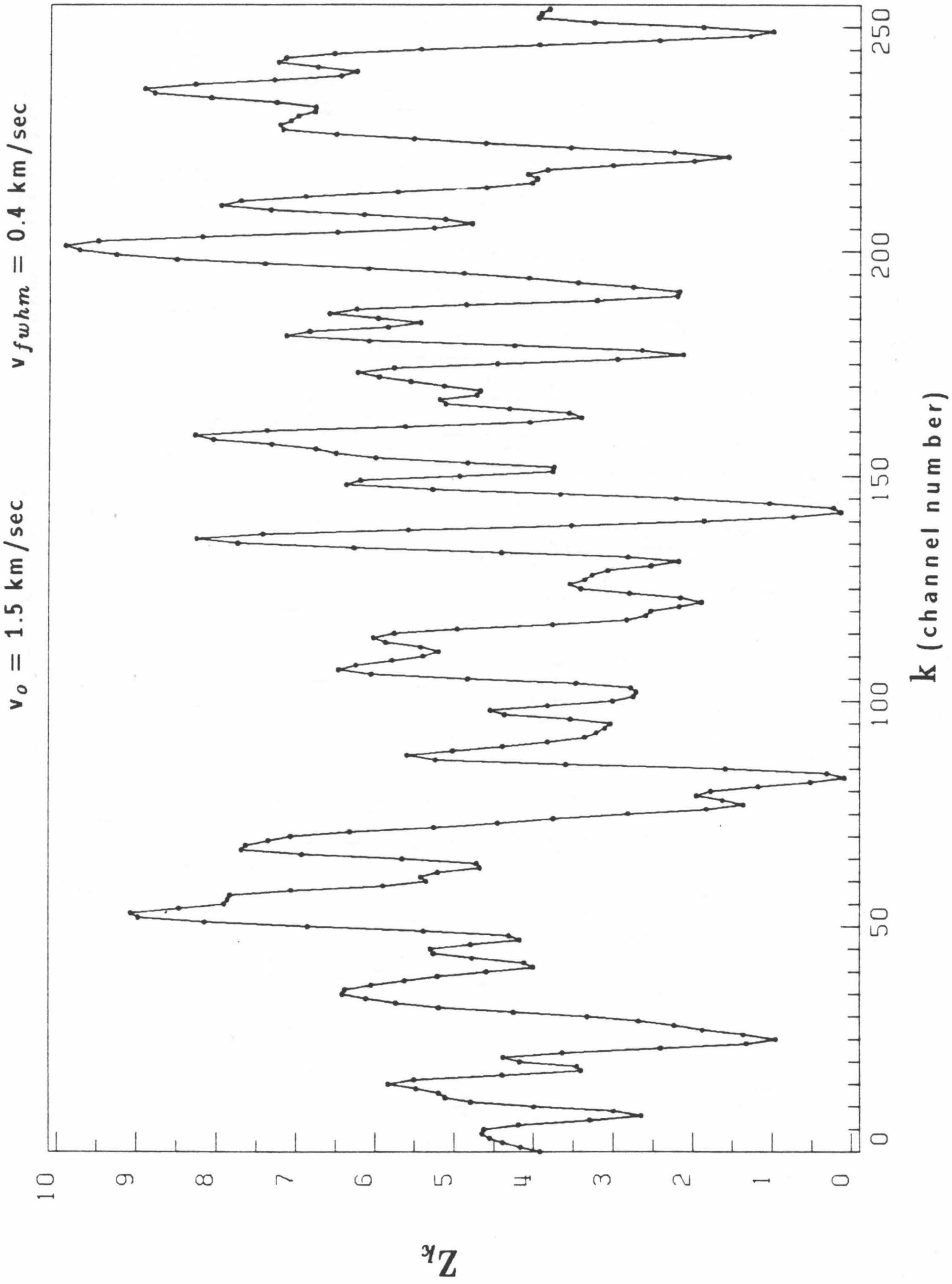

Figure 4c. Convolution of a Gaussian velocity distribution.

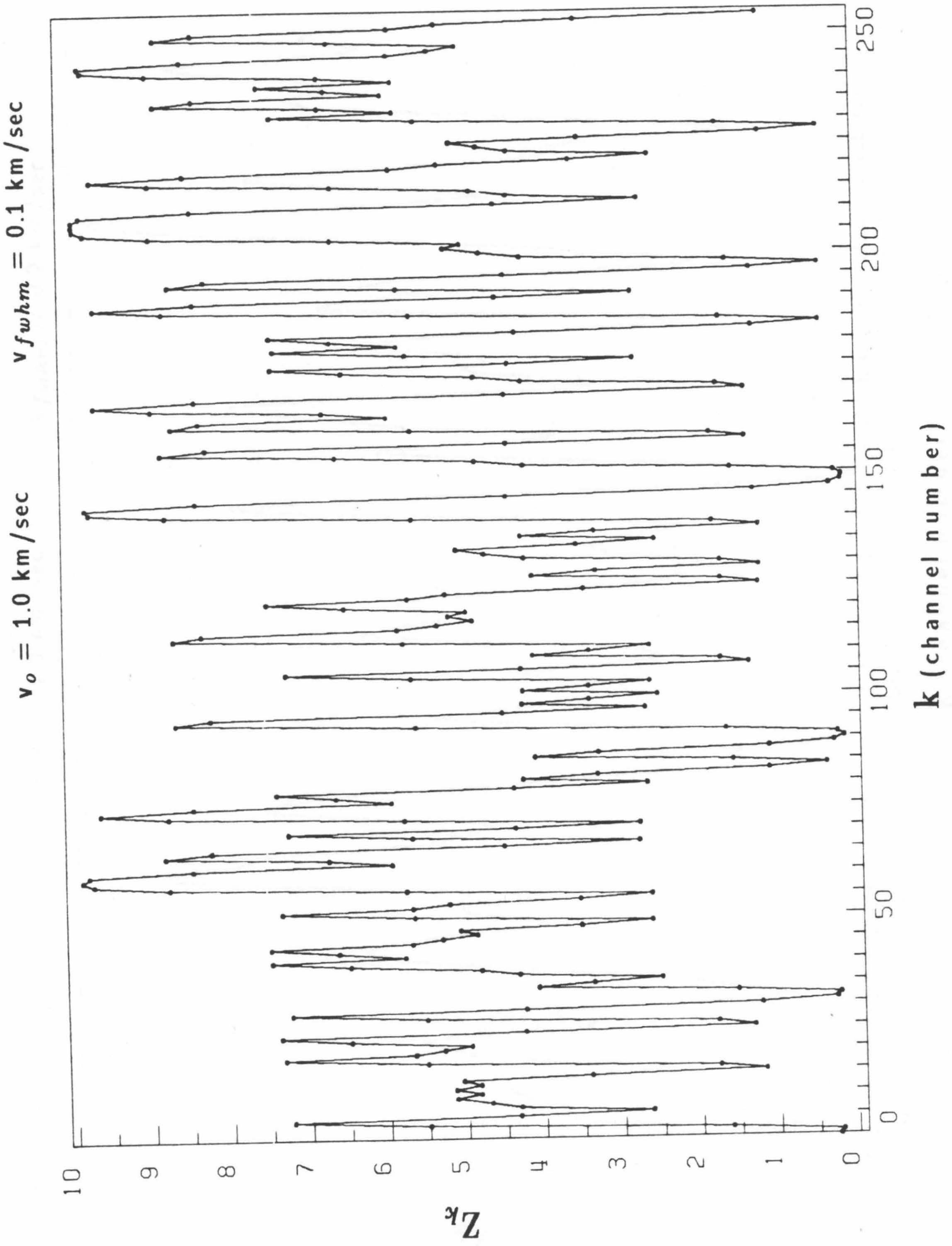

Figure 5a. Convolution of a Gaussian velocity distribution.

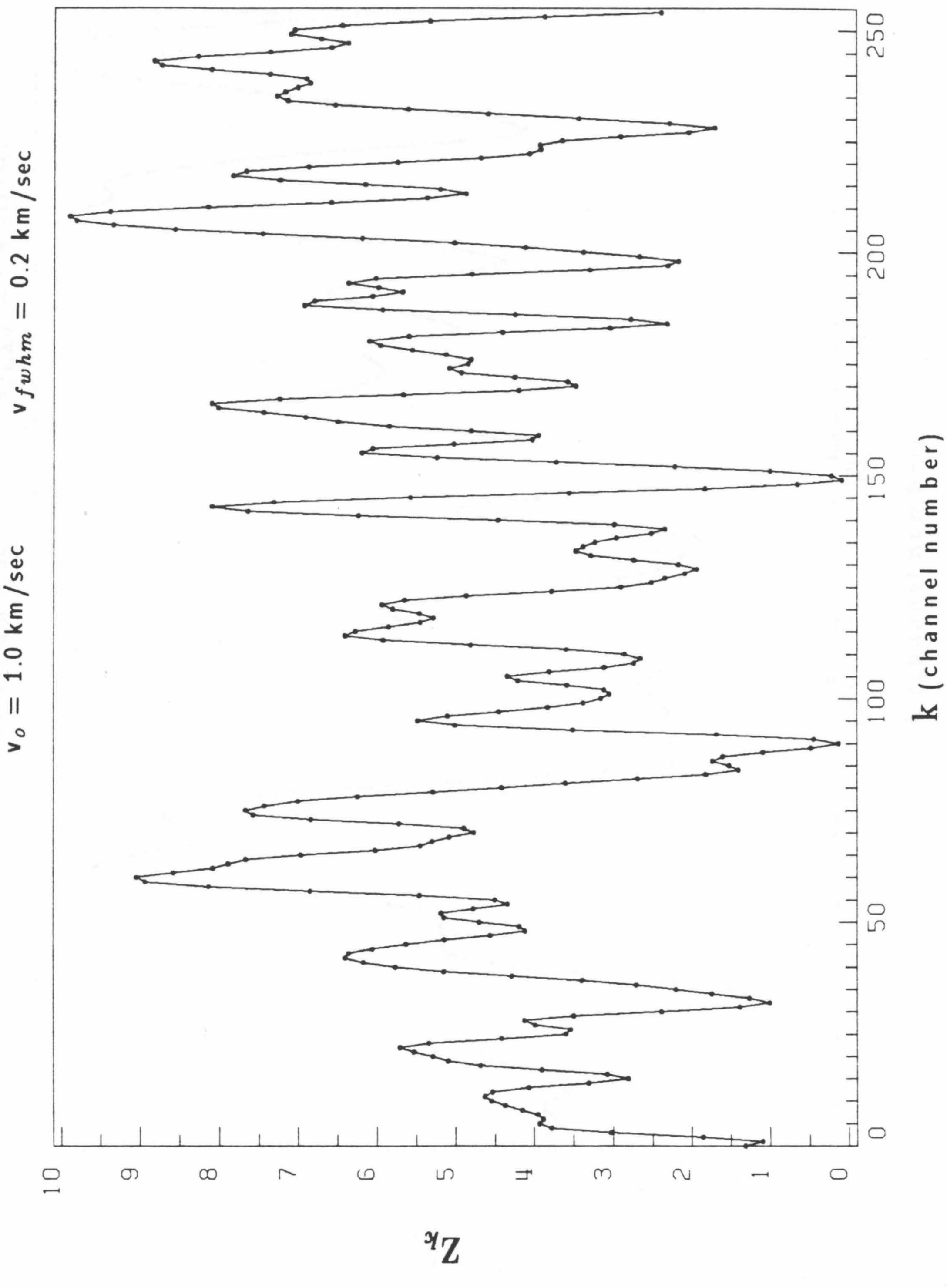

Figure 5b. Convolution of a Gaussian velocity distribution.

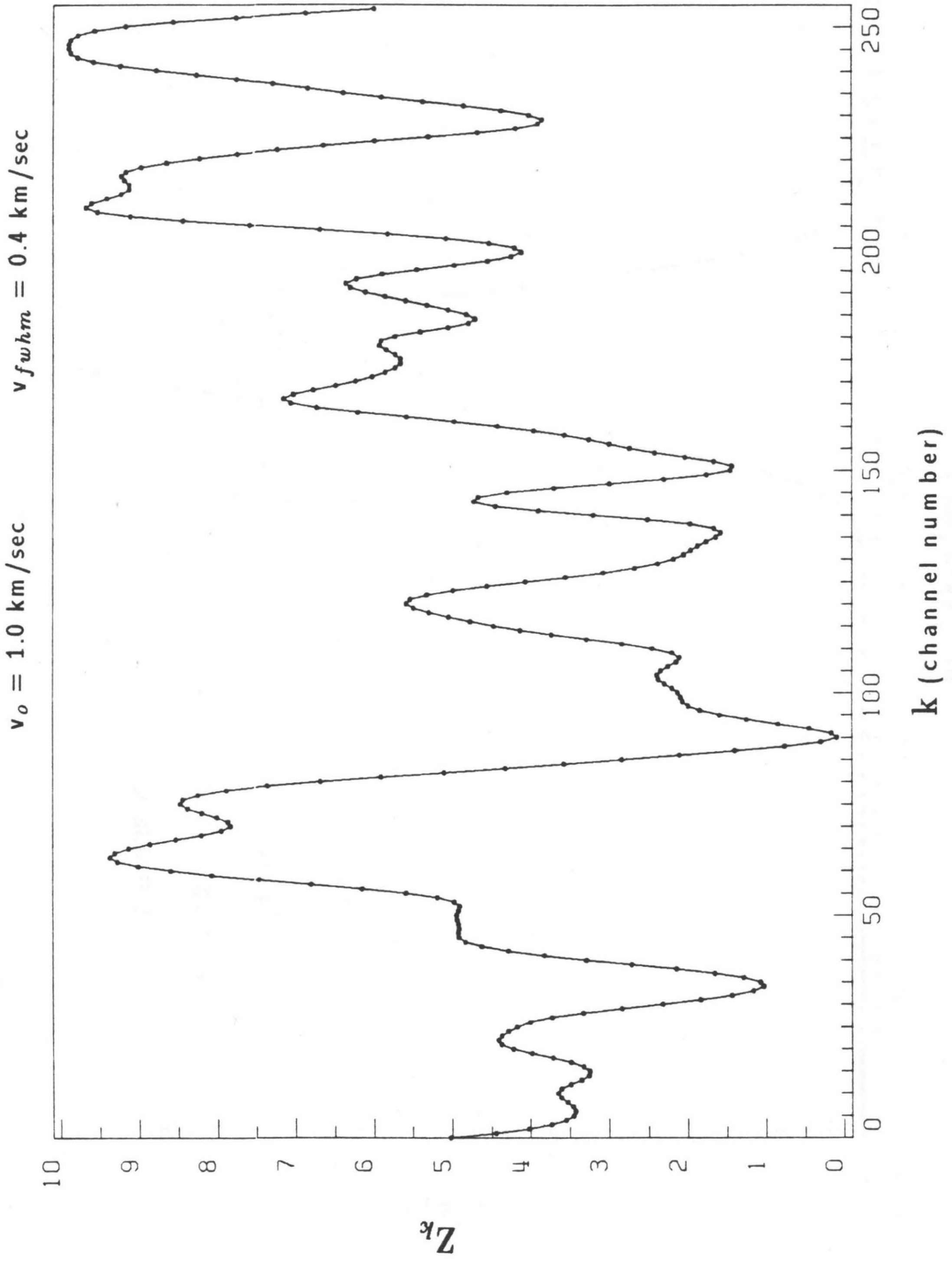

Figure 5c. Convolution of a Gaussian velocity distribution.

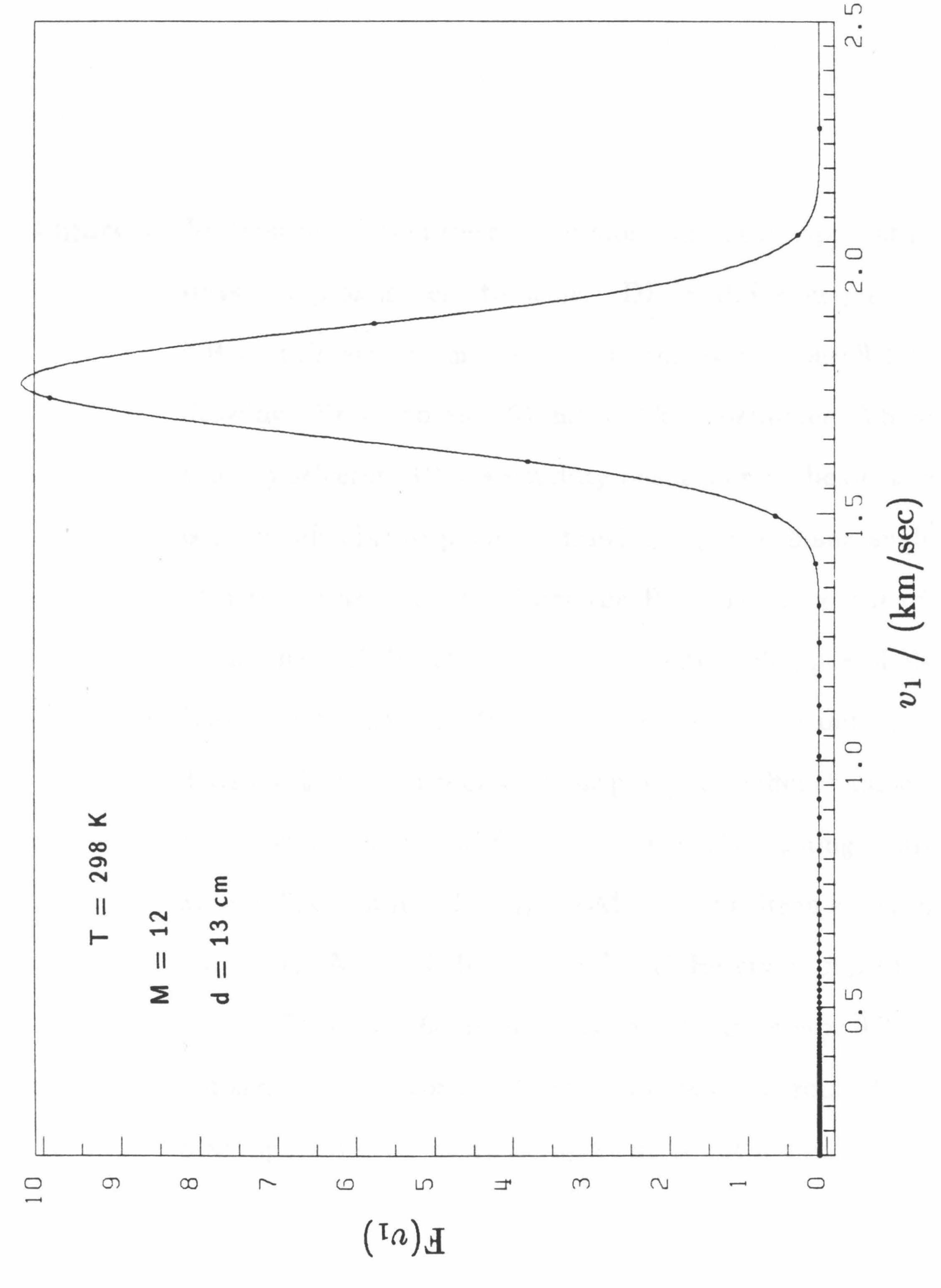

Figure 6. He velocity distribution.

Figure 7. Vertical cut view of the crossed molecular beam apparatus, drawn approximately to scale. DP = diffusion pumps, PB = primary beam source - beam axis is parallel to drawing, Nz = nozzle (64 mm), Sk = skimmer, VS = velocity selector, SB = secondary beam source - beam axis is perpendicular to plane of drawing, θ_h = in plane angle of detector as measured from the PB axis, θ_v = out-of-plane angle of detector, CC = correlation chopper blade (motor not shown), MS = mass spectrometer detector, TMP_b = 50 l/sec turbomolecular pump for buffer chamber, I = ionizer and ion focus lenses (l-N_2 cooling coils around filament not shown), CEM = Channeltron electron multiplier (Model 4816), CP = liquid He cryopump (350 l/sec), TMP = 360 l/sec turbomolecular pump, IG = ionization gauge, for clarity the gate valve in front of the mass spectrometer entrance aperture is not shown.

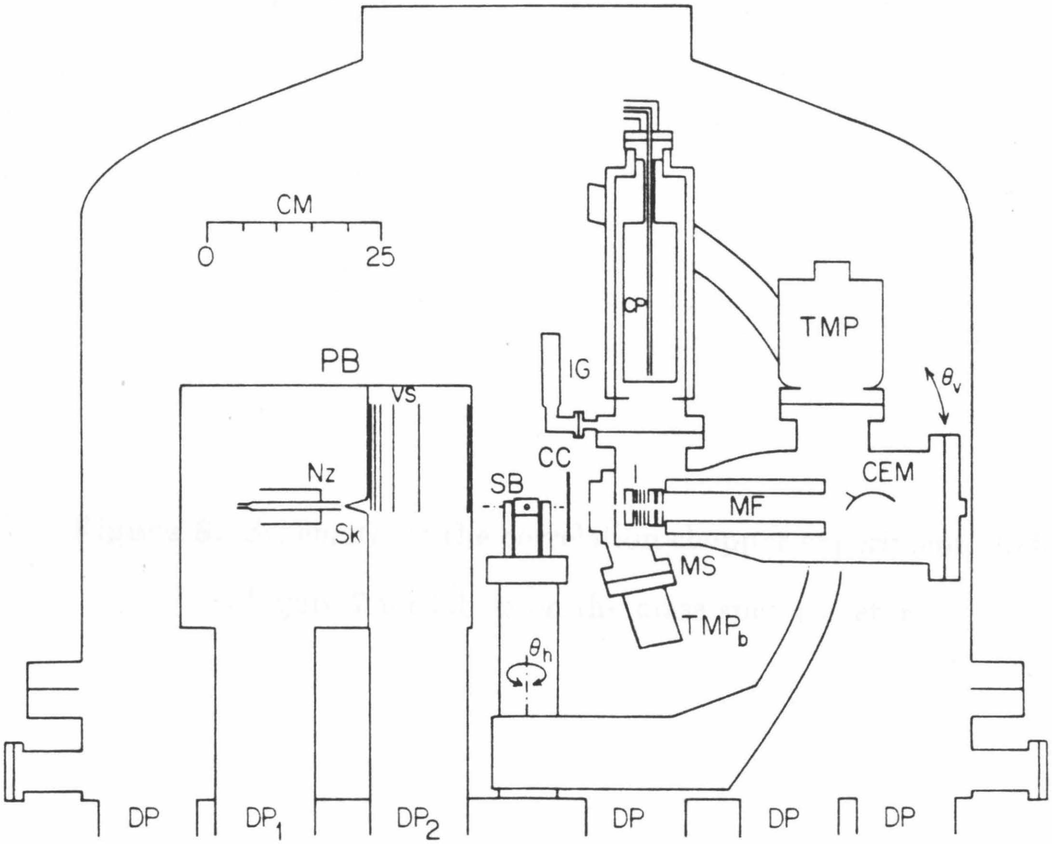
CM
0
25
PB
VS
Nz
Sk
CP
IG
CC
SB
I
TMP
θv
CEM
MF
MS
TMPb
θh
DP
DP1
DP2
DP
DP
DP

Figure 7.

Figure 8. Schematic of the correlation chopper experiment. Refer to Figure 7 for labels on the mass spectrometer.

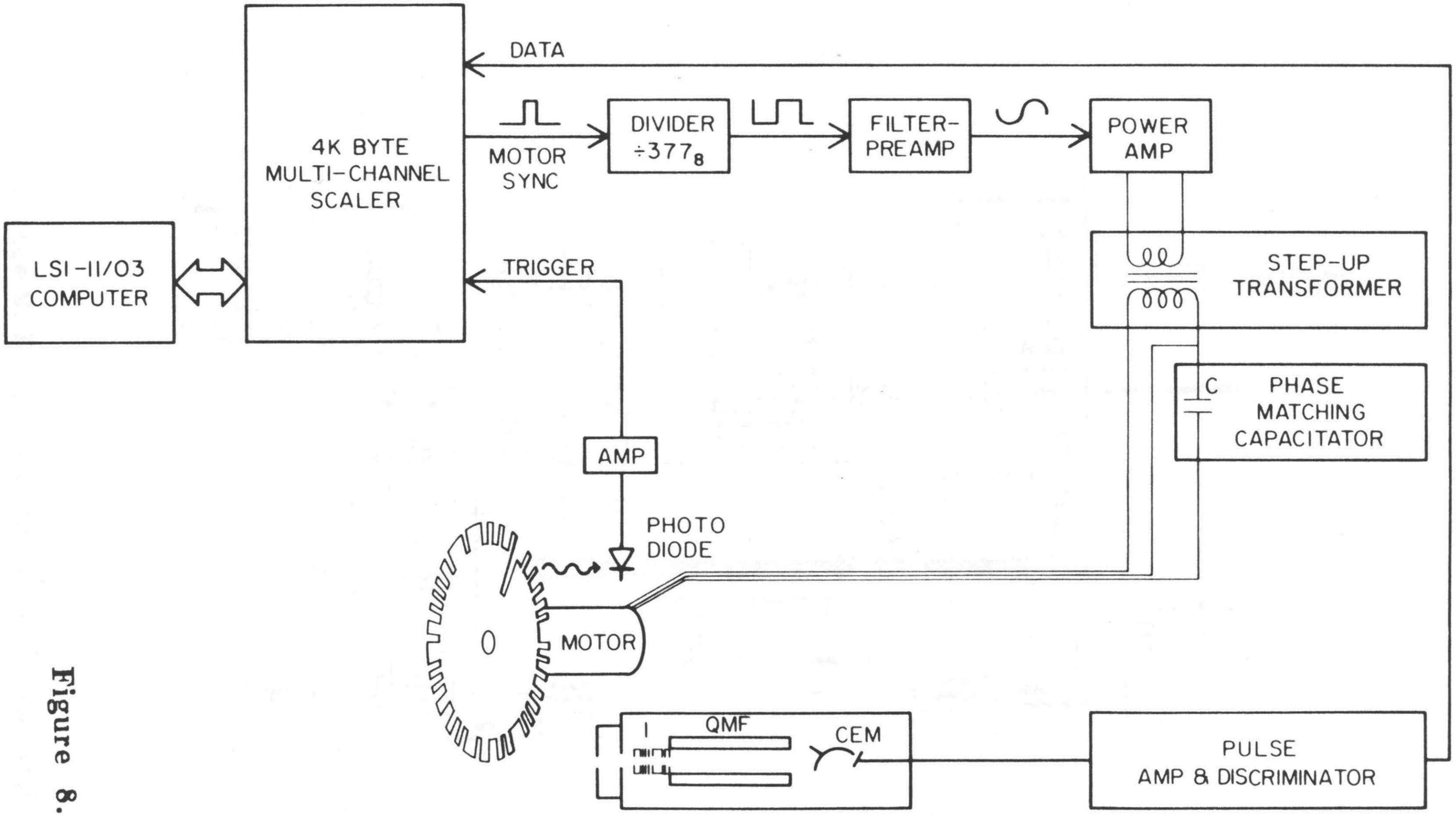
DATA
4K BYTE MULTI-CHANNEL SCALER
MOTOR SYNC
DIVIDER ÷377₈
FILTER-PREAMP
POWER AMP
LSI-11/03 COMPUTER
TRIGGER
STEP-UP TRANSFORMER
C
PHASE MATCHING CAPACITATOR
AMP
PHOTO DIODE
MOTOR
I
QMF
CEM
PULSE AMP & DISCRIMINATOR

Figure 8.

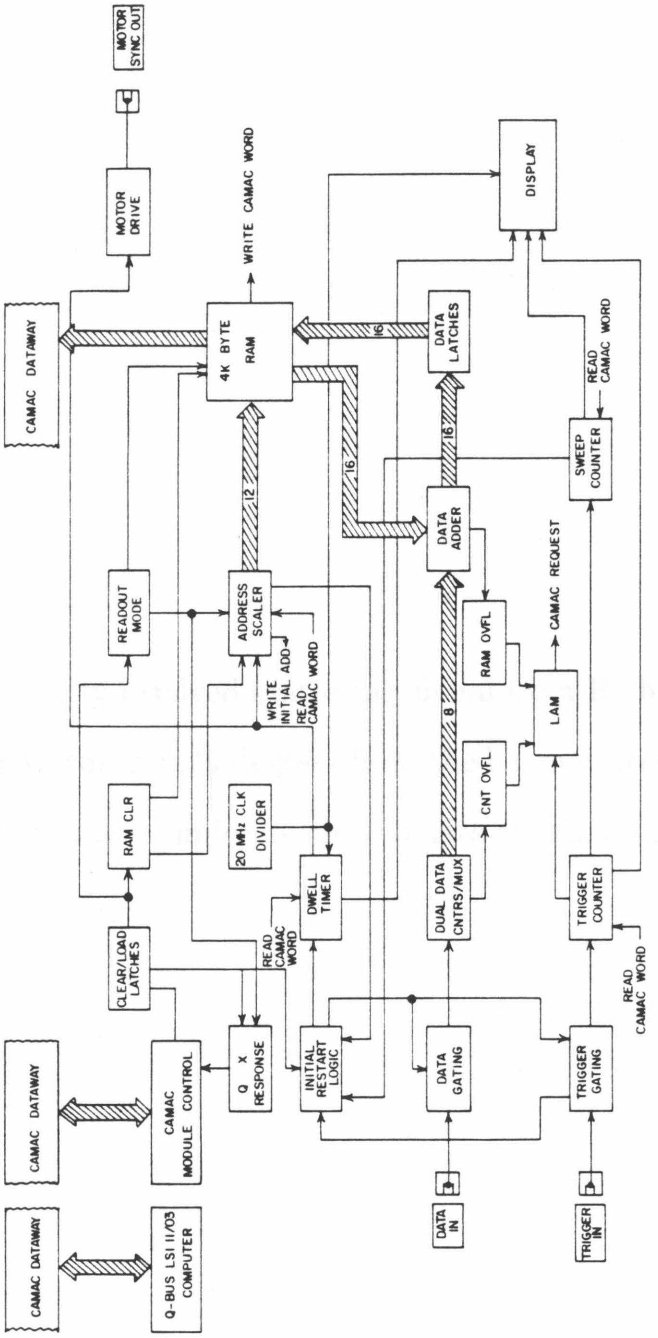

Figure 9. Schematic of the multi-channel scaler.

Figure 10. Velocity resolved scattering signal for a He beam with the detector at 0.75 degrees from the beam center, Figure 10a. The "raw" (undeconvoluted) data are shown in Figure 10b.

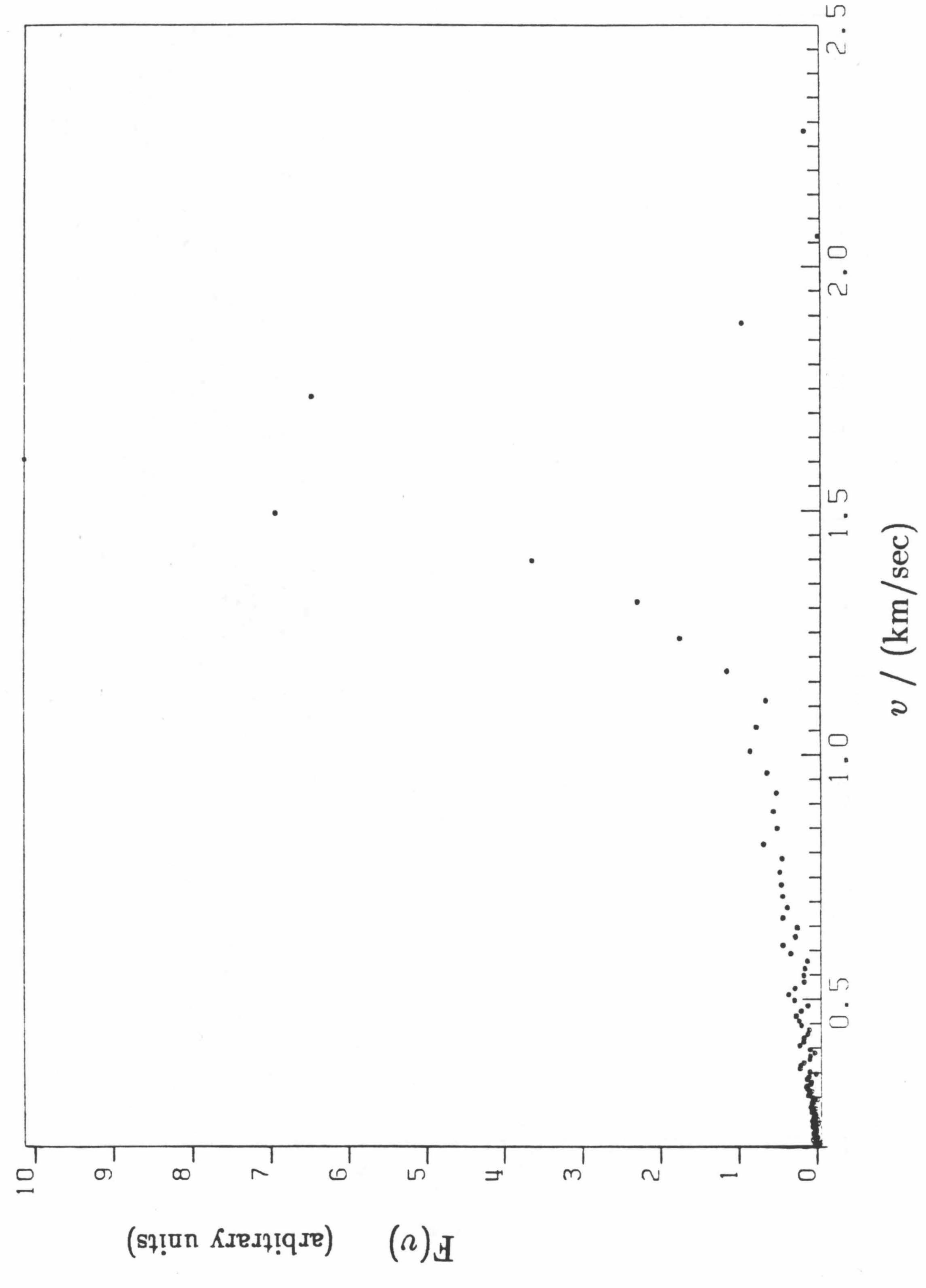

Figure 10a.

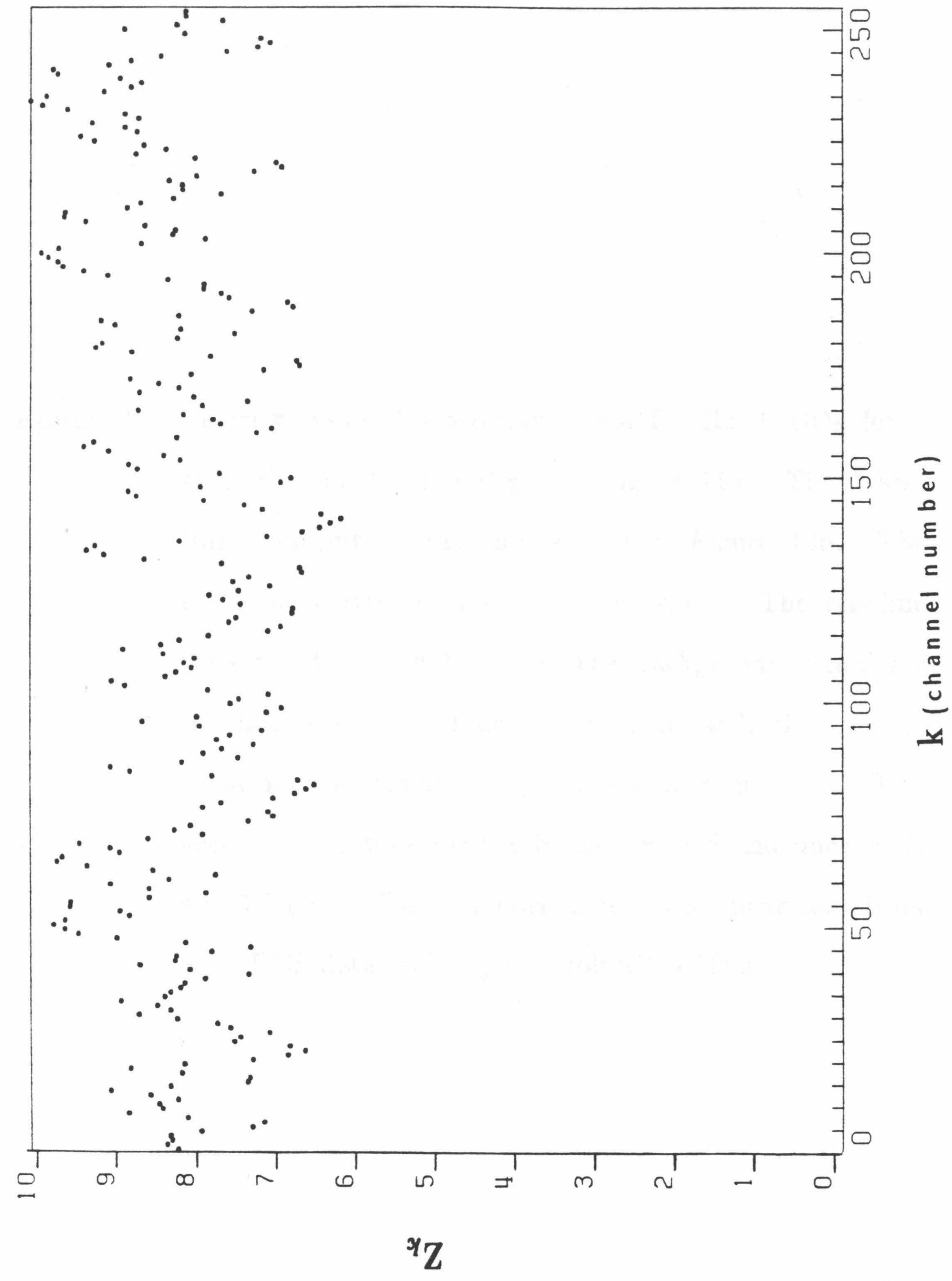

Figure 10b.

Figure 11. Velocity resolved scattering signal for He + CO_2 for a scattering angle of 5 degrees, Figure 11a. The "raw" (undeconvoluted) data are shown in Figure 10b. The full scale corresponds to 240 counts/sec. The baseline corresponds to 4260 counts, the background signal for the beams uncrossed has been subtracted, the average signal for the beams uncrossed is 1700 counts/sec. Data accumulation time for the beams crossed and uncrossed, was 3.6 hours. Relative normalization for peak area from total DCS data (velocity unresolved) is 500.0 .

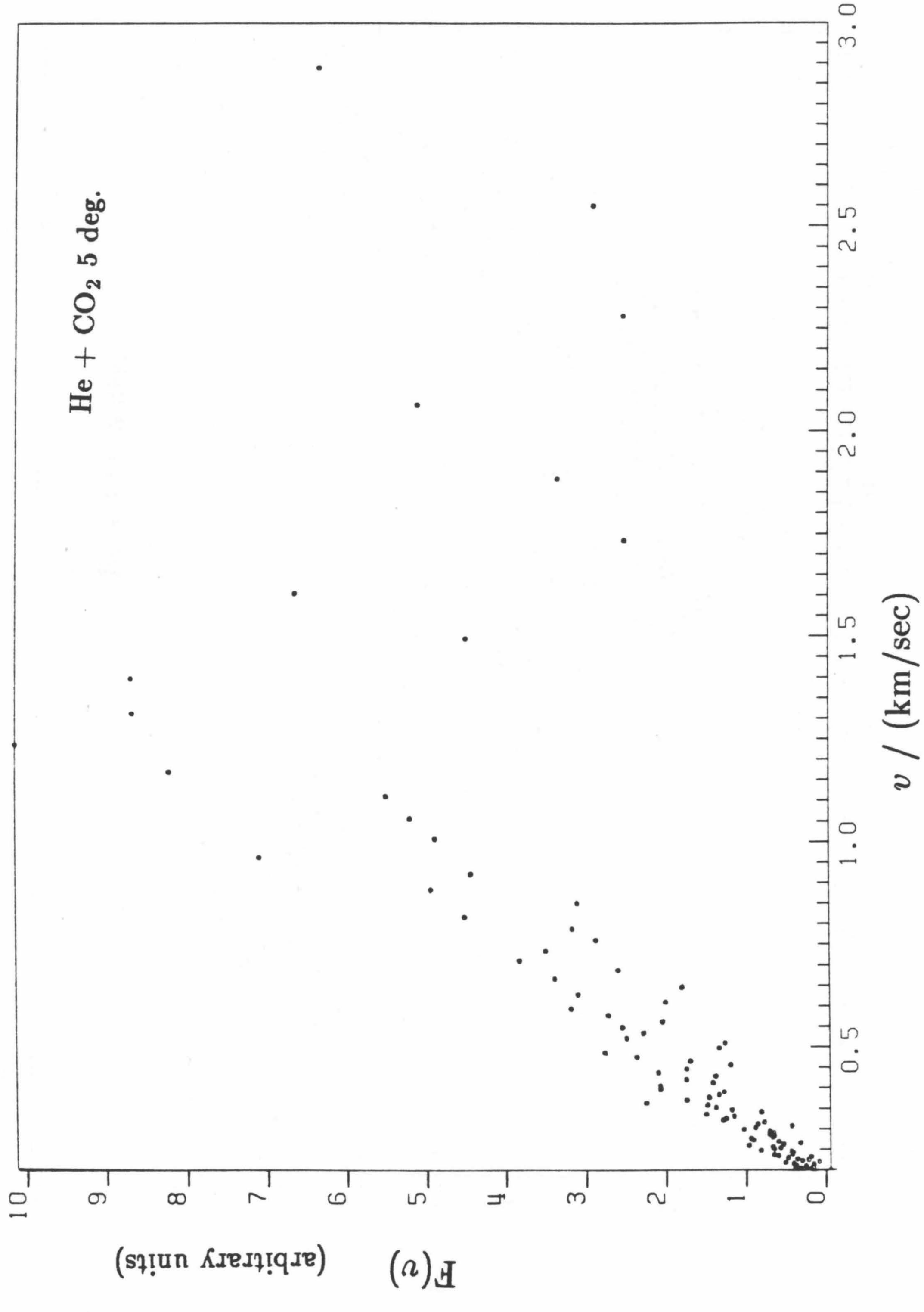
He + CO2 5 deg.
F(v)
(arbitrary units)
0
1
2
3
4
5
6
7
8
9
10
v / (km/sec)
0.5
1.0
1.5
2.0
2.5
3.0

Figure 11a.

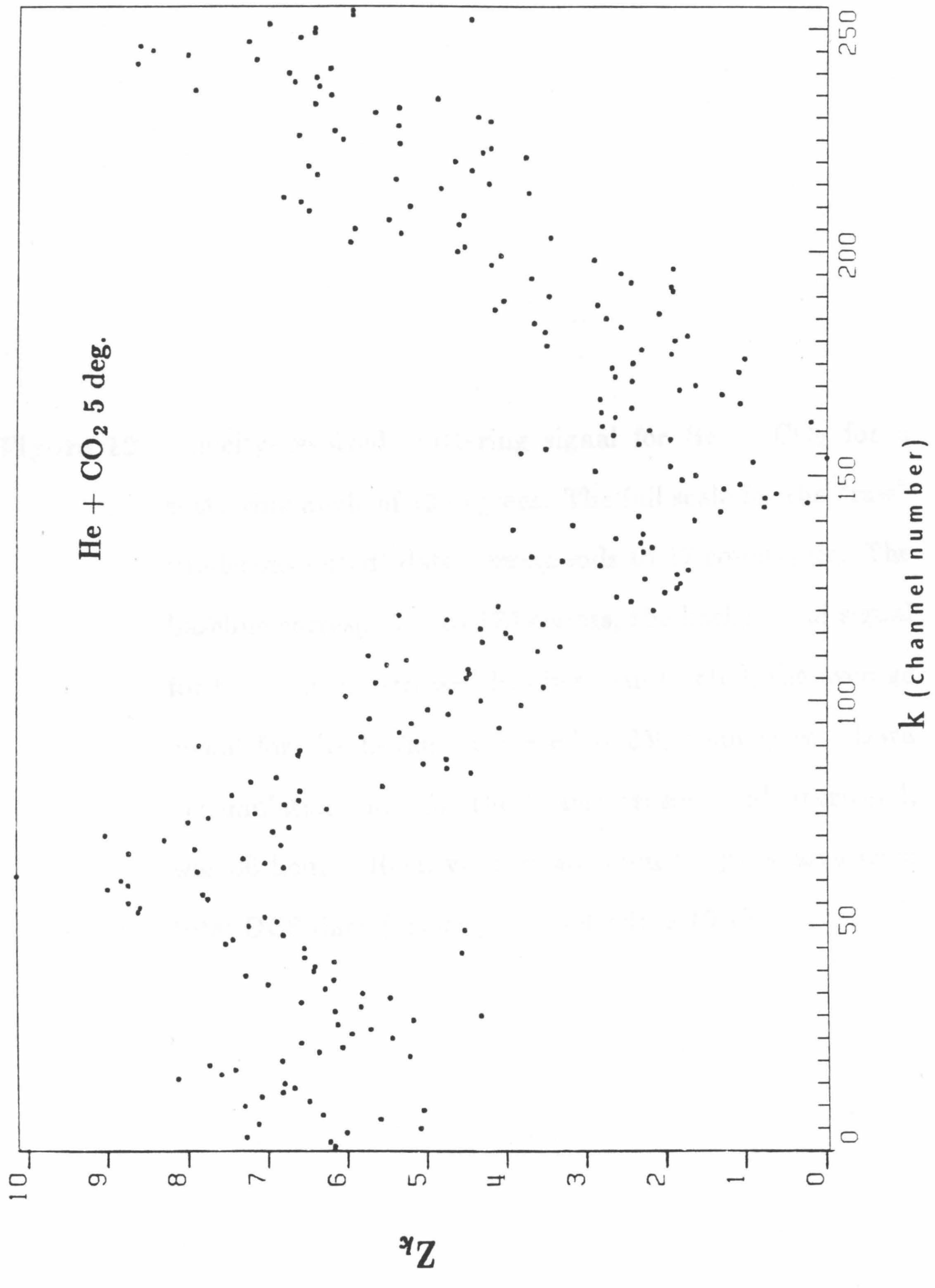
He + CO$_2$ 5 deg.
Z_k
k (channel number)
0
1
2
3
4
5
6
7
8
9
10
0
50
100
150
200
250

Figure 11b.

Figure 12. Velocity resolved scattering signal for He + CO_2 for a scattering angle of 13 degrees. The full scale for the "raw" (undeconvoluted) data corresponds to 17 counts/sec. The baseline corresponds to 170 counts, the background signal for the beams uncrossed has been subtracted, the average signal for the beams uncrossed is 330 counts/sec. Data accumulation time for the beams crossed and uncrossed, was 36 hours. Relative normalization for peak area from total DCS data (velocity unresolved) is 19.15.

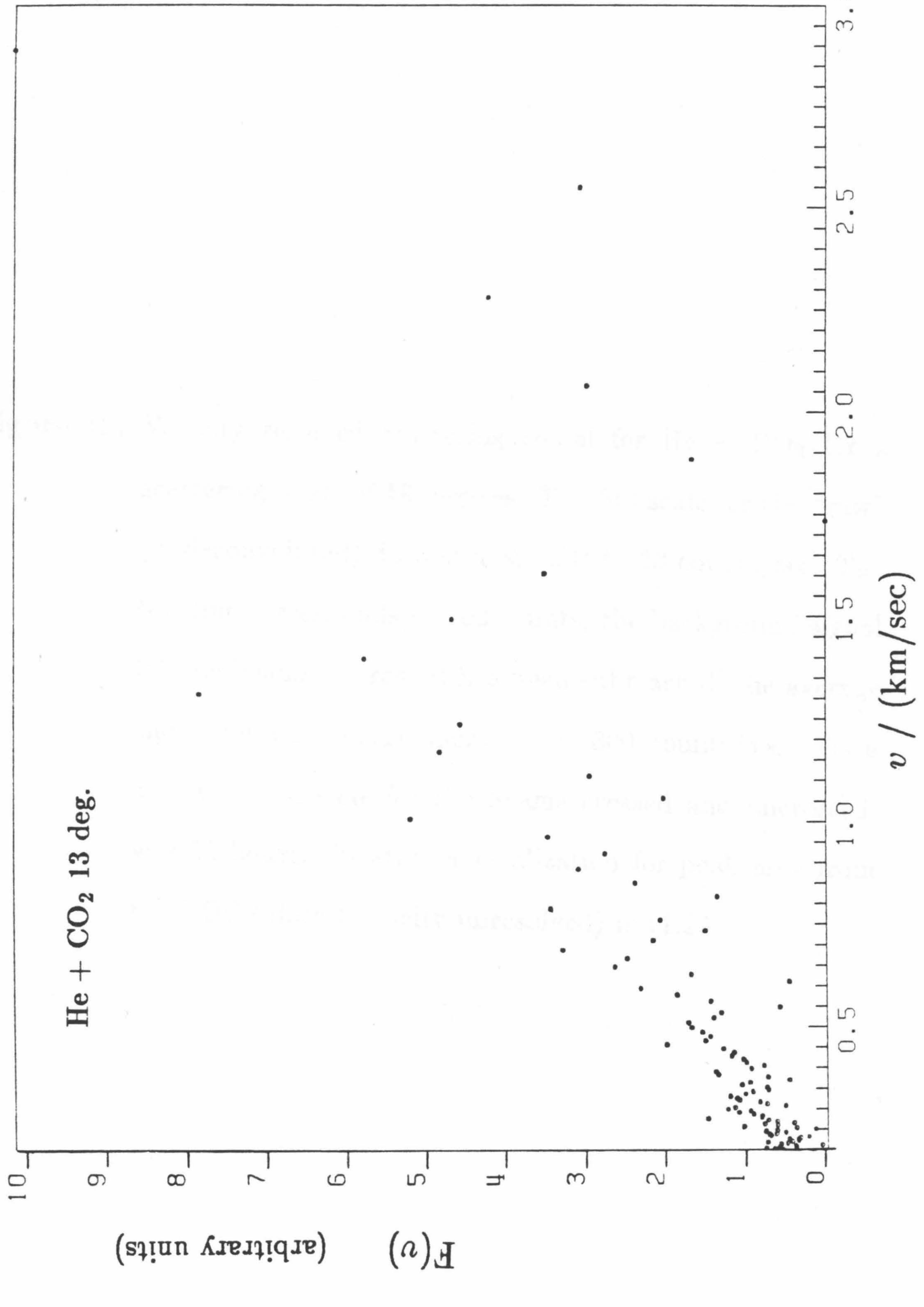
He + CO_2 13 deg.
v / (km/sec)
0.5
1.0
1.5
2.0
2.5
3.0
$F(v)$
(arbitrary units)
0
1
2
3
4
5
6
7
8
9
10

Figure 12.

Figure 13. Velocity resolved scattering signal for He + CO_2 for a scattering angle of 18 degrees. The full scale for the "raw" (undeconvoluted) data corresponds to 23 counts/sec. The baseline corresponds to 102 counts, the background signal for the beams uncrossed has been subtracted, the average signal for the beams uncrossed is 300 counts/sec. Data accumulation time for the beams crossed and uncrossed, was 30 hours. Relative normalization for peak area from total DCS data (velocity unresolved) is 11.29.

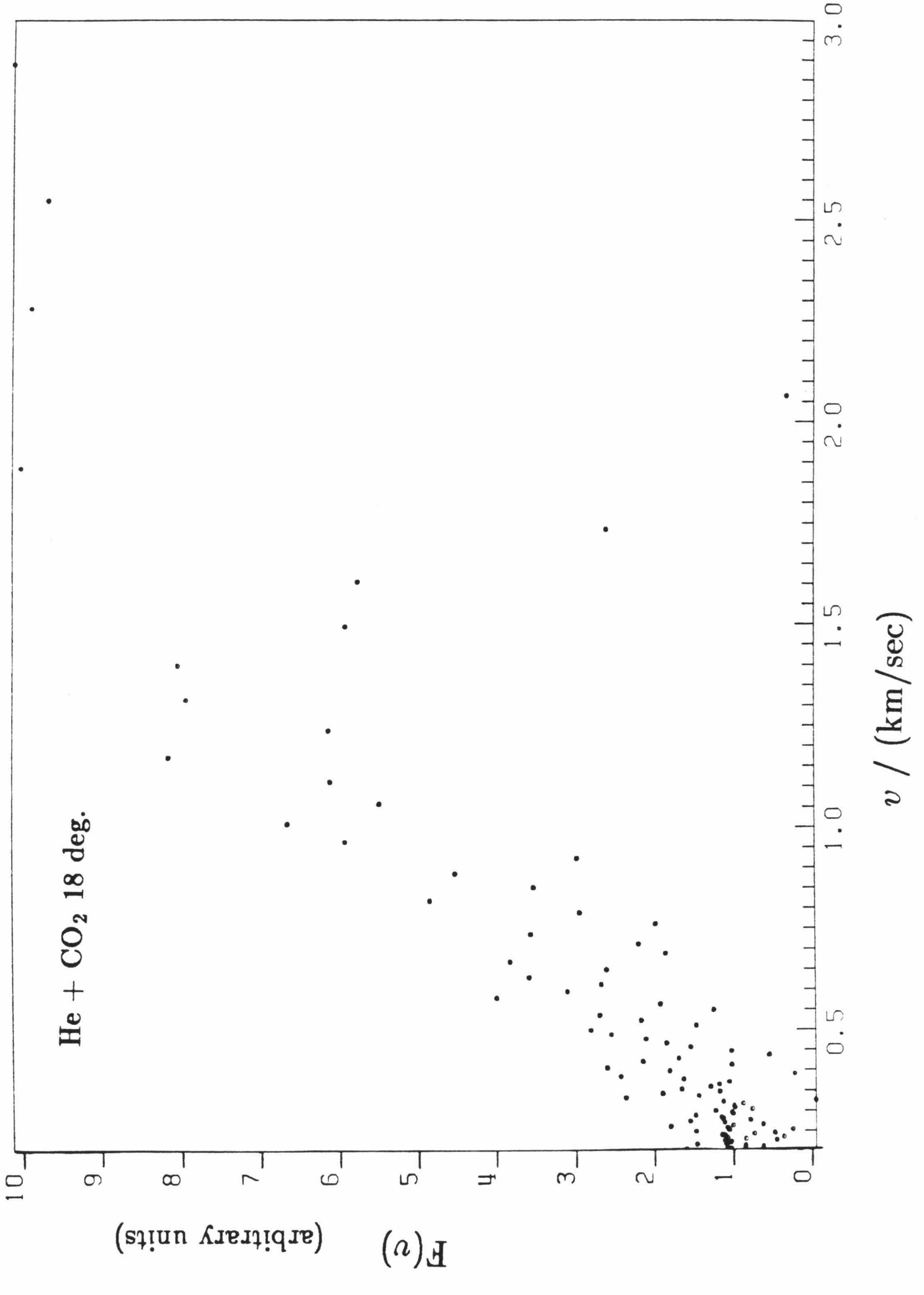
He + CO_2 18 deg.
0
1
2
3
4
5
6
7
8
9
10
$F(v)$
(arbitrary units)
0.5
1.0
1.5
2.0
2.5
3.0
v / (km/sec)

Figure 13.